Title
Criticality in the Far-Field of a Granitic Repository for Used Nuclear Fuel

Author
Salazar, Alex

Publication Date
2018

Criticality in the Far-Field of a Granitic Repository for Used Nuclear Fuel

by

Alex Salazar III

A dissertation submitted in partial satisfaction of the

requirements for the degree of

Doctor of Philosophy

in

Engineering – Nuclear Engineering

in the

Graduate Division

of the

University of California, Berkeley

Committee in charge:

Assistant Professor Massimiliano Fratoni, Chair
Professor John Arnold
Dr. Jens Birkholzer

Summer 2018

Criticality in the Far-Field of a Granitic Repository for Used Nuclear Fuel

Abstract

Criticality in the Far-Field of a Granitic Repository for Used Nuclear Fuel

by

Alex Salazar III

Doctor of Philosophy in Engineering – Nuclear Engineering

University of California, Berkeley

Assistant Professor Massimiliano Fratoni, Chair

A repository for used nuclear fuel (UNF) must employ several barriers to reduce the risk of a lethal dose to the biosphere over geological periods of time. It is presumed that waste canisters can be engineered to prevent a critical configuration of fissile material by design. However, given the quantity of UNF in interim storage in the United States intended for final deposition, a comprehensive failure scenario involving the repository-wide leaching of fissile isotopes from used fuel, radionuclide transport in groundwater, and re-concentration in the far-field may eventually present a concern for criticality. Such a criticality event may create a pathway for fission products to the environment if the host rock is compromised.

This dissertation explores the impact of far-field criticality on repository performance over long periods of time. It attempts to integrate all necessary processes and considerations under a notion of conservatism favoring the formation of a critical mass from used nuclear fuel. A critical deposition is hypothesized to pose a threat to the material integrity of the host rock through the steady release of heat over time, as opposed to the explosive releases of energy considered in previous studies. In particular, the role of thermal creep is evaluated as a steady-state failure metric, which emphasizes the combined role of reactivity feedback mechanisms and heat transfer in determining the temporal extent of chain reactions underground.

The failure scenario is isolated among other relevant features, events, and processes as the primary concern of the performance assessment for a crystalline granitic repository. Repository loading cases are established based on the uncertainty in the current inventory of used nuclear fuel. These source terms are used in a radionuclide transport model that incorporates the Latin hypercube sampling method to probe the uncertainty in the total accumulation of uranium from advection in fractures. The configurations of fissile material in host rock required for criticality are evaluated based on representative precipitate compositions obtained from the transport analysis, where the role of a reducing and reflecting region of shale is emphasized.

Given the nature of the critical depositions as both open reactor systems and porous media, a thermo-hydrological analysis is employed to evaluate the coupled heat and mass transfer in the geology when energy is released from fission reactions. This analysis is motivated by the assumption that reactivity behavior with evolving water content and temperature must be fully coupled, and boundary conditions are imposed to evaluate a maximal extent of desaturation. The observed changes in fluid content and densities in the system over time are used to guide an integrated neutronics evaluation incorporating the Doppler effect.

Feedback coefficients covering the simultaneous effects of Doppler broadening, the loss of moderator, and the arriving plume of uranium solutes from the repository array are applied to a quasi-steady-state heat transfer model. This model provides insight on the dynamic evolution of system temperature over time parametrized on the source term of incoming fissile material, and results are applied to a thermal creep model to evaluate total integrated strain and system failure. Given the time dependence of the creep phenomenon, optimal source terms of fissile material may be conducive to failure via creep. However, these mass fluxes exceed those observed in the transport analysis, which employed assumptions to maximize these quantities.

The conditions under which repository performance can be impacted by steady-state criticality prove to be heavily dependent on the repository inventory and the specific choice of host rock. This mandates that a site intended for final UNF disposition be subject to increasing scrutiny in proportion to the amount of waste that is loaded. Based on the results of the study, it is strongly proposed that the threat of a far-field criticality event can be dramatically reduced by the introduction of depleted uranium to waste canisters. Overall, given the compounded effect of utilizing many heavily conservative assumptions in the study, the far-field criticality phenomenon is not deemed to be of especial importance to repository engineering, especially with additional enhancements to existing engineered barrier systems.

In memory of
Professor Joonhong Ahn

Contents

Abstract

Contents . . . . **ii**

Nomenclature . . . . **vii**

List of Tables . . . . **xi**

List of Figures . . . . **xiv**

Acknowledgments . . . . **xxi**

1 Introduction **1**
  1.1 State of the art 2
  1.2 Scope of the dissertation 3
  1.3 Methodology 5

2 The source term of used nuclear fuel **7**
  2.1 Introduction 7
  2.2 Background 8
  2.3 Used nuclear fuel 9
    2.3.1 Data sets 9
    2.3.2 Representative cases 11
  2.4 Nuclide inventory of used fuel assembly 13
    2.4.1 Setup 13
    2.4.2 Results 17
  2.5 Discussion 19

3 Uncertainty analysis of far-field precipitation **21**
  3.1 Introduction 21
  3.2 Background 22
    3.2.1 Natural analog 22
    3.2.2 Previous work 22

3.3 Methodology 23
3.3.1 Overview 23
3.3.2 Radionuclide transport in fractures 24
3.3.3 Variation in transport properties 29
3.3.4 Latin hypercube sampling 35
3.3.5 Source term and repository tunnel layout 37
3.4 Results 43
3.4.1 Overview 43
3.4.2 Nuclide behavior among the sampling cases 44
3.4.3 Effect of the UNF subsets and heterogeneity 45
3.4.4 Fluxes 50
3.4.5 Representative precipitates 52
3.5 Discussion 53

4 Critical configurations in the host rock 57
4.1 Introduction 57
4.2 Background 58
4.3 Methodology 60
4.3.1 Parametrization 60
4.3.2 Computation 60
4.3.3 Configurations 62
4.3.4 Host rock conditions at the precipitate location 63
4.3.5 Material compositions 64
4.4 Results 67
4.4.1 Optimal aperture of the fractured geometry 67
4.4.2 Scope of critical masses 68
4.4.3 Moderator defect 73
4.4.4 Reactivity feedback effect of enriched repository plume 77
4.4.5 Reactivity feedback effect of a U-238-dominated plume 78
4.4.6 Thermal expansion 80
4.4.7 Neutron thermalization and the prompt removal lifetime 81
4.4.8 Benchmarking 84
4.5 Discussion 84

5 Depletion analysis 92
5.1 Overview 92
5.2 Background and methodology 92
5.2.1 Overview 92
5.2.2 Power output 93
5.2.3 Computation 95
5.3 Results 96
5.3.1 Fission power distribution 96

- 5.3.2 Multiplication and burnup . . . 98
- 5.3.3 Fissile content . . . 99
- 5.3.4 Radioactivity . . . 101
- 5.3.5 A note on hazard . . . 105
- 5.4 Discussion . . . 107

6 Unsaturated heat and mass transport . . . 109
- 6.1 Introduction . . . 109
- 6.2 Methodology . . . 109
  - 6.2.1 Overview . . . 109
  - 6.2.2 Problem setup . . . 114
  - 6.2.3 Material parameters . . . 116
  - 6.2.4 Source term . . . 118
  - 6.2.5 Computation . . . 119
- 6.3 Results . . . 120
  - 6.3.1 Optimal power levels . . . 120
  - 6.3.2 Temperature and saturation . . . 122
- 6.4 Discussion . . . 125

7 Reactivity feedback in unsaturated critical mass . . . 129
- 7.1 Introduction . . . 129
- 7.2 Methodology . . . 129
  - 7.2.1 Computation . . . 129
  - 7.2.2 Extension of temperature results . . . 131
  - 7.2.3 Doppler broadening . . . 133
  - 7.2.4 Regression . . . 134
- 7.3 Results . . . 135
  - 7.3.1 Homogeneous . . . 135
  - 7.3.2 Fractured . . . 136
  - 7.3.3 Dry critical configurations . . . 138
  - 7.3.4 Regression . . . 138
  - 7.3.5 Temperature defect . . . 143
  - 7.3.6 Effective cross sections . . . 144
- 7.4 Discussion . . . 145

8 Dynamics of critical mass at quasi-steady-state . . . 149
- 8.1 Introduction . . . 149
- 8.2 Model . . . 150
  - 8.2.1 Scenario . . . 150
  - 8.2.2 Reactivity balance . . . 151
  - 8.2.3 Power . . . 153
  - 8.2.4 Lumped capacitance approach . . . 154

8.2.5 Heat transfer 157
8.2.6 Integration 163
8.2.7 Initial conditions 165
8.3 Results 166
8.3.1 TTB source terms 166
8.3.2 Modified source terms 168
8.3.3 Limitations 176
8.4 Discussion 176

9 Failure via thermal creep 179
9.1 Introduction 179
9.2 Methodology 180
9.3 Results 181
9.3.1 Enhanced uranium source terms 181
9.3.2 Pu-239 source terms 182
9.3.3 Worst-case scenario 182
9.3.4 Sensitivity 184
9.4 Discussion 184

10 Integrated conclusions 187
10.1 Summary 187
10.2 A proposed canister modification 190
10.3 Recommendations for future studies 191
10.3.1 Site-specific data 191
10.3.2 Modeling of fractures 192
10.3.3 Modeling of the unsaturated precipitate 194
10.3.4 Neutronics 195
10.3.5 Feedback 195

References 197

A Material composition development 208
A.1 Input 208
A.2 Script 210

B MCNP Input 227

C TOUGH2 parametric study 242
C.1 Effect of λ 242
C.2 Effect of the air entry value 243
C.3 Effect of thermal conductivity 245
C.4 Discussion 246

D Analytical studies of the QSS model 247
D.1 System with fuel and lasting poison at steady-state 247
D.1.1 Introduction 247
D.1.2 General assumptions 247
D.1.3 Initial Conditions 249
D.1.4 Governing Equations 249
D.1.5 Analysis 250
D.2 Transient system with fuel and lasting poison 253
D.2.1 Governing equations 253
D.2.2 Analysis 253
D.3 System with fuel and xenon 256
D.3.1 Background 256
D.3.2 Governing equations 256
D.3.3 Analysis 257

E Heat transfer relationships 260
E.1 Solid system 260
E.2 Saturated Porous medium 262

F Feedback models 267
F.1 Influx of U-235 267
F.2 Temperature 267
F.2.1 Piecewise function of exponential relationship and power law 267
F.2.2 Gaussian fit 269
F.2.3 Polynomial fit for dry configurations 270

Nomenclature

Abbreviations

ADE	advection dispersion equation
AVF	air volume fraction
BWR	boiling water reactor
CDF	cumulative distribution function
CF	capacity factor
CV	control volume
DOE	U.S. Department of Energy
DU	depleted uranium
DV	differential control volume
EBS	engineered barrier system
EIA	U.S. Energy Information Administration
ENDF	Evaluated Nuclear Data File
FP	fission product
FVF	fluid volume fraction
HEU	highly-enriched uranium
HLW	high-level waste
HM	heavy metal
HMVF	heavy metal volume fraction
IAEA	International Atomic Energy Agency
JAEA	Japan Atomic Energy Agency
LANL	Los Alamos National Laboratory
LHS	Latin hypercube sampling
LWR	light water reactor
MCNP	Monte Carlo N-Particle transport code
MOX	mixed oxide
MPC	maximum permissible concentration
MTU	metric ton of uranium
NWPA	Nuclear Waste Policy Act
ORIGEN	Oak Ridge Isotope Generation code
ORNL	Oak Ridge National Laboratory
OTFDB	On-The-Fly Doppler Broadening code
PDF	probability distribution function
PRIS	Power Reactor Information System
PWR	pressurized water reactor
QSS	quasi-steady-state
TFM	thermally-fissile material

TH	thermo-hydrological
tHM	metric ton of heavy metal
TMI	Three Mile Island
TOUGH2	Transport of Unsaturated Groundwater and Heat code, version 2
TRU	transuranics
TSPA	total system performance assessment
TTB	Transport to Biosphere code
UNF	used nuclear fuel
UTS	ultimate tensile stress
VVF	void volume fraction
w-Pu	weapons-grade plutonium
WVF	water volume fraction
YMR	Yucca Mountain repository

Dimensionless Constants

Bi	Biot number
Gr	Grashof number
Nu	Nusselt number
Pe	Péclet number
Pr	Prandtl number
Ra	Rayleigh number
Re	Reynold’s number

Greek Symbols

α	reactivity feedback coefficient
β	cubic expansion coefficient
χ	atom fraction
δ	error
ϵ	fast fission factor
$\dot{\epsilon}$	strain rate
η	reproduction factor
γ	fission yield
λ	decay constant
μ	molar mass
ν	kinematic viscosity
$\bar{\nu}$	neutrons per fission
ω	tortuosity
ϕ	neutron flux
ρ	reactivity
$\bar{\rho}$	total system reactivity
σ_s	shear stress
σ	cross section
τ	tortuosity correction factor

Mathematical Symbols

$\dot{f}$	rate of f over time
∇f	gradient of f
$\nabla \cdot f$	divergence of f
f'	linear flux of f
f''	areal flux of f
div	divergence
grad	gradient

Roman Symbols

B	bulk modulus

b	fracture aperture
C	concentration
C^*	solubility
C_p	average heat capacity
c_p	isobaric specific heat
c_v	isochoric specific heat
D	Darcy unit of permeability
D_M	moderator defect
D_T	temperature defect
E	elastic modulus
$\bar{E}_n$	average neutron energy causing fission
E_f	useable energy per fission
F	mass flux
f	thermal utilization factor
$\mathcal{F}_p$	power fraction
f_r	fraction of total radius
G	shear modulus
g	acceleration due to gravity
H	total hydraulic head
h	heat transfer coefficient
$\mathcal{H}$	enthalpy
$\bar{i}$	the set of fissile nuclides that produce nuclide i upon fission
$\hat{i}$	the set of nuclides that produce nuclide i upon decay
$\tilde{i}$	the set of nuclides that produce nuclide i upon neutron capture
K	hydraulic conductivity
k	thermal conductivity
$\mathcal{K}$	permeability
k_∞	infinite multiplication factor
K_d	sorption distribution coefficient
k_{eff}	effective multiplication factor
l_p	prompt removal lifetime
M	total mass
M_c	critical mass
N	total nuclides in coupled system
n	amount of nuclide
N_A	Avogadro's number
P	pressure
p	resonance escape probability
P_f	power from fission
Q	energy of reaction
$\dot{q}$	heat source term
q_{opt}	power required for desaturation
R	thermal resistance
r	radius
$\mathcal{R}$	ideal gas constant
r_c	critical radius
S	saturation
$\dot{S}$	source term
$\mathcal{S}$	spontaneity
S_l^{env}	saturation of surrounding host rock

T	temperature
$t_{\frac{1}{2}}$	half-life
T_∞	ambient temperature
$\mathcal{U}$	internal energy
$\bar{v}$	average neutron speed

List of Tables

2.3.1 Operational characteristics devised for a BWR (140478 assemblies) and PWR (104428 assemblies) based on subsets of burnup defined by regions spanning 10% of the total sample size for certain quantiles. 15
2.4.1 Inventory characteristics at discharge based on 1 MTU. 19
2.4.2 Inventory characteristics at emplacement based on 1 MTU. 19
2.4.3 Inventory characteristics at anticipated canister failure based on 1 MTU. . . . 19
2.4.4 Masses in grams of actinides in the assembly at anticipated canister failure, based on 1 MTU. 20

3.3.1 Emplacement parameters held constant for the analysis. 28
3.3.2 Parameter ranges assumed in this study expressed in terms of lower and upper bound values. 36
3.3.3 Summary of actinide transport parameter distributions employed for LHS sampling. 38
3.3.4 Masses in grams of actinides in an average LWR assembly at anticipated failure from a 1 MTU basis for each UNF subset. 41
3.3.5 Number of canisters and the mass of contents (in MTU) used in the heterogeneous repository array configuration based on the mass loadings per subset M^c (see table 2.3.1 on page 15) and modified (*) values used to obtain a square array of side $\sqrt{N_{tot}^*}$. 42
3.4.1 Interpolated values of Los Alamos criticality figures for hydrogen-moderated spherical volumes of uranium metal at certain mass fractions of U-235. [68] . 51
3.4.2 Time periods after canister failure necessary to achieve median precipitate mass values shown with corresponding enrichment ($\tilde{e}$, wt%) and U-235 and U-238 fluxes (F_{25}, F_{28}). Minimum uranium masses needed for criticality are interpolated from Los Alamos data using the enrichment. [68] 51
3.4.3 Atom fractions (χ) of isotopes selected as median values from the LHS sampling cases, shown with relevant time after canister failure and the median values of uranium mass (M_U) and U-235 and U-238 fluxes (F_{25}, F_{28}) corresponding to the selected enrichment figures. 54

4.3.1 Fractional composition assumed for air. 65

4.3.2 Composition assumed for shale presented in terms of constituents and atomic composition, where the composition of smectite is used for clay minerals. . . . 66
4.3.3 Composition of granite presented in terms of constituents and atomic composition. 66
4.4.1 Criticality parameters and moderator defects for the homogeneous, undermoderated precipitates. 71
4.4.2 Criticality parameters for the fractured, undermoderated precipitates. Moderator defects are shown for cases where $\frac{N_H}{N_{25}} > 10$ 72

5.3.1 Gaussian fits for the time-averaged fission power distribution in various critical masses. 97

6.2.1 Material properties used to guide inputs for MCNP composition scripts, TOUGH2, and strain model. Here, $\mathcal{K}$ is the intrinsic permeability, τ is a tortuosity correction factor, ϵ is the porosity, E is the elastic modulus, B is the bulk modulus, and UTS is the ultimate tensile strength. 118
6.2.2 Fluid properties at 15 MPa used to guide inputs for MCNP composition scripts and TOUGH2 results. [98–100] 118
6.2.3 Average fit parameters of equation (5.3.1) for critical masses in the analysis. . 119
6.3.1 Power levels Q_{opt} of critical homogeneous masses (in MTU) needed to achieve saturation temperature at steady-state based on the saturation of the encapsulating granitic environment (S_l^{env}). Temperatures are in celsius, while liquid densities are shown in units of $\frac{kg}{m^3}$. 123
6.3.2 Power levels Q_{opt} of critical fractured masses (in MTU) needed to achieve saturation temperature at steady-state based on the saturation of the encapsulating granitic environment (S_l^{env}). Assumed FVF values are shown in bold. Temperatures are in celsius, and liquid densities are shown in units of $\frac{kg}{m^3}$. . 124

7.3.1 The temperature defects in two separate temperature ranges, where fractured data correspond to the first approach with shale laminate desaturation. The initial reactivity of the homogeneous geometry was close to zero, while that of the fractured geometry was around 0.02. 144

F.1.1 Polynomial fits of reactivity when enriched uranium is added to the pore space of critical configurations in the homogeneous geometry at $k_{eff} = 1.02$, corresponding to a functional form $\rho(x) = a + bx + cx^2 + dx^3 + ex^4 + fx^5 + gx^6$ where x is the change in moles of U-235. 268
F.1.2 Polynomial fits of reactivity as enriched uranium is added to the pore space of critical configurations in the fractured geometry at $k_{eff} = 1.02$, corresponding to a functional form $\rho(x) = a + bx + cx^2 + dx^3 + ex^4 + fx^5 + gx^6$ where x is the change in moles of U-235. 268
F.2.1 Piecewise fits of the form specified in equation (F.2.1) for the homogeneous configuration. 269

F.2.2 Piecewise fits of the form specified in equation (F.2.1) for the fractured configuration (approach 1 in chapter 7). 270
F.2.3 Gaussian fits of the form specified in equation (F.2.3) for the homogeneous configuration. 271
F.2.4 Gaussian fits of the form specified in equation (F.2.3) for the fractured configuration (approach 1 in chapter 7). 272
F.2.5 Polynomial fits of the form specified in equation (F.2.5) for the fractured configuration (approach 2 in chapter 7). 272

List of Figures

1.3.1 Methodology of the study. 6

2.3.1 Plot of burnup and initial enrichment for 10,000 random samples of the UNF-ST&DARDS database for both BWR and PWR used fuel assemblies. The size of the plot points is proportional to the initial loading of uranium, while the color scale indicates the time since discharge. 10
2.3.2 PDF of initial uranium mass per assembly in the UNF-ST&DARDS database, with a cutoff line at 280 kg to manually separate the data into BWR (left) and PWR (right) categories. 13
2.3.3 PDF (left axis) and CDF (dashed, right axis) of burnup for used fuel assemblies shown with quantiles of interest as vertical lines. 14
2.3.4 Historical net power output of commercial reactors calculated via PRIS, [21] with the mean values shown in black and median values in white. 14
2.3.5 Historical core size of online commercial reactors via EIA and PRIS, [21] [1] with the mean values shown in black and median values in white. 16

3.3.1 Visualization of model for nuclide transport in granite fractures from individual waste emplacements to a common point of precipitation, where the inset shows the major processes involved in one individual transport pathway of unique length L. 25
3.3.2 Decay chains of interest, with nuclides chosen for the transport study shown in bold. 29
3.3.3 Variation of the partition coefficient from the JAEA Sorption Database visualized with box plots, [45] where the mean is shown in black, the median is shown in dark blue, and the sample size is indicated within parentheses. . . . 31
3.3.4 PDF (left axis) and CDF (right axis, dashed) for the $\log_{10}$ values of the partition coefficient based on the JAEA Sorption Database. [45] 32
3.3.5 Relationship between K_d and pH for uranium. [45] 32
3.3.6 The effective diffusion coefficient of bentonite based on the JAEA Diffusion Database, [50] where the mean is shown in black and the median is shown in dark blue. Data on curium was too limited to be included in the figures. . . . 34

3.3.7 The effective diffusion coefficient of bentonite in terms of the experimental density and porosity for given ionic states. 34
3.3.8 PDF, CDF, and samples (red points) for the randomly-generated log-normal distribution of the K_d^r value of uranium in granite. The vertical lines mark one hundred K_d^r intervals of equal probability. 38
3.4.1 Total accumulated mass of the far-field precipitate (in MTU) for the average subset of the homogeneous UNF composition. The 10%, 50%, and 90% quantiles are shown, as well as the average and standard deviation of the $\log_{10}$values for visualization purposes. The individual hypercube samples amounting to more than 1 μg are plotted in the background. 46
3.4.2 Enrichment $\left(\frac{M_{23}+M_{25}}{M_U}\right)$ of the far-field precipitate (in wt%) for the average subset of the homogeneous UNF composition. The 10%, 50%, and 90% quantiles are shown, as well as the average and standard deviation of the $\log_{10}$ values for visualization purposes. The individual hypercube samples above 0.711 wt% are plotted in the background. 47
3.4.3 Comparison of uranium isotope breakthrough (in moles) for the normal and mixed sampling spaces based on averages of the UNF subsets, shown with 10%, 50%, and 90% quantiles of the total mass of the precipitate (also in moles). (The order of isotopes follows the 4n → 4n+3 decay chain progression in figure 3.3.2.) 48
3.4.4 Distribution of U-235 mass normalized to emplacement for the various hypercube sampling spaces at an arbitrary times. 48
3.4.5 Comparison of the U-235 precipitate mass normalized with respect to emplacement and the corresponding enrichment for subsets 1, 2, and 6 in the averaged (AVG) and heterogeneous (HET) approaches for the log-normal LHS sampling space, shown for 10% (light), median (normal), and 90% (dark) quantiles. (Labels for enrichment are merged into "UNF" due to overlap.) 50
3.4.6 Total mass and enrichment of the precipitate for the different LHS sampling spaces, based on averages of UNF subsets 1, 2, and 6. 52
3.4.7 Superimposed fluxes of U-235 and U-238 at the precipitate location for the different LHS sampling spaces, based on averages of UNF subsets 1, 2, and 6. 52

4.3.1 Model for configurations of the far-field precipitate with critical radius r_c (not to scale). The fractured geometry has an aperture of width b. 62
4.4.1 Minimum VVF required for $k_{eff} > 0.98$ in terms of the fracture aperture for various enrichments based on 1 MTU depositions unless otherwise noted. The corresponding HMVF values are indicated in the labels. 68
4.4.2 Minimum VVF required for $k_{eff} > 0.98$ in terms of the fracture aperture for 1 and 5 MTU depositions of the 3 wt% precipitate in the fractured geometry. The corresponding HMVF values are indicated in the labels. 69

4.4.3 Minimum critical masses evaluated up to 500 MTU for the space of VVF and HMVF for the 2 wt% enriched precipitate. 71
4.4.4 The minimum VVF required for $k_{eff} > 0.98$ for various masses of the 6 wt% precipitate, with the corresponding HMVF, l_p, and $\bar{E}_n$ shown in the labels. . 72
4.4.5 The effect of enrichment on the minimum VVF required for $k_{eff} > 0.98$, with the corresponding HMVF, l_p, and $\bar{E}_n$ shown in the labels. 73
4.4.6 The effect of replacing water with air in a uniform manner throughout the void space of critical configurations. 74
4.4.7 The effect of increasing the void space for a fixed HMVF and mass of moderator for systems that can reach $k_{eff} = 1.02$. 76
4.4.8 The effect of displacing water with uranium metal in the void space for two different enrichments, expressed in terms of the change in heavy metal volume. 78
4.4.9 The effect of displacing water with uranium metal in the void space expressed in terms of U-235 addition (within UO_2 of the indicated enrichment) and shown with polynomial regression curves. 79
4.4.10 The effect of diluting precipitates of specified enrichments to 1.5 wt% expressed in terms of the U-238 addition (within pure $^{238}UO_2$). Linear regression curves are shown, indicating feedback coefficients between $-5.7*10^{-11}$ and $-1*10^{-10}$ reactivity per mole U-238. 80
4.4.11 Effect of expansion on 2 wt% homogeneous configuration in terms of relative change in radius, shown for two different critical masses. 81
4.4.12 The effective multiplication factor for the 5 MTU precipitates, where a contour indicating $k_{eff} = 1$ is drawn in yellow. 85
4.4.13 The factor η for all cells in the 5 MTU precipitates, where a contour indicating $k_{eff} = 1$ is drawn in yellow. 86
4.4.14 The percentage of neutrons causing fission in the thermal range ($< 0.625\,eV$) for the 5 MTU precipitates, where a contour indicating $k_{eff} = 1$ is drawn in yellow. 87
4.4.15 The average neutron energy $\bar{E}_n$ in MeV for the 5 MTU precipitates, where a contour indicating $k_{eff} = 1$ is drawn in yellow. 88
4.4.16 The prompt removal lifetime l_p in seconds for 5 MTU precipitates, where a contour indicating $k_{eff} = 1$ is drawn in yellow. 89
4.4.17 Comparison of homogeneous (H) and fractured (F) $k_{eff}^{min} = 1$ results with extrapolated Los Alamos criticality data on hydrogen-moderated water-reflected U-235 systems of uranyl fluoride solution or uranium hexafluoride in paraffin wax (C_nH_{2n+2}). 90

5.3.1 Fission power distribution for the 2 wt% precipitate in the homogeneous geometry, shown with a Gaussian fit of the time-averaged data (black, dashed). 98
5.3.2 Fission power distribution for the 6 wt% precipitate in the homogeneous geometry, shown with a Gaussian fit of the time-averaged data (black, dashed). 99

5.3.3 Behavior of the full-step k_{eff} over the $\log_{10}$ of time (years) from initial criticality for different enrichments, shown with error bars. 100
5.3.4 Burnup in the 6 wt% homogeneous critical sphere. 100
5.3.5 Behavior of fissile isotopes in the homogeneous precipitate. 102
5.3.6 Profile of Pu-239 generation for 6 wt% critical masses at $1\,kW_t$. 102
5.3.7 Activity of actinides ($Z \geq 90$) in the homogeneous configuration. 103
5.3.8 The activity over time for nuclides with $Z \geq 90$ in the 0.1 MTU 6 wt% homogeneous precipitate. 104
5.3.9 Activity of non-actinides and isotopes in the natural-uranium decay chains for the homogeneous 2 wt% precipitate. 105
5.3.10 Activity of non-actinides and isotopes in the natural-uranium decay chains for the homogeneous 6 wt% precipitate. 106
5.3.11 Comparison of activity results for the homogeneous and fractured geometries of the 2 wt% enriched precipitate. 106
5.3.12 Activity in the 2 wt% fractured geometry. 107

6.2.1 Saturation-dependent models employed in the code. 117
6.3.1 Power output needed to reach liquid-gas phase boundary as a function of the critical radius. 121
6.3.2 The spatially-averaged behavior of temperature (black, left axis) and saturation (blue, right axis) over time in the TOUGH2 simulation of the 6 wt% homogeneous critical masses, assuming $S_l^{env} = 0.1\%$. 125
6.3.3 The behavior of saturation with temperature for each discrete region of the critical mass ("CRM") as steady-state is reached for $S_l^{env} = 0.1\%$. The regions are numbered from the core outwards. 125
6.3.4 The behavior of saturation with temperature for each discrete region of the critical mass ("CRM") as steady-state is reached for $S_l^{env} = 10\%$. The regions are numbered from the core outwards. 126
6.3.5 The saturation distribution evaluated at the $\log_{10}$ of time for $S_l^{env} = 0.1\%$. The critical radii are indicated with vertical lines. 126

7.2.1 An xy cross section of the MCNP input geometry for the partially unsaturated 0.1 MTU 6 wt% fractured configuration colored by material number, where spherical shell discretization is shown for four regions 8 cm from the origin. Numbered labels appear in red for materials and black for surfaces. The saturation is approximately 54% throughout the system at 400 years into the TOUGH2 simulation, driven at $q_{opt} = 228\,W$. The densities of shale, water, and air all vary by shell, and are shown in units of $\frac{g}{cm^3}$. 132
7.3.1 Reactivity feedback with increasing average temperature of configurations in the homogeneous approach. 136
7.3.2 Percentage of neutrons causing fission in various energy ranges as determined by the enrichment. 136

7.3.3 Reactivity feedback with increasing average temperature of configurations in the first fractured geometry approach. 137
7.3.4 Reactivity feedback with increasing average temperature of configurations in the second fractured geometry approach. 137
7.3.5 Reactivity feedback with increasing average temperature of configurations with $FVF \leq 1\%$ in the first fractured geometry approach, shown with color-coded piecewise exponential/power law fits (solid lines) and Gaussian fits (dashed lines). 138
7.3.6 Reactivity feedback with increasing average temperature of configurations with $FVF \leq 1\%$ in the second fractured geometry approach, shown with color-coded polynomial fits. 139
7.3.7 Different fittings for the reactivity results of the 1 MTU 3 wt% fractured configuration (approach #1). 141
7.3.8 Feedback coefficients for the dry critical configurations in the first fractured geometry approach, split into two regions to demonstrate application of equation (7.3.8).. 142
7.3.9 Feedback coefficients for the dry critical configurations in the first fractured geometry approach using the gaussian solution in equation (7.3.3).. 142
7.3.10 Feedback coefficients for the dry critical configurations of the second fractured geometry approach. 143
7.3.11 Effective microscopic cross sections in fractured critical configurations (approach 1). 146
7.3.12 Effective microscopic cross sections in fractured critical configurations (approach 2). 146

8.2.1 The temperature distribution in the system as time progresses, with the critical radius indicated with the vertical line. 155
8.2.2 Examples of temperature-dependent heat transfer terms using initial volume fractions. 165
8.3.1 The evolution of ΔT over time for 5 MTU precipitates using the 90% quantile source terms from chapter 3, where α_T is modeled as a piecewise function (solid) or Gaussian (dashed). 168
8.3.2 Temperature feedback coefficient (α_T) for the 5 MTU precipitates derived from reactivity modeled as a piecewise function (solid) or Gaussian (dashed). . . . 169
8.3.3 The evolution of ΔT over time for 2 wt% precipitates using the 90% quantile source terms from chapter 3, where α_T is modeled as a piecewise function (solid) or Gaussian (dashed). 169
8.3.4 The evolution of ΔT over time for 1.5 wt% fractured geometry precipitates using the 90% quantile source terms from chapter 3, where α_T is modeled as a piecewise function (solid, top) or Gaussian (dashed, bottom). 170

8.3.5 The effect of increasing the total uranium source term $\left[\frac{mmol}{yr}\right]$ in the 5 MTU, 2 wt% precipitate in the homogeneous geometry for piecewise (solid) and Gaussian (dashed) treatments of α_T. 171

8.3.6 The effect of increasing the total uranium source term $\left[\frac{mmol}{yr}\right]$ in 1 MTU, 3 wt% configurations for piecewise (solid) and Gaussian (dashed) treatments of α_T. The original source terms from TTB are $\dot{S}_{25} = 1.5 * 10^{-8} \frac{mol}{yr}$ and $\dot{S}_{28} = 1.1 * 10^{-6} \frac{mol}{yr}$. 172

8.3.7 The effect of selectively increasing the source term of U-235 $\left[\frac{mmol}{yr}\right]$ in the 5 MTU, 2 wt% precipitate in the homogeneous geometry while maintaining the U-238 influx fixed at the original TTB value, where α_T is determined by piecewise (solid) and Gaussian (dashed) functions. 173

8.3.8 The effect of selectively increasing the source term of Pu-239 $\left[\frac{mmol}{yr}\right]$ in the 5 MTU, 2 wt% precipitate in the homogeneous geometry while maintaining the mass fluxes of U-235 at $10^{-1} \frac{mmol}{yr}$ and $5.5 * 10^{-6} \frac{mol}{yr}$ for U-238, where α_T is determined by piecewise (solid) and Gaussian (dashed) functions. 174

8.3.9 The neutron flux observed in the 5 MTU, 2 wt% precipitate in the homogeneous geometry when selectively increasing the Pu-239 source term $\left[\frac{mmol}{yr}\right]$, based on mass fluxes fixed at $10^{-1} \frac{mmol}{yr}$ for U-235 and $5.5 * 10^{-6} \frac{mol}{yr}$ for U-238, where α_T is determined by piecewise (solid) and Gaussian (dashed) functions. . . . 174

8.3.10 The effect of selectively increasing the influx of pure Pu-239 $\left[\frac{mmol}{yr}\right]$ in the 5 MTU, 2 wt% precipitate in the homogeneous geometry, based on U-235 and U-238 mass fluxes fixed at TTB values and α_T determined by piecewise (solid) and Gaussian (dashed) functions. 175

8.3.11 Neutron flux in the 5 MTU, 2 wt% precipitate in the homogeneous geometry for selected source terms of pure Pu-239 $\left[\frac{mmol}{yr}\right]$, based on U-235 and U-238 mass fluxes fixed at TTB values and α_T determined by piecewise (solid) and Gaussian (dashed) functions. 176

8.3.12 Divergent behavior observed for the 5 MTU, 2 wt% fractured configuration when increasing the total uranium source term $\left[\frac{mmol}{yr}\right]$ for piecewise (solid) and Gaussian (dashed) treatments of α_T. 177

9.3.1 The integrated strain for various source terms of uranium $\left[\frac{mmol}{yr}\right]$ in the 5 MTU, 2 wt% homogeneous configuration (see figure 8.3.5). 182

9.3.2 The integrated strain for source terms of plutonium $\left[\frac{mmol}{yr}\right]$ in the 5 MTU, 2 wt% homogeneous configuration that overlap with those of uranium determined in the TTB calculation (see figure 8.3.8). 183

9.3.3 The integrated strain for various source terms of uranium $\left[\frac{mmol}{yr}\right]$ in the 5 MTU, 2 wt% fractured configuration before the rock melting point (see figure 8.3.12) where the piecewise model is indicated with solid lines and the Gaussian model with dashed lines. 183
9.3.4 The effect of adjusting certain parameters in equation (9.2.1) on figure 9.3.1, while maintaining other default parameters. 185
9.3.5 The effect of adjusting Q in equation (9.2.1) on figure 9.3.1, where A is chosen to calibrate the strain rate to $10^{-9}\,s^{-1}$ at $150°C$. 185

10.2.1 A mid-length cross section of a proposed canister for used Westinghouse 17 by 17 PWR assemblies, modified with slots for plates of depleted uranium oxide. The dimensions are indicated in millimeters. 192
10.3.1 It is proposed that nuclide transport in the fractures surrounding the EBS can be modeled with N pathways of M heterogeneous segments with varying apertures $2b$ and inlet fluxes $F(t)$ leading to a fixed point of convergence. . . 193

C.1.1 The global effect of varying the λ parameters on the steady-state temperature level for critical depositions in the 2 wt% homogeneous configuration at q_{opt} . 244
C.1.2 The effect of varying λ for relative permeability and capillary pressure in certain regions for critical depositions in the 2 wt% homogeneous configuration at q_{opt}. 244
C.2.1 Effect of varying the air-entry value in equation (6.2.14) for the critical masses in the 2 wt% homogeneous system at q_{opt}. 245
C.3.1 Effect of varying the wet thermal conductivity in the 2 wt% homogeneous critical masses for a fixed q_{opt}. 245

D.1.1 Series of nuclear reactions on high-yield Ce-149 and Pr-149 leading to stable neutron absorbers, with stable isotopes in bold and capture cross sections shown in barns. 248
D.3.1 Nuclear reactions involving the burnable poison Xe-135 with long-lived isotopes in bold. 256

E.2.1 Parallel representation of thermal resistances R in a porous medium with metal content ϵ_m and water content ϵ_l, where the source term in UO_2 is ignored. . . 265
E.2.2 Series representation of thermal resistances R in a porous medium with metal content ϵ_m and water content ϵ_l, where the source term in UO_2 is ignored. . . 266

Acknowledgments

Before his untimely passing, Professor Ahn had provided invaluable guidance on the manner of conducting research in an area of high societal impact. If there is anything vital to learn as an engineer, it is learning how to learn effectively, and he imparted these principles in a manner unique to his own at every group meeting. His advice and criticism allowed me to grow personally and trained my eye to be discerning and critical in my approach to problem-solving. In what became our very last conversation, we discussed the final direction of my studies, and it is my hope to honor his legacy through the work detailed in this dissertation and my pursuits hereafter.

I would like to thank Professor Fratoni for stepping into the role of advisor and providing crucial direction in my final studies. Taking on this role with a busy schedule and a growing family was no small task, and for that, I am grateful.

I would like to thank Xudong Liu for his exceptional guidance in all areas of the nuclear fuel cycle during my time at Berkeley. I would also like to acknowledge the technical feedback, inspiration, and moral support of other members of the nuclear waste management laboratory, in particular Elsa Lemaître-Xavier, Seung Min Woo, Miloš Atz, and Franziska Schmidt.

For all others who have inspired and encouraged me on my academic journey, I would like to thank my parents, my department head, Karl van Bibber, my administrator, Sara Harmon, and my good friends and hiking buddies Joseph Bower and Ellen Edwards.

Finally, I would like to acknowledge the support of the Japan Atomic Energy Agency, the Jane Lewis Fellowship, and the U.S. Nuclear Regulatory Commission.

Thank you.

Chapter 1

Introduction

A repository for used nuclear fuel (UNF) must reduce the risk of imparting a lethal dose to the biosphere over long periods of time through the use of both engineered and natural barriers. In the United States, the quantity of UNF in interim storage is growing, and the capacity of the now-defunct Yucca Mountain repository (YMR) was exceeded in 2013. [1] While the current waste management strategy calls for continued interim storage, it will still be necessary to implement final storage in a permanent geologic repository. These systems are a means of safeguarding the environment from radionuclides over extensive periods of time, and this is accomplished with a series of barriers comprised of both robust engineered components, such as the metallic canister, buffer material, backfills, liners, etc., and the natural barrier provided by the host rock surrounding the excavated waste disposal tunnels.

The repository performance assessment involves an analysis of all features, events, and processes that can affect the integrity of these barriers provided a site characterization and an understanding of the UNF inventory for a given fuel cycle. Although research and development can be employed to verify the durability of the engineered barrier system (EBS), no man-made device or structure can be assured to withstand natural degradation processes exceeding several millennia. Given the uncertainty associated with the inherently long time scale and lack of predictability of geological processes, the most prudent approach to repository modeling is to evaluate scenarios with a manner of conservatism. In this study, it is considered plausible that the extensive failure of waste canisters will eventually lead to the leaching of fuel followed by transport in groundwater and the accumulation of heavy metal in the surrounding host rock. Since the current inventory of UNF is in tens of thousands of metric tons, a final repository will contain a considerable quantity of unused fissile material. It is hypothesized that reconfigurations of this material in porous media may constitute a critical mass that can release energy through sustained chain reactions.

It is uncertain as to whether or not a critical formation poses a risk to the natural barriers, or if such an amalgamation is feasible at all through known radionuclide transport phenomena in a repository context. However, natural analogs for the hydrological transport and accumulation of uranium exist in the form of high grade ore deposits. In the case of the Oklo deposit in the Franceville basin of Gabon, chain reactions were verified to have occurred over the course of a million years, and the reactor zones remained largely intact upon the cessation of criticality. [2] It is proposed that radionuclide transport processes that led to the formation of this deposit two billion years ago can be applied to an engineered system in a worst-case direct disposal scenario.

The goal of this study is to present an integrated analysis of all processes and conditions needed for both a critical re-concentration of used nuclear fuel in porous media and a subsequent release of energy that can compromise the ability of the host rock to retain radionuclides from entering the environment. It is proposed that if a critical deposition cannot pose a threat to the integrity of the host rock after the use of modeling assumptions that conservatively favor the phenomenon, the issue of criticality in the far-field can be de-prioritized in the implementation of repository engineering guidelines. If conditions leading to system failure are identified, then recommendations can be made on the manner of initial repository loading, and modifications to the modeling assumptions can be proposed for further investigation. Within this scope, it will be necessary to integrate diverse considerations into a centralized study, including source term characterization, nuclide transport, neutronics, depletion, heat and mass transport, reactor dynamics, and mechanical deformation. The use of crystalline granite as the host rock is of particular interest because of its reducing, water-saturated environment that is antagonistic of waste dissolution. This presents new geochemical considerations compared to previous YMR studies and emphasizes the role of nuclide transport in fractured media and critical depositions in water-saturated geology.

1.1 State of the art

Modeling approaches to radionuclide transport on a repository-wide basis have been developed since at least the late 1970s. The modeling of repository source terms for nuclide transport can be referenced in a number of reports from Pigford, Chambré, and others, including the analytical solutions presented in Ref. [3]. The transport model applied in this dissertation falls within a series of studies regarding one-dimensional nuclide transport in fractured media, and systems of parallel fractures were analyzed by Sudicky and Frind beginning in 1982. [4, 5] In 1988, Hodgkinson and Maul devised an analytical improvement on fracture-based transport using the numerical inversion of Laplace transforms. [6] Ahn applied the solution from Hodgkinson and Maul to a spherical source term that modeled diffusive transport of radionuclides in arbitrary-length decay chains from high-level waste (HLW) through a surrounding buffer material. [7] This model was applied in a repository criticality context for vitrified high level waste disposal in YMR in 1997. [8] Ahn's model was then extended by van den Akker in 2013 to heterogeneous geological formations, [9] although this detailed model is not used here. Given the adequacy of the analytical formulations in representing the anticipated phenomena of interest, this study aims to provide an innovative use of the model based on a statistical sampling method to evaluate uncertainty in both mass flux and total precipitation, particularly within a direct disposal context.

Criticality events have consistently played a role in the performance assessment of geological repositories, although emphasis has usually been placed on near-field events. An early report in 1978 from the Swedish disposal program highlighted the potential for criticality from depositions of uranium in a repository and made brief discussions of consequences, although it was dismissive of the processes needed to attain such depositions. [10] With regards to the the studies motivating this dissertation, a series of reports were published in the mid 1990s regarding the final disposition of weapons-grade material following nonproliferation policy developments. In 1996, Bowman and Venneri postulated scenarios in which depositions of fissile material from these highly-enriched waste forms could lead to autocatalytic chain reactions and explosive releases of energy, although the feasibility of these scenarios was criticized. [11] Kastenberg and others employed various geometric configurations of fissile material to investigate the potential for autocatalytic criticality in the YMR context in 1997, and although a improved methodology illuminated the mechanisms involved, the overall possibility of such an event was found to be improbable. [12, 13] Liu extended the criticality modeling approach of Kastenberg et al. to a parametric study based on geologically-relevant configurations to analyze the criticality concern of Fukushima Daiichi damaged fuel. [14] This dissertation builds off the modeling approach of Liu and extends it into a dynamic analysis of criticality in a partially-unsaturated heavy metal precipitate formed from typical UNF. However, the focus is shifted from autocatalytic criticality to a different performance metric.

The analysis of the consequences of criticality is heavily inspired by a series of British studies beginning in the mid 2000s. [15] These reports have focused on post-closure criticality safety of used nuclear fuel, high level waste, and intermediate level wastes, and the quasi-steady-state consequence model of interest to this study has been employed successfully in simulations of the Oklo natural analog. [16] This dissertation will use the consequence model as a guide for the analysis of reactivity feedback effects on the energy balance of a critical mass, although this study will be be unique and independent in the exact manner of incorporating the feedback relationships, the heat transfer correlations, and the time-dependent mechanical deformation model.

1.2 Scope of the dissertation

The dissertation aims to present an investigation into the far-field criticality issue that confines the problem using heavily conservative assumptions to emphasize mechanistic plausibility rather than present a simulation of reality. The time scales of processes involved in the study are geological, and an attempt to precisely extrapolate hydrological phenomena to the hundreds to thousands of years is both impossible and not conducive to expanding knowledge of events significant to repository engineering. Rather, the goal is to model phenomena in a logical sequence where their roles in affecting repository performance are properly emphasized with regard to the final performance metric. This precludes unnecessary degrees of realism and exactitude, as the natural system is abstracted in order to deal with the lack of a specific site selection and field data. Results of the study will be analyzed with regard to the conservatism and abstractness of the models, and aspects that can be treated more sufficiently with a reduction in conservatism or with additional realism can be discussed. It is readily noted that several previous studies have negated assumptions that are employed early in this analysis; these are purposefully maintained not only for exploratory purposes but to provide more definitive conclusions on the phenomena using a wider lens.

The scope of the study is fixed to characteristics of direct disposal, and considerations employed in past studies for high-level waste are not usually held to be applicable. Although transport models that have been used for HLW in past studies can be reapplied with careful assumptions, the leaching of uranium oxide waste cannot be modeled according to behavior observed for vitrified waste forms. While characteristics of fuel cycles incorporating partitioning and transmutation would certainly be conducive to alleviating concerns discussed in this study, it is presumed that the sum of used nuclear fuel will be emplaced in a crystalline granitic repository as-is with no further reprocessing or implementation into stages of advanced fuel cycles. The only free parameter for the back-end of this open cycle fuel would be the interim cooling period of the fuel and the assumed tunnel emplacement characteristics.

It is considered that in-canister criticality events in the near-field can be excluded by engineering design. If the characteristics of the oxide waste can be measured or extrapolated from the reactor operating history, it is proposed that sufficient information exists to design the package to prevent criticality through reconfigurations within the canister and in the periphery of the buffer and backfill. This study assumes that individual emplacements of UNF in a repository will be designed and separated to the extent that only through repository-wide waste dissolution and transport can enough fissile material aggregate to a point where criticality may be a concern. This is defined as occurring in a region in the host rock where the geochemistry favors precipitation of actinide species. Therefore, while the results of the study can certainly provide recommendations on enhancements to the EBS, the features of this region of the repository are abstracted to the point where only crucial phenomena are acknowledged, and the use of specific design parameters is rather limited.

In this study, a new performance metric is proposed to evaluate the far-field criticality scenario as part of an innovation to the state of the art. As opposed to considering an explosive release of energy, this study aims to evaluate the steady release of energy from a critical mass that is sustained from an incoming plume of uranium from an extensively compromised repository. Rather than provide an analysis of the fine kinetic behavior of criticality over certain time periods, the approach emphasizes the role of various reactivity feedback mechanisms in maintaining a continual balance between sustained criticality and heat transfer with the surrounding geology. It essentially models the deposition as a natural reactor with online refueling, and while the thermal hydraulics of engineered reactors ensure optimal heat transfer with rising power, there are obvious limits on what can be attained with natural processes.

Crystalline granitic bedrock is proposed as the host rock of interest given favorable geochemical and hydrological characteristics. This constitutes a major departure from the unsaturated and largely oxidizing conditions of welded volcanic tuff relevant to Yucca Mountain, which as of this study is considered to be defunct. All analyses in this study should be considered relevant to the context of this reducing and water-saturated geology.

1.3 Methodology

The core objectives of the dissertation include the following:

1. Quantify the extent of heavy metal accumulation in the far-field within a band of uncertainty using a radionuclide transport model
2. Identify critical configurations of the heavy metal as part of a porous medium
3. Determine the reactivity feedback mechanisms that can affect a critical system in the far-field context
4. Characterize the long-term release of energy from the critical mass provided these feedback mechanisms
5. Identify the circumstances under which the release of energy corresponds to material failure

The methodology employed to meet these core objectives is summarized in figure 1.3.1, where the individual analyses are shown to be heavily integrated. In chapter 2, the inventory of used nuclear fuel is characterized based on a statistical analysis of the current inventory in interim storage. Representative compositions of UNF are used to develop point sources for a fracture-based transport analysis that approximates the repository tunnels as a simple grid of EBS components. The transport analysis in chapter 3 will yield mass fluxes of uranium $\left(\dot{S}\right)$ from the abstracted repository and compositions of precipitates that may accumulate at a fixed point in the far-field.

In chapter 4, a parametric neutronics evaluation will employ these compositions to explore the geometric configurations necessary for criticality, and the parametric reactivity (ρ) data will be analyzed to provide inventory-based feedback relationships $\left(\frac{\partial\rho}{\partial n}\right)$. Burnup simulations will be described in chapter 5 that will provide the spatial distribution of fission reactions in the critical masses. This information can then be employed as the energy source term for a simulation of partially-unsaturated heat and mass transfer in the porous medium in chapter 6. Results from this simulation will then inform a detailed neutronics analysis in chapter 7 that will analyze reactivity feedback given system-wide changes in temperature and water content. All feedback mechanisms will be integrated into a heat transfer model in chapter 8, and the numerically-obtained results of time-dependent temperature will be applied to a thermal creep model in chapter 9 to evaluate the expected mechanical deformation of the system. Finally, chapter 10 will attempt to integrate all observations from the analyses to draw conclusions on the importance of the criticality issue in the direct disposal scenario.

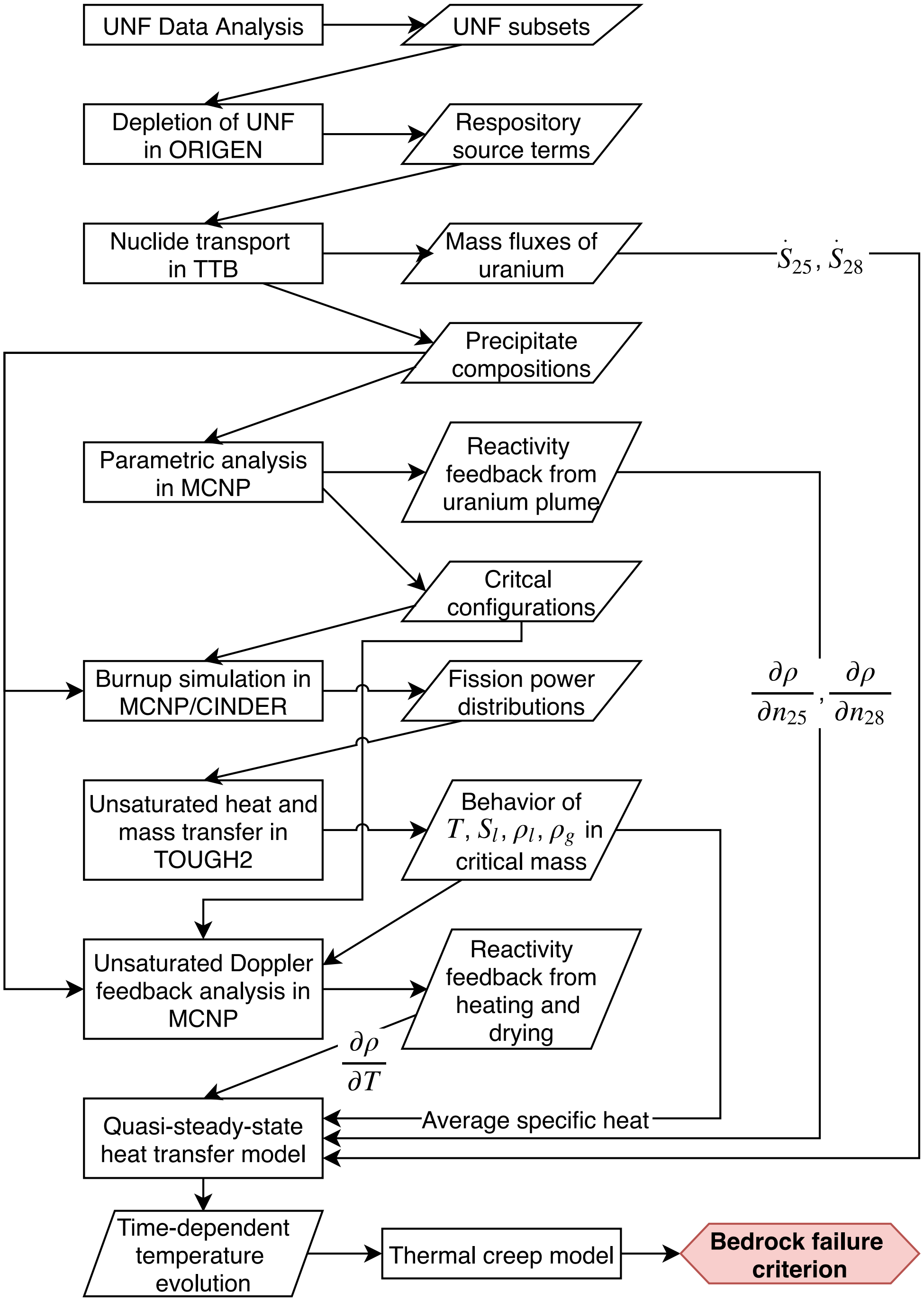

Figure 1.3.1: Methodology of the study.

Chapter 2

The source term of used nuclear fuel

2.1 Introduction

The fundamental motivation for pursuing a study on far-field criticality is the sheer magnitude of used nuclear fuel in interim storage in the United States. The quantity of fissile nuclides remaining in the fuel at the end of light water reactor operation may pose criticality issues when emplacement in a permanent repository is finally undertaken. An over-arching assumption in this study is that in-canister criticality events can be prevented through careful engineering of the waste package. Furthermore, plutonium-driven criticality risks in the near field are reduced through the relatively lower concentration in used nuclear fuel compared to defense wastes, and altogether these risks are mitigated through a well-designed engineered barrier system. However, it is considered plausible that the quantity of fissile isotopes present in the total inventory of used nuclear fuel in a single repository can be re-concentrated into what may constitute a critical mass after the catastrophic and comprehensive failure of waste canisters and subsequent repository-wide nuclide transport.

In order to characterize the source term for nuclide transport, it is necessary to understand the current inventory of used nuclear fuel for direct disposal. It is anticipated that the variation in assembly inventories will vary broadly due to differences in reactor type, capacity factor, discharge date, and burnup from various periods of commercial operation. These differences would be compounded with the uncertainty in host rock transport parameters when transport calculations are undertaken. Therefore, in order to bound the scope of the study, representative cases of used nuclear fuel assemblies will be developed based on statistical groupings, which can then be used to characterize canister contents for a transport analysis. This will allow for transport results to indicate the importance of burnup and discharge period on far-field accumulation.

2.2 Background

A light water reactor is unable to burn all fissile nuclides in the fuel due to material constraints, assembly design, core power profiles, and operational schedules. The current inventory of UNF emanates largely from first and second generation reactors, with the bulk coming from Gen-II reactors that went online starting in the early 1970s. It would be possible to process this used nuclear fuel to reutilize fissile material in an advanced fuel cycle, e.g. using mixed-oxide fuel in specialized MOX reactors. However, there is no reprocessing infrastructure available for commercial nuclear power plants in the United States.

A facility intended for this purpose was constructed in Barnwell, SC, by Allied Corporation and General Atomics, and it went through industrial tests with uranium surrogates. In 1977, confronted with growing proliferation concerns with plutonium separating technologies, the Carter administration determined that the U.S. commercial fuel cycle could be economical without reprocessing and ceased all federal funding and sanctioning for such activities. [17] A subsequent decision by the Reagan administration in 1981 officially relegated development of reprocessing to the private sector, despite imparting federal approval for such operations. This proved to be infeasible and compounded with lingering uncertainty over an outright federal ban, leading to Barnwell being decommissioned before actual UNF assemblies could be received and processed. The Nuclear Waste Policy Act (NWPA) would follow these decisions in 1982, which placed ultimate responsibility of the waste inventory on the Department of Energy (DOE) and effectively mandated direct disposal in one of several candidate repository sites. These sites included salt beds and domes, basalt (Hanford, WA), and welded volcanic tuff (Yucca Mountain, NV). The amendment to the NWPA in 1987 specified Yucca Mountain for further consideration, limiting emplacement to 70,000 metric tons. Considerable R&D for the total system performance assessment of the site was undertaken, with nuclide transport studies tailored specifically to the site characteristics and oxidizing geochemistry. Federal regulatory standards on dose limits evolved from a period of 10,000 years to a million years.

A license application for YMR was submitted by the DOE to the Nuclear Regulatory Commission in 2008. However, due to political issues stemming from a lack of hindsight on consent-based siting, work on Yucca Mountain was halted by the Obama administration in 2011. From 2010 to 2012, the Blue Ribbon Commission on America's Nuclear Future was tasked by the DOE to evaluate a new back end strategy for the fuel cycle. [18] Among the options considered for final disposal was a mined repository deep in crystalline rock, which paralleled concepts under development in Europe. The total inventory of UNF exceeded the now-defunct YMR design capacity by 2013, and policies will likely have it remain in interim storage for up to a hundred years before final deposition. Motivation to pursue concrete solutions to the back end of the nuclear fuel cycle comes in the form of increased liability faced by the DOE in failing to consolidate UNF from commercial sites into a central facility. Given the uncertainty surrounding the licensing of YMR, this study considers crystalline host rock as a viable alternative for the path forward.

2.3 Used nuclear fuel

2.3.1 Data sets

Data on the inventory of used nuclear fuel assemblies in the United States was obtained from the unified database of the Used Nuclear Fuel-Storage, Transportation & Disposal Analysis Resource and Data System (UNF-ST&DARDS) from Oak Ridge National Laboratory. [19] Figures on the initial enrichment, uranium loading, maximal burnup, and the time of discharge were provided on an assembly basis. Plots of this data are shown in figure 2.3.1, where a correlation is observed between maximal assembly burnup and initial enrichment. Assembly data points falling below this trend may be low-enriched assemblies used during initial reactor loading in order to attain specific power profiles at the beginning of life (known as "enrichment zoning"). They may also be damaged assemblies removed from the core into interim storage before full burnup can be realized. Values noticeably above the trend may be caused by the choice of burnable poison or whether the assembly has a long core residence time in a multiple-batch fuel management scheme.

Newer assemblies have progressively higher initial enrichment and higher burnup, with 4-5 wt% and 60 GWd/t being reasonable upper bounds for typical operation. Higher burnup assemblies are liable to require more time in interim storage due to the anticipated increase in both the magnitude of decay heat emission and heat reduction period. However, an economic tradeoff would be the lower initial fuel requirements for given power output. In general, there is a negative correlation with maximal burnup and the time of discharge, while no correlation is observed with the initial uranium loading.

Information on assembly origins was redacted from the Oak Ridge dataset due to export controls, and it was not possible to directly assign certain characteristics such as the reactor type, operational periods, and shuffling patterns (if any) to each assembly. Therefore, the discharge period was used to juxtapose the ORNL dataset with two others from the Energy Information Administration (EIA) and the International Atomic Energy Agency (IAEA) in order to estimate reactor operation characteristics. The EIA provides data on the vendor, reactor type, years of operation and licensing, and total core size for commercially operating nuclear power plants. [1] Published assembly characteristics for each manufacturer (obtained via Knief [20]) were utilized with the theoretical density of UO_2 to determine the total uranium mass loaded into the core. The IAEA Power Reactor Information System (PRIS) contains information on the design thermal and electrical output (and hence, efficiency) and yearly data on the net electrical capacity, capacity factor, and operation factor for both commercial and prototype reactors. [21] Vendor information is used to tie together PRIS and EIA information to approximate the specific power at certain times of discharge.

A few reactors were planned or operated in the U.S. that were considered exceptions to this analysis, and were therefore expunged from the data analysis as outliers. First, experimental reactors that were not of the light water variety were removed by default to confine the scope of the analysis. This included the Carolinas–Virginia Tube Reactor, which employed a heavy water moderator. The two new units at the Vogtle power station (3 and 4)

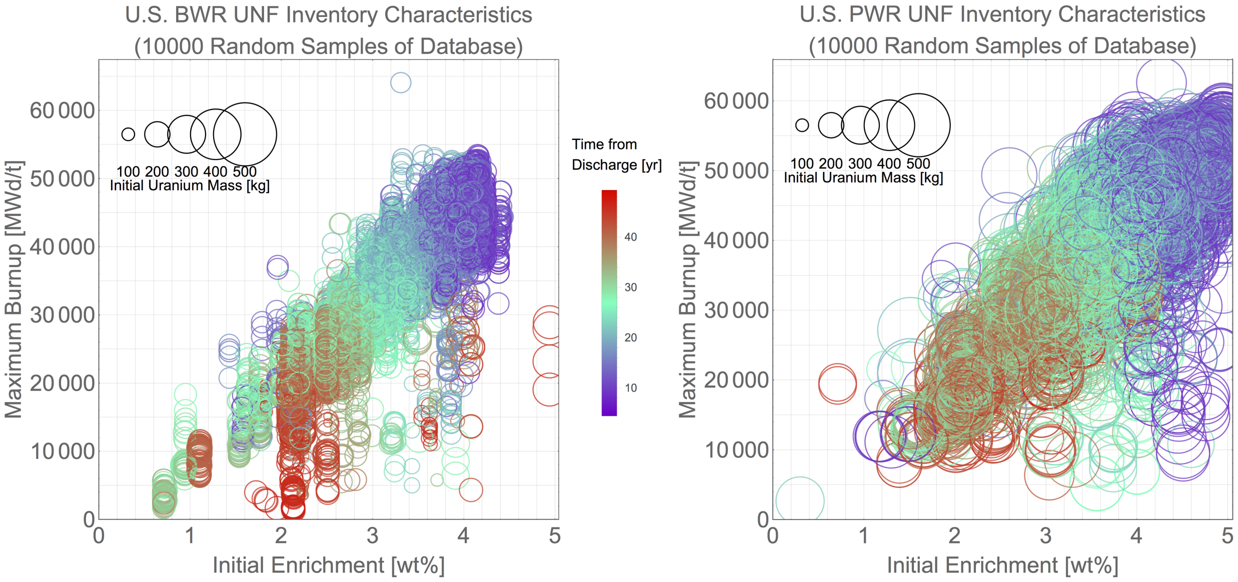

(a) BWR (b) PWR

Figure 2.3.1: Plot of burnup and initial enrichment for 10,000 random samples of the UNF-ST&DARDS database for both BWR and PWR used fuel assemblies. The size of the plot points is proportional to the initial loading of uranium, while the color scale indicates the time since discharge.

from Southern Company were not acknowledged since neither had been placed online by the publication of this study. This excluded the first American deployment of the Westinghouse AP-1000 PWR design. The Saxton (Pennsylvania), Vallecitos (California), and Boiling Nuclear Superheater (BONUS, Puerto Rico) reactors were excluded for the poor quality of data and the experimental/prototypical nature of their operation. The Allis-Chalmers Elk River BWR employed U-Th fuel elements as part of a thorium fuel cycle, and a portion of the used nuclear fuel generated from the 22 MW_t unit was sent to the Itrec experimental reprocessing plant in Rotondella of southern Italy. These characteristics and circumstances caused the reactor to be excluded from the analysis as an anomaly.

The Pathfinder BWR of South Dakota did not get commissioned after a test at full power failed due to complications caused by the incorporation of a superheater into the design. The used fuel from the first criticality and subsequent tests are assumed to be minor. The General Electric BWR in Shoreham, NY, did not get commissioned after public opposition stemming from concerns of the accident evacuation route. This came in the wake of the accident at the unit 2 of Three Mile Island (TMI, a Babcock and Wilcox PWR) in 1979, whose damaged fuel was removed and stored at Idaho National Laboratory. While theTMI-2 damaged fuel is likely to be emplaced in a permanent repository, the actinide inventory in this waste is considered anomalous and the reactor is excluded from the analysis to allow the burnup calculations to be relevant to normal UNF.

2.3.2 Representative cases

The commercial nuclear power plants of the United States are either boiling water or pressurized water reactors. The core of a PWR employs relatively fewer assemblies of higher uranium loading, as demonstrated in figure 2.3.1. When the probability distribution of assembly loading is calculated from the ORNL dataset, roughly bimodal behavior is observed that is clearly indicative of distinct BWR and PWR characteristics, as shown in figure 2.3.2. Given the difference in both neutronic and operational differences between the two LWR types, it is considered prudential to separate the data based on the two different modes. An estimation is made that the dataset can be divided into both BWR and PWR sets based on an imposed cutoff of 280 kilograms of uranium per assembly. Altogether, the dataset accounts for 70,429 MTU of used nuclear fuel; after data is separation, 45,402 MTU is found to be from PWR operation and 25,027 MTU from BWR operation.

For both the BWR and PWR data sets, subsets are chosen based on quantiles of the maximal burnup along with the overall mean. Figure 2.3.3 shows probability distributions for burnup in both reactor types, where BWR data is most evenly distributed about the mean while that of the PWR is right-acute towards higher values of burnup. In either set, quantiles at 10%, 25%, 50%, 75%, and 90% are evaluated, which serve as the medians for subsets spanning 10% of the total sample sizes. This procedure is meant to capture the full variation in burnup properties while ignoring outliers at the top and bottom 5%.

Once subsets are created, averages are made of the burnup, initial enrichment, uranium loading, and the discharge period, which are shown in the first four columns of table 2.3.1. Mass-weighted averages are employed for the burnup and enrichment, while an arithmetic average is used for the discharge time. Comparing both tabulations, a UNF assembly is liable to have had an initial enrichment between 2.2 and 4.4 wt%, with the median subset value of the BWR being 3.183 wt% and that of the PWR being 3.840 wt%. The median burnup is likewise lower for the BWR and higher for the PWR, although the average discharge periods per given subset are roughly comparable. For the PWR, assemblies discharged at earlier dates appear to have higher mass loadings, which is compensated by lower burnup, enrichment, and capacity factor.

The EIA and PRIS data are concatenated via the specific reactor unit and then separated into BWR and PWR categories. Altogether, these data provide the total energy generated in GWh, reference net electrical capacity in MW_e, actual time online (including the operation factor), energy availability, and capacity factor per operating year. The reference net capacity acknowledges power losses in transformers and auxiliary infrastructure, but also corresponds to a maximal full-power operation limit. This value is related to the total energy produced by way of the capacity factor and time online. The actual net output per reactor is derived from the reported energy generation and operating period, and the historical spread in these values in shown in figure 2.3.4 for BWRs and PWRs. The monotonic increase in the mean power output given an increasingly stable number of operating units in the fleet indicates a trend towards higher burnup conditions in light water reactors; this point may be further corroborated in figure 2.3.1. Notable intermittent shutdowns in this analysis include the unit

3 BWR at Browns Ferry from 1986 to 1994 and the unit 1 PWR at Three Mile Island from 1980 to 1984.

In order to juxtapose datasets, the average discharge periods of the ORNL burnup subsets are used to tie together figures from these annual data on reactor operations. Using the discharge years implied from these periods, the average electrical output, thermal output, and capacity factor (CF) up to the corresponding year of operation can be calculated for units that were online. Data for years where reactors went offline before the discharge date were weighted appropriately in the averaging procedure. As mentioned previously, for each reactor, the net electrical output is an operation-weighted figure derived from the total amount of energy generated up to the discharge date divided by the actual amount of time online. This allows for the statistical effects of reactors that were not operated at full-power to be acknowledged. These averages are calculated for each reactor and then further weighted by core sizes to produce the figures in table 2.3.1. While not shown in the table, the thermal output is calculated using the efficiency implied from the reference net capacity and thermal capacity in PRIS, which on average is related to the net electrical output by a factor slightly greater than 3, as expected.

The theoretical uranium core loading of each reactor unit is derived from the EIA figures on core size and reactor design data. In order to bound the study, core sizes are assumed to remain constant with no addition or removal of assemblies from the original configuration. The core sizes of reactors put online historically is diagrammed in figure 2.3.5a for BWRs and figure 2.3.5b for PWRs. In either case, earlier technology tended to employ smaller cores to serve smaller energy markets. With the increasing importance of the economy of scale over time, the median core size increased to a steady level as these older, outlier reactors were brought offline.

To calculate the specific power per assembly, the procedure employed two knowns from the subsets: assembly mass loading and the operation-weighted thermal output of reactors operating up the discharge point. While these figures are directly obtainable from the data, deriving specific power for purposes of a single assembly calculation would require knowledge of the size of the reactor core, which is dissociated from the Oak Ridge set. Therefore, the known core sizes of each reactor were weighted based on the years of operation up the discharge year specified in the subsets in order to create representative core sizes. Given the behavior of figure 2.3.5, the validity of this procedure is strongest for more recently-discharged assemblies. For the BWR, the table 2.3.1 figures of 21 $\mathrm{MW_t/t}$ are lower than modern values, which are closer to 26 MW/MTU, due to the low power operating characteristics of older reactors. [22] For the PWR, the subset figures lie around a typical specific power of 33 $\mathrm{MW_t/t}$, although modern designs could be liable to reach 38 MW/MTU. The average burnup is divided by the specific power figure to determine the total irradiation period for a given UNF subset, which is shown to range from 2.5 to 6 years. The assumption is made that specific power determined on the reactor-level can approximate that of an individual assembly for depletion calculations.

Capacity factors are shown both averaged at the discharge date alone and then cumulatively averaged for all years of operation up to that point in time. There is a correlation

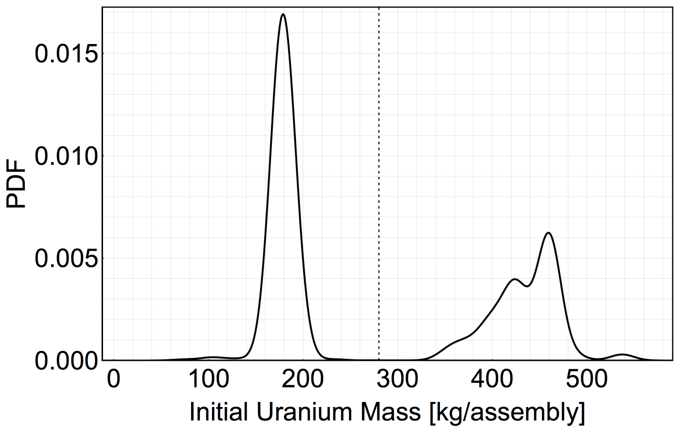

Figure 2.3.2: PDF of initial uranium mass per assembly in the UNF-ST&DARDS database, with a cutoff line at 280 kg to manually separate the data into BWR (left) and PWR (right) categories.

between the CF and the discharge date, as well as with the derived irradiation period. This implies that older reactors were not able to produce maximal amounts of energy in a set period of time compared to their design basis. This could stem from operational constraints (e.g. refueling and maintenance) or any number of external factors.

An assumption is made that canisters for UNF may hold either 4 PWR assemblies or 12 BWR assemblies, as inspired by canister concepts from SKB (Sweden), JAEA (Japan), POSIVA (Finland), and NAGRA (Switzerland). Using the average mass loading per assembly, a canister for PWR used nuclear fuel contains 1.74 MTU while that for BWR UNF contains 2.14 MTU. This would require 11,707 BWR canisters and 26,107 PWR canisters (37814 total) for comprehensive disposal of the source term given in the study. These figures will be important for the use of a discrete point source treatment for nuclide transport, and will be explained later in chapter 3.

2.4 Nuclide inventory of used fuel assembly

2.4.1 Setup

ORIGEN is an inventory code included as part of the SCALE package from Oak Ridge National Laboratory. [23] The code is based on the matrix exponential method for solving coupled, time-dependent point depletion equations in a multiplying system. Given the refinement of the UNF source term into representative BWR and PWR cases, ORIGEN-ARP ("Automatic Rapid Processing") is used for a problem-specific treatment with specialized neutron cross section libraries. These libraries are generated through interpolation algorithms for set fuel types and operating conditions.

For simplicity, it is assumed that the fuel type for BWR used fuel can be reliably emulated

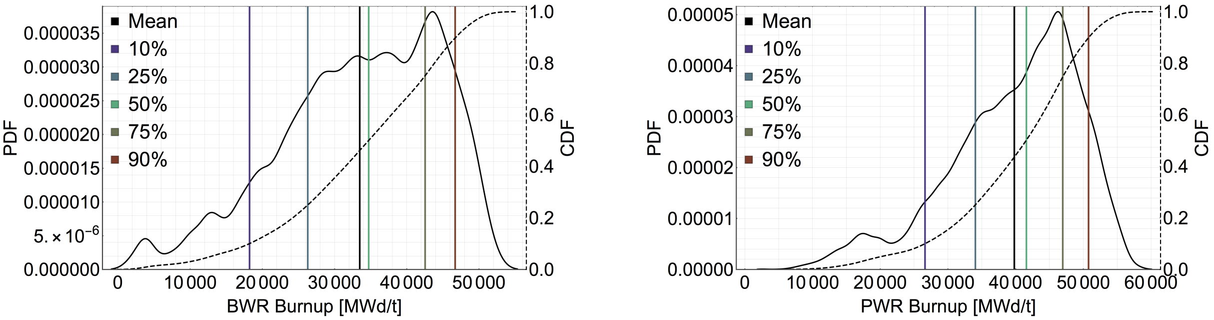

(a) BWR (140478 assemblies) (b) PWR (104428 assemblies)

Figure 2.3.3: PDF (left axis) and CDF (dashed, right axis) of burnup for used fuel assemblies shown with quantiles of interest as vertical lines.

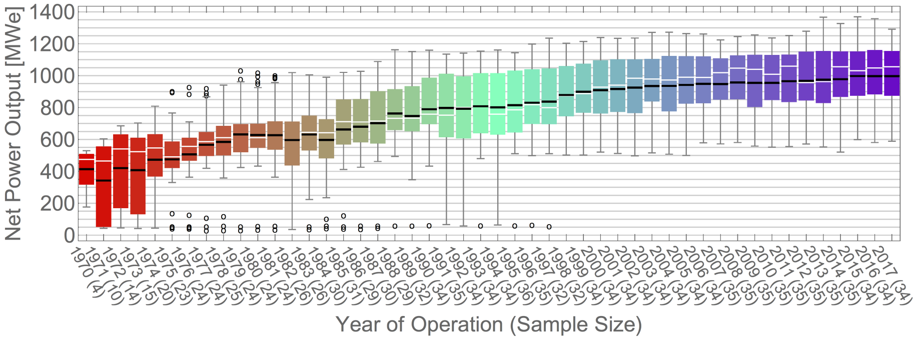

(a) 40 historically-operating BWRs

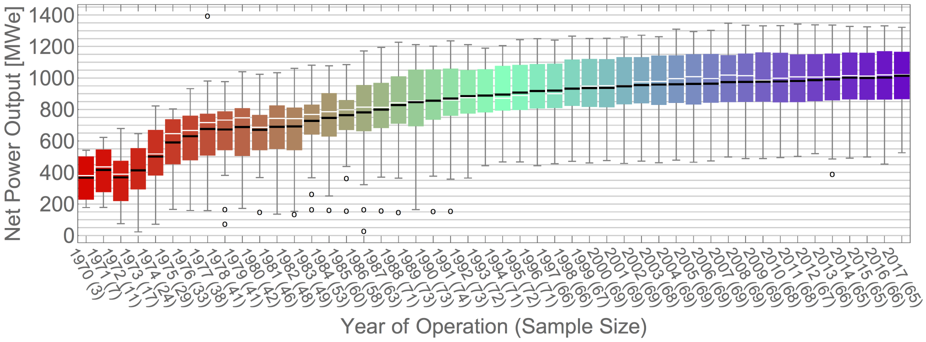

(b) 80 historically-operating PWRs

Figure 2.3.4: Historical net power output of commercial reactors calculated via PRIS, [21] with the mean values shown in black and median values in white.

Subset			Burnup [$MW_t d/t$]	Initial Enrichment [wt%]	Assembly Loading [kgU]	Time since Discharge [yr]	Net Capacity at Discharge [MW_e]	Capacity Factor at Discharge [%]	Cumulative CF at Discharge [%]	Typical Core Size	Specific Power at Discharge [MW_t/t]	Irradiation Period [d]	Downtime [d]
BWR	1	Mean	33319	3.134	178	21.4	807	78.9	67.0	601	21.2	1574	776
	2	90%	46752	3.972	175	9.6	863	91.0	76.2	624	21.7	2152	673
	3	75%	42502	3.830	175	11.7	855	91.4	75.4	621	21.6	1964	640
	4	50%	34690	3.183	177	20.4	811	83.3	67.2	603	21.2	1636	798
	5	25%	26270	2.637	183	31.1	723	72.4	61.5	570	20.2	1300	814
	6	10%	17862	2.208	180	34.3	638	62.3	59.7	559	18.4	972	657
PWR	1	Mean	39777	3.720	435	20.7	887	79.1	71.1	176	33.0	1205	490
	2	90%	50778	4.388	432	11.8	913	88.2	78.1	178	33.6	1511	423
	3	75%	46976	4.185	438	14.1	909	89.9	77.1	178	33.5	1403	416
	4	50%	41542	3.840	435	18.4	897	87.4	74.3	177	33.2	1250	433
	5	25%	33997	3.358	434	27.9	853	73.9	66.4	172	32.4	1048	529
	6	10%	26099	2.855	438	32.6	761	72.9	63.5	168	30.1	868	498

Table 2.3.1: Operational characteristics devised for a BWR (140478 assemblies) and PWR (104428 assemblies) based on subsets of burnup defined by regions spanning 10% of the total sample size for certain quantiles.

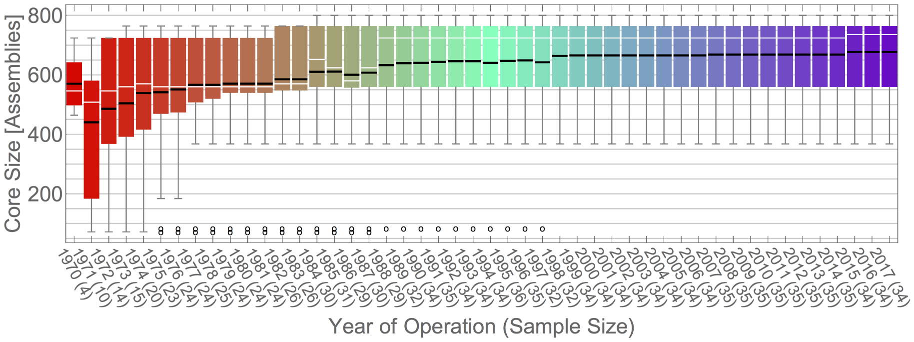

(a) 40 historically-operating BWRs

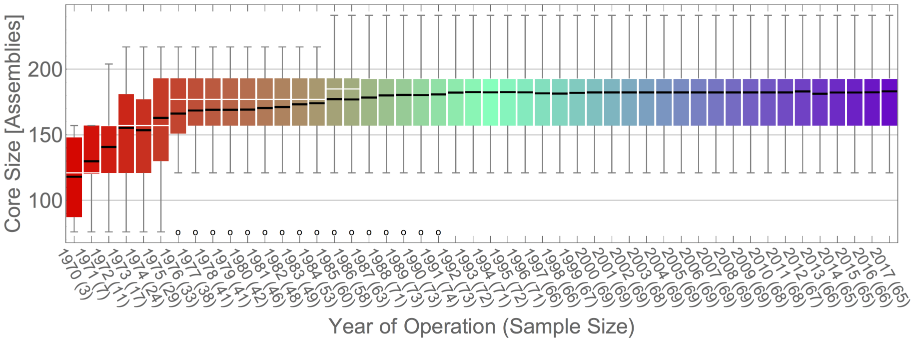

(b) 80 historically-operating PWRs

Figure 2.3.5: Historical core size of online commercial reactors via EIA and PRIS, [21] [1] with the mean values shown in black and median values in white.

by the General Electric 8 by 8 assembly configuration with a moderator density of 0.438 g/cm^3. [24] Allis Chalmers is the only other BWR vendor of note, and these reactors are likely to have been stripped from the analysis as outliers given their limited commercial deployment. For PWR used fuel, a Westinghouse 17 by 17 assembly configuration is employed with a moderator density of 0.723 g/cm^3. The PWR designs from Babcock and Wilcox (B&W) employ the same assembly geometry, while those of Combustion Engineering (CE) use the 16 by 16 geometry. It may be that assemblies from CE reactors would be misrepresented with this approach in that the fuel pin arrangement would cause the neutron mean free path, and hence the effective cross sections, to be different, but this possibility is ignored for simplicity.

Inventories are calculated using a basis of 1 MTU of fresh fuel using the enrichments specified in table 2.3.1, with the U-234 and U-236 content specified according to an enrichment fractions algorithm. These values fall between the 1.5-6 wt% range limits for the aforementioned fuel type libraries. The specific power figures employed for irradiation are based on average thermal outputs from actual operation, which did not factor in the amount of time reactors were offline for a given year. The cumulative capacity factors can be used with the associated irradiation periods to determine effective offline times for depletion, which are also shown in table 2.3.1. Three cycles of operation and shutdown are employed for the PWR to simulate the combined irradiation and downtime period, while four are employed for the BWR given the long irradiation periods resulting from relatively lower burnup values. For example, for the PWR subset 6 calculation, one cycle consists of the assembly being irradiated for 289 days and then cooled for 166 days.

Reactor discharge is defined as the end of the final offline period, where assemblies are transferred to spent fuel pools. The typical residence time of assemblies in spent fuel pools is typically no more than ten years. For the corresponding discharge periods in each UNF case, the first ten years of decay is held to correspond to cooling in a spent fuel pool while any remaining time is taken up by dry storage. A major assumption in the study is that the physical form of assemblies is not modified at any point in interim storage, e.g. fuel rods are not consolidated to reduce assembly volumes for limited pool storage areas. After discharge from the reactor, the assembly is cooled for another 100 years in dry casks, which represents the anticipated time period before final disposition in the U.S. Finally, to coincide with the canister failure assumptions (to be explained in chapter 3) another 1000 years of decay is employed to calculate the actinide source term for nuclide transport. While the statistical discharge periods will be important for emplacement inventories, their impact on the source term for transport is expected to be negligible, and this procedure is maintained for purposes of diligence.

2.4.2 Results

When calculating nuclide inventories for waste management purposes, it is usually important to identify the level of radioactivity and heat emission characteristics over time. These figures help engineers design shielding to prevent doses to the biosphere and determine proper arrangements of assemblies or canisters in spent fuel pools, dry casks, and repository tunnels to allow for adequate heat emission. These considerations often have implications on material resources, the economy of space, and site selection. Another matter of importance is the inventory of thermally fissile material (TFM), which is used for criticality safety analyses and often creates further restrictions on the design of storage systems. Factoring all such considerations for interim storage is beyond the scope of this study. However, for direct disposal, there is key importance in characterizing the actinide inventory at reactor discharge, repository emplacement, and eventual failure to provide the source term for nuclide transport, which in turn may create the source term for criticality in the far-field.

A post-processing script was written for the Origen-ARP output files to collect and organize data on actinides and fission products for both irradiation and decay periods, and to also create part of the input deck for the transport code in chapter 3. A summary of results at discharge is shown in table 2.4.1 for the six different UNF cases that includes enrichment, fissile content, the mass of uranium M_U, the mass of transuranics (TRU) M_{TRU}, the mass of non-actinides M_{NA}^{g} that are gaseous at $100°C$, and the mass of other non-actinides $M_{NA}^{l,s}$. The enrichment is defined as the ratio of the mass of fissile U-233 and U-235 over the total mass of uranium. This figure is important for making comparisons with the initial enrichment of the assembly and, for nuclide transport, determining the role of transuranics in making up the fissile composition of a critical mass. Regardless of half-life, the fissile nuclides acknowledged in this chapter include Np-236, Pu-237, Pu-239, Pu-241, Am-242, Am-244m, and Cm-245 as a matter of a conservatism, and the fissile content is based on the mass of all fissile nuclides over the total mass of heavy metal (HM). The mass of heavy metal covers all elements in the f-block, including thorium and protactinium, although these two elements are not included in the mass of TRU. Furthermore, these elements do not contain fissile nuclides of importance, and will be ignored in the transport study. It should be noted that there is minuscule difference between M_{HM} and $M_U + M_{TRU}$.

On average, the total amount of uranium consumed by the end of reactor operation per metric ton initially loaded is about 45 kg for the BWR and 53 kg for the PWR. The enrichment figures of the BWR data in table 2.4.1 indicate that burnup levels can deplete the U-235 concentration below the 0.711 wt% level of natural uranium, with the exception of the low-burnup, low-enrichment of subset 6. For the PWR used fuel, since the initial enrichments are relatively higher than those for the BWR (see table 2.3.1 on page 15), enrichment at discharge is around 0.9 wt%. Within the 1 MTU basis, the high values of initial enrichment and burnup in the PWR fuel lead to relatively stronger generation of TRU, which results in TFM content as high as 1.67 wt%. Nonetheless, given the assembly loadings per canister described in section 2.3.2, the actual mass of TFM per canister is roughly the same between the two UNF types.

During the cooling period after discharge, some shorter-lived transuranics decay to uranium isotopes to increase the uranium inventory, with losses of TRU on the order of hundreds of grams, as shown in table 2.4.2. This reduces the mass of heavy metal, and there are decreases in the overall fissile content and small increases in the enrichment. There are decreases in the gaseous non-actinide inventories on the order of tens of grams due to decay, which are directly compensated by increases in the liquid/solid inventory, maintaining the total M_{NA} constant.

Table 2.4.3 shows data at canister failure, where the fissile content among different UNF subsets for either reactor is slightly larger than emplacement values from further decay of TRU. However, the increases in enrichment are much more dramatic, which implies the stronger role of U-235 and Pu-239 in determining the content of TFM in the assembly at long cooling periods. Since the fissile mass for either canister type will be very similar, unique behavior in transport results will likely be dependent on specific actinide compositions among the subsets. The canister inventory of certain isotopes is shown table 2.4.4, where the masses of Pu-239 in the PWR assemblies are higher per given subset. This will allow for more considerable generation of U-235 via decay. The content of Np-237 is usually higher in the BWR subsets, which will likely impart interesting U-233 behavior.

	BWR						PWR					
Subset	$\frac{M_{23}+M_{25}}{M_U}$[wt%]	TFM [wt%]	M_U [g]	M_{TRU} [g]	M_{NA}^{g} [g]	$M_{NA}^{l,s}$ [g]	$\frac{M_{23}+M_{25}}{M_U}$[wt%]	TFM [wt%]	M_U [g]	M_{TRU} [g]	M_{NA}^{g} [g]	$M_{NA}^{l,s}$ [g]
1	0.703	1.241	956542	8807	5741	28939	0.901	1.655	947157	11570	6895	34435
2	0.611	1.201	941065	10429	7985	40555	0.848	1.674	934124	13267	8745	43945
3	0.703	1.283	945946	9920	7257	36873	0.879	1.684	938590	12707	8113	40697
4	0.674	1.218	954972	8992	5972	30108	0.901	1.668	945042	11849	7188	35932
5	0.72	1.221	964806	7829	4541	22789	0.927	1.636	954216	10580	5898	29352
6	0.845	1.289	974984	6405	3095	15555	0.95	1.587	963718	9127	4553	22587

Table 2.4.1: Inventory characteristics at discharge based on 1 MTU.

	BWR						PWR					
Subset	$\frac{M_{23}+M_{25}}{M_U}$[wt%]	TFM [wt%]	M_U [g]	M_{TRU} [g]	M_{NA}^{g} [g]	$M_{NA}^{l,s}$ [g]	$\frac{M_{23}+M_{25}}{M_U}$[wt%]	TFM [wt%]	M_U [g]	M_{TRU} [g]	M_{NA}^{g} [g]	$M_{NA}^{l,s}$ [g]
1	0.704	1.14	956679	8665	5718	28962	0.903	1.502	947351	11368	6868	34462
2	0.613	1.076	941274	10214	7955	40585	0.849	1.492	934397	12985	8711	43979
3	0.705	1.165	946126	9732	7229	36901	0.881	1.511	938833	12455	8081	40729
4	0.675	1.113	955116	8842	5949	30131	0.903	1.51	945246	11636	7159	35961
5	0.722	1.136	964910	7720	4523	22807	0.929	1.501	954374	10414	5874	29376
6	0.846	1.228	975047	6337	3082	15568	0.952	1.479	963828	9013	4534	22606

Table 2.4.2: Inventory characteristics at emplacement based on 1 MTU.

	BWR						PWR					
Subset	$\frac{M_{23}+M_{25}}{M_U}$[wt%]	TFM [wt%]	M_U [g]	M_{TRU} [g]	M_{NA}^{g} [g]	$M_{NA}^{l,s}$ [g]	$\frac{M_{23}+M_{25}}{M_U}$[wt%]	TFM [wt%]	M_U [g]	M_{TRU} [g]	M_{NA}^{g} [g]	$M_{NA}^{l,s}$ [g]
1	0.716	1.141	957082	8240	5718	28962	0.92	1.503	947852	10838	6868	34462
2	0.626	1.077	941788	9671	7955	40585	0.867	1.493	935011	12335	8711	43979
3	0.717	1.165	946602	9230	7229	36901	0.899	1.512	939407	11846	8081	40729
4	0.688	1.114	955533	8405	5949	30131	0.92	1.511	945763	11089	7159	35961
5	0.733	1.136	965256	7356	4523	22807	0.945	1.501	954817	9946	5874	29376
6	0.857	1.228	975317	6055	3082	15568	0.967	1.479	964198	8620	4534	22606

Table 2.4.3: Inventory characteristics at anticipated canister failure based on 1 MTU.

2.5 Discussion

Representative used nuclear fuel cases have been calculated based on several datasets describing the current inventory in the United States. These cases were used to evaluate the actinide inventories of both BWR and PWR canisters when emplaced into a repository, along with that of the anticipated point in time when canisters fail and become subject to nuclide transport processes. This methodology was employed to condense a multitude of used fuel assembly characteristics into reliable groups covering the scale of variation, such that nuclide transport studies would correspond to probable source terms without necessarily attempting to simulate reality. Assumptions were made to connect diverse datasets and derive quantities important to depletion calculations for the fresh fuel, and specific reactor assembly models were employed in depletion code to evaluate the inventory of fission products and fissile nuclides upon irradiation and subsequent cooling. It was demonstrated that despite the effects of diverse values of burnup and initial enrichment, the total content of fissile material between different canisters for BWR and PWR UNF will be roughly similar per subset. It is predicted that specific actinide inventories will be a very important factor in determining unique transport behaviors among the various subsets of fuel to be employed in chapter 3.

		BWR Subsets						PWR Subsets					
Nuclide	$t_{1/2}$ [yr]	1	2	3	4	5	6	1	2	3	4	5	6
U-233	1.59E+05	3.30E-01	4.40E-01	4.07E-01	3.42E-01	2.66E-01	1.79E-01	4.87E-01	6.06E-01	5.66E-01	5.06E-01	4.20E-01	3.23E-01
U-234	2.46E+05	3.16E+02	4.63E+02	4.18E+02	3.28E+02	2.47E+02	1.85E+02	4.12E+02	5.63E+02	5.09E+02	4.34E+02	3.43E+02	2.61E+02
U-235	7.04E+08	6.86E+03	5.89E+03	6.79E+03	6.57E+03	7.08E+03	8.36E+03	8.72E+03	8.11E+03	8.44E+03	8.70E+03	9.03E+03	9.32E+03
U-236	2.34E+07	4.41E+03	5.93E+03	5.59E+03	4.53E+03	3.53E+03	2.58E+03	5.22E+03	6.44E+03	6.06E+03	5.43E+03	4.55E+03	3.62E+03
U-238	4.47E+09	9.46E+05	9.30E+05	9.34E+05	9.44E+05	9.54E+05	9.64E+05	9.34E+05	9.20E+05	9.24E+05	9.31E+05	9.41E+05	9.51E+05
Np-237	2.14E+06	1.24E+03	1.63E+03	1.52E+03	1.29E+03	1.01E+03	6.88E+02	1.84E+03	2.26E+03	2.12E+03	1.91E+03	1.59E+03	1.23E+03
Pu-239	2.41E+04	4.15E+03	4.35E+03	4.35E+03	4.17E+03	3.97E+03	3.70E+03	5.69E+03	6.03E+03	5.93E+03	5.75E+03	5.45E+03	5.06E+03
Pu-240	6.56E+03	2.07E+03	2.49E+03	2.34E+03	2.13E+03	1.81E+03	1.36E+03	2.28E+03	2.62E+03	2.51E+03	2.33E+03	2.06E+03	1.75E+03
Pu-241	1.43E+01	1.09E-03	3.60E-03	2.41E-03	1.29E-03	4.58E-04	8.64E-05	3.17E-03	7.67E-03	5.77E-03	3.69E-03	1.72E-03	6.04E-04
Pu-242	3.74E+05	5.05E+02	7.98E+02	6.76E+02	5.42E+02	3.62E+02	1.83E+02	6.36E+02	8.75E+02	7.88E+02	6.71E+02	5.07E+02	3.42E+02
Am-241	4.33E+02	1.82E+02	2.26E+02	2.14E+02	1.87E+02	1.51E+02	1.07E+02	2.68E+02	3.20E+02	3.04E+02	2.77E+02	2.35E+02	1.88E+02
Am-243	7.39E+03	8.75E+01	1.74E+02	1.37E+02	9.70E+01	5.30E+01	1.91E+01	1.37E+02	2.22E+02	1.90E+02	1.49E+02	9.73E+01	5.34E+01
Cm-245	8.56E+03	6.53E-01	2.17E+00	1.45E+00	7.75E-01	2.75E-01	5.19E-02	1.90E+00	4.61E+00	3.47E+00	2.22E+00	1.03E+00	3.63E-01
Cm-246	4.76E+03	7.05E-02	3.21E-01	1.88E-01	8.80E-02	2.45E-02	3.21E-03	1.69E-01	5.03E-01	3.52E-01	2.03E-01	8.04E-02	2.30E-02

Table 2.4.4: Masses in grams of actinides in the assembly at anticipated canister failure, based on 1 MTU.

Chapter 3

Uncertainty analysis of far-field precipitation

3.1 Introduction

It was demonstrated in chapter 2 that quantities of fissile material from both uranium and transuranics remain in used fuel assemblies after reactor operation. On a single assembly basis, the contents are not significant due to the level of depletion, and packages with multiple assemblies can be engineered to meet criticality safety limits under a number of circumstances that include reconfigurations of the assembly components. [25] In order for criticality to be of concern for the far-field, the used fuel must be dissolved by groundwater, transported through buffer material and rock fractures, and finally reconcentrated into a critical mass at a single location. Criticality will depend on both the mass and fissile nuclide content of the accumulation, among other geometric considerations; if hydrological conditions favor the mobility of TRU relative to uranium, there may be an increase in enrichment compared to any single canister in the repository. Therefore, this chapter will describe an analysis that will characterize repository-wide actinide transport over a geologic time scale.

Canisters for used nuclear fuel will be treated discretely in a matrix intended to model an abstracted repository, and assumptions will be made to conservatively overestimate the mass of nuclides accumulating in the far-field in order to observe minimal time periods of relevance. Variation in the source term of used nuclear fuel is liable to introduce uncertainty in the mass and heavy metal composition of a far-field precipitate. Furthermore, there is also a spread in measured values for chemical properties important to the release and hydrological transport of actinides contained within the waste. To reduce the compounded uncertainty, the representative UNF assembly characteristics from chapter 2 will be utilized to bound the source term; this will allow transport results to be tied to particular values of burnup, discharge time, mass loading, and fissile content.

A sampling method will be used to acknowledge the scope of variation in the transport parameters in the calculations. Results from multiple iterations based on this sampling procedure will be used to evaluate the uncertainty in total mass and composition of a hypothetical heavy metal deposition in the far-field. In turn, representative precipitate compositions will be defined based on a statistical treatment of these results. These compositions can be used to as the source term for the criticality scoping analysis in chapter 4, which will probe the natural geometric configurations needed for said compositions to be relevant to a critical mass. This study will provide a basis for evaluating the feasibility of obtaining such masses in a worst case scenario.

3.2 Background

3.2.1 Natural analog

The scenario concerns the leaching of uranium into groundwater and re-concentration into a reducing region conducive to precipitation, upon which the reconfiguration of heavy metal oxides creates a critical mass. Given the lack of an applied repository for a direct disposal application, and for that matter an immensely compromised one, there is no site data for uranium transport from a man-made engineered system, especially in such a massive context. However, high grade ore deposits from around the world can serve as natural analogs for uranium migration and geochemistry for a variety of geologies, such as Cigar Lake and Great Bear Lake of Canada and Peña Blanca in Mexico. One such analog is the Oklo ore deposit, which is one of six main deposits in the Franceville basin of Gabon, West Africa. This analog has particular importance in that there is evidence of critical chain reactions taking place at this site some two billion years ago. At this point in geological time, there was a major oxidative shift in the environment caused by the emergence of photosynthetic life on earth. The oxidizing environment led to the dissolution of low-grade ore into hydrothermal fluids, and via a repetitive fractionation process, concentrated tabular pitchblende deposits were formed in sandstone with significant quantities of organic carbonaceous material. [26–30] High grade ore as high as 10-15% was created from the reducing environment provided in fracture zones adjacent to clay shale deposits. With natural groundwater acting as a moderator and the lack of boron and rare-earth elements that would serve as poisons, along with the spontaneous fission of U-238, chain reactions proceeded intermittently for about a million years, leading to the consumption of hundreds of tons of uranium. Altogether, the low degree of metamorphosis in the basin has allowed for the preservation of the reactor zones and confirmation of criticality via isotopic analysis of uranium and stable fission products.

3.2.2 Previous work

Research has been undertaken on repository-wide nuclide transport from compromised waste packages in a repository. Discrete emplacements of waste forms have been modeled as arrays of finite areal "patches" of constant source strength that directly interact with fractures. In this finite plane source model, radionuclides released from the patches were transported by advection along the length of the fractures while being dispersed transversally according to the the dispersion coefficient D^T, all while interacting diffusively with the rock matrix. [31–34] Via the superposition of contributions from individual sources, this approach allowed for the characterization of the concentration field in the fracture. Comparisons were also be made with an infinite planar source to draw conclusions on the role of discretization in determining concentration behavior using a distance-based parameter, i.e. identifying the points when the plumes would be completely smeared.

For purposes of overestimating accumulations of TFM in the far-field for criticality studies, the superposition approach was employed with a fracture-based transport model with source terms emulating the interaction between high level waste and the engineered barrier system. [7, 8] This model included the effects of multiple parallel planar fractures, and modeled the release from discrete EBS units into these fractures through independent linear pathways. While the point of precipitation was held to be common for all independent mass fluxes in these pathways, the solutes emerging from the each emplacement were considered to be non-interacting, where the full solubility-limit could be reached for each nuclide. These very conservative assumptions were made to purposely overestimate the magnitude of mass precipitating in the far-field.

A compartment-based model was devised to understand the effect of the concentration gradient on a succession of waste forms on a linear transport pathway. [35–37] In this approach, adjacent discrete emplacements were modeled as “compartments” comprised of the waste form matrix enveloped by a buffering material, which in turn was surrounded by near-field rock. These compartments would be arranged into a row aligned parallel or perpendicular to groundwater flow, where nuclides would be congruently-released from the waste into the buffer, and then subsequently into the adjoining host rock. Nuclides from upstream compartments would progress into the rock of downstream compartments, which would effect the amount of solute entering the host rock from the downstream buffer. Thus, the spatial behavior of concentration was determined in a Markov-chain analysis, which could allow for the determination of total precipitation at the host rock exit of the last downstream compartment. [38] This spatially-dependent model assisted in understanding the peak far-field exit concentration and the effects of the HLW leach period given canister interference. Nonetheless, while adding a necessary degree of realism to the approach, the methodology was unable to acknowledge the multi-member decay chain effects needed to understand the behavior of TRU. This would be particularly important for evaluating the fissile inventory at the far-field exit for direct disposal.

3.3 Methodology

3.3.1 Overview

The scenario acknowledges emplacements of metallic UNF canisters in a granitic repository that form a uniformly-spaced planar array, which is visualized in figure 3.3.1. Each canister is surrounded by an engineered barrier system that is simplified into one buffering layer of bentonite (montmorillonite) clay adjoining the granitic host rock, and each EBS is separated by a uniform pitch distance. A hydraulic gradient across the repository plane induces the flow of groundwater with a uniform average linear velocity. Although the bentonite is completely saturated from this groundwater flow, inadequate heat dissipation from the waste has formed a small gap between the buffer and the granite, such that any sort of solute diffusively transported to the surface of the buffer can directly infiltrate the natural fractures of the host rock. These fractures are planar, evenly spaced, and intersecting the entire repository host rock with a set aperture. The overall hydraulic conductivity of these fractures is very high relative to the continuous rock matrix, which allows for mass transport directly from the buffer surface into the rock pores to be ignored.

The loading of canisters into the repository has introduced defects to the shell material, and the interaction of groundwater coupled with the presence of corrosion-enhancing ionic species promotes localized corrosion. Over the course of one thousand years, pinhole corrosion causes groundwater infiltration and the dissolution of the UO_2 fuel. Degradation of the fuel pellets, cladding, rod spacers, and assembly spacers is extensive such that the dissolution process would not be hindered by solubility and diffusion limits that would normally be poised by adjacent fuel rods. Rather, the dissolved fuel assumes the total surface area available to the outside of the compromised canister. Nuclides arriving to the canister surface undergo diffusive mass transport into the surrounding buffer.

Once nuclides have diffused to the surface of the buffer, nuclides infiltrate the entrances of the fractures and become transported by advection along the longitudinal length of the fracture. Diffusion drives some solutes from the fracture into the adjoining rock matrices as the concentration gradient would allow. Given the interconnected nature of the fractures, it is assumed that the concentration of nuclides is not affected by the amount of solutes leached from adjacent emplacements, i.e. the nuclides in the waste can enter solution up to their solubility limit without effects from canisters upstream. This assumption is taken further in that the mass fluxes from each waste form can be superposed, wherein a combined precipitate can form at the fracture exits where reducing, sorbing conditions are present. The precipitate is assumed to form homogeneously.

3.3.2 Radionuclide transport in fractures

The use of crystalline granite as a host medium requires the role of fractures to be acknowledged in radionuclide transport. The rock matrix of granite is too impervious to warrant any appreciable transport through the continuous medium, as transport here is mainly determined by a diffusion process governed by the concentration gradient. The most significant pathway for transport will be through advection in fractures that intersect the solid rock matrix, where solute nuclides can interact diffusively at the boundaries. For this reason, when the effective porosities of samples of granite are discussed, it is often an indirect measure of the fracture density.

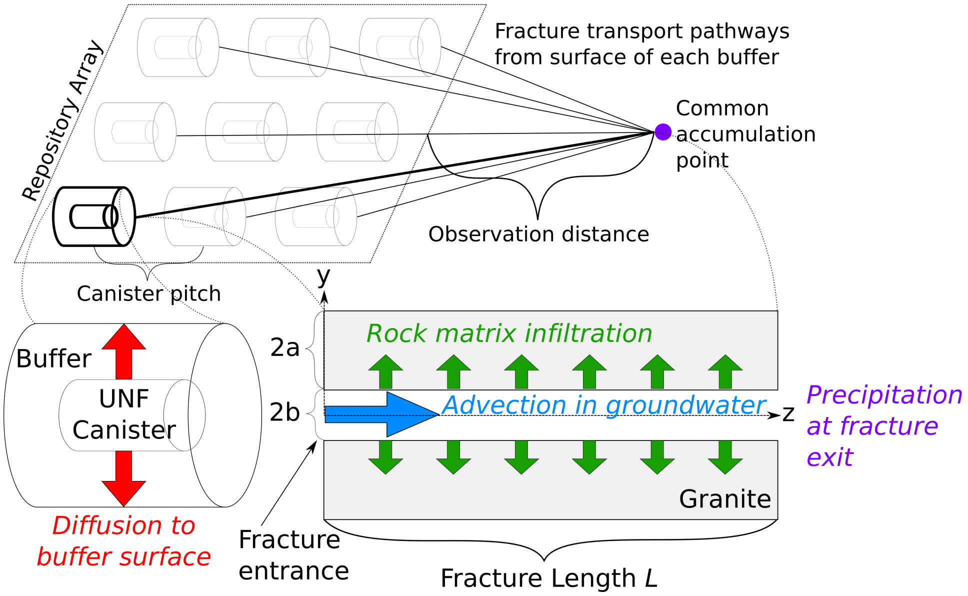

Figure 3.3.1: Visualization of model for nuclide transport in granite fractures from individual waste emplacements to a common point of precipitation, where the inset shows the major processes involved in one individual transport pathway of unique length L.

The Transport-to-Biosphere (TTB) code was developed to calculate the one dimensional fracture-based transport of radionuclides in arbitrary-length decay chains. [7, 39] It models the release of radionuclides from a spherical waste form through a diffusing buffer layer, where radionuclides are released uniformly at the surface of the buffer and immediately infiltrate the entrances of parallel planar fractures of set aperture (width). Within the fractures, nuclides are longitudinally dispersed along the fracture length while simultaneously infiltrating the pore space of the surrounding rock matrix according to the concentration gradient. By coupling the advection dispersion equation for a fracture and a continuous rock matrix surrounding the fracture, the mass flux and total mass of precipitates forming at a given transport distance can be determined. Parameters of importance to the TTB calculations are shown in table 3.3.1, where the waste canister dimensions are inspired by Swedish and Finnish concepts, while the buffer thickness is adapted from the JAEA.

The simplification of the source term into the spherical geometry allows for the use of the radial non-volatile advection-dispersion equation (ADE) to model transport for all nuclides in the decay chain. Angular dependence is further neglected to provide a uniform flux at the waste surface, and spatial dependence is reduced to r. Due the use of bentonite as a low-permeability buffer component, advection is ignored and only diffusive mass transport is employed. The appropriate form of the ADE for the saturated buffer is shown in equation (3.3.1), which shows the relationship for the concentration C^b over time of nuclides $k = 1 \ldots n$ with decay constants λ_k in a decay chain. It is applicable to the region between the surface of the waste at r_1 and the surface of the surrounding buffer at r_2.

$$
\begin{aligned}
K_{e(k+1)}\frac{\partial C^b_{k+1}}{\partial t} + \lambda_{k+1}K_{e(k+1)}C^b_{k+1} &= \\
&\frac{D_{e(k+1)}}{r^2}\frac{\partial}{\partial r}\left(r^2\frac{\partial C^b_{k+1}}{\partial r}\right) + \lambda_k K_{e(k)}C^b_k,\ t > 0,\ r_1 < r < r_2 \quad (3.3.1)
\end{aligned}
$$

In this relationship, $K_{e(k)}$ is the retardation factor of the element e comprising nuclide k, which is a measure of the congruency between the groundwater velocity and the measured velocity of the solute due to sorption on porous surfaces. It is a function of the buffer density ρ_b, the porosity ϵ_b, as well as the measured partition, or sorption distribution, coefficient $K_{d,e(k)}$, as shown in equation (3.3.2). $K^b_{d,e(k)}$ relates the equilibrium distribution of the solid (sorbed) and dissolved phases, and in this model, a linear isotherm assumption allows for this quantity to remain constant per given aqueous phase concentration. The molecular diffusion coefficient $D_{e(k)}$ is a constant relating the steady-state flux of solute with its concentration gradient, as governed by Fick's first law. In the equation, the coefficient is dependent on the tortuosity factor for the buffer material (τ_b), which corrects for the diversion of the transport pathway from a straight line, and the diffusion coefficient as measured in free water: $D^F_{e(k)}$. (Given the similarity in D^F for the actinides of interest in this study, it was modeled as a constant.)

$$
K_{e(k)} = 1 + \rho_b K^b_{d,e(k)}(1-\epsilon_b)/\epsilon_b \qquad (3.3.2)
$$

TTB allows for either congruent-release or solubility-limited boundary conditions to be specified per nuclide in the waste. That is, a nuclide can be modeled as being released congruently with the dissolution rate of the waste form over a leach period T_L, or else released at a rate limited by their solubility $C^*_{e(k)}$ in groundwater. Given the low solubility and numerical dominance of uranium atoms in the UO_2 fuel, the release of uranium from the canister is solubility-limited. A precipitate will form uniformly on the surface of the waste and then dissolved into solution when the concentration gradient permits until the precipitate disappears at a time t^*. Using a pivoting term $\sigma_k \in \{0,1\}$, the boundary condition for each nuclide in the decay chain can be described using the solution of equation (3.3.1) in equation (3.3.3), where h is the Heaviside step function, $m_k(t)$ is the congruent release rate from the waste form, and $\gamma_k(t)$ is the solubility allocation (which is approximated by m_k and T_L).

$$
-(1-\sigma)D_{e(k)}\epsilon_b\left.\frac{\partial C^b_k}{\partial r}\right|_{r=r_1} + \sigma_k C^b_k(r_1,t) = \begin{cases}\gamma_k(t)C^*_{e(k)}\left[h(t) - h\left(t-t^*\right)\right] & \sigma_k = 1\\ m_k(t)\left[h(t) - h\left(t-T_L\right)\right] & \sigma_k = 0\end{cases},\ t > 0 \qquad (3.3.3)
$$

The waste surface precipitation model emphasizes considerations for vitrified high level waste, where the mass-release behavior of the waste type and contained radionuclides can be effectively separated. For direct disposal, since the waste form and majority waste constituent are the same, a leach period was set to correspond to the precipitate disappearance time. This was performed by specifying the solubility-limited boundary condition in the code and then determining $T_L \approx t^*$ iteratively using the bisection method. With an appropriately selected T_L, all TRU were then assumed to be congruently released according to the uranium release rate due to their proportionately smaller fractions in the waste. Considering that the solubility of actinides is usually very low, particularly plutonium, this is considered a conservative assumption meant to enhance heavy metal transport through the buffer.

The flux of nuclides from the surface of the buffer $\left(-\epsilon_b D_{e(k)} \frac{\partial C_k^b}{\partial r}\bigg|_{r=r_2}\right)$ is adjusted based on the spacing between waste forms relative to the buffer surface area. This adjusted quantity is used as the inlet boundary condition for the fractures, which are modeled as planar and extending some distance L into the z direction (with the inlet at $z = 0$) with apertures b and parallel spacing a as components in the y direction. The ADE for the fracture (equation (3.3.4)) solves for the fracture concentration C by coupling the solution of the solute concentration in the rock matrix C^r (equation (3.3.5)) at the interface $y = 0$, and analytical solutions are discussed in Ref. [6]. The mass transport terms consist of the longitudinal dispersion coefficient D^L and the molecular diffusion coefficient $D^*_{e(k)}$ of the adjoining rock matrix. Dispersion is a phenomenon where random variations in the groundwater velocity, e.g. via pore opening or water density variations, lead to a spreading of the solute concentration relative to the average linear velocity v. Given the mixing ensured by dispersion and the fact that $b \ll L$, the use of a one-dimensional flow field model for the fracture is considered valid. Transverse dispersion is ignored within this 1D treatment, and D^L is considered to be common for all elements.

$$\begin{aligned} R_{e(k+1)} \frac{\partial C_{k+1}}{\partial t} + v \frac{\partial C_{k+1}}{\partial z} - D^L \frac{\partial^2 C_{k+1}}{\partial z^2} - \frac{D^*_{e(k+1)}}{b} \frac{\partial C^r_{k+1}}{\partial y}\bigg|_{y=0} \\ = -R_{e(k+1)} \lambda_{k+1} C_{k+1} + R_{e(k)} \lambda_k C_k,\ t > 0,\ z > 0 \end{aligned} \tag{3.3.4}$$

$$\alpha_{e(k+1)} \frac{\partial C^r_{k+1}}{\partial t} = D^*_{e(k+1)} \frac{\partial^2 C^r_{k+1}}{\partial y^2} - \alpha_{e(k+1)} \lambda_{k+1} C^r_{k+1} + \alpha_{e(k)} \lambda_k C^r_k = 0,\ t > 0,\ z > 0,\ 0 < y < a \tag{3.3.5}$$

A retardation factor $R_{e(k)}$ is included in the governing equation of the fracture to account for the tendency of fracture-filling materials to retard the movement of solutes relative to the average velocity. However, in this study, the fractures are considered to be completely filled with water with no porous material, which leads to $R_{e(k)} = 1$ for any element. It is assumed that advective and dispersive transport in the fracture is much faster than the strictly diffusive transport of the rock matrix, such that mass transport via molecular diffusion would occur perpendicular to the fracture plane (y relative to z). The effective molecular diffusion coefficient is described in equation (3.3.6) in terms of the rock matrix porosity ϵ_r, tortuosity correction factor τ_r, and the free water diffusion coefficient.

Quantity	Value
Uranium oxide density $[kg/m^3]$	10,950
Canister height (H_c) $[m]$	4.817
Canister radius (r_c) $[m]$	0.508
Buffer thickness (t_b) $[m]$	0.7
Spherical equivalent fuel radius (r_f) $[m]$	1.164
Buffer spherical equivalent radius (r_b) $[m]$	2.119
Canister spacing $[m]$	20

Table 3.3.1: Emplacement parameters held constant for the analysis.

$$D^*_{e(k)} = \epsilon_r \tau_r D^F_{e(k)} \tag{3.3.6}$$

The capacity factor for the rock is analogous to the retardation factor of the buffer, and is defined in equation (3.3.7), where $K^r_{d,e(k)}$ is distinct from $K^b_{d,e(k)}$ by virtue of being relevant to the geochemistry of granite, not bentonite.

$$\alpha_{e(k)} = \epsilon_r + \rho_r \left(1 - \epsilon_r\right) K^r_{d,e(k)} \tag{3.3.7}$$

In terms of decay chain specification, the elements of interest in this study are those whose isotopes are fissile or give rise to fissile isotopes through radioactive decay. In general, focus lies on the uranium isotopes U-233 and U-235 and plutonium isotopes Pu-239 and Pu-241. For ease of calculation, engineering-informed decisions were made to exclude most isotopes in the decay chains with minuscule quantities, half-lives shorter than the expected canister failure time of 1000 years, or a combination of both. The only exception is fissile Pu-241, with a half-life of 14 years. From this exception, the longer lived daughter Am-241 (432 years) is included to realistically model the effect of Np-237 generation.

The decay chains of interest are shown in figure 3.3.2 grouped by the common “4n” nomenclature, where the nuclides chosen for TTB calculation are emphasized in bold. Ultimately, the nuclides of interest consist of five actinides: uranium through curium. The decay products of the final uranium isotopes, like thorium 229, 230, and 232, are not considered significant for criticality, although the generation of U-233 from absorption on Th-232 could theoretically have importance on reactivity feedback depending on the neutron spectrum. Intermediary protactinium and thorium isotopes are ignored due to very short half lives, although for completeness it should be noted that direct beta decay from Pa-234m is more probable than the isomeric transition. There is also a higher probability for direct alpha decay from Cm-243 to Pu-239 apart from the listed pathway, but the short half-life of this isotope (29 years) warrants the assumption that all of its mass is effectively lumped into that of Pu-239. There is also generation of Pu-240 via the alpha decay of Cm-244, but the same assumption as before is applied due to the short half life (18 years). Other transmutation pathways not indicated in the figure, such as spontaneous fission, are ignored.

$$\text{4n: } {}^{248}_{96}\mathrm{Cm} \xrightarrow{\alpha} {}^{244}_{94}\mathrm{Pu} \xrightarrow{\alpha} {}^{240}_{92}\mathrm{U} \xrightarrow{\beta^-} {}^{240}_{93}\mathrm{Np} \xrightarrow{\beta^-} \mathbf{{}^{240}_{94}Pu} \xrightarrow{\alpha} \mathbf{{}^{236}_{92}U} \rightarrow \ldots$$

$$\text{4n+1: } \mathbf{{}^{245}_{96}Cm} \xrightarrow{\alpha} \mathbf{{}^{241}_{94}Pu} \xrightarrow{\beta^-} \mathbf{{}^{241}_{95}Am} \xrightarrow{\alpha} \mathbf{{}^{237}_{93}Np} \xrightarrow{\alpha} {}^{223}_{91}\mathrm{Pa} \xrightarrow{\beta^-} \mathbf{{}^{233}_{92}U} \rightarrow \ldots$$

$$\text{4n+2: } \mathbf{{}^{246}_{96}Cm} \xrightarrow{\alpha} \mathbf{{}^{242}_{94}Pu} \xrightarrow{\alpha} \mathbf{{}^{238}_{92}U} \xrightarrow{\alpha} {}^{234}_{90}\mathrm{Th} \xrightarrow{\beta^-} {}^{234m}_{91}\mathrm{Pa} \xrightarrow{IT} {}^{234}_{91}\mathrm{Pa} \xrightarrow{\beta^-} \mathbf{{}^{234}_{92}U} \rightarrow \ldots$$

$$\text{4n+3: } {}^{243}_{96}\mathrm{Cm} \xrightarrow{\varepsilon} \mathbf{{}^{243}_{95}Am} \xrightarrow{\alpha} {}^{239}_{93}\mathrm{Np} \xrightarrow{\beta^-} \mathbf{{}^{239}_{94}Pu} \xrightarrow{\alpha} \mathbf{{}^{235}_{92}U} \rightarrow \ldots$$

Figure 3.3.2: Decay chains of interest, with nuclides chosen for the transport study shown in bold.

The far-field precipitate is expected to largely consist of uranium isotopes given their preeminence in the UO_2 fuel, as shown in table 2.4.3 on page 19. Criticality will largely be governed by the content of U-233 and U-235 relative to other uranium isotopes. Therefore, to lessen computational expense, results for uranium will only be included for the total precipitate mass, and the inventory of TRU will be factored into the final results only through their role as precursors.

3.3.3 Variation in transport properties

There is considerable variation in the parameters controlling dissolution, diffusion, and advection for solutes in the waste in the engineered barriers and granitic host rock. These differences are based on a variety of conditions, including the specific porewater chemistry and the methods used to determine the quantities in the laboratory. A summary of the expected differences in important variables in shown in table 3.3.2.

Sorption

To measure K_d, an experiment needs to determine the relative equilibrium concentrations of a contaminate in the aqueous and sorbed phase, usually with conditions specific to a porous medium and the expected redox environment. This can be performed via a number of means. One example is a method where a solution with a specific concentration of solute is mixed with the medium or interest, whereby the solution is eventually separated from the solute for the remaining solute concentration to be measured. [40] The sorbed concentration of the solute can be determined from the initial (injected) and final concentrations of the solution. Another method factors the effects of advection by passing the solution through the porous medium, and then comparing the relative velocity of the solute to that of the solvent. In this case, K_d would be derived via the retardation factor. Altogether, such experimental measurements would indicate the availability of “parking spots” in the pore space where the aqueous component can drop out of solution. The opposite process of desorption is also applicable, as the process is considered reversible.

For granite K_d^r data, water types included natural and synthetic groundwater and seawater, distilled water, deionized water, granitic pore water, and calcium chloride solution. Water composition can influence uranium deposition; for example, the presence of the carbonate can increase the solubility of the uranyl anion $\left(UO_2^{2+}\right)$ and the rate of oxidative dissolution, while calcium ions and silicates can stabilize uranyl precipitates. [41] Because of these effects, the ionic strength, or the concentration of such ions, are usually given per K_d evaluation. The corresponding redox conditions in the granitic water ranged from reducing (sometimes controlled with sodium dithionite, nitrogen, or iron(II)), oxidizing, atmospheric, and inert (Argon). The ion charges of uranium are either 4+ and 6+, with the hexavalent value comprising the median and both quartiles, while Pu(IV), Np(V), Am(III), and Cm(III) firmly describe the speciation of the other actinides. The corresponding pH values are slightly basic, where the medians fall between 8.0 and 8.4 for uranium, neptunium, and plutonium. The data for curium are most basic, with a median of 9.9, while there is a wider spread for americium data, where the average is 7.3.

Bentonite K_d^b data included bentonite-specific pore water and a greater variation in the concentrations of $NaCl$ in solution for saline solutions, along with solutions of sodium bicarbonate and those expected for cement. Some data further specified a controlled quantity or total absence of CO_2 in the environment. The redox states of actinides are the same as those observed in granite, although there is more of a spread in the ion charges for neptunium, with a lower quartile of 4.5+ and median of 5+. The corresponding pH values range from slightly acidic to slightly basic, with median values lying between 6.8 (uranium) and 9.1 (curium).

The spread in values for the partition coefficient of actinides in granite and bentonite is diagrammed in figure 3.3.3, and associated distribution functions are plotted in figure 3.3.4. Without data from site-specific samples, the approach of this thesis acknowledges the full range of conditions for the supplied values of K_d that are evident in these plots. This will allow the transport results to cover both reducing and oxidizing conditions in the buffer and host rock, with different ranges of possible hydrogen activity.

There is a lack of unimodal behavior in the probability curves for K_d, especially for granite. The differences in redox state are suspected to be the cause of this behavior, as certain redox states will correspond more strongly with a certain range of K_d. For example, in granite, the 6+ states of uranium mostly cover the lower range of K_d^r from $3 * 10^{-4}$ to $2\,\frac{m^3}{kg}$ while the 4+ state mostly covers the next range from 2 to $270\,\frac{m^3}{kg}$. This supports the general observation that reducing conditions relevant to the 4+ state are most antagonistic of dissolution, while the 6+ state is observed in aqueous uranyl. For neptunium, K_d^r above ≈ 0.1 are more likely to correspond to the 4+ state as opposed to the 5+ state. In bentonite, there is less lopsidedness in the K_d^b relative to the space of redox states per actinide, as values are more clustered near the centers of the distributions.

No correlation was found between K_d and the initial concentration from the associated

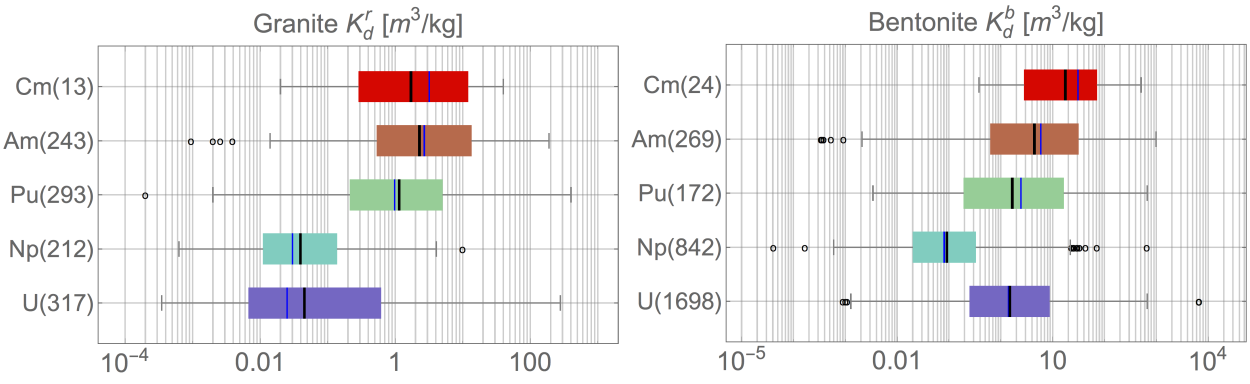

(a) Granite

(b) Bentonite

Figure 3.3.3: Variation of the partition coefficient from the JAEA Sorption Database visualized with box plots, [45] where the mean is shown in black, the median is shown in dark blue, and the sample size is indicated within parentheses.

experiments. However, the behavior of K_d with respect to pH is based on the effects acidity would have on speciation of the aqueous solute, along with the total concentration of ions in solution. In figure 3.3.5, an exemplary trend in pH behavior can be ascertained for certain levels of ionic strength of solution ($\approx 0.1 - 0.3\,M$). These peaked data points correspond to air-based redox conditions in either deionized water for granite (with injection concentrations between $10^{-6} - 10^{-5}\,M$), or sodium bicarbonate solutions for bentonite (with injection concentrations between $10^{-7} - 10^{-6}\,M$). For bentonite, the rise in K_d^b is likely caused by the formation of UO_2OH^+ or $(UO_2)_2\,CO_3\,(OH)_3^-$ species from the uranyl ion, while after $pH = 7$, the decline is caused by the dominating presence of the weakly-sorbing $UO_2\,(CO_3)_3^{4-}$ aqueous species. [42, 43] For granite, the behavior can be attributed to the formation of $UO_2\,(OH)_2$ with increasing pH, followed by a transition to aqueous $UO_2\,(OH)_3^-$. [44] Given the inability to accurately predict the long-term geochemistry of a repository, the reliance of of K_d on speciation further compounds the uncertainty of the scenario. It also demonstrates the importance of using site-specific samples of groundwater and rock during engineering design.

Diffusion

Diffusion describes the transport of a dissolved solute by way of its concentration gradient as driven by random molecular motion in the solvent. Fick's First Law (3.3.8) describes the relationship of the steady state diffusive flux F of the species in an ideal solution to the gradient ∇C using the hydrodynamic dispersion tensor $\mathbf{D_h}$. This proportionality term accounts for the contributions of both molecular diffusion and mechanical dispersion. The molecular component covers the effects of random molecular motion, while the other compo-

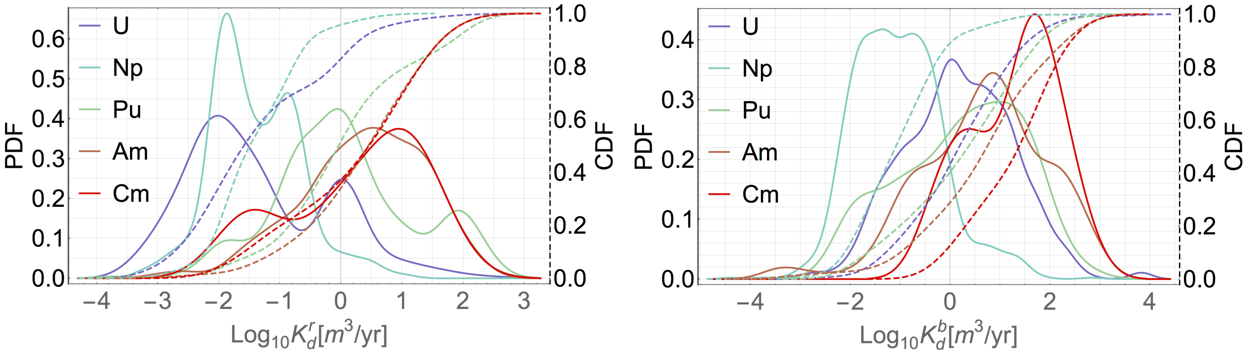

(a) Granite

(b) Bentonite

Figure 3.3.4: PDF (left axis) and CDF (right axis, dashed) for the $\log_{10}$ values of the partition coefficient based on the JAEA Sorption Database. [45]

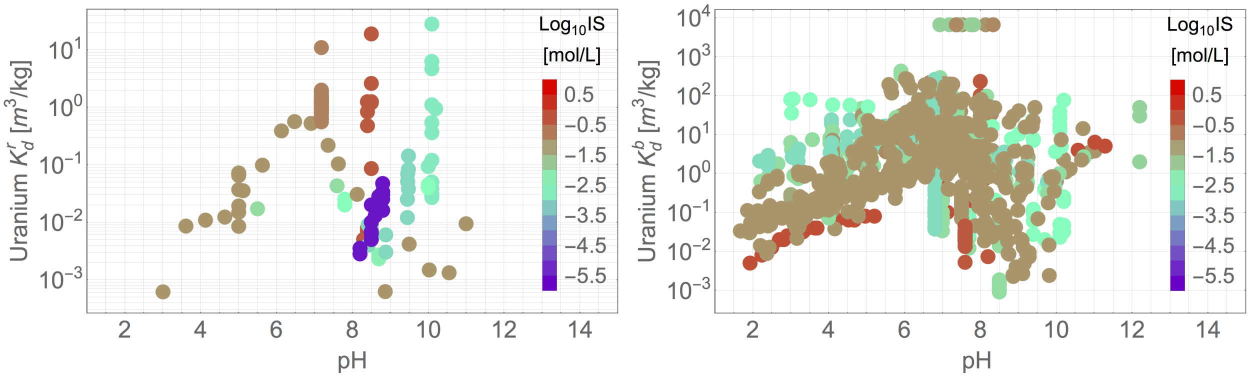

(a) Granite

(b) Bentonite

Figure 3.3.5: Relationship between K_d and pH for uranium. [45]

nent takes into account physical mixing processes using the dispersivity and a characteristic length scale.

$$F = -\mathbf{D_h}\nabla C \tag{3.3.8}$$

Since the solute mass is a conserved quantity for a given volume, the second form of Fick's law (3.3.9), which is derived from the continuity equation, employs the mass flux to solve for unsteady concentration over time. This form of expression is emulated in the governing equations for the ADE in 3.3.1, 3.3.4, and 3.3.5.

$$\frac{\partial C}{\partial t} = \nabla \cdot (\mathbf{D_h}\nabla C) \tag{3.3.9}$$

Variation in the diffusion coefficient of actinides in free-water $\left(D^F_{e(k)}\right)$ is not considered to be significant and is chosen to be a representative value of $10^{-2}\,\frac{m^2}{yr}$. This constant was used to calculate the rock matrix diffusion coefficient via equation (3.3.6) based on a sampled rock porosity, where a constant tortuosity correction factor was employed to bound the study. It is anticipated that the combined effect of varying fracture aperture and rock porosity can roughly simulate the diffusive transport effects posed by the variation in the tortuosity of the rock matrix, in that the total flux of infiltrating nuclides will be affected. Tortuosity factors can be determined experimentally by using the known D^F and the measured diffusion coefficient of a mostly non-sorbing tracer.

The effective diffusion in the buffer as a whole was chosen to be a sampled quantity, and the sampled bentonite porosity in turn allows for the determination of the retardation factor for solutes in this region (see equation (3.3.2)). Since the buffer is expected to act as a time-delaying component for the arrival of nuclides to the fracture entrances, the choice of $D_{e(k)}$ is likely to influence the arrival rate of nuclides to the precipitation location for given distance. The JAEA Diffusion Database was employed to understand the scales of variation of $D_{e(k)}$ in the bentonite buffer, which can be assessed from the box plot and distributions in figure 3.3.6. There was a lack of published data in curium within the database, so the element was excluded from the plot. Values from other publications were employed to determine the anticipated scale of D_{Cm} for this study.

Given that the median values of the effective diffusion coefficients lied around $10^{-3}\,\frac{m^2}{yr}$, a value of $D^L = 1$ was employed for longitudinal dispersion to establish Péclet numbers on the order of $\approx 10^3$. [46, 47] This was done to ensure that hydrodynamic dispersion could be described mainly through the mechanical component and that transport in the fractures could be described as dominantly advective rather than diffusive.

The effective diffusion coefficient can be measured using a wide variety of experimental means, including methods based on diaphragm cells, Taylor dispersion analysis, spectrophotometry, and mass spectrometry (e.g. Rutherford backscattering spectrometry). In one particular technique used for bentonite, a set concentration of radiotracer is uniformly applied to one end of a saturated cylindrical clay sample in an air tight cell. [48, 49] The tracer is allowed to diffuse and then the cylinder is extracted, upon which radiation detectors are used to measure the activity for axial sections of the sample. The activity is used to determine the concentration profile, which is applied to a cylindrical solution of equation (3.3.9) to determine the effective diffusion coefficient.

Given the dependence of experimental results on the conditions of the sample, figure 3.3.7 shows the relationship between D and the density of the sample. For a given ionic state, a negative correlation is observed between the diffusion coefficient and solid density of the bentonite, while a positive correlation is indirectly observed with the porosity. This is likely caused by an implied decrease in tortuosity with increasing porosity and decreasing density as a result of relatively larger pore sizes. Lower tortuosities would allow for diffusion pathways in the water to be more congruent with straight lines given fewer interactions with solid particles, which in turn would allow for the diffusive flux in to be more strongly tied to the

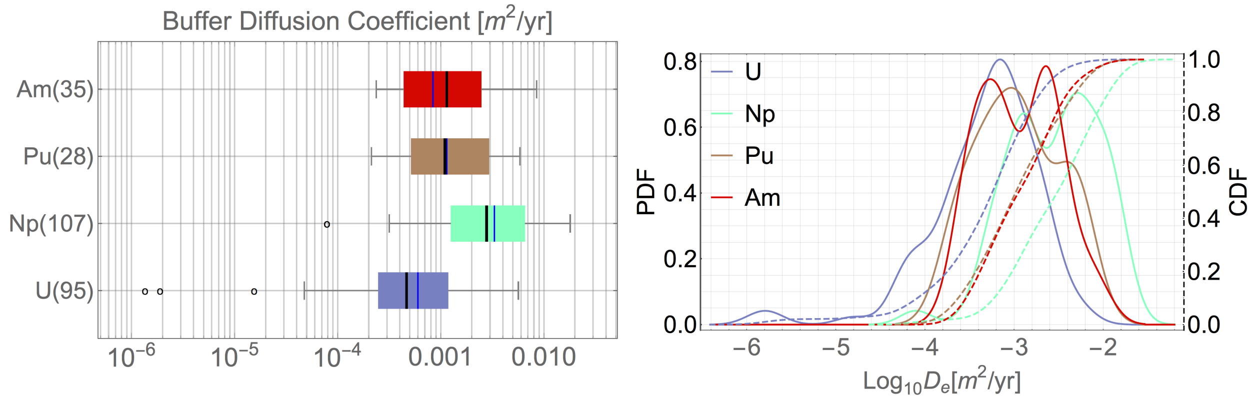

(a) Box plot

(b) PDF (solid) and CDF (dashed)

Figure 3.3.6: The effective diffusion coefficient of bentonite based on the JAEA Diffusion Database, [50] where the mean is shown in black and the median is shown in dark blue. Data on curium was too limited to be included in the figures.

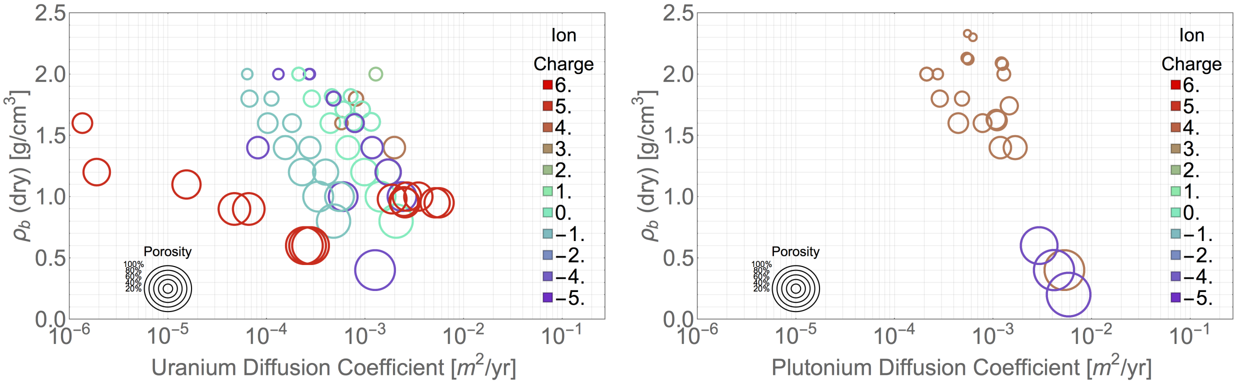

(a) Uranium

(b) Plutonium

Figure 3.3.7: The effective diffusion coefficient of bentonite in terms of the experimental density and porosity for given ionic states.

concentration gradient.

Solubility

The solubility of an element is defined as the concentration at which an aqueous solute precipitates in a particular solvent under specific conditions of temperature and pressure. In this study, the solvent is groundwater with the unique chemical environment provided in the bentonite pore space, and the solutes of interest are actinides released from the used nuclear fuel. Within the contents of the UNF are heavy elements like plutonium which are universally known to be quite insoluble. Evidence from the Oklo analog indicated that U, Np, and Pu remained largely within the vicinity of the uranium ore, [30] implying minimal impact from leaching in the migration of species over geological time. Therefore, solubility is expected to play a major role in determining the mobility of fissile material from the waste.

The solubility of the UO_2 waste is expected to increase as the material progresses from the original crystallinity to a more amorphous form. The very low value of $10^{-10}\,\frac{mol}{m^3}$ for uranium (as UO_2) in table 3.3.2 is inspired by Refs. [51, 52] and acknowledged to probe the effects of relatively mobile TRU in the buffer. The upper solubility bound is assumed to correspond to highly degraded fuel pellets. It may be possible that thermal cycling in both interim storage and final disposal may cause this level of wear in the worst-case scenario.

Groundwater velocity

The average linear velocity in the fractures is poised to affect the residence time of a solute for a given extent of the fracture. That is, for advective transport in the fractures, the velocity will determine the rate at which nuclides emerge at the far-field exit. Given natural variations in the fracture aperture, rock matrix porosity, tortuosities, and material densities in the system, along with effects from the hydraulic gradient, the rate of groundwater flow through the host rock is essentially a random process. By central limit theorem, the actual velocity of groundwater can be modeled according to a normal distribution. By sampling velocities from such a distribution, the effect of the hydraulic gradient on a random fracture network (with natural variations in density and aperture) can be simulated despite the assumption of linear transport pathways.

3.3.4 Latin hypercube sampling

In a random sampling approach to the parameter space, there is no constraint on relative probability when selecting different input samples. A selection can fall anywhere in range of the parameter distribution as part of an entirely random process, and it is likely that the samples that are drawn will lie in the most probable part of the distribution. This results in a selection of samples that is concentrated in the portion of the cumulative probability distribution curve with the highest rate of change. In order to probe behavior on the tail ends of the distribution, a large number of samples would be required.

The Latin hypercube sampling (LHS) method is an approach that constrains the sampling of a parameter space to stratifications of equal probability. [60] It divides the distributions of certain variables into intervals of equal probability, and then samples randomly within these intervals as an attempt to ensure sampling amongst all portions of the distribution. When this is done for all variables in the parameter space with a fixed stratification, each random variable selection corresponds to a zone of equal probability. This approach was utilized in the past to understand the uncertainty of far-field precipitation in for high level waste repository studies, where terms in a compartment-based transport model were sampled. [35]

Variable	Element	Lower	Upper
Solubility C^* $\left[\frac{mol}{m^3}\right]$ [7,8,13,35,51–54]	U	$1.0 * 10^{-10}$	$2.0 * 10^{-3}$
	Np	$1.0 * 10^{-9}$	$1.0 * 10^{-5}$
	Pu	$1.0 * 10^{-11}$	$1.0 * 10^{-5}$
	Am	$3.0 * 10^{-8}$	$2.0 * 10^{-4}$
	Cm	$3.0 * 10^{-8}$	$2.8 * 10^{-4}$
Rock Matrix K_d^r $\left[\frac{m^3}{kg}\right]$ [45,55,56]	U	$1.0 * 10^{-4}$	$2.8 * 10^{+2}$
	Np	$6.3 * 10^{-4}$	$1.0 * 10^{+2}$
	Pu	$2.0 * 10^{-4}$	$4.0 * 10^{+2}$
	Am	$9.5 * 10^{-4}$	$1.9 * 10^{+2}$
	Cm	$1.0 * 10^{-2}$	$4.0 * 10^{+1}$
Buffer K_d^b $\left[\frac{m^3}{kg}\right]$ [8,45,56]	U	$1.0 * 10^{-3}$	$6.7 * 10^{+3}$
	Np	$4.0 * 10^{-5}$	$6.6 * 10^{+2}$
	Pu	$3.4 * 10^{-3}$	$6.7 * 10^{+2}$
	Am	$3.4 * 10^{-4}$	$9.8 * 10^{+2}$
	Cm	$2.1 * 10^{-1}$	$5.1 * 10^{+2}$
Buffer Diffusion D^* $\left[\frac{m^2}{yr}\right]$ [50,53]	U	$1.4 * 10^{-6}$	$2.1 * 10^{-2}$
	Np	$7.9 * 10^{-5}$	$2.1 * 10^{-2}$
	Pu	$1.6 * 10^{-4}$	$2.1 * 10^{-2}$
	Am	$1.6 * 10^{-4}$	$8.5 * 10^{-3}$
	Cm	$1.6 * 10^{-4}$	$7.3 * 10^{-3}$
Groundwater velocity v $\left[\frac{m}{yr}\right]$	[35,57]	0.1	100
Rock matrix porosity (ϵ_r, granite) [35]		0.001	0.5
Buffer porosity (ϵ_b, bentonite)		0.17	0.48
Fracture aperture b $[m]$ [58,59]		$1 * 10^{-4}$	$1.1 * 10^{-3}$

Table 3.3.2: Parameter ranges assumed in this study expressed in terms of lower and upper bound values.

A Fortran code was written to generate LHS samples for distributions of variables within the TTB parameter space. [61] Random numbers were generated using the built-in subroutine in GNU Fortran ("xorshift1024*"), [62] where the random seeds were changed automatically with each invocation, either for constructing the distribution of a given variable or for sampling within the strata. A hundred thousand samples were generated for each distribution. Four sampling cases are proposed based on the application of uniform, log-uniform, normal, and log-normal distributions to certain variables along with fixed constants, and these are shown in table 3.3.3. Given the distributions imposed on K_d, C^*, and D, cases 1 through 4 are referred to as log-normal, normal, uniform, and mixed, respectively.

The uniform and log-uniform distributions both encompass the lower the upper bounds of table 3.3.2. The uniform distribution uses evenly-spaced intervals for the probability distribution functions (PDFs) while the log-uniform uses even-spacing on the log base 10 scale (although the distribution itself is based on the natural log with base e). Normal and log-normal distributions were created using the Marsaglia polar method from Box-Muller standard normals. [63] For the normal distribution, the mean was taken to be the arithmetic average, while the variance was chosen assuming that the upper and lower bounds comprised 95% of all samples, which corresponds to two standard deviations from the mean. Given the application to a linear scale, this approach intentionally biases results towards higher parameter values. The log-normal distributions used the average of the natural logarithms of the lower and upper bounds as the location parameter. The scaling parameter was iterated manually in a spreadsheet to provide a 95% confidence interval between the upper and lower bounds.

The PDFs were based on histograms of the generated points based on 5000 bins. These were bounded by the minimum (non-negative) and maximum sampled values generated for each distribution, which removed the need to incorporate infinity into sampling. For variable parameters, 100 divisions of equal probability within the cumulative distribution functions (CDFs) were determined based on the discrete intervals of the PDF. The fineness provided by the 5000 bins proved suitable enough to reduce error with the actual CDF below 0.1% on average, making this methodology acceptable.

For each equal-probability interval, a sample from the distribution was chosen using a random number between zero and one. After all 100 samples were taken for each variable, each sample selection index was Knuth shuffled to provide the final indices of randomly generated variable sets. This was meant to ensure that one sample space did not, for example, cover only tail-end behavior among the PDFs. While this technique does not ensure complete orthogonality in sampling the whole parameter space, the random permutations ensure a high degree of orthogonality by more uniformly covering each stratum. An example log-normal variable distribution is shown in figure 3.3.8 with samples chosen from unique sections of the CDF. The clustering of interval markers indicate higher probabilities near the center of the distribution.

3.3.5 Source term and repository tunnel layout

Heterogeneous approach

It is assumed that a representative repository for used fuel can be constructed by uniting a given burnup subset from either the BWR and PWR data on mass loading (see table 2.3.1). While the average burnup values of a given subset are different between each reactor type, the associated discharge periods are very similar. Rather than create a repository unifying the subsets into a single array with a high degree of heterogeneity, the study intends to analyze the repository-wide transport from individual arrays corresponding to characteristics of a given subset, where heterogeneity is restricted to the reactor type. Afterwards, comparisons can be made among the final transport results for each subset to draw conclusions on the effect of the discharge period on the formation of a far-field precipitate.

Variable	Case 1	Case 2	Case 3	Case 4	Ref.
Rock matrix porosity ϵ_r	U			N	
Velocity v $[m/yr]$	N				
Buffer porosity ϵ_b	U				
Fracture aperture b $[m]$	N				[58]
Solubility C^* $[mol/m^3]$	LN	N	LU	LU	
Rock matrix K_d^r $[m^3/kg]$				LN	
Buffer K_d^b $[m^3/kg]$				LN	
Buffer D^* $[m^2/yr]$				LU	
Fracture spacing a $[m^{-1}]$	1				[64]
Rock matrix density ρ_r $[kg/m^3]$	2750				[65]
Rock matrix tortuosity τ_r	0.055				[66]
Buffer density ρ_b $[kg/m^3]$	2100				
Buffer tortuosity τ_b	1				[7]
Free water diffusion D^F $[m^2/yr]$	0.01				
Longitudinal dispersion coefficient D^L $[m^2/yr]$	1				
N: Normal; U: Uniform; LN: Log-normal; LU: Log-uniform					

Table 3.3.3: Summary of actinide transport parameter distributions employed for LHS sampling.

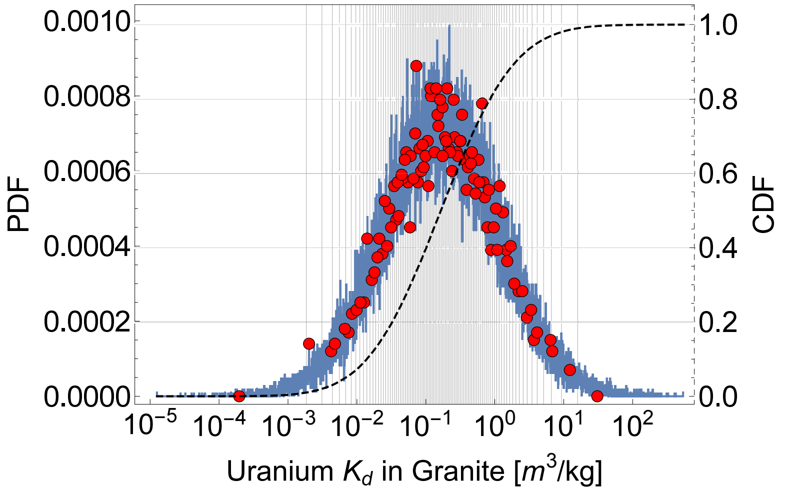

Figure 3.3.8: PDF, CDF, and samples (red points) for the randomly-generated log-normal distribution of the K_d^r value of uranium in granite. The vertical lines mark one hundred K_d^r intervals of equal probability.

As discussed in chapter 2, the total inventory of UNF is comprised of 25,027 tHM of BWR used fuel and 45,402 tHM of PWR used fuel (70,429 tHM total). Based on foreign concepts of metallic canisters for final deposition in a geologic repository, this study assumes that a single BWR canister will contain twelve spent assemblies, while those for PWR UNF will contain four. The number of canisters needed to accommodate the entire mass source term of used nuclear fuel is slightly different among the subsets given the discrepancies in the typical mass per assembly. Nonetheless, in order to constrain geometric aspects of the analysis, the repository is modeled as a square array that can meet the total mass source term as close as possible without exceeding the amount.

In this procedure, the total source term of BWR UNF (M^t_{BWR}) is divided by the number of assemblies per canister (n_{BWR}) and the mass loading per assembly (M^a_{BWR}) defined in the subset, and this figure is rounded to the nearest integer to get the number of needed BWR canisters: $N_{BWR} \approx \frac{M^t_{BWR}}{M^a_{BWR} n_{BWR}}$. The rounding procedure was found to better represent the total combined mass source term when compared to using the ceiling. The same procedure is done to obtain N_{PWR}, and the total number of canisters is calculated as $N_t = N_{BWR} + N_{PWR}$. To devise the most representative square array, the next lowest integer of the quantity $\sqrt{N_t}$ is used to to create a new number of canisters $N^*_t = \left\lfloor \sqrt{N_t} \right\rfloor^2$. The new number of BWR canisters would be calculated as the following rounded quantity: $N^*_{BWR} \approx \left(\frac{N_{BWR}}{N_t} \right) N^*_t$, and likewise for N^*_{PWR}. The new modeled mass source terms $M^{t,*}$ are calculated using the original assembly loaded, and the total deficit in the modeled array ΔM is shown in table 3.3.5. Altogether, between 324 and 564 MTU (0.44-0.80%) are not accounted for as a result of this simplifying procedure, covering a loss of 52-91 BWR canisters and 115-210 PWR canisters. However, given the similarity in final array sizes, the loci of transport distances will be consistent among the different subsets, which compensates for the deficit in canisters.

Given the calculated array structures, if one UNF type is placed in a distinct section of the repository array, bias would be introduced to the transport results. For example, if all BWR canisters occupied a continuous portion of the repository closest to the observation point, nuclides at this point in space will portray stronger behavior from the BWR composition than the PWR composition. Therefore, to remove dependence on repository tunnel configuration, the grid locations of individual PWR and BWR canisters is completely randomized. This is achieved by creating a vector containing the total number of modeled PWR and BWR canisters (N^*_{BWR} and N^*_{PWR}) as string identifiers, and then performing a Knuth shuffle on the vector using random numbers created with a Wolfram Alpha algorithm. [67] The vector is then partitioned to create individual rows of labels representing the square repository array, which can then be processed by the LHS code to determine the appropriate discrete source term per transport distance. That is, if a "BWR" point is specified in the input, the corresponding inventory from table 2.4.4 is applied to TTB.

Given the compounded computational expense from specifying individual source points for a vast array, the convergence script for finding $T_L \approx t^*$ is removed from the calculation. Instead, a constant leach period of 10^{10} years is artificially assumed, which would cover about two and a quarter half-lives of U-238. This will likely introduce inaccuracy for samples pertaining to very soluble uranium, such as with the second LHS sampling case. Effectively, an infinite leach period is modeled where TRU are released congruently with the UO_2 matrix.

Homogeneous approach

The canister compositions at failure listed in table 2.4.4 are roughly similar and commensurate to employing an approach that averages the inventories between the BWR and PWR subsets. Consider the mass of heavy metal loaded per BWR canister to be defined as $M^{c,s}_{BWR} = M^{a,s}_{BWR} n_{BWR}$ and likewise for the PWR. Per given subset s, the average mass loading per canister $M^{c,s}_{AVG}$ is obtained by weighting the relative source terms between the two LWR fuel types:

$$M^{c,s}_{AVG} = \frac{M^{c,s}_{BWR} M^{t}_{BWR} + M^{c,s}_{PWR} M^{t}_{PWR}}{M^{t}_{BWR} + M^{t}_{PWR}}$$

The total number of virtual canisters needed to account for the total source term is obtained as

$$N^{s}_{t} = \frac{M^{t}_{BWR} + M^{t}_{PWR}}{M^{c,s}_{AVG}}$$

For a square array, the same procedure from the heterogeneous approach is applied, although without the use of number fractions for the different fuel types. These dimensions are shown in table 3.3.5, where the averaging procedure reduces the size of the repository array by a tunnel length on either side. However, with the exception of subset 5, the mass deficit is relatively larger, ranging from 375-560 MTU (0.5-0.8 wt% of the total inventory) and amounting to 200-300 canisters.

With regards to the canister contents, the masses m of nuclides i in the compositions of table 2.4.4 are averaged by once again weighting the source term for each LWR fuel type:

$$m^{i,s}_{AVG} = \frac{m^{i,s}_{BWR} M^{t}_{BWR} + m^{i,s}_{PWR} M^{t}_{PWR}}{M^{t}_{BWR} + M^{t}_{PWR}}$$

These averages for the 1 MTU Origen-ARP basis are shown in table 3.3.4. The fissile content of the average waste or more closely related to PWR used fuel given preeminence of that waste type. Overall, the total mass of fissile material in the repository should be conserved for homogeneous approach. Among the subsets, the one centered on the 10% quantile has the highest enrichment and fissile content, while that centered on the 90% quantile has the opposite. This is based on the opposing extremes of burnup and initial enrichment for either LWR type in the inventory (see 2.3.1 on page 15). Despite having a slightly higher Pu-239 mass, the subset centered on the median has lower enrichment and TFM content compared to the average. To provide a better picture of the full range of expected results, and for computational expense, UNF subsets 1, 2, and 6 are prioritized for

Nuclide	$t_{1/2}$ [yr]	m^i_{AVG} [g]					
		1	2	3	4	5	6
U-233	1.59E+05	4.31E-01	5.47E-01	5.09E-01	4.48E-01	3.65E-01	2.72E-01
U-234	2.46E+05	3.78E+02	5.27E+02	4.76E+02	3.96E+02	3.08E+02	2.34E+02
U-235	7.04E+08	8.06E+03	7.32E+03	7.86E+03	7.94E+03	8.33E+03	8.98E+03
U-236	2.34E+07	4.93E+03	6.26E+03	5.89E+03	5.11E+03	4.19E+03	3.25E+03
U-238	4.47E+09	9.38E+05	9.23E+05	9.28E+05	9.36E+05	9.46E+05	9.56E+05
Np-237	2.14E+06	1.62E+03	2.04E+03	1.91E+03	1.69E+03	1.38E+03	1.04E+03
Pu-239	2.41E+04	5.14E+03	5.43E+03	5.37E+03	5.19E+03	4.93E+03	4.58E+03
Pu-240	6.56E+03	2.20E+03	2.57E+03	2.44E+03	2.26E+03	1.97E+03	1.61E+03
Pu-241	1.43E+01	2.43E-03	6.22E-03	4.58E-03	2.84E-03	1.27E-03	4.20E-04
Pu-242	3.74E+05	5.89E+02	8.48E+02	7.48E+02	6.25E+02	4.56E+02	2.85E+02
Am-241	4.33E+02	2.38E+02	2.87E+02	2.72E+02	2.45E+02	2.05E+02	1.59E+02
Am-243	7.39E+03	1.19E+02	2.05E+02	1.71E+02	1.30E+02	8.15E+01	4.12E+01
Cm-245	8.56E+03	1.46E+00	3.74E+00	2.75E+00	1.70E+00	7.64E-01	2.53E-01
Cm-246	4.76E+03	1.34E-01	4.39E-01	2.94E-01	1.62E-01	6.05E-02	1.60E-02

$\frac{M_{23}+M_{25}}{M_U}$ [wt%]	0.847	0.781	0.834	0.837	0.869	0.927
TFM [wt%]	1.373	1.344	1.388	1.369	1.371	1.389

Table 3.3.4: Masses in grams of actinides in an average LWR assembly at anticipated failure from a 1 MTU basis for each UNF subset.

analysis. For the transport calculation, these quantities can be adjusted to the canister basis $M^{c,s}_{AVG}$:

$$m^{i,c,s}_{AVG} = m^{i,s}_{AVG} M^{c,s}_{AVG}$$

Superposition

The mass contributions from all individual canisters in the repository are superposed at a set location in the far-field without regard to lateral spreading or concentration limitations posed by adjoining canisters. This is assumed in order to maximize the total quantity of actinides entering solution, because in reality the ability of fuel from downstream canisters to enter solution would be limited by the concentration of solutes leeched from the upstream canisters. A linear transport pathway connects each failed canister with a point 10 meters deep from the edge of the repository. This distance, measuring as half of the canister separation distance,[1] was chosen because preliminary studies demonstrated that increasing the observation distance with a fixed groundwater velocity will result in a time delay of

---

[1] The use of this observation point implies an interpretation of the far-field as any point outside of the excavated tunnel network in the host rock.

Subset	Actual				Modeled: Heterogeneous								Modeled: Homogeneous					
	$M^t_{BWR} = 25027$		$M^t_{PWR} = 45402$		BWR		PWR		N_t^*	$\sqrt{N_t^*}$	$M^{t,*}$	ΔM^t	M^c_{AVG}	N_t	N_t^*	$\sqrt{N_t^*}$	$M^{t,*}$	ΔM^t
	M^c_{BWR}	N_{BWR}	M^c_{PWR}	N_{PWR}	N^*_{BWR}	$M^{t,*}_{BWR}$	N^*_{PWR}	$M^{t,*}_{PWR}$										
1	2.136	11717	1.740	26093	11663	24912.2	25973	45193.0	37636	194	70105.2	324	1.880	37448	37249	193	70054.9	374
2	2.100	11918	1.728	26274	11866	24918.6	26159	45202.8	38025	195	70121.4	308	1.860	37861	37636	194	70010.1	419
3	2.100	11918	1.752	25914	11856	24897.6	25780	45166.6	37636	194	70064.2	365	1.876	37549	37249	193	69866.5	562
4	2.124	11783	1.740	26093	11708	24867.8	25928	45114.7	37636	194	69982.5	447	1.876	37533	37249	193	69896.1	533
5	2.196	11397	1.736	26153	11306	24828.0	25943	45037.0	37249	193	69865.0	564	1.899	37078	36864	192	70021.7	407
6	2.160	11587	1.752	25914	11509	24859.4	25740	45096.5	37249	193	69955.9	473	1.897	37127	36864	192	69930.4	499

Table 3.3.5: Number of canisters and the mass of contents (in MTU) used in the heterogeneous repository array configuration based on the mass loadings per subset M^c (see table 2.3.1 on page 15) and modified (*) values used to obtain a square array of side $\sqrt{N^*_{tot}}$.

uranium nuclides at the precipitate location, in particular the fissile species decaying from relatively immobile TRU. While the general behavior of fissile content in the precipitate is similar at each distance (albeit time-lagged), the peak fissile content is suppressed with distance. Therefore, even if the groundwater velocity is sampled, acknowledging excessively far observation points may not be conservative. It is suggested that distances of 1000 meters or more be analyzed if the failure metric in chapter 9 is met too easily.

The locus of individual transport distances leading up to the observation point in space is adequate in representing the vast array of possible pathways for the compromised repository, which can adequately capture effects on the deposition of uranium from the decay of slow-moving transuranics. This should be commensurate with providing a composition of the precipitate in the worst case scenario. Furthermore, in a macroscopic sense, the locus of transport distances can simulate the tortuosity of naturally fractured host rock.

3.4 Results

3.4.1 Overview

Calculations were performed for the discrete repository arrays of UNF described by subset 1 (total average), subset 2 (10% quantile-centered), and subset 6 (90% quantile-centered) for the unique LWR cases in chapter 2 and the homogenization described in table 3.3.4. Important behavior observed from these results will be discussed, and the procedure to develop representative precipitate cases for a criticality study using these results is as follows:

1. For each UNF subset, among the 100 hypercube samples calculated for one repository, interpolate the 10%, 25%, 50%, 75%, and 90% quantile behavior for uranium mass, enrichment, and fluxes of U-235 and U-238, along with the average.

2. For each quantile, the values observed amongst the UNF subsets are arithmetically averaged per given point in time

3. Based on a juxtaposition of averaged mass and enrichment, evenly-spaced values of enrichment are suggested based on masses likely to correspond to criticality. The Los Alamos criticality data is used to aid in this determination. [68]

4. For each LHS sampling space, interpolations are made in each quantile to determine the mass, enrichment, fluxes, and uranium isotope atom fractions, at the specified times from canister failure needed to achieve the specified enrichment levels (bounded by $10^8\,yr$).

5. For the median, upper quartile, and 90% quantile, the sampling cases are compared to based on the smallest total mass of uranium leading up to the specified enrichment level.

3.4.2 Nuclide behavior among the sampling cases

The average UNF composition in the homogeneous approach is employed primarily to illustrate specific behavior in the total precipitate mass and enrichment. The total superimposed precipitate mass for each sampling case in table 3.3.3 is plotted in figure 3.4.1, where 10%, median, and 90% behavior is diagrammed along with lines from the original hypercube samples. In general, within a scope of a hundred million years, maximal accumulations between 10^2 and 10^3 metric tons are feasible in the context of this worst case scenario.

The associated behavior of enrichment is plotted in figure 3.4.2. For all LHS sampling cases, the long-term median enrichment settles around the fissile content figures in table 3.3.4, where stability is rooted in the extremely long half lives of U-235 and U-238. This demonstrates that eventually the composition of the precipitate matches the composition of the repository canisters (or at least the average). It is therefore implied that at some point in time, the non-fissile uranium contributions from canisters in the posterior of the repository become more and more considerable. These isotopes dilute the U-233 and U-235 generated from TRU that have arrived at the precipitate earlier from the anterior portion of the repository. If the anterior canisters contribute significant mass to the precipitate, the corresponding higher enrichment from mobilized TRU may result in criticality at earlier points in the time.

The log-normal sampling case shows humped behavior in the total mass around 10^6 years. This suggests that contributions of U-233 (which has a half life of $1.5 * 10^5$ years) to the precipitate are significant before the onset of decay. This is corroborated in the breakthrough curves in figure 3.4.3a, where U-236 and U-238 eventually become dominant. These considerations imply that U-235 would be major determinant for enrichment, as shown in figure 3.4.2a, where the median value settles near the TFM percentage in table 3.3.4 due to increasing dilution from non-fissile uranium.

A cluster of samples begins with enrichments of 40 wt% at 1000 years post-failure, which is due to earlier arrival of U-238 caused by the tail end of the K_d^U distribution. This cluster leads to a peak that forms the onset of median behavior, which is caused by the limited effect of Pu-239 decay. A smaller cluster of samples exists at the initial enrichment of the canister, which link up with the median behavior after a much longer time.

Transport of uranium in the normal case is severely retarded due to the heavy bias towards higher values of K_d in both the buffer and rock matrix, despite the concurrent biases towards higher actinide solubilities. The total mass is limited to a accumulations of 10 kg, as the 90% quantile behavior would indicate in figure 3.4.1b. Median values of accumulation eventually reach the kilogram scale, but overall uranium is heavily immobile, with significantly breakthrough occurring after two million years. Nonetheless, given these low masses, a higher proportion of fissile isotopes is accounted for in the deposition, as the enrichment curves in figure 3.4.2b demonstrate. For the normal case, U-233 generated from the decay fo Np-237 and U-235 generated from the decay of Pu-239 typically breakthrough sooner than U-238 as shown in figure 3.4.3b.

The log-uniform results for total accumulation span the widest range of variation for a given point in time. This is due to even sampling amongst the log-scale values of each parameter, allowing for extremes of sorption, diffusivity, and solubility to be taken into account in the parameter space. The 90% quantile of this sample set has the earliest breakthrough above $1\,\mu g$ among all the hypercube sets, with some outlier cases reaching the accumulation point 1000 years after canister failure. These early contributions stem from a high mass flux from a high value of D coupled to a source term enhanced by a high C^*. As a result of the spread, the median reaches a maximal accumulation of half a metric ton, which is lower than the median of the log-normal case.

The spread in results for mass are emulated in the enrichment behavior of figure 3.4.2c. A decline in median enrichment is observed around 10^5 years, which mirrors median behavior in the log-normal and mixed cases as well, although the 10%-90% range is much wider. This is related to the especially broad probability distribution for accumulating a certain mass of U-235, as shown in figure 3.4.4. As time proceeds, the distribution becomes narrower (i.e. with a lower scale parameter) although a tail exists due to contributions from Pu-239 decay in the upstream portion of the repository.

The mixed case combines attributes from both the log-normal and log-uniform distributions. The median behavior in figure 3.4.1d has an intermediate breakthrough time, and maximal accumulation is greatest among all the cases. The 10%-90% band is much narrower than the log-uniform case, and the curves appear to be much less affected by the decay of U-233. This implies a dominant role of non-fissile uranium from early on, which is demonstrated in the steady enrichment level being reached earlier in figure 3.4.2d. The 10% quantile enrichment samples appear to more frequently begin at the initial enrichment value (listed in table 3.3.4) before converging to the steady level, which happens much sooner time compared to the log-normal and log-uniform cases. This implies more consistency in the higher degree of uranium mobility when compared to that of TRU.

The distribution of normalized U-235 mass is the most narrow (i.e. lowest scale parameter) for the mixed case than for any other case at a given time (see figure 3.4.4). At very long times, the means of the PDFs of the log-normal and log-uniform cases nearly approach that of the mixed case, albeit with more skewness and/or tailing. In fact, the mixed distribution has very limited tailing due to the predictability of individual samples. The small bump in the plot may be caused by the outlier curves observable in the bottom right quadrant of figure 3.4.1d.

3.4.3 Effect of the UNF subsets and heterogeneity

For a given UNF subset, the heterogeneous case requires a larger repository to accommodate BWR- and PWR-specific canisters compared the virtualized average canisters. That is, all values of $\sqrt{N^*}$ are larger for the former as opposed to the latter, as shown in table 3.3.5. Therefore, for the short ten meter distance into the far-field considered in this analysis, the normalized U-235 mass is larger for the heterogeneous repository by this geometric consideration alone, as shown in figure 3.4.5a. This is caused by more numerous transport pathways being available to contribute to precipitation at the observation point.

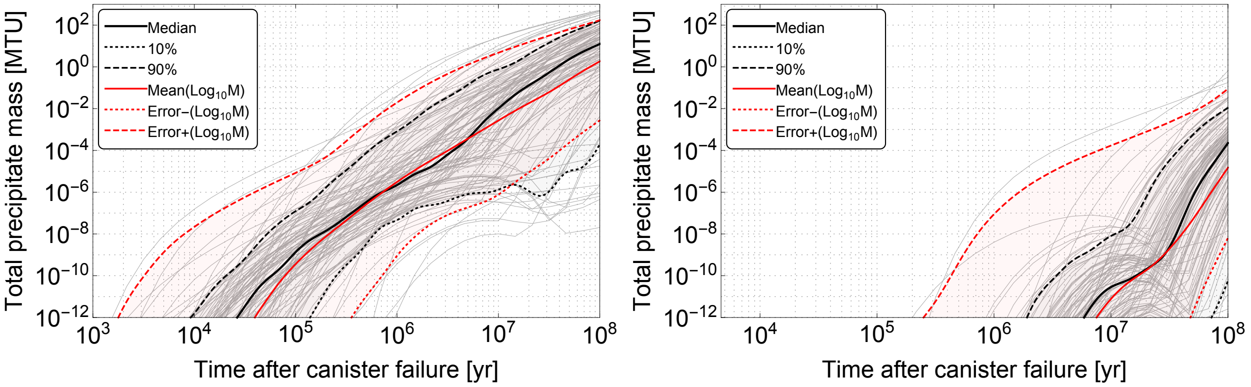

(a) Log-normal

(b) Normal

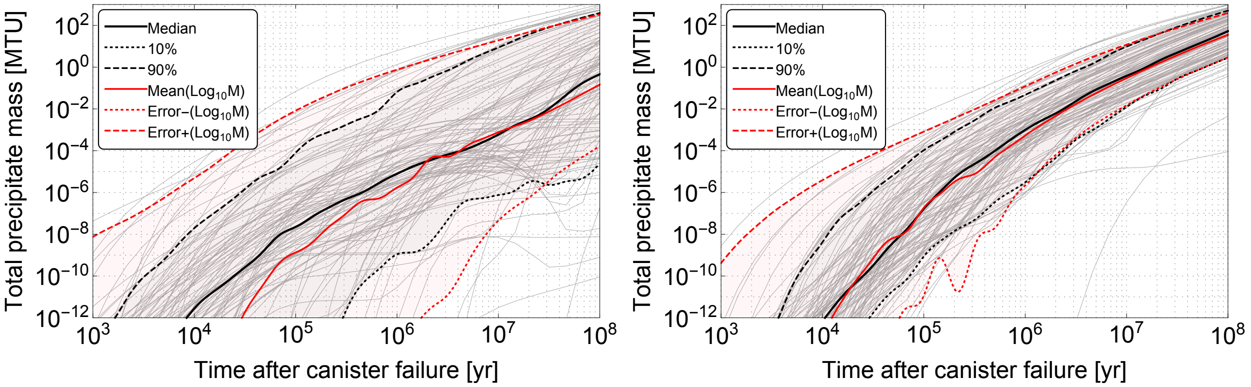

(c) Log-uniform

(d) Mixed

Figure 3.4.1: Total accumulated mass of the far-field precipitate (in MTU) for the average subset of the homogeneous UNF composition. The 10%, 50%, and 90% quantiles are shown, as well as the average and standard deviation of the $\log_{10}$values for visualization purposes. The individual hypercube samples amounting to more than $1\,\mu g$ are plotted in the background.

For a given configuration, the difference between specific UNF subsets is very negligible, especially at long times. This could be predicted from the similarity in compositions and fissile content tabulated in tables 2.4.4 and 3.3.4. Similarities are stronger for the 90% quantiles than the 10% quantiles, indicating that fine-scale differences in composition are more apparent for the outlying hypercube samples.

The enrichment behavior is an intensive property compared to the extensive nature of U-235 accumulation, and figure 3.4.5b demonstrates that behavior between the homogeneous and heterogeneous configurations is far more similar. At increasingly longer times from canister failure, the individual UNF subsets are observed to overlap for each configuration before proceeding to overlap universally. This confirms the validity of the averaging procedure, and heterogeneity does not necessarily have to acknowledged for the development of precipitate

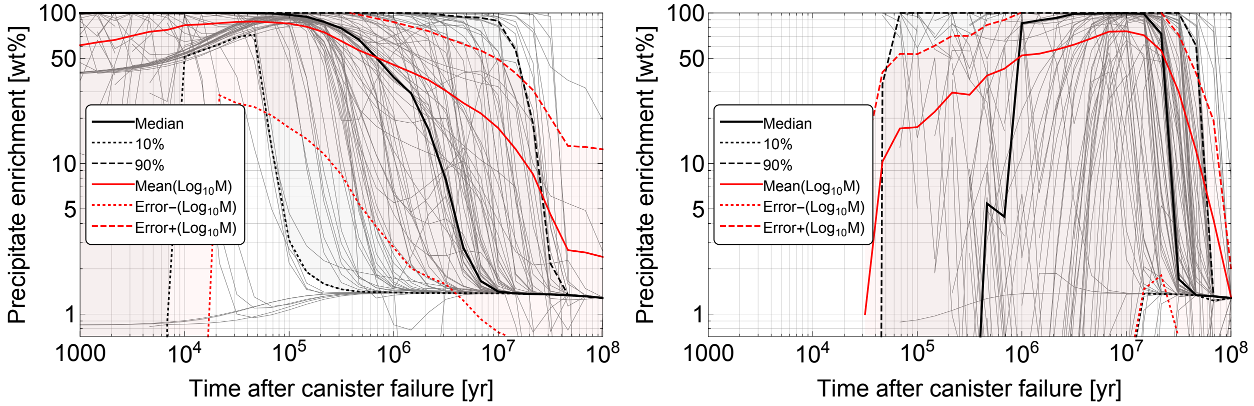

(a) Log-normal (b) Normal

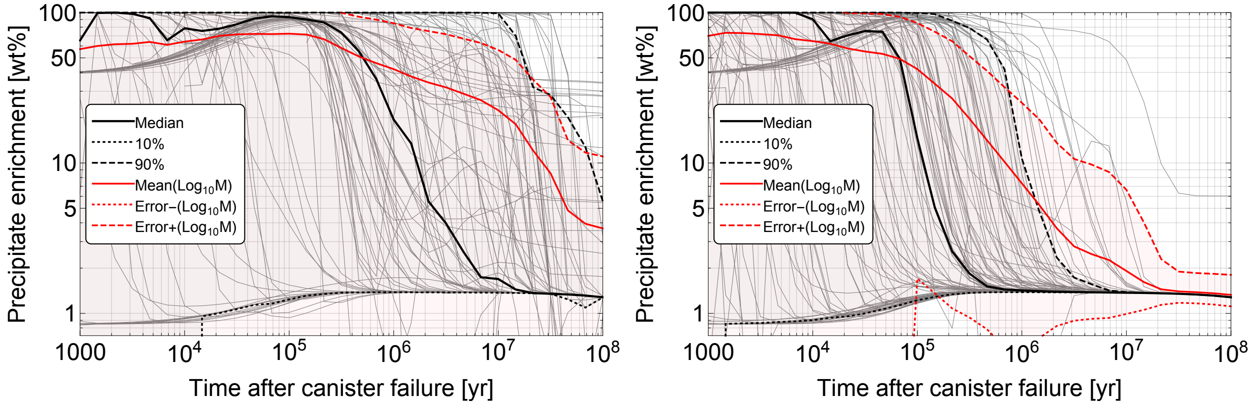

(c) Log-uniform (d) Mixed

Figure 3.4.2: Enrichment $\left(\frac{M_{23}+M_{25}}{M_U}\right)$ of the far-field precipitate (in wt%) for the average subset of the homogeneous UNF composition. The 10%, 50%, and 90% quantiles are shown, as well as the average and standard deviation of the $\log_{10}$ values for visualization purposes. The individual hypercube samples above 0.711 wt% are plotted in the background.

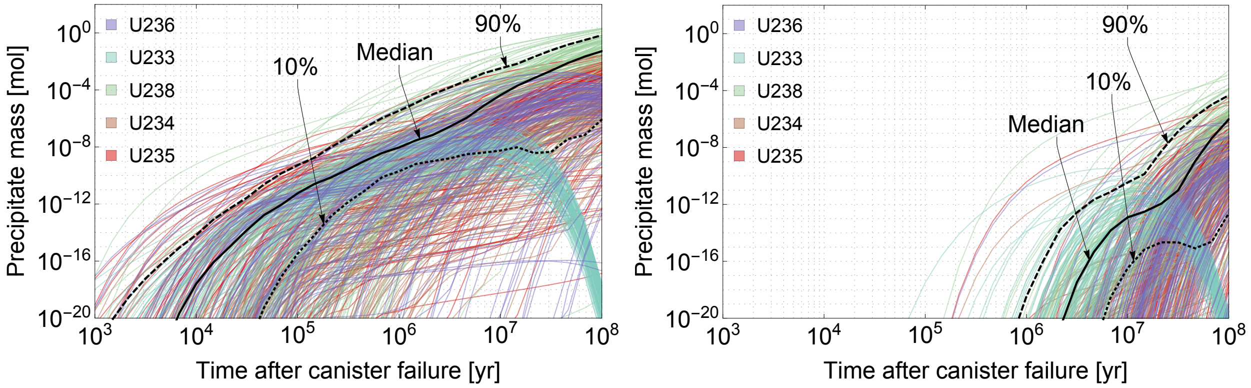

(a) Log-normal (b) Normal

Figure 3.4.3: Comparison of uranium isotope breakthrough (in moles) for the normal and mixed sampling spaces based on averages of the UNF subsets, shown with 10%, 50%, and 90% quantiles of the total mass of the precipitate (also in moles). (The order of isotopes follows the 4n → 4n+3 decay chain progression in figure 3.3.2.)

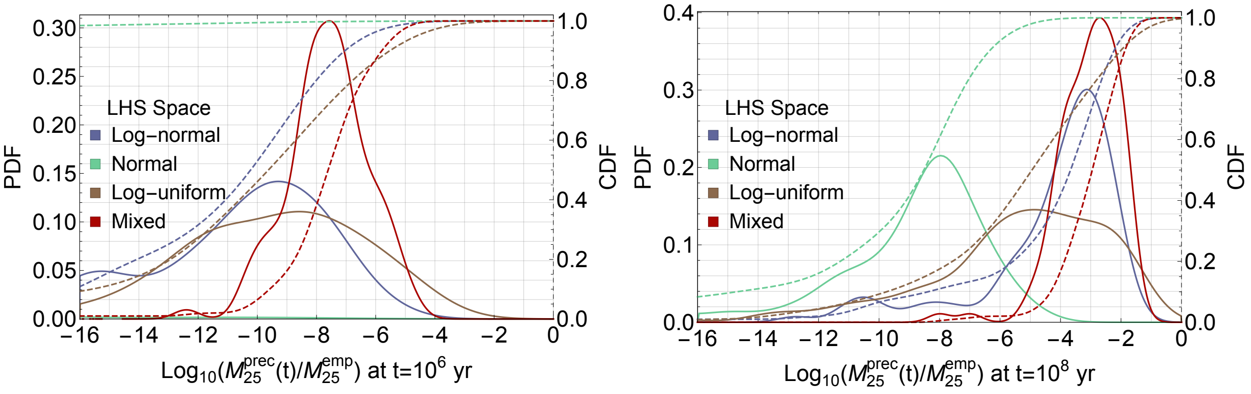

(a) $t = 10^6\, yr$ (b) $t = 10^8\, yr$

Figure 3.4.4: Distribution of U-235 mass normalized to emplacement for the various hypercube sampling spaces at an arbitrary times.

compositions by way of enrichment cases. Nonetheless, the role of specific UNF actinide compositions in determining precipitate enrichment is important at early times for the 10% quantile samples.

Given this observed behavior among the UNF subsets, figure 3.4.6 shows the averaged behavior for each sampling space. In summary, the median behavior of the mixed case may contribute up to 1 MTU of precipitate no sooner than $1.5 * 10^7$ years (with an enrichment of $\approx 1.4\,wt\%$), while 90% behavior in the mixed and log-normal cases can produce the same quantity in four million years. By coincidence, the 90% tier for the log-uniform case follows the median of the mixed case very closely. The median of the log-normal case reaches 1 MTU at forty million years, although the median for the log-uniform case cannot reach 1 MTU. The lower quartile behavior for the mixed case requires $4 * 10^7\,yr$ to achieve 1 MTU, but the lower quartiles of the other three cases cannot achieve this mass at all within the scope of the study. Based on the 90% behavior for the normal case, where there is a strong bias towards higher K_d, no more than 10 kg may be precipitated at the observation point in a hundred billion years. The log-uniform case can be confirmed to have the widest interquartile range and 10%-90% range.

The large repository footprints implied in table 3.3.5 allow for relatively earlier arrival rates of uranium species from TRU precursors of the canisters nearest to the accumulation point. This is especially the case for individual samples with higher solubility, lower K_d, and higher buffer diffusion coefficients for the transuranics. Figure 3.4.6b shows the very high enrichments resulting from these samples at early times, which correspond to insignificant masses no more than a few tens or hundreds of grams (for the 50% quantile). All results settle to enrichment levels closely corresponding to the initial fissile content of the canisters. This implies that eventually canister uranium compositions become emulated in the precipitate, and that opportunities to create a more-enriched critical mass may occur in a narrow margin of time before the steady-state is reached. The enrichment level corresponding to a 1 MTU accumulation in the 90% bracket for the mixed case is approximately $6\,wt\%$, which, as mentioned, occurs at four million years post-failure. This enrichment would also correspond to a 10 kg deposition for the median log-normal case at $10^7\,yr$, and 15 kg for the median log-uniform case at $3 * 10^7\,yr$.

A 0.1 MTU accumulation is achievable in the median mixed bracket in five million years, which corresponds to the steady enrichment level of $\approx 1.4\,wt\%$. Based on the Los Alamos criticality data for uranium metal in hydrogen-moderated systems (table 3.4.1), more than 1.3 MTU would be needed for a critical mass, which implies that this precipitate has no means of attaining criticality. For the 0.1 MTU accumulation in the 90% mixed bracket reached at $1.4 * 10^6\,yr$, an extremely high value of $35\,wt\%$ is observed in the corresponding enrichment plot. The tonnage alone would clearly be adequate for criticality, but the percentage is too outlandish for a deposition in natural media, especially for direct disposal. This is identified as a limitation of the approach. Therefore, the study will be constrained to $6\,wt\%$, which should provide a useable parameter space for the criticality analysis.

The transport time scales needed to accumulate certain median precipitate masses are tabulated in table 3.4.2. The normal case was excluded due to heavy retardation and un-

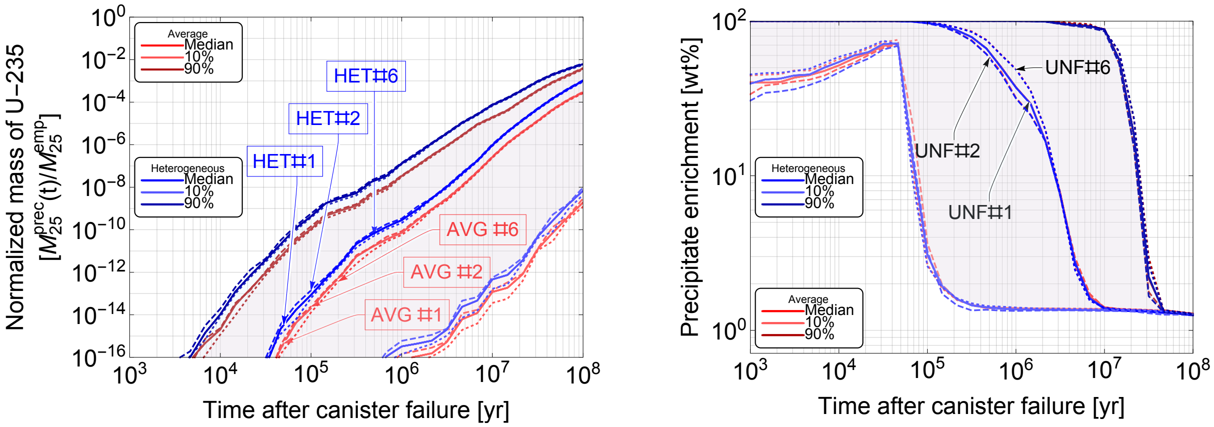

(a) U-235 mass normalized to total loading at emplacement.

(b) Enrichment

Figure 3.4.5: Comparison of the U-235 precipitate mass normalized with respect to emplacement and the corresponding enrichment for subsets 1, 2, and 6 in the averaged (AVG) and heterogeneous (HET) approaches for the log-normal LHS sampling space, shown for 10% (light), median (normal), and 90% (dark) quantiles. (Labels for enrichment are merged into "UNF" due to overlap.)

steady accumulation behavior. The 10 kg masses in the table are not pertinent to criticality based on the laboratory data for the specified enrichment. Masses 100 kg and above have some potential for criticality, but natural configurations will have less favorable conditions for criticality compared to the lab, and the actual minimum critical masses will be larger.

3.4.4 Fluxes

The individual mass fluxes F of actinides will be important for the consequence analysis as they serve as the heavy metal source terms that displace water from the pore space of the critical mass. To bound the scope of the study, focus lies on the isotopes U-235 and U-238 due to their prominence in the uranium inventory and their long half-lives. The former will be important for its anticipated positive additions to reactivity, while the latter will be studied for poisonous effects.

Figure 3.4.7 shows the molar fluxes over time of the two isotopes as averages of the three chosen UNF subsets for each LHS sampling space. The U-235 breakthrough precedes that of U-238, which explains the very high enrichments in the precipitate at early times. There is a depression in the F_{23} curves until $\approx 2 * 10^5$ years when all Pu-239 ($t_{1/2} = 2.41 * 10^4\, yr$) contributions are liable to be realized. This effect is most obvious in the log-normal and log-uniform median results, while it is masked in the mixed results due to stronger sampling of mobile plutonium parameters. The U-238 flux (F_{28}) eventually surpasses that of U-235 to bring the enrichment to a stable level. The stronger similarity in the two curves for the

$\tilde{e}\left[\frac{M_{25}}{M_U}\right]$	Spherical $M_{25}^{min}\,[kg]\ (M_U[kg])$		
	Homogeneous unreflected	Homogeneous water reflected	Heterogeneous water reflected
1.5	19. (1266.7)	10.9 (726.7)	4.7 (313.3)
2	7.5 (375.)	5. (250.)	3. (150.)
3	4. (133.3)	2.6 (86.7)	2.1 (70.)
4	3.1 (77.5)	2. (50.)	1.7 (42.5)
5	2.79 (55.8)	1.79 (35.8)	1.55 (31.)
6	2.5 (41.7)	1.56 (26.1)	1.4 (23.3)
10	2.1 (21.)	1.25 (12.5)	1.15 (11.5)
20	1.8 (9.)	1.05 (5.2)	1. (5.)*
30	1.7 (5.7)	1. (3.3)	0.94 (3.1)*
50	1.55 (3.1)	0.92 (1.8)	0.86 (1.7)*

*extrapolation

Table 3.4.1: Interpolated values of Los Alamos criticality figures for hydrogen-moderated spherical volumes of uranium metal at certain mass fractions of U-235. [68]

LHS Set	$M_U\,[MTU]$	t [yr]	$\tilde{e}\left[\frac{M_{23}+M_{25}}{M_U}\right]$	$F_{25}\left[\frac{mol}{m^2yr}\right]$	$F_{28}\left[\frac{mol}{m^2yr}\right]$	Spherical $M_U^{min}\,[MTU]$		
						Homogeneous unreflected	Homogeneous H_2O-reflected	Heterogeneous H_2O-reflected
Log-normal	0.01	9.90E+06	7.440%	2.35E-11	1.66E-09	0.030	0.018	0.017
	0.1	1.78E+07	1.635%	1.02E-10	7.28E-09	0.933	0.550	0.254
	1	3.68E+07	1.342%	3.38E-10	2.45E-08	1.787	1.000	0.403
	5	6.64E+07	1.311%	7.15E-10	5.31E-08	1.910	1.064	0.424
	10	8.92E+07	1.287%	1.01E-09	7.64E-08	2.010	1.116	0.441
	50	-	-	-	-	-	-	-
Log-uniform	0.01	3.13E+07	2.343%	5.55E-12	3.93E-10	0.144	0.118	0.099
	0.1	5.74E+07	3.500%	2.52E-11	1.86E-09	0.099	0.064	0.053
	1	-	-	-	-	-	-	-
	5	-	-	-	-	-	-	-
	10	-	-	-	-	-	-	-
	50	-	-	-	-	-	-	-
Mixed	0.01	2.37E+06	1.487%	6.45E-11	4.54E-09	1.304	0.746	0.320
	0.1	5.40E+06	1.386%	2.11E-10	1.49E-08	1.626	0.915	0.375
	1	1.56E+07	1.362%	6.81E-10	4.85E-08	1.712	0.960	0.390
	5	3.18E+07	1.346%	1.39E-09	1.00E-07	1.772	0.992	0.401
	10	4.48E+07	1.333%	1.93E-09	1.41E-07	1.822	1.018	0.409
	50	9.75E+07	1.279%	4.07E-09	3.10E-07	2.045	1.134	0.447

Table 3.4.2: Time periods after canister failure necessary to achieve median precipitate mass values shown with corresponding enrichment ($\tilde{e}$, wt%) and U-235 and U-238 fluxes (F_{25}, F_{28}). Minimum uranium masses needed for criticality are interpolated from Los Alamos data using the enrichment. [68]

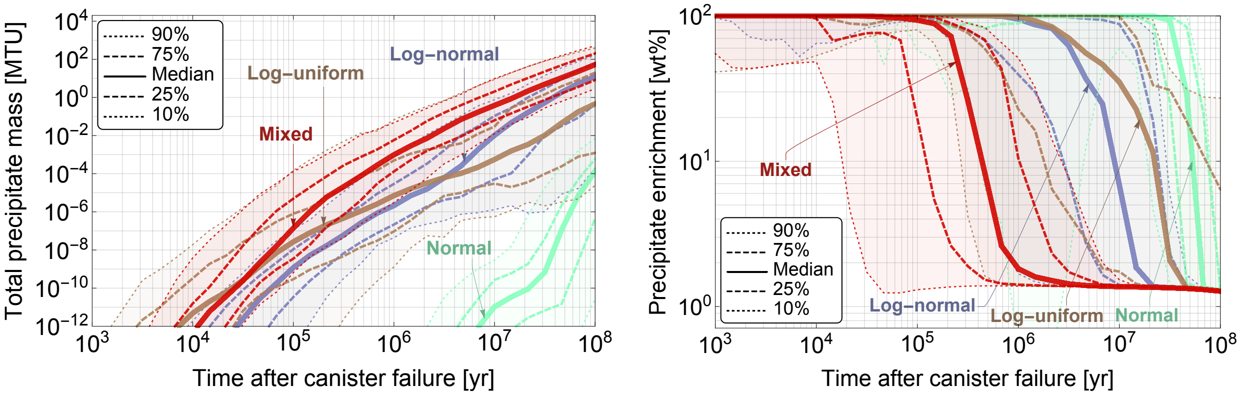

(a) Mass (b) Enrichment

Figure 3.4.6: Total mass and enrichment of the precipitate for the different LHS sampling spaces, based on averages of UNF subsets 1, 2, and 6.

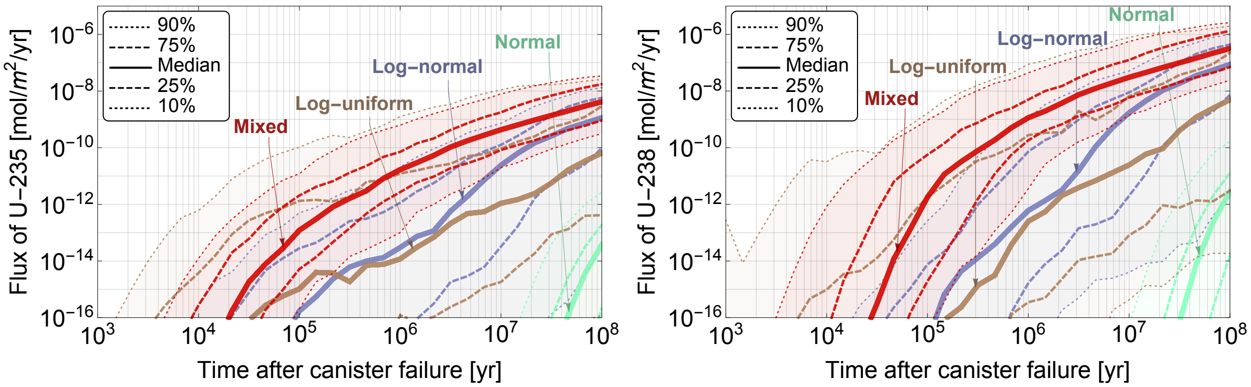

(a) U-235 (b) U-238

Figure 3.4.7: Superimposed fluxes of U-235 and U-238 at the precipitate location for the different LHS sampling spaces, based on averages of UNF subsets 1, 2, and 6.

mixed case demonstrate how enrichment is stabilized more quickly in figure 3.4.6b compared to the other cases.

3.4.5 Representative precipitates

The nuclide composition of the critical mass is the most controlling parameter for criticality. The nuclides U-233 and U-235 control the fissile content, U-238 is the dominant nuclide that also serves as fertile material (for burnup calculations), and U-234 and U-236 are the bystander components that do not contribute to effective multiplication in any spectrum. Therefore, representative precipitates are proposed based on fixed values of enrichment, where the transport results are used to craft atomic compositions needed for the criticality study. The procedure to determined the necessary atom fractions (χ) is summarized as follows:

1. Nuclide atom and mass fractions are determined for each sample for each point in time from the UNF subset results
2. The median fractions of the hypercube samples are obtained for each point in time
3. The fractions for all isotopes in the median are re-normalized
4. The re-normalized fractions from each UNF subset (1, 2, and 6) are averaged
5. The enrichment is devised from the mass fractions, and interpolations are made of $\tilde{e}(t)$ using Mathematica. [67]
6. The time required to achieve the specified enrichment level is found through root-finding
7. Each averaged atom fraction (χ) is determined using the time value

The interpolated results for median behavior are shown in table 3.4.3. The log-normal and normal tabulations demonstrate that U-233 is most controlling of enrichments higher than the original TFM content of the canisters at emplacement. This is caused by TRU mobility that is significantly higher than uranium over time, which leads to the dominance of the Np-237 flux as over the U-238 flux. The log-uniform and mixed sampling cases show the opposite tendency, where U-235 is most controlling of elevated fissile content. In these cases, plutonium may have similar mobility to uranium to some extent, allowing for more Pu-239 contributions from the nearest canisters, until U-238 eventually dominates the precipitate. The higher proportions of U-234 in the mixed case may be a result of its secular equilibrium with U-238, which has the highest flux to the precipitate location per given time and steadies the enrichment level the earliest among the other sampling cases.

Given the U-235 dominance of the mixed case, along with the predictability of its variation, high flux, and more realistic TRU behavior, its median compositions will be carried over to the criticality study. Results for minimum critical mass can be compared to the findings in this chapter to establish a transport basis for criticality.

3.5 Discussion

Repository-wide nuclide transport has been demonstrated using the very conservative application of a fracture-based advection-dispersion relationship to waste emplacements in a discrete array. A sampling method was employed to understand the effects of applying certain distributions to certain key transport variables on total accumulation in the far-field, along with enrichment and mass flux. Within the scope of the results, masses on the order of

LHS Set	$\tilde{e}\left[\frac{M_{23}+M_{25}}{M_U}\right]$	t [yr]	χ_{23}	χ_{24}	χ_{25}	χ_{26}	χ_{28}	$M_U\ [MTU]$	$F_{25}\left[\frac{mol}{m^2yr}\right]$	$F_{28}\left[\frac{mol}{m^2yr}\right]$
Log-normal	1.5	1.97E+07	0.134%	0.005%	1.386%	0.571%	97.904%	1.32E-01	1.25E-10	8.96E-09
	2	1.45E+07	0.643%	0.005%	1.387%	0.604%	97.360%	4.63E-02	6.25E-11	4.44E-09
	3	1.36E+07	1.658%	0.005%	1.393%	0.616%	96.328%	3.89E-02	5.46E-11	3.88E-09
	4	1.27E+07	2.654%	0.005%	1.413%	0.598%	95.329%	3.15E-02	4.66E-11	3.31E-09
	5	1.17E+07	3.635%	0.005%	1.436%	0.576%	94.349%	2.40E-02	3.87E-11	2.75E-09
	6	1.08E+07	4.641%	0.005%	1.467%	0.530%	93.358%	1.66E-02	3.08E-11	2.18E-09
Normal	1.5	4.57E+07	0.157%	0.005%	1.343%	0.212%	98.282%	1.74E-07	2.13E-16	1.32E-14
	2	4.58E+07	0.571%	0.005%	1.330%	0.280%	97.814%	1.79E-07	2.15E-16	1.34E-14
	3	4.60E+07	1.688%	0.005%	1.312%	0.276%	96.718%	1.84E-07	2.18E-16	1.36E-14
	4	4.62E+07	2.706%	0.005%	1.295%	0.273%	95.722%	1.89E-07	2.20E-16	1.37E-14
	5	4.63E+07	3.723%	0.005%	1.278%	0.269%	94.725%	1.95E-07	2.23E-16	1.39E-14
	6	5.22E+07	4.740%	0.005%	1.261%	0.266%	93.728%	1.03E-06	1.57E-15	1.06E-13
Log-uniform	1.5	3.26E+07	0.118%	0.005%	1.402%	0.607%	97.868%	1.16E-02	6.37E-12	4.56E-10
	2	3.17E+07	0.597%	0.005%	1.433%	0.552%	97.413%	1.06E-02	5.75E-12	4.11E-10
	3	3.04E+07	0.903%	0.002%	2.150%	0.629%	96.316%	9.04E-03	5.27E-12	3.67E-10
	4	2.91E+07	0.769%	0.002%	3.305%	0.931%	94.993%	7.81E-03	4.86E-12	3.28E-10
	5	2.79E+07	0.774%	0.002%	4.314%	1.189%	93.721%	6.81E-03	4.48E-12	2.91E-10
	6	2.68E+07	0.778%	0.001%	5.322%	1.448%	92.450%	5.99E-03	4.11E-12	2.56E-10
Mixed	1.5	2.27E+06	0.069%	0.023%	1.452%	0.730%	97.727%	8.58E-03	5.93E-11	4.17E-09
	2	9.28E+05	0.111%	0.029%	1.910%	0.804%	97.145%	7.79E-04	1.48E-11	9.98E-10
	3	6.67E+05	0.154%	0.031%	2.874%	1.027%	95.914%	2.60E-04	7.84E-12	4.89E-10
	4	6.29E+05	0.233%	0.030%	3.821%	1.283%	94.632%	2.12E-04	6.95E-12	4.33E-10
	5	5.92E+05	0.313%	0.030%	4.768%	1.538%	93.350%	1.71E-04	6.06E-12	3.77E-10
	6	5.54E+05	0.393%	0.029%	5.715%	1.794%	92.068%	1.36E-04	5.17E-12	3.21E-10

Table 3.4.3: Atom fractions (χ) of isotopes selected as median values from the LHS sampling cases, shown with relevant time after canister failure and the median values of uranium mass (M_U) and U-235 and U-238 fluxes (F_{25}, F_{28}) corresponding to the selected enrichment figures.

several metric tons were observed to accumulate at the observation point. The fissile content of these precipitates was determined by the relative mobility uranium and TRU based on sampled parameters of sorption, solubility, and diffusivity, among others.

Median behavior of precipitation, enrichment, and flux was evaluated from the sampling results to develop compositions at representative enrichments levels between 1.5 and 6 wt%. It was found that the particular sampling approach plays a role in the prominence of U-233 or U-235 in the makeup of the fissile content. A sampling case assigning log-uniform distributions to solubility and diffusivity and log-normal distributions to the sorption distribution coefficient was found to produce the highest magnitudes of accumulation with more narrow bands of uncertainty and more predictable enrichment. This case was chosen to determine compositions for the criticality study due to U-235-dominated accumulation that was considered more realistic to direct disposal.

The plume of U-238 at the precipitate location determines the steady level of enrichment, and higher U-238 fluxes will determine how early this steady level can be achieved. At long periods of time, the enrichment of the precipitate mirrors the original fissile content of the original, non-compromised canister, and the total mass happens to be highest at this point. Therefore, it is plausible that criticality conditions can be made significantly less favorable by increasing the quantity of non-fissile uranium (i.e. U-238) in the original canisters. It is proposed that the large quantity of depleted uranium (DU) from fuel fabrication components of the nuclear fuel cycle can be employed in some manner within the canister inserts. This material has $\approx 0.2\,wt\%$ U-235, which is less than the natural abundance and can serve as a plentiful source of U-238. Preferably, some process would be implemented to ensure the encapsulated form would have chemical similarity with the used fuel matrix. Typically, DU is stored as U_3O_8, which is more thermodynamically stable than UO_2 in oxidizing conditions; it would be necessary to have both the UNF and DU leach at the same time.

A high degree of conservatism was employed in the methodology. Despite liberal treatment of the groundwater velocity and other aspects of the transport parameter space, along with superposed linear transport to a nearby observation point at ten meters, significant accumulation occurred no less than two million years after canister failure. Higher masses occurring after this point in time have lower enrichments, which, as mentioned, eventually emulate the original fissile content at emplacement. This implies that criticality conditions become increasingly less favorable, and that opportunities to achieve a critical mass would correspond to a point before steady state when mass and enrichment are at appropriate levels.

The use of individual UNF subsets to determine the canister compositions for an entire repository array is defensible given the strong similarity of results, especially at long times. Specific nuclide compositions at emplacement are most important at early times, but these effects eventually become smeared as more canisters in the repository begin to make contributions. While heterogeneous repositories comprised of unique BWR/PWR canisters require larger arrays, the ultimate fissile content of the precipitates are still the same as the homogenized version of the repository. Therefore, the averaging procedure employed for the homogeneous canisters is considered legitimate. The use of a completely heterogeneous repository employing the full scale of variation for assemblies in chapter 2 is unnecessarily realistic and runs counter to the study, since the wide range of transport distances implied by $\sqrt{N^*}$ in table 3.3.5 would cause biases towards packages closest to the observation point. This would require a large number of calculations for different random permutations of the repository array.

There is opportunity to expand the study in a number of ways. A sampling case can be proposed where rock matrix porosity or groundwater velocity are fixed, which would emphasize their relative effects on advective transport. The range of porosities in the bentonite and granitic rock matrix can also be narrowed to less conservative bounds. If the discrete array approach is abandoned in favor of a single source approach, the D^L term can be set to zero, and the diffused front from longitudinal dispersion can be simulated through sampling the groundwater velocity.

Chapter 4

Critical configurations in the host rock

4.1 Introduction

The time-dependent accumulation of uranium at a fixed point in the far-field has been demonstrated in chapter 3 using a conservative nuclide transport model. Within the scope of uncertainty in the results, representative precipitates have been proposed based on a statistical sampling set lending to a conservative overestimate of total mass. It is now necessary to perform a scoping analysis of the configurations necessary for these uranium compositions to reach criticality in the far-field rock within the range of masses observed from transport. This requires a scoping analysis that searches for critical configurations based on variations of the precipitate geometry.

This chapter will describe a parametric approach for determining the critical masses and dimensions of the precipitates. Two spherical configurations are proposed to probe the effects of heterogeneity on the neutron economy of the precipitate. Minimum critical masses are obtained for each composition using a Monte Carlo neutron transport code. Feedback effects stemming from the arrival of key nuclides U-235 and U-238 from the repository plume are interpolated to provide valuable information for the consequence analysis of chapter 8. Other quantities of importance will be analyzed, including the prompt neutron lifetime, reproduction factor, and spectrum hardness.

Prior to an analysis of heating effects on the pore water, which will be covered in chapter 6, the moderator defect will be analyzed in a strictly neutronic context for the different configurations. This will illuminate the role of pore water expulsion on the reactor for both undermoderated and overmoderated conditions. For the latter environment, the potential for positive feedback will be investigated that can potentially enhance the positive additions from the U-235 source term in the dynamics analysis.

4.2 Background

As discussed in chapter 3, primary evidence for criticality underground comes from on experimental measurements of isotopic anomalies in the uranium ore deposits of Oklo, Gabon. This geological formation sustained chain reactions for about a million years and was formed after an oxidative shift in the environment two billion years ago that allowed for the transport of dissolved uranium species and eventual re-concentration into a critical configuration. The geological environment of the ores consists of reducing sediments and inspires the modeling approach of this study, albeit with conservative geometry and simplification of the ore into pure UO_2 as opposed to pitchblende or other minerals of varying stoichiometry. Modeling and simulation of the Oklo reactor has been performed in the past, [69, 70] but it should be noted that the scope of this study is to tie a repository-based source term with a mechanistic treatment of criticality to impart engineering principles.

Following an re-concentration of fissile material, neutrons from spontaneous fission serve as the kinetic source term required for sustained criticality. Two years after the discovery of fission by Hahn, Straussman, and Meitner in 1938, spontaneous fission in uranium was confirmed by Flerov and Petrzhak using ion chambers. A year later, plutonium was verifiably produced from uranium by Seaborg and others at Lawrence Berkeley National Laboratory using a cyclotron. Minute quantities of plutonium would later be discovered in high grade ore deposits such as Great Bear Lake as demonstrative of subcritical reactions taking place in nature. In 1942, the first nuclear waste began to be generated during the Manhattan project from the reactors at Hanford.

Fleming and Thode confirmed the existence of spontaneous fission in natural ore in 1953. [71] The application of the four factor formula from reactor theory first appeared in the mid-1950s in studies by Kuroda and others. [72, 73] These geochronology studies aimed to shed light on the physical stability of uranium minerals (like pitchblende) using criticality parameters, where a "stable" ore would have an infinite multiplication below unity. This work included a parametric study based on relative ratios of uranium and water and considerations of mineral components as moderators or poisonous impurities.

Using the Oklo analogue as a reference, scientists proposed the need for a criticality safety assessment for the direct disposal of used nuclear fuel in 1978. [10] Given the large source term of fissile material that would be emplaced in the canisters, it was hypothesized that a critical mass could be formed underground after the breaching of canisters. However, it was determined that the mass of the deposition would have to be much larger than that observed at Oklo given the low enrichment of UNF. This, along with the improbable configuration required to achieve criticality, led to the issue being discarded.

In 1979, the U.S. government had established the Waste Isolation Pilot Plant (WIPP) for the disposal of transuranic waste generated from weapons production facilities. [74] A report from the year prior suggested that although short-term criticality events from storage configurations were infeasible, criticality control would be a long-term concern if the thermally fissile material were to leach and re-concentrate. While model development was recommended to describe the transport mechanisms involved, the phenomenon was removed from consideration due to the relatively small concentrations of fissile nuclides in TRU waste.

As mentioned in chapter 2, the Department of Energy was tasked with the final disposal of high-level waste and UNF through the Nuclear Waste Policy Act of 1982. The subsequent amendment in 1987 designated the Yucca Mountain Repository as the site of interest. Criticality control standards were established through the 10-CFR-60 regulation of 1983, where criticality events upon emplacement were prohibited by engineering design. However, post-closure criticality was left as part of the total system performance assessment (TSPA) prescribed in 2001 with 10-CFR-63.

The long-term criticality issue gained momentum in the early half of the 1990s with the impending issue of long-term disposal for excess weapons-grade plutonium (w-Pu) to satisfy non-proliferation agreements. This brought about an initiative to evaluate the environmental hazards of potential options for final disposition. As a result, the immobilization of the plutonium stockpile followed by disposal deep underground (along with burnup in existing reactors) was eventually chosen as the solution. In 1995, a controversial report from Los Alamos proposed scenarios in which w-Pu and highly-enriched uranium (HEU) could be naturally reconfigured underground into a supercritical mass with autocatalytic, or self-sustaining, chain reactions. [11] This study analyzed certain water-ejection and ingress scenarios for idealized, homogenous critical configurations of TFM with host rock and groundwater serving as moderators. It was suggested that for certain cases, given positive reactivity feedback, the lack of a negative feedback mechanism could lead to a substantial release of energy. Criticisms of this study included the incongruence in the time scales for the events involved, the neglect of preventative engineering practices, and inadequate details on the necessary transport processes. [75] Nonetheless, the paper was an impetus for further investigation.

The studies pursued at UC Berkeley in response the autocatalytic criticality concern are summarized in Ref. [76]. These were based on the unsaturated and oxidizing geological environment of Yucca Mountain, with emphasis on vitrified waste forms (i.e. borosilicate glass in steel drums). Modeling of transport phenomena was adjusted to the particular concerns poised by this environment for high level waste, including colloid-facilitated transport, mixed solute and colloidal transport, and flocculation. It was through these studies that explosive criticality events from highly-enriched materials were deemed to be improbable in the far-field, but not completely excluded.

The critical mass evaluation in this study is inspired by the methodology of Ref [14] along with its predecessor in Ref. [13], and focuses on direct disposal of typical commercial used nuclear fuel. As a notable departure, a carbonaceous clay shale layer is employed as the rock type immediately surrounding the critical mass. This is chosen given the presence of clay minerals surrounding the reactor zones at the Oklo natural analog, [29, 77–79] as opposed to sandstone used in Liu et al. Furthermore, the precipitate is modeled as a uranium-only deposition commensurate with the assumptions for direct disposal, where specific isotope compositions are derived from the nuclide transport analysis. Plutonium and other TRU are not lumped into the mass of the precipitate in any manner; only their uranium decay daughters are taken into account. Therefore, the results for this neutron transport analysis should be considered unique but relatable to previous studies.

In this study, a critical mass is subject to a slow release of energy from an increase in reactivity caused by an influx of fissile material, and the system is hypothesized to reach subcritical conditions given a sufficient increase in temperature due to negative reactivity feedback from the Doppler effect. Other negative feedback mechanisms may come in the form of the exfiltration of pore water or the generation of neutron-absorbing fission products. If these negative feedback mechanisms do not bring the system back to ambient temperature, then the system may reach temperatures that expand the spherical region and cause subcriticality via changes in volume or else catastrophic failure by way of thermal strain or melting of the far-field rock.

4.3 Methodology

4.3.1 Parametrization

The nature of the critical mass as a porous medium calls for a parametrization employing the porosity, or the volume available to both the pore fluid and the heavy metal precipitate. This parameter will be referred to as the void volume fraction (VVF). Likewise, the other parameter of key interest is the volume fraction of heavy metal in the precipitate (HMVF), which must be less than or equal to the VVF. In later chapters, the fluid volume fraction (FVF), which is the difference between the VVF and HMVF (4.3.1), will be split between water and air depending on the saturation (S_l) specified by particular regions in the critical mass (4.3.2 and 4.3.3).

$$FVF = VVF - HMVF,\ HMVF \leq VVF \tag{4.3.1}$$

$$WVF = FVF * S_l,\ 0 \leq S_l \leq 1 \tag{4.3.2}$$

$$AVF = FVF * (1 - S_l)\,,\ 0 \leq S_l \leq 1 \tag{4.3.3}$$

However, in this chapter, given the focus on a granitic repository lying below the water table, this preliminary investigation assumes full saturation, where water completely occupies the FVF before heating from fission. Therefore, the water volume fraction (WVF) is equal to the FVF. The scope of VVF and HMVF is chosen to vary between 1.5 vol% to 36 vol% in 1.5 vol% increments for a total of 300 coordinates, where the extreme value is chosen to represent highly porous or fractured regions of the far-field either caused by erosion or extensive fracturing.

4.3.2 Computation

The MCNP (Monte Carlo N-Particle, version 6.1) code is used to evaluate stochastic neutron transport for this study. [80] The code and its cross section libraries have been benchmarked for low-enriched uranium $\left(\frac{M_{25}}{M_U} < 10\,wt\%\right)$ criticality studies via data from the International Criticality Safety Benchmark Evaluation project handbook. [81] These data include a variety of neutron spectra for different moderators, reflectors, and geometries. The thermal spectrum data expected to be most relevant to the precipitates include benchmarks based on fuel pin lattices and homogeneous solutions (e.g., uranyl fluoride) at room temperature and atmospheric pressure.

Given the ordering and formatting specifications of the MCNP inputs, a template file was created where lines could modified by Perl scripts using a separate input file containing the following problem characteristics:

1. Thickness of each spherical annulus
2. The number of discrete radial units employed in each region (kept at one in this chapter)
3. The initial conditions in each region (pressure, temperature, and saturation)
4. The material filling each region
    a) Names of composition input files
    b) Names of $S(\alpha, \beta)$ libraries
    c) Thermo-hydrological code parameters (e.g. every input line for each materials in the ROCKS deck for TOUGH2, which will be explained in chapter 6)
5. For the fractured composition
    a) The fracture aperture
    b) The material composition files and $S(\alpha, \beta)$ libraries for the rock and fuel
    c) The set porosities and saturations of the rock and fuel
6. The critical radius, VVF, and HMVF (used in later chapters) and the default densities of water and air
7. The burnup time points for chapter 5

The template file also includes flags to insert criticality source points, burnup and tally specifications, and nuclide lists for doppler broadening treatment (chapter 7). A framework of scripts were written to generate MCNP files based on coordinates of VVF, HMVF, mass, and saturation, and subsequently reap data from the output file.

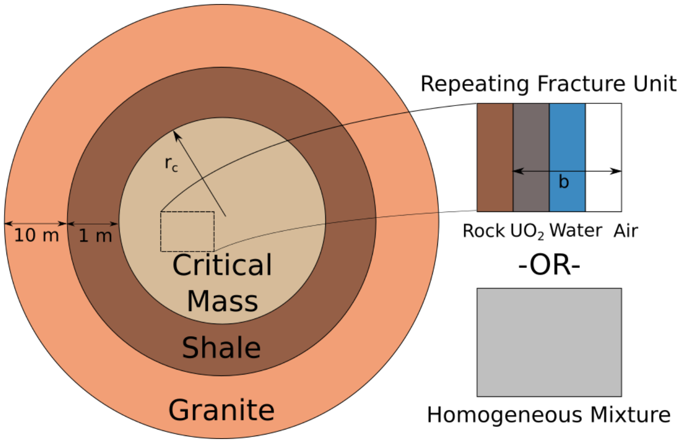

Figure 4.3.1: Model for configurations of the far-field precipitate with critical radius r_c (not to scale). The fractured geometry has an aperture of width b.

4.3.3 Configurations

The precipitate is modeled as a sphere containing either a homogeneous mixture of rock, fuel, water, and air, or repeating laminar units of those components in a heterogeneous, fractured geometry (see figure 4.3.1). This geometry is employed as opposed to the wide, flat prismatic or cylindrical geometries that would be expected in the strata of the far-field rock to reduce neutron leakage and ensure that critical masse figures are minimal. The stoichiometry of the uranium oxide is assumed to be UO_2 [with U(IV)] as opposed to the more thermodynamically stable U_3O_8 [U(V,VI)] found in nature. This is done to maximize the proportion of uranium atoms in a given volume which in turn maximizes uranium absorptions. For either configuration, the radius of the sphere is adjusted to accommodate the mass of UO_2 being analyzed as determined by the VVF and HMVF based on the theoretical density. In the fractured configuration, the aperture (b) is the width accommodating the fuel, water, and air laminates, and serves as a further constraint when determining the fracture spacing, the thickness of the rock laminate, and the spherical radius. The mass of UO_2 is chosen based on the U(IV) stoichiometry in order to accommodate set masses of heavy metal.

For the homogeneous configuration, the UO_2 is assumed to be interspersed with sandstone and pore fluid on a fine intergranular scale. This represents the form of uranium ore most commonly found in nature. [82] The fractured configuration employs shale as the rock lamination given its geological fissility, or planar layering. Although ore deposits in shale formations are known to be relatively lower in grade, in this report, the uranium depositions in the shale layers are modeled as veins of pure crystal at the full theoretical density of 10.95 g/cm^3. This is a conservative assumption made to minimize the critical dimensions. For criticality calculations, a source point from spontaneous fission was placed in the centroid of each cell containing U-235. In this chapter, no special energy distribution is used for the spontaneous fission of U-238. The homogeneous configuration employs seven source points: six along the positive and negative axes of three-dimensional cartesian coordinates covering half the radius, and one at the origin. When annular discretization is employed in later chapters, this same logic is maintained for the outer shells where the placement is based on half of the shell thickness.

The shale laminates in the fractured configuration are set at a constant saturated porosity of 10%, and full saturation is maintained in this material throughout the dynamics analysis regardless of temperature changes. This assumption is employed to isolate the effect of water removal strictly to the VVF parameter as a simplification of the study. Furthermore, this is hydrologically justifiable considering the vast difference in permeabilities between the shale and an empty fracture. The solid density of shale, 2.80 g/cm^3, is used to determine the water-saturated density of 2.625 g/cm^3 for the shale slabs.

The critical region as a whole is surrounded by a spherical annulus of shale. This physically serves as the reducing sedimentary rock that allows the uranyl anion transported from the repository to drop out of solution. Given the limited extent of the shale deposits at Oklo, this layer is given a finite thickness of one meter (see figure 1 in Ref. [29]). The porosity is set at 10% and considered to be fully saturated.

The shale layer is surrounded by a granite region of 10 meter thickness at 1% porosity at full saturation. The density of the region is modeled as $2.732\,g/cm^3$, which is very similar to the solid density of $2.75\,g/cm^3$ given the low porosity. The granite is employed in the neutronics analysis mostly to allow for the system to be modeled as interfacing with an "infinite" absorber as opposed to a vacuum. Nonetheless, a vacuum is modeled as surrounding the granite, and the granite thickness is considered arbitrary since the neutron collision density is considered to be negligible. While the water contents of the shale and granite comprise the total void space in this initial criticality analysis, the water content will later be allowed to vary based on results from the thermo-hydrological (TH) simulation in chapter 6. Furthermore, as opposed to using a void boundary condition, an infinite extent of unsaturated granite will be used instead.

4.3.4 Host rock conditions at the precipitate location

A granitic repository is anticipated to have an emplacement depth of 500 m, which corresponds to a maximal overburden stress of 15 MPa (see Ref. [83]). This is similar to the $\approx 400 - 450\,m$ depth currently considered for the Finnish repository, which is expected to have a footprint on the order of $\approx 2\,km^2$. While the hydrostatic pressure is about 5 MPa at this depth, the steam tables indicate that the liquid phase would have a wider space of states per given temperature at the 15 MPa level, where the boiling point is $342.2°C$ compared to $262.8°C$. Therefore, if the pressure is modeled at 15 MPa, water would be present in the liquid phase for a broader range of temperatures, which would allow for greater neutron thermalization in the pore space as Doppler broadening takes place in the fuel. This would allow for a more thorough interplay between water expulsion and Doppler broadening in determining the reactivity feedback balance, which will be discussed later in chapter 7. Furthermore, given the time-dependence of the creep phenomenon and temperature threshold needed for plastic deformation, this artificial assumption would also allow for a greater extent of plasticity when evaluating mechanical failure in chapter 9.

The ENDF-B/VII.1 cross sections at room temperature (the "80c" libraries collected at $20.45°C$) are employed throughout the analysis, as the geothermal gradient in the saturated rock is considered negligible. Using data at room temperature serves as a reliable reference point for the critical configuration before the Doppler effect is analyzed post-TH evaluation. Furthermore, the room temperature libraries are a more reliable starting point for generating the Doppler energy grids and interpolations in chapter 7. It should be noted that for consistency of results with the Doppler study, the temperatures per cell were explicitly set at $20.45°C$.

4.3.5 Material compositions

A Perl script was written to generate isotope-specific MCNP atomic densities based on constituent minerals by using their solid densities, compositions, stoichiometries, porosities, saturations, and isotopic enrichments in a convenient input file (see appendix A). This facilitates the application of multiple precipitate compositions from TTB, and multiple rock types, pore fluid chemistries, etc. can be easily applied in future iterations of this study. For these inputs, the uranium component of the UO_2 mineral is the only case where specific isotopes are necessarily specified for enrichment. Otherwise, the most abundant isotope is used for other elements in the composition, and the "00" designation is used if libraries are only available for the natural substance (e.g. carbon). The script also generates mass-averaged specific heats, number-averaged thermal conductivities (dry and wet), and a bulk density for the creation of input files for the TOUGH2 code (to be explained in chapter 6).

The pore fluid is comprised of water (pure H_2O) and air, whose composition is shown in table 4.3.1. The pore fluids densities of 1.005 g/cm^3 and 0.00177 g/cm^3 are chosen for water and air, respectively, to match what would be expected at 15 MPa (see figure 6.2.2 on page 118). In this study, when water undergoes a phase change, it is simply replaced with air as opposed to water vapor, which reduces the hydrogen content in the gas phase. While this is expected to decrease neutron thermalization in the gas, the overall effect from the use of air is expected to be negligible since reaction rates are dependent on density. Furthermore, the presence of air in water as an aqueous component is not considered when calculating the composition of the pore liquid. This allows for the voiding effect to be simulated with a continuous layer of gaseous material as opposed to bubbling in the pore water itself (which would roughly correlate to a BWR-type analysis).

The sandstone in the homogeneous composition is modeled as 90% SiO_2, used to represent the mineral quartz, and 10% $KAlSi_3O_8$, which represents feldspar. The solid density is assumed to be 2.65 g/cm^3.

The composition of shale for use in both the fracture laminates and the reflector is shown in table 4.3.2, where the constituent components are inspired by Ref. [84]. A smectite composition sampled from Upton, WY is used to represent the clay mineral component of shale. [85] This allows for TH modeling of the reflector layer to have similar effects from the

Compound	vol%	wt%
N_2	7.81E-01	7.56E-01
O_2	2.09E-01	2.31E-01
Ar	9.34E-03	1.29E-02
CO_2	3.83E-04	5.46E-04
Ne	1.82E-05	1.27E-05
He	5.24E-06	7.23E-07
CH_4	1.75E-06	9.03E-07
Kr	1.40E-08	4.06E-08
H_2	5.50E-09	3.82E-10
N_2O	3.00E-09	4.17E-09
Xe	9.00E-10	4.11E-09
O_3	7.00E-10	1.06E-09
I_2	7.00E-10	2.67E-06
NO_2	2.00E-10	2.91E-10

(a) By molecule.

Element	at%
N	7.60E-01
O	2.33E-01
Ar	6.48E-03
C	2.75E-04
Ne	6.37E-06
I	2.69E-06
H	1.82E-06
He	3.64E-07
Kr	2.04E-08
Xe	2.07E-09

(b) By element.

Table 4.3.1: Fractional composition assumed for air.

bentonite buffer that would surround the waste canisters. As mentioned previously, the solid density is assumed to be $2.8\,g/cm^3$.

The strongest and most prominent reducing agent in the shale composition is aluminum, although sodium and iron can also contribute. Among the elements listed in the composition, K-40, Ca-43, Ti-48, and Sr-87 are isotopes with appreciable cross sections for neutron capture, along with iron isotopes in general. Given the low presence of these elements and the further reduction from the isotopic natural abundance, absorbing species not expected to drastically dampen the scattering characteristics of prominent oxygen and silicon. Carbon is present in 1.6 at% and can also aid in neutron moderation.

The granite composition is detailed in table 4.3.3 and based on Ref. [86]. The water component listed in the table represents the presence of H_2O in hydrated molecules in the minerals, not the water present in the pore space. Since feldspar is a typical component of granite, the potassium content is much larger compared to shale. The aluminum content is similar among both rock types. A solid density of 2.75 g/cm^3 is employed for this rock type.

To capture molecule-specific scattering behavior, the Si(SiO_2) $S(\alpha, \beta)$ thermal scattering library is used for both shale and granite, whereas the U(UO_2) library is used for cells with U. The H(H_2O) library is used for cells filled strictly with water (i.e. in the fractured geometry).

Compound	wt%
Clay minerals	59
Quartz	22
Feldspar	8
Carbonate	8
Fe-Oxide	3

(a) By compound.

Element	at%
O	63.379
Si	20.043
Al	8.553
Fe	2.728
Ca	1.602
C	1.600
Sr	0.921
K	0.619
Mg	0.472
Na	0.041
Ti	0.022
P	0.014
Mn	0.003
S	0.003

(b) By element.

Table 4.3.2: Composition assumed for shale presented in terms of constituents and atomic composition, where the composition of smectite is used for clay minerals.

Compound	wt%
SiO_2	55.588
Al_2O_3	21.379
K_2O	8.851
Na_2O	4.661
CaO	2.004
FeO	2.578
Fe_2O_3	3.744
MgO	0.474
TiO_2	0.395
P_2O_5	0.204
MnO	0.075
H_2O	0.047

(a) By compound.

Element	at%
O	62.055
Si	21.795
Al	8.725
K	2.493
Na	2.233
Fe	1.246
Ca	0.551
H	0.508
Mg	0.215
Ti	0.091
P	0.073
Mn	0.015

(b) By element.

Table 4.3.3: Composition of granite presented in terms of constituents and atomic composition.

4.4 Results

4.4.1 Optimal aperture of the fractured geometry

The aperture of the fractured configuration was first optimized by finding the minimum VVF observed for fixed masses of UO_2 in different precipitates. The effective multiplication factor (k_{eff}), which is a measure of the net generation of neutrons, was evaluated for the parameter space of VVF and HMVF using various centimeter-scale apertures of 0.01 (100 μm), 0.1, 0.25, 0.5, 0.75, 1, 2, 3, 4, 5, and 10, although the smaller end of the scale is more apt to be observed in the natural setting. Results were evaluated based on a criterion of $k_{eff} > 0.98$ to allow the fixed-aperture studies to encompass the full range of minimum critical configurations.

The results for the aperture scoping study are shown in figure 4.4.1, where the minimum VVF needed to meet a criterion of $k_{eff} > 0.98$ is listed per aperture. For each curve, there is an optimal aperture where this VVF is minimized, and it is evident that the associated HMVF is minimized as well. However, within the scope of apertures considered, this minimum becomes less pronounced as the precipitate enrichment increases. Furthermore, as the enrichment increases, the optimal VVFs become increasingly more occupied with heavy metal where $HMVF \approx VVF$. This implies that the higher probability of fission absorptions outweighs the losses due to resonance absorptions, since lower quantities of porewater would be available to bring neutrons below resonance energies.

The lowest values of minimum VVF correspond to apertures between 0.1 and 1 cm for precipitates 6 through 1, respectively. Although precipitate #6 was optimized with $b = 0.1\,cm$, an aperture of 0.25 was employed to match that of precipitate #5. This was done to simplify the aperture assortment to 0.25, 0.5, and 1 cm (see table 4.4.2).

Prior to the minimum VVF, the optimal void fractions for the smallest apertures are larger due to relatively poorer moderation from the rock components in the repeating lattice. For these small apertures, the fuel layers are very thin, which reduces resonance energy self-shielding and thermal utilization. The neutron mean free path will likely be larger than the thickness of the water plane, hence reducing the probability of scattering in H_2O. Therefore, the amount of volume available to water would need to be larger to counter these effects.

After the minimum, the VVF increases with aperture because of increased resonance absorptions occurring in the relatively thicker fuel layers. Prompt neutrons generated from fission will more likely interact with the fuel first prior to entering the water layer for thermalization. Therefore, higher VVFs are required to counter the decrease in resonance escape probability. No points meeting the multiplication criterion were found for the 10 cm aperture as a result increased resonance absorption from a lack of self-shielding.

For precipitate 2, the multiplication criterion was satisfied for 1 MTU at 0.75 cm and a more optimal 1 cm, but not for higher aperture values within the scope of VVF and HMVF. Therefore, the results for 5 MTU are included in figure 4.4.1 to provide more details on k_{eff} behavior, where 1 cm appears to be the optimal aperture figure. For precipitate 1, large masses were observed to be required for criticality, so results for 1000 MTU are plotted instead.

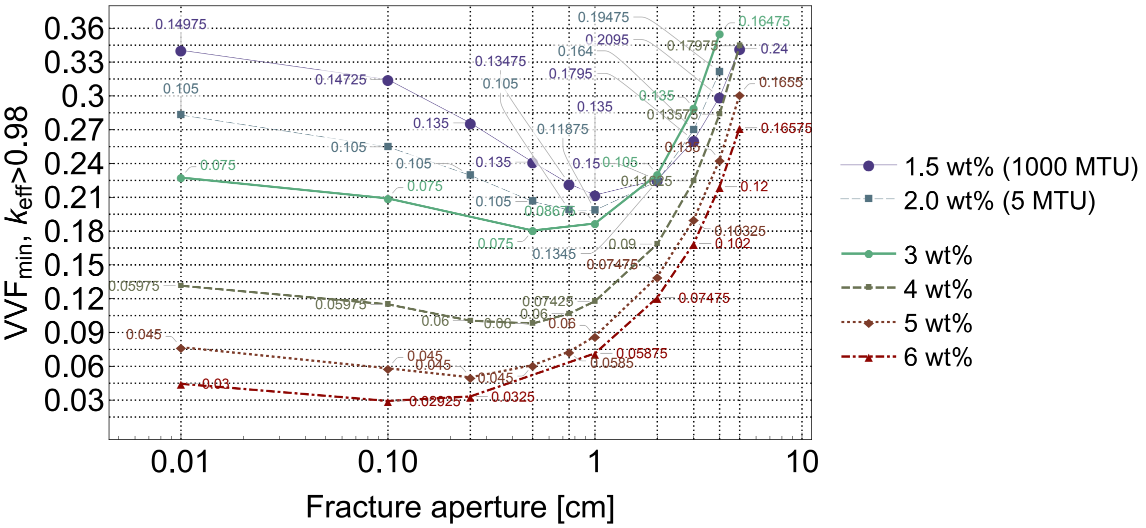

Figure 4.4.1: Minimum VVF required for $k_{eff} > 0.98$ in terms of the fracture aperture for various enrichments based on 1 MTU depositions unless otherwise noted. The corresponding HMVF values are indicated in the labels.

To more precisely highlight the effect of the total heavy metal mass, figure 4.4.2 shows that as the total amount of fuel increases from 1 to 5 MTU, the minimal VVFs are shifted downwards per given aperture. This means that the space of critical VVFs will be wider for larger masses. This is likely caused by an increase in neutron leakage with decreasing surface area of the sphere, such that more saturated void would be needed to reflect neutrons back into the fuel slabs. In general, as the radius of the sphere becomes larger relative to the neutron mean free path, leakage will occur mostly at the surface of the sphere and be scaled at a rate of r^2, while fission absorptions will occur throughout the entire volume and be scaled according to r^3. [87]

4.4.2 Scope of critical masses

To determine the locus of minimum critical masses M_c in the parameter space, a script was written to employ a bisection root-finding scheme to find the critical radius and mass per (VVF, HMVF) coordinate. A primary run of MCNP was first performed based on an initial guess of the critical radius in order to develop the upper and lower bounds for investigation depending on whether k_{eff} is above or below unity. The initial guesses were inspired by the fixed mass exploratory analysis. Subsequent MCNP calculations proceed until the final k_{eff} figure is between unity and 1.005 within error. Due to inadequate moderation conditions, a critical mass may not be realizable for certain porosities and heavy metal contents. Therefore, the search is set to end after a fixed number of iterations or when a steady state appears to be reached (four repeated values of the average k_{eff}).

Given the large quantities of heavy metal required for precipitate 1 to reach criticality in

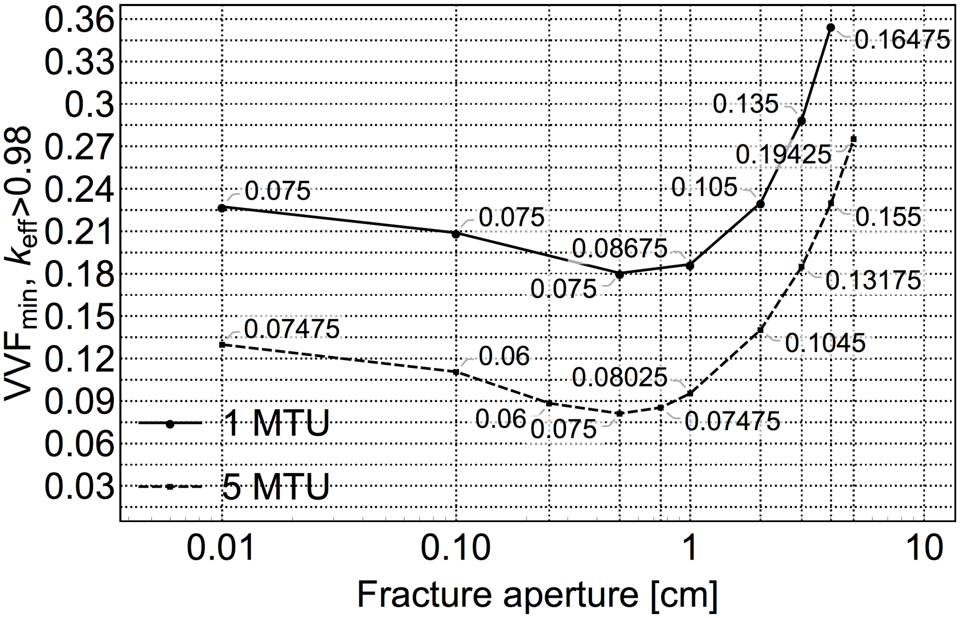

Figure 4.4.2: Minimum VVF required for $k_{eff} > 0.98$ in terms of the fracture aperture for 1 and 5 MTU depositions of the 3 wt% precipitate in the fractured geometry. The corresponding HMVF values are indicated in the labels.

the preliminary aperture-optimization analysis, the scoping analysis was initiated with 2 wt% precipitate to find a more plausible locus critical masses. These masses observed for each coordinate in this case are expected to decrease with higher enrichment. The results of the root-finding analysis is shown in figure 4.4.3 for both configurations, where the $\log_{10}$ values of mass in MTU are presented up to 2.7. It is clear that the scope of critical masses for the homogeneous geometry is drastically more limited than that of the fractured, heterogeneous geometry. No VVF less than approximately 28 vol% can reach criticality for masses relevant to the worst-case scenario for nuclide transport. For the fractured geometry, the VVF limit is about 12.5 vol%, and in either case, the HMVF needs to be at least 6.5 vol%. Smaller critical masses correspond to void spaces less realistic for granite. The low HMVF points below the contours correspond to overmoderated systems, while those above would be undermoderated.

The effective multiplication was evaluated for each VVF, HMVF coordinate for fixed masses of heavy metal inspired by both figure 4.4.3 and figure 3.4.1. Tabulations of minimum critical coordinates corresponding to these masses are shown in tables 4.4.1 and 4.4.2, along with associated values of the prompt removal lifetime (l_p), the average neutron energy resulting in fission $\left(\bar{E}_n\right)$, the hydrogen/U-235 ratio $\left(\frac{N_H}{N_{25}}\right)$, and the average number of neutrons produced from fission over the total quantity absorbed for cells with fissionable material (η_{fuel}) and the system overall (η). The moderator defect (D_M) will be explained in section 4.4.3. The optimal apertures from section 4.4.1 are also shown in table 4.4.2.

For the homogeneous configuration, lower bound critical masses range from 0.1 MTU for the 6 wt% precipitate to 5 MTU for the 2 wt% precipitate. The low-enriched precipitate (#1) closely emulating the fissile content of the used nuclear fuel at discharge does not reach criticality for evaluations up to 1000 MTU within the parameter space. As shown in figure 3.4.6a, the mixed transport modeling set cannot reach higher levels of precipitation in a hundred million years post canister failure. Therefore, the steady state enrichment level observed at the precipitate location cannot correspond to criticality if all geological components are finely mixed.

For the low-enriched fractured geometry, the 500, and 1000 MTU configurations have critical radii meeting or exceeding to the heights of the original canisters, which implies a repository failure scenario of massive scale that would not appear to be plausible from the transport results. Nonetheless, the 100 MTU configuration implies that the steady-state enrichment level can attain criticality albeit with very high VVF and HMVF.

For a given mass in a precipitate category, the minimum VVF and critical radius will be smaller in the heterogeneous geometry relative to the homogeneous. For a given enrichment, as the critical radius increases, the minimum VVF decreases, which typically corresponds to decreases in the HMVF, especially for the lower-enriched precipitates. Figure 4.4.4 shows the minimum VVF required for $k_{eff} > 0.98$ obtained for certain masses of the 6 wt% precipitate in either geometry. It is apparent that as critical masses get smaller, increasingly larger VVFs are required to meet the multiplication criterion, which in turn correspond to less realistic crystalline host rock characteristics. This is caused by the increase in neutron leakage with decreasing mass, which requires a larger presence of moderator to compensate. The associated HMVF tends to decrease with mass, but this happens in a less pronounced fashion, since the contours of figure 4.4.3 tend to be flatter per given HMVF. Actually, for the homogeneous configuration, increasingly larger critical masses could be expected with a steady 3 vol% proportion of heavy metal. For more highly-enriched precipitates, it appears that the rock serves sufficiently as a moderator such that water does not need to occupy much of the void space. This is especially the case for the fractured geometry, since individual shale laminates moderate more effectively than a sandstone matrix.

For a precipitate mass fixed at 5 MTU, as enrichment proceeds from 2 to 6 wt%, the minimum VVF and HMVF required for $k_{eff} > 0.98$ decrease, as shown in figure 4.4.5. This is caused by the higher probability of fission absorptions in the fuel with increasingly thermal neutron energies, which is caused by increasingly greater moderation from the host rock. The prompt neutron lifetime generally appears to get longer as both enrichment increases and HMVF decreases because more time is required for the neutrons to thermalize and be absorbed. This is caused by a proportionally lower amount of fuel relative to rock, as the rock is liable to have more scattering qualities than absorptive. The overall effect is an increase in the neutron absorption mean free path (see equation (4.4.4)). In line with previous observations, the optimal void space becomes increasingly more occupied with heavy metal as enrichment increases, since less water would be needed to reach criticality with higher probabilities of fission absorptions.

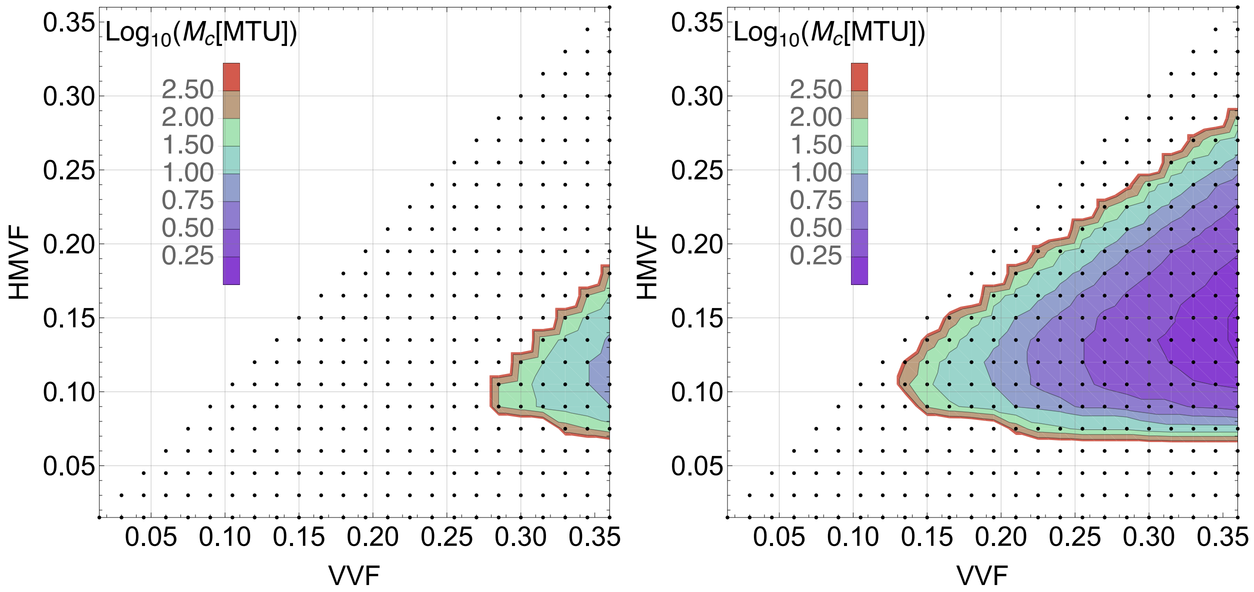

(a) Homogeneous (b) Fractured

Figure 4.4.3: Minimum critical masses evaluated up to 500 MTU for the space of VVF and HMVF for the 2 wt% enriched precipitate.

Precipitate		M_c [MTU]	VVF	HMVF	r_c $[cm]$	$\frac{N_H}{N_{25}}$	D_M	δD_M	$l_p\,[s]$	$\bar{E}_n\,[MeV]$	η_{fuel}	η
2	2.0 wt%	5	0.3375	0.105	105.6	300.8	-1.5530	0.0012	8.37E-5	1.11E-1	1.05	0.981
		10	0.3075	0.1045	133.3	263.9	-1.5408	0.0011	7.79E-5	1.17E-1	1.03	0.981
		100	0.2565	0.09	301.8	251.3	-1.5801	0.0010	7.40E-5	1.14E-1	0.994	0.982
3	3.0 wt%	1	0.2965	0.075	69.1	267.5	-1.4986	0.0011	1.06E-4	8.07E-2	1.14	0.983
		5	0.2005	0.06	127.3	212.1	-1.3939	0.0012	9.66E-5	7.96E-2	1.06	0.984
		10	0.181	0.0595	160.8	184.9	-1.3279	0.0011	9.01E-5	8.36E-2	1.04	0.983
4	4.0 wt%	0.5	0.263	0.0595	59.2	232.3	-1.4605	0.0014	1.20E-4	6.57E-2	1.20	0.981
		1	0.2065	0.045	81.9	243.8	-1.3984	0.0013	1.20E-4	5.71E-2	1.13	0.979
		5	0.1405	0.045	140.1	144.1	-1.1538	0.0013	9.80E-5	6.83E-2	1.06	0.982
5	5.0 wt%	0.5	0.203	0.045	65.0	190.8	-1.3350	0.0014	1.25E-4	5.66E-2	1.21	0.981
		1	0.1615	0.043	83.2	149.7	-1.1835	0.0013	1.16E-4	6.03E-2	1.16	0.981
		5	0.109	0.03	160.3	143.1	-0.9956	0.0013	1.11E-4	4.98E-2	1.06	0.981
6	6.0 wt%	0.1	0.36	0.045	38.0	317.0	-1.7869	0.0013	1.42E-4	4.14E-2	1.32	0.978
		0.5	0.166	0.03	74.4	205.3	-1.2676	0.0014	1.35E-4	4.15E-2	1.19	0.978
		1	0.129	0.03	93.8	149.4	-1.0909	0.0013	1.25E-4	4.57E-2	1.15	0.980
		5	0.0895	0.03	160.3	89.8	-0.8315	0.0012	9.92E-5	5.32E-2	1.07	0.982

Table 4.4.1: Criticality parameters and moderator defects for the homogeneous, undermoderated precipitates.

Precipitate		$b\,[cm]$	$M_c\,[MTU]$	VVF	HMVF	r_c $[cm]$	$\frac{N_H}{N_{25}}$	D_M	δD_M	$l_p\,[s]$	$\bar{E}_n\,[MeV]$	η_{fuel}	η
1	1.5 wt%	1	100	0.271	0.1499	254.58	146.328	-0.1930	0.0012	6.98E-5	1.76E-1	1.24	0.985
			500	0.2544	0.1498	435.423	126.475	-0.1586	0.0011	6.67E-5	1.81E-1	1.22	0.984
			1000	0.2528	0.15	548.354	124.133	-0.1548	0.0011	6.59E-5	1.82E-1	1.22	0.985
2	2.0 wt%	1	5	0.2229	0.12	101.008	116.488	-0.1759	0.0010	9.20E-5	1.49E-1	1.34	0.981
			10	0.1905	0.1188	127.689	81.9879	-0.1129	0.0011	8.67E-5	1.58E-1	1.31	0.983
			100	0.1424	0.105	286.656	48.3871	-0.0344	0.0011	8.41E-5	1.61E-1	1.30	0.982
3	3.0 wt%	0.5	0.5	0.2925	0.094	50.8595	191.244	-0.4729	0.0013	1.14E-4	9.31E-2	1.48	0.983
			1	0.20175	0.089	65.2572	114.731	-0.2462	0.0014	1.08E-4	1.02E-1	1.44	0.982
			5	0.093	0.075	118.139	21.7354	-0.0257	0.0012	9.83E-5	1.17E-1	1.38	0.984
			10	0.07375	0.07325	150.022	0.618184	-	-	9.62E-5	1.25E-1	1.37	0.984
4	4.0 wt%	0.5	0.5	0.1763	0.0746	54.9332	92.5975	-0.2312	0.0016	1.21E-4	8.97E-2	1.51	0.980
			1	0.107	0.06	74.4231	53.2064	-0.0752	0.0015	1.20E-4	8.88E-2	1.51	0.979
			5	0.0522	0.0522	133.309	0.	-	-	1.18E-4	1.06E-1	1.50	0.981
			10	0.0469	0.0469	174.061	0.	-	-	1.21E-4	1.01E-1	1.52	0.979
5	5.0 wt%	0.25	0.5	0.1139	0.045	65.0146	83.1981	-0.1306	0.0015	1.26E-4	5.93E-2	1.55	0.980
			1	0.0571	0.045	81.9132	14.611	-0.0180	0.0016	1.22E-4	7.40E-2	1.52	0.980
			5	0.032	0.032	156.927	0.	-	-	1.28E-4	6.76E-2	1.58	0.981
			10	0.0296	0.0296	202.921	0.	-	-	1.30E-4	6.55E-2	1.59	0.981
6	6.0 wt%	0.25	0.1	0.2969	0.0598	34.5826	179.538	-0.7021	0.0016	1.38E-4	5.46E-2	1.64	0.978
			0.5	0.0672	0.0449	65.0628	22.4897	-0.0434	0.0016	1.28E-4	6.96E-2	1.55	0.979
			1	0.038	0.0379	86.7385	0.119478	-	-	1.30E-4	7.28E-2	1.58	0.979
			5	0.0271	0.0271	165.866	0.	-	-	1.35E-4	6.42E-2	1.63	0.978
			10	0.0261	0.0261	211.614	0.	-	-	1.36E-4	6.32E-2	1.64	0.977

Table 4.4.2: Criticality parameters for the fractured, undermoderated precipitates. Moderator defects are shown for cases where $\frac{N_H}{N_{25}} > 10$

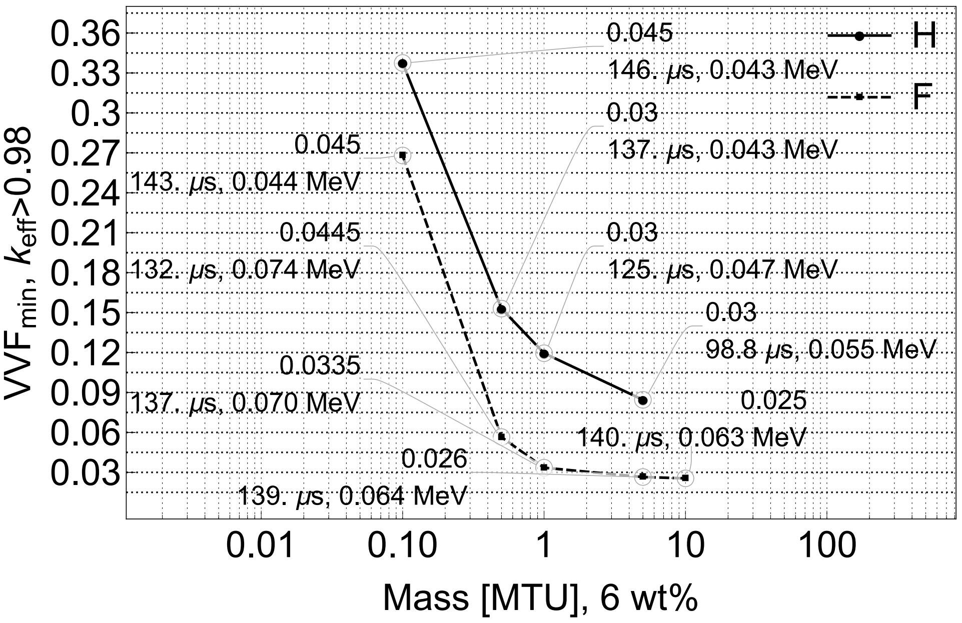

Figure 4.4.4: The minimum VVF required for $k_{eff} > 0.98$ for various masses of the 6 wt% precipitate, with the corresponding HMVF, l_p, and $\bar{E}_n$ shown in the labels.

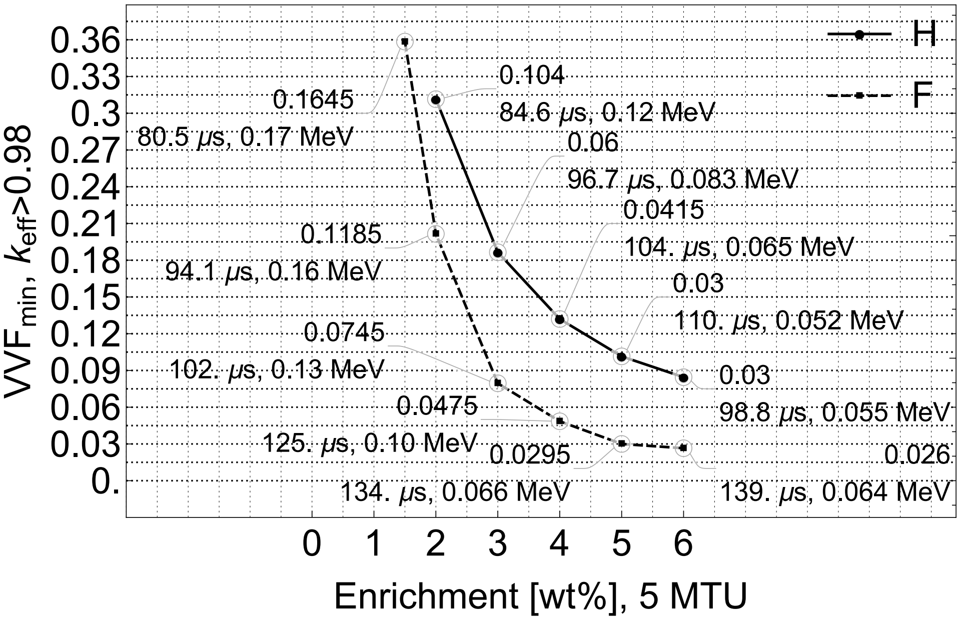

Figure 4.4.5: The effect of enrichment on the minimum VVF required for $k_{eff} > 0.98$, with the corresponding HMVF, l_p, and $\bar{E}_n$ shown in the labels.

4.4.3 Moderator defect

Undermoderated conditions

The moderator defect is the change in reactivity observed in a reactor when the moderator is removed. While the rock component has some moderating qualities, the pore water is considered to be the most important moderating component in the context of the dynamics analysis. Given the nature of the critical mass as a heat-generating porous medium, the evolution of saturation is governed by the conservation of energy and mass, where capillary pressure and water retention effects are applicable. However, from a neutronics perspective, valuable information on the role of pore water can be obtained by studying the effect of globally-applied saturation changes to the precipitate as opposed to analyzing spatial variability in the sphere.

A analysis was performed where water was uniformly removed from the void space of a critical configuration to monitor changes in k_{eff}. The shale reflector was maintained at full saturation. Configurations in table 4.4.2 with very low WVF were excluded from the analysis. Feedback for these critical masses is expected to be largely determined by heating of the fuel and whatever amount of TFM can be accommodated in the pore space. Results of the analysis for the 6 wt% precipitate are shown in figure 4.4.6a, where the effect of water removal is strongest in the homogeneous geometry, with D_M between -1.8 to -0.8. Larger critical radii are less affected by moderator withdrawal because of reduced leakage. The moderator defects are observed to be much smaller for the fractured geometry, ranging from

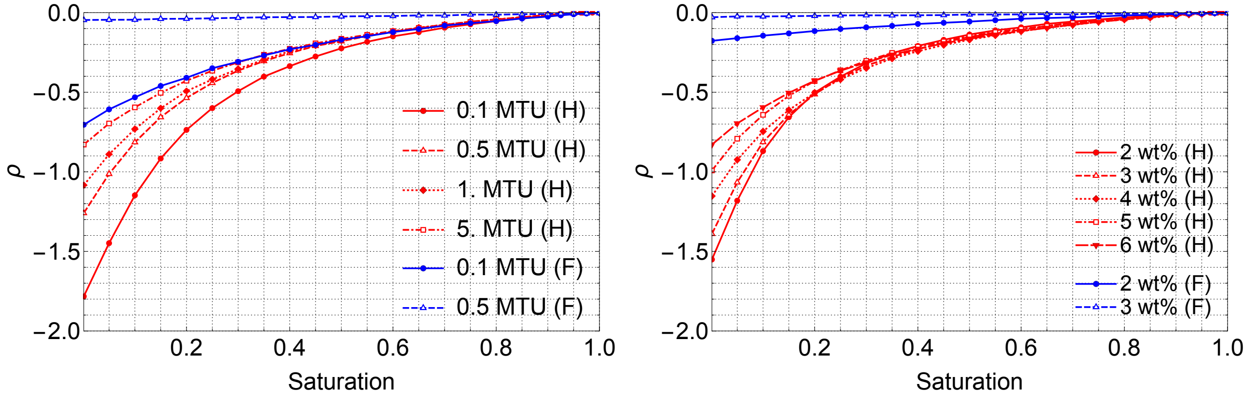

(a) 6 wt% (b) 5 MTU

Figure 4.4.6: The effect of replacing water with air in a uniform manner throughout the void space of critical configurations.

-0.7 to -0.05 for 0.1 and 0.5 MTU, respectively. This difference comes from the fact that neutrons are able to scatter in the rock between fractures even when water is not present, whereas in the homogeneous geometry, neutrons have more opportunities to be captured in the fuel before thermalizing to such an extent that fission is probable.

When fixing the critical mass at 5 MTU and steadily reducing the liquid saturation, lower-enriched precipitates have much stronger moderator defects, as shown in figure 4.4.6b. Without the moderating contribution of the pore water, non-fission absorptions are much more probable in the lower-enriched fuel compared to those that are higher-enriched. While not plotted, this is confirmed in the decrease in η with decreasing saturation, which coincides with increased spectrum hardening with regards to neutrons causing fission. The discrepancy in D_M between the homogeneous and fractured geometries for 2 wt% and 3 wt% precipitates is further emphasized in this plot. It is predicted that dynamic behavior for the heterogeneous depositions will be heavily determined by the Doppler effect.

Altogether, for a critical precipitate newly formed from nuclide transport, given the anticipated negative effects of heating on reactivity (i.e. the "temperature defect"), it seems very likely that chain reactions can be shut down if heating completely expels water from the homogeneous core. However, these effects would have to counteract the positive mechanism imparted by the uranium plume from the repository. Since the $\rho(S_l)$ curves can be fitted to quadratic functions, the expected feedback coefficients for non-heated water removal would conform to monotonically-decreasing linear functions of S_l.

Investigation of overmoderated conditions

In an overmoderated environment, the proportion of pore-water relative to heavy metal is such that its absorptive properties outweigh its scattering effects when subject to neutron interactions. These conditions can lead to positive reactivity feedback in the event of water expulsion from the pore space. By removing water from the saturated pore space, there are less absorptions in the moderator relative to the fuel, and the improved moderation allows chain reactions to continue until the system becomes undermoderated or the Doppler effect sufficiently counteracts the positive feedback mechanism. In this section, the presence of positive feedback from water exfiltration from an overmoderated system is investigated in a purely neutronic context at room temperature with no considerations of spatial distributions introduced by natural heat and mass transfer.

Past approaches to evaluating overmoderated positive feedback involved the arrival of highly fissile (weapons-grade) solutes from high level waste that had been naturally washed of packaged poisons. The addition of fissile material would lead to heating and water expulsion, which would lead to positive feedback. Extreme heating of the TFM to the point of vaporization was postulated to serve as a compounded positive feedback mechanism that would lead to autocatalytic reactions. While results in chapter 3 indicate that the plume of TRU-generated U-235 can be considerable at early times, the contributions of U-238 eventually become dominant, especially for masses on the order of MTU more relevant to criticality. It is not considered plausible to have pure U-233 or U-235 oxide displacing water from the pore space in the direct disposal context.

A more appropriate approach is suggested based on altering the total volume of moderator available to the fuel, which would be based on the natural sealing of fractures or pore space by sediments and microbes, coupled with the lengthening of fractures due to crack propagation and seismic processes. The procedure for investigating overmoderated configurations within this scope is described as follows:

1. For every VVF and HMVF in the parameter space, interpolations of k_{eff} are made using Mathematica for each calculated mass based on 0.15 vol% increments. [67]
2. The HMVF and VVF are identified for a slightly supercritical configuration ($k_{eff} = 1.02$).
3. The VVF is reset to be equal to the HMVF, such that all pore space is occupied by UO_2.
4. The initial HMVF is kept constant, along with the mass of water comprising the original WVF, as the VVF is varied in increments of 0.15 vol%
5. For each VVF, the new uranium mass is determined along with the total spherical volume required to meet the fixed HMVF
6. An interpolation is found that matches the VVF and HMVF of the iteration, or else slightly exceeds either of those values. The interpolation is applied to the mass of uranium to calculate k_{eff}.
7. k_{eff} is evaluated in this manner until the VVF reaches 36 vol%

The results of this analysis are shown in figure 4.4.7 for two different enrichments. As one progresses from left to right on the chart, the total amount of saturated void available to

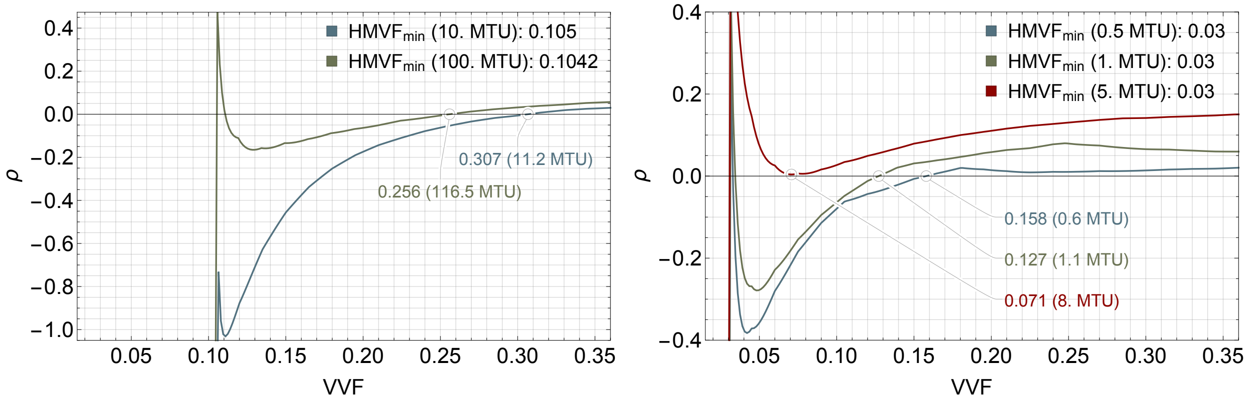

(a) Homogenous, 2 wt% (b) Homogeneous, 6 wt%

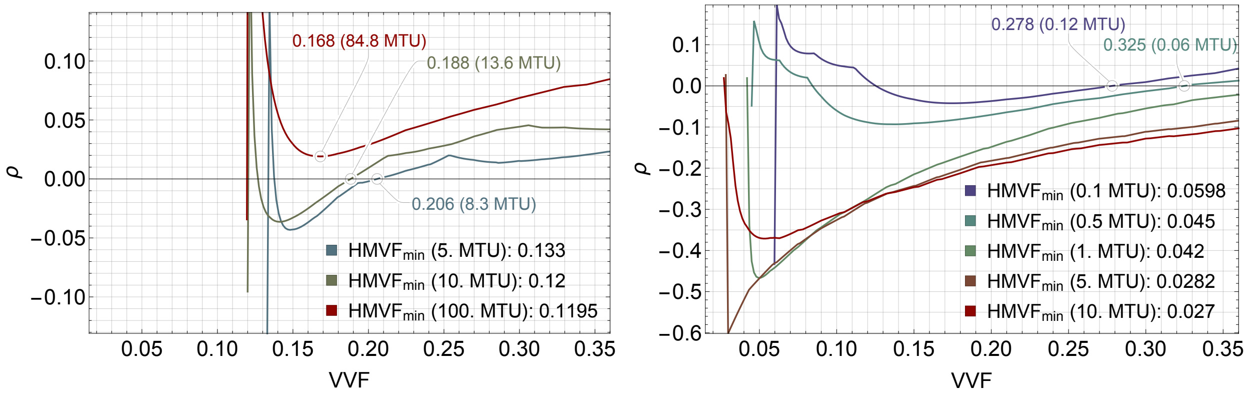

(c) Fractured, 2 wt% (d) Fractured, 6 wt%

Figure 4.4.7: The effect of increasing the void space for a fixed HMVF and mass of moderator for systems that can reach $k_{eff} = 1.02$.

the heavy metal precipitate increases. All curves indicate that at some VVF, the deposition reaches an extreme of overmoderation, where the system either becomes most subcritical or reaches a minimal reactivity. This point of extreme overmoderation often occurs immediately after the VVF exceeds the initial value of HMVF (the sharp vertical lines in the plot). The point of overmoderation is more gradually approached for lower masses, as shown in figure 4.4.7d. This is observable mostly a result of the interpolation fineness employed in the approach.

The masses of heavy metal at which the precipitate ceases to become to overmoderated are indicated in the labels. At these points, enough fuel exists to counteract the larger volume of water in a repeating unit. For some tests, such as masses 1-10 MTU in figure 4.4.7d, this point is never reached within the parameter space, indicating persistent overmoderation. In some instances, such as 5 MTU in figure 4.4.7b and 100 MTU in figure 4.4.7c, the heavy metal is never overmoderated to the point of reaching subcriticality.

4.4.4 Reactivity feedback effect of enriched repository plume

The source term of the dynamics analysis will be the arrival of the uranium plume from the repository. This will also serve as the persistent positive feedback mechanism, since the minimum critical configurations are undermoderated (see figure 4.4.6). As the plume arrives to the precipitate location, it displaces water in the pore space. The reactivity imparted from this enriched material can be modeled in order to determine feedback coefficients. For simplicity, U-235 is considered the only fissile nuclide of the critical mass, which is defensible given the quantities observed in chapter 4. The procedure is described as follows:

1. For every VVF and HMVF in the parameter space, interpolations of k_{eff} are made for each calculated mass based on 0.1725 vol% increments. This provide 200 sampling points for both coordinates.
2. An optimal configuration of VVF and HMVF is selected for $k_{eff} = 1.02$ for a certain mass, which provides information on the total volume of the initial critical mass.
3. The HMVF is reset to 1.5 vol%, and the total mass of uranium is determined based on the fixed volume.
4. An interpolation is found meeting the fixed VVF and test HMVF value, if not slightly exceeding those values.
5. The interpolation is applied to the uranium mass to calculate k_{eff}.
6. The HMVF is incremented by 0.345%, and the calculations continue until $HMVF = VVF$.

The effect on reactivity of varying heavy metal content for configurations capable of reaching $k_{eff} = 1.02$ is shown in figure 4.4.8. When displacing water in the critical sphere by adding more enriched uranium, reactivity increases for only a brief period before undermoderation causes ρ to drop below zero. In general, this drop in reactivity is more rapid with larger critical masses, and for a given enrichment and mass, lower degrees of sub-criticality are reached for the homogeneous geometry. These observations suggest that the positive feedback effect of the uranium plume will be limited over time. the As would be suspected, decreasing heavy metal content from the configuration at $\rho = 0$ (e.g. through oxidation or an erosion process) results in a sharper drop in reactivity.

The choice of α_{25} for n_{25} in equation (8.2.13) in chapter 8 will based on the associated change in U-235 content (in moles) from the uranium plume for a given change in HMVF. Examples of such curves are shown in figure 4.4.9 for the 2 wt% precipitate. These ρ versus Δmol curves are fitted with an even-ordered polynomial, such that the derivative, $\frac{\partial \rho}{\partial m_{25}}$, decreases monotonically. The point where this feedback coefficient becomes negative is unique for each case. The polynomial fits are included in section §F.1.

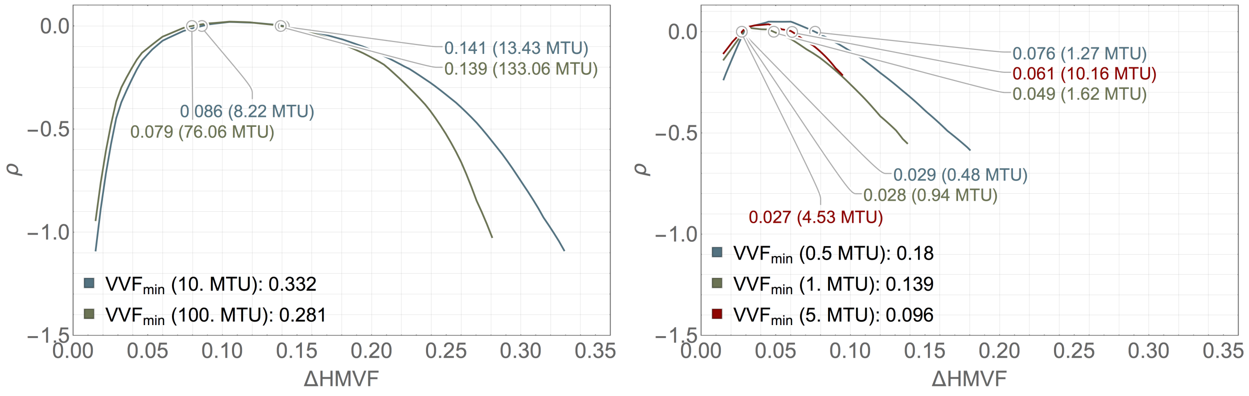

(a) Homogeneous, 2 wt%

(b) Homogeneous, 6 wt%

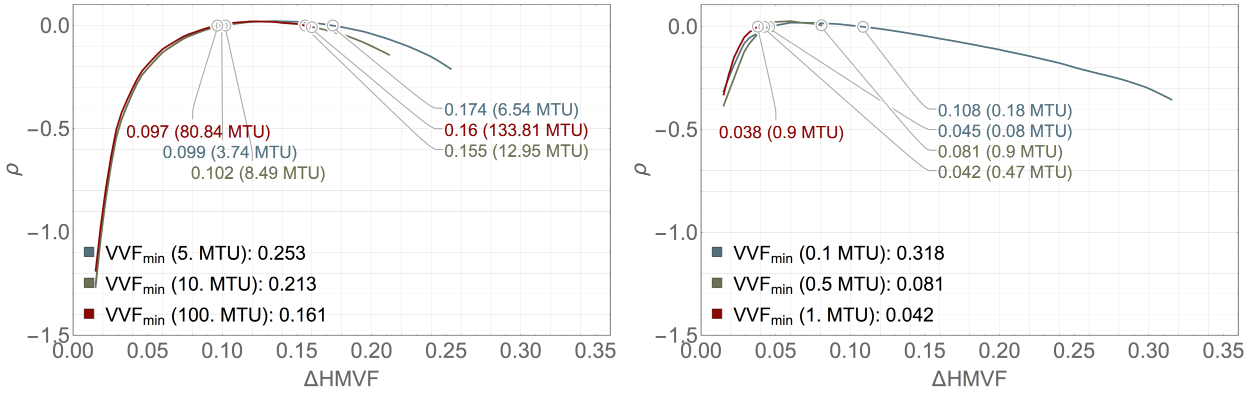

(c) Fractured, 2 wt%

(d) Fractured, 6 wt%

Figure 4.4.8: The effect of displacing water with uranium metal in the void space for two different enrichments, expressed in terms of the change in heavy metal volume.

4.4.5 Reactivity feedback effect of a U-238-dominated plume

In chapter 3, it was observed that at some point in the time, the plume of actinides arriving at the precipitate location eventually becomes dominated by U-238, which is the majority radionuclide comprising each waste package. This dilution leads to a steadying of the enrichment level at long periods of time.

Given that the representative precipitates span multiple enrichments, two-dimensional interpolations of the parametric criticality data can be used to probe the effects of decreasing the fissile content of the system. By incrementally increasing the volume of $^{238}UO_2$ in the void space, anticipated poisonous reactivity feedback effects can be observed.

The procedure for evaluating this phenomenon is described as follows:

1. An initial precipitate enrichment and mass is specified for dilution by U-238.

2. Two-dimensional interpolations of k_{eff} data are made for the parameter space of VVF

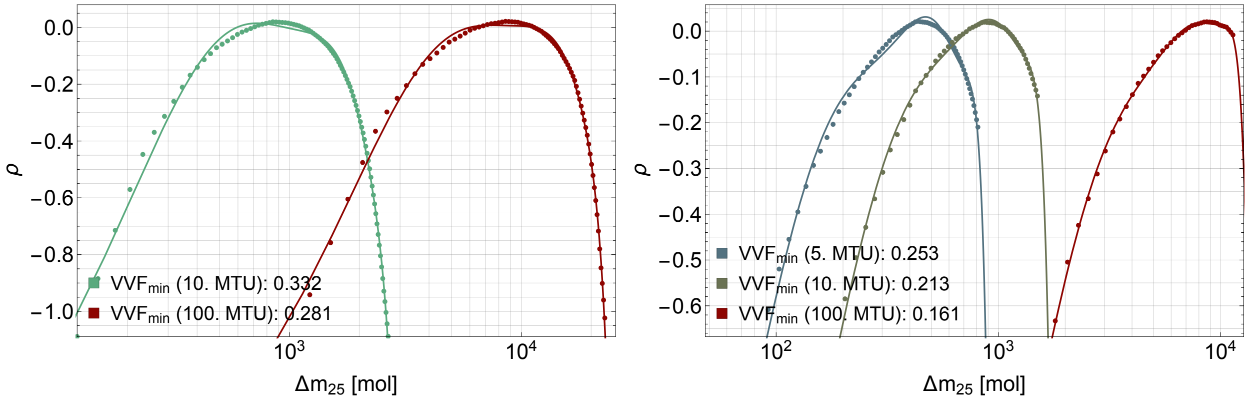

(a) Homogeneous, 2 wt%

(b) Fractured, 2 wt%

Figure 4.4.9: The effect of displacing water with uranium metal in the void space expressed in terms of U-235 addition (within UO_2 of the indicated enrichment) and shown with polynomial regression curves.

and HMVF for all precipitates evaluated at the specified mass for 0.1 vol% increments between 1.5 and 36 vol%.

3. A maximum void space of 36 vol% is specified, with an initial HMVF of 1.5 vol%.

4. The HMVF is increased by an increment of 0.1 vol%, which corresponds to a volumetric increase in $^{238}UO_2$ mixed evenly and instantaneously with the original heavy metal. The added uranium displaces water from the pore space.

5. The enrichment is modified by the increase in the U-238, where the initial mass fissile material is held constant.

6. An interpolation is found that either matches the fixed VVF and new HMVF or is based on values that are slightly greater. This is applied to the new enrichment to find k_{eff}.

7. The HMVF continues to be incremented until HMVF=VVF or when enrichment reaches the interpolation limit of 1.5 wt%.

The results for water displacement via $^{238}UO_2$ addition are shown in figure 4.4.10 for both configurations. For either configuration, the addition of pure $^{238}UO_2$ consistently reduces reactivity via increasing the probability of non-fission absorptions in the fuel. The reactivity curves are monotonically decreasing, leading to a feedback coefficient $\left(\frac{\partial \rho}{\partial m_{28}}\right)$ that is consistently negative. These coefficients range between $-6.6 * 10^{-11}\, mol^{-1}$ and $-4.0 * 10^{-11}\, mol^{-1}$, where dilutions beginning at a lower precipitate enrichment have more negative values.

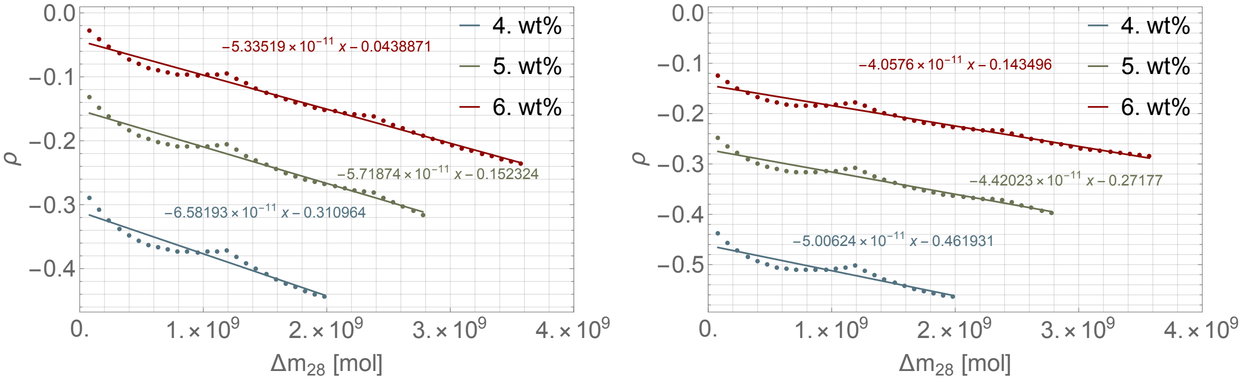

(a) Homogeneous (b) Fractured

Figure 4.4.10: The effect of diluting precipitates of specified enrichments to 1.5 wt% expressed in terms of the U-238 addition (within pure $^{238}UO_2$). Linear regression curves are shown, indicating feedback coefficients between $-5.7 * 10^{-11}$ and $-1 * 10^{-10}$ reactivity per mole U-238.

4.4.6 Thermal expansion

A hypothesized means of shutting down chain reactions is the expansion of the precipitate with heating. That is, the overall reduction in atom density could possibly bring the system to a subcritical state. A calculation was devised to investigate the reactivity effects of thermal expansion where homogeneous critical volumes were steadily incremented by way of their radii while maintaining a constant total mass of UO_2. This was achieved by changing the densities and surfaces in the MCNP input deck. The thicknesses of the shale and granite layers were fixed, and the pore space was maintained at full saturation. The calculation proceeds as follows:

1. For critical configuration, determine the average precipitate density using the composition script.
2. Set a maximal expanded radius equal to a maximum of ≈ 20% of the original critical radius.
3. Discretize this expanded region into 25 segments.
4. For each discretization, using the critical mass, determine the appropriate density based on the change in volume.
5. Determine k_{eff} for each discretized change in volume.

Results from the study are shown in figure 4.4.11a for the 2 wt% precipitate, where the change in reactivity with fractional increase in radius is more pronounced for 5 MTU than 100 MTU. For the 5 MTU critical mass, the reactivity drop from a 20% increase in the

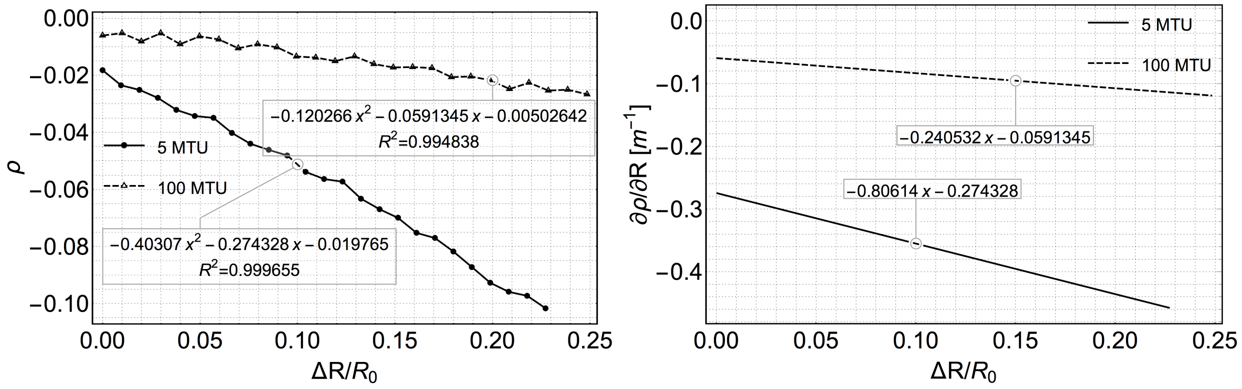

(a) Reactivity, shown with quadratic fit equations. (b) Feedback coefficient based on quadratic fits.

Figure 4.4.11: Effect of expansion on 2 wt% homogeneous configuration in terms of relative change in radius, shown for two different critical masses.

radius of the sphere is about the same as removing about 40% of water from the pore space in the original sphere, as implied in figure 4.4.6. Quartz, the main component of sandstone, has a linear expansion coefficient of $\sim 10^{-6\circ}C^{-1}$. Therefore, with heat emission from the critical mass, it is reasonable to suspect de-saturation will be more liable to shut down chain reactions before thermal expansion. This can simplify the dynamics analysis by removing $\frac{\partial \rho}{\partial R}$ considerations and prioritizing a feedback coefficient based on coupled temperature and saturation effects.

4.4.7 Neutron thermalization and the prompt removal lifetime

The infinite multiplication factor (k_∞) describes the generation of neutrons from one generation to the next in the absence of leakage effects, and is defined in terms of the reproduction factor η, the thermal utilization factor f, the fast fission factor ϵ, and the resonance escape probability p:

$$k_\infty = \eta \epsilon f p \tag{4.4.1}$$

The effective multiplication factor can be determined using the neutron non-leakage probability P_{NL}:

$$k_{eff} = k_\infty P_{NL} \tag{4.4.2}$$

To elaborate, f is defined as the ratio of thermal neutrons absorbed in the fuel relative to total absorptions in the fuel and moderator. This quantity is expected to be larger for the homogeneous system rather than the heterogeneous, since the thermal flux is suppressed in the fuel slab as a result of spatial self-shielding. p describes the probability of neutrons escaping resonance capture as they are moderated, and is it is a quantity obtained through simulation or any of various computational procedures. As a result of self-shielding, p is higher for the heterogeneous system because less neutrons are captured in resonances on the interior of the slab, which counteracts the lower f. ϵ describes the total number of neutrons emitted from fission in general to the number emitted from fission specifically at thermal energies. This value is anticipated to increase as the HMVF grows larger than the WVF. It is also expected to be higher for the fractured layout since there are more opportunities for neutrons to interact with the fuel while still above the fission energy threshold.

The reproduction term, η, is defined as:

$$\eta = \bar{\nu} \cdot \frac{\text{neutron absorptions resulting in fission}}{\text{thermal neutron absorptions in the fuel}} \tag{4.4.3}$$

where $\bar{\nu}$ is the number of fast neutrons produced per fission induced by thermal neutron absorption. Therefore, the total number of fission neutrons produced per absorption can be described as $\eta\epsilon$. The terms in the fraction are dependent on macroscopic cross sections for the fuel in the thermal energy group.

Values of k_{eff} are plotted in figure 4.4.12 for the 2 and 6 wt% precipitates. The ability for the homogeneous geometry to reach criticality is far more limited than the heterogeneous, which corresponds to behavior in figure 4.4.3. For the highly-enriched precipitate in the fractured geometry, critical configurations encompass much of the whole parameter space of VVF and HMVF. The behavior observed in previous sections regarding heavy metal filling the entire void space is confirmed in this plot, where a region between 3 and 20 vol% corresponds to criticality. Overall, these results would classify a deposition with this enrichment as a worst-case scenario meant to incorporate precipitates with as small critical radii as possible. For the homogeneous 6 wt% deposition, criticality cannot be obtained on the $HMVF = VVF$ line, but the criticality space is still larger than that of the 2 wt% fractured deposition.

It is clear that within the parameter space of VVF and HMVF, the homogeneous system is more sensitive to undermoderation given the spacings between contours for a given VVF above the maximal k_{eff} value. In the fractured geometry, there is less sensitivity to filling the void space with more precipitate because the moderating properties of the rock laminate are still appreciable.

η is directly calculated in MCNP, and contour plots are shown in figure 4.4.13. The $k_{eff} = 1$ contour from figure 4.4.12 is superposed on the plots to illuminate the parameter space of critical configurations. Given the effectiveness of the shale reflector, there is good agreement with the $\eta = 1$ contour for the highly enriched precipitate, and overall, there is strong similarity between η and k_{eff} results. For a given enrichment, VVF, and HMVF, the fractured geometry has more fission neutrons produced than neutrons absorbed. This is due to the reduced resonance absorptions in the heterogeneous configuration. As enrichment increases, the range of HMVF corresponding to a certain level of η becomes more confined per given VVF, and this tendency is much stronger with the homogeneous geometry. Given maximal values of η in the plots, the breeding potential of Pu-239 appears limited.

The percentage of neutrons in the thermal range causing fission in the thermal range is plotted in figure 4.4.14, while a similar plot of the average neutron energy resulting in fission is shown in figure 4.4.15. For the low-enriched precipitates, it is apparent that regions with $k_{eff} \geq 1$ correspond to those where at least 70% of neutrons causing fission are in the thermal range. For the higher-enriched precipitates, the roles of fast and high energy neutrons are more prominent, especially for higher HMVF/VVF combinations. In either case, the average neutron energy causing fission will likely fall between 0.025 eV and 300 keV depending on the HMVF. Decreasing the HMVF has a consistent thermalization effect.

For values of HMVF close to the VVF (where metal fills all or a majority of the pore space), spectrum hardening is observably stronger in the homogeneous geometry compared to the heterogeneous due to the lack of separation between the fuel and moderating components. The prominence of heavy metal in the sphere allows more prompt neutrons to interact with fuel and increase the frequency of fast fission. This behavior is supported by the sharper decreases in the contours of η and $\bar{E}_n$ in that region.

To further characterize spectrum hardening, the prompt removal lifetime (l_p) can indicate the time scale for prompt neutrons to be absorbed. It is defined as:

$$l_p = \frac{\text{prompt neutron population from fission}}{\text{rate of neutron loss to absorption}} = \frac{\lambda_a(E)}{\bar{v}(E)} = \frac{1}{\bar{v}(E)\Sigma_a(E)} \tag{4.4.4}$$

where $\bar{v}$ is the average neutron speed. In figure 4.4.16, the prompt lifetime is much more consistent per given HMVF over the span of VVF in the fractured case. In the homogeneous geometry, increasing the amount of void space relative to metal extends the neutron lifetime much more considerably by increasing the atom density of water. Here, when metal occupies most of the void space, there are not enough collisions with moderating material to extend the neutron lifetime before absorption, which is why the spectrum is harder in these configurations. In general, as the HMVF increases, it takes less time for neutrons to be absorbed somewhere in the reactor.

For considerations of high energy release events, the value of l_p would likely have to be minimized. Conditions more favorable to criticality correspond to decreases in l_p, and the decrease is stronger for the fractured geometry. In a supercritical system, where $k_{eff} > 1$, the fission power output is expected to rise according to a time constant α: [11, 12]

$$P = P_0 e^{\alpha t} \tag{4.4.5}$$

This time constant can be expressed in terms of the effective multiplication and the prompt removal lifetime:

$$\alpha = \frac{k_{eff} - 1}{l_p} \tag{4.4.6}$$

This constant will be positive until negative feedback mechanisms force it to become negative. From figure 4.4.16, it appears that minimal values of l_p for supercritical configurations of VVF and HMVF are around 50 μs. For a supercritical k_{eff} of 1.30, $\frac{P}{P_0}$ can increase by a factor of e in a about 0.15 milliseconds. The material properties of the precipitate would determine whether or not this energy output would pose shock effects, and the lithostatic pressure and compressive strength of the host rock would ultimately determine the pressure buildup from the energy release. If α is not brought below 0, autocatalytic criticality is thought to lead to explosive releases of energy.

This study considers long-term criticality, such as that sustained by a light water reactor with online refueling. Rather than analyze an autocatalytic means of introducing a biosphere exposure pathway, the goal is to identify long-term wear on the natural barriers rather than an explosive burst. Using the logic of equation (4.4.5), if a just-critical configuration is maintained, fission energy can be released steadily to surrounding rock, and the Doppler effect can be analyzed in a heat transfer context as opposed to an exponential relationship. Given the extremely long time scales needed for an appreciable flux of TFM (see figure 3.4.7a), and the low-enriched nature of this plume in the direct disposal context, a just-critical assumption is reasonable. Supercritical configurations would either require external mechanisms for expanding the void space perhaps through seismic fracturing and immediate groundwater flooding, or perhaps a selective washing of absorptive species from the rock. This consideration would be especially important in a study implementing fracture mechanics in the rock failure metric.

4.4.8 Benchmarking

The MCNP results of this study were benchmarked with Los Alamos data on critical dimensions for water-reflected hydrogen-moderated systems containing U-235. [68, pg 37] While the systems considered in this chapter are shale-reflected, where only 10% of the reflector volume is water, the LANL data can provide reasonable lower bounds on U-235 mass given that water is a more effective moderator. Hydrogen-to-fuel ratios from tables 4.4.1 and 4.4.2 are juxtaposed with the homogeneous hydrogen-moderated uranium-bearing mixtures in figure 4.4.17. There is good agreement between the fractured configuration data for the enrichment levels of 2, 3, and 5 wt%, while this is not necessarily the case for the homogeneous configuration. This may be due to the presence of continuous water volumes adjoining the UO_2 slabs in the fractured configuration, while water is interspersed evenly in the homogeneous configuration. This would allow for the reflective aspects of H_2O to be emphasized in the fractured geometry.

4.5 Discussion

This chapter has described a static neutronics analysis that has provided the scope of criticality for the precipitate compositions calculated from the transport analysis. Fundamental reactivity behavior has been demonstrated for two main configurations of fuel, rock, and water encapsulated in a shale trap. A parametrization was employed based on the volume of saturated void and heavy metal, and within this space of coordinates, attaining a critical

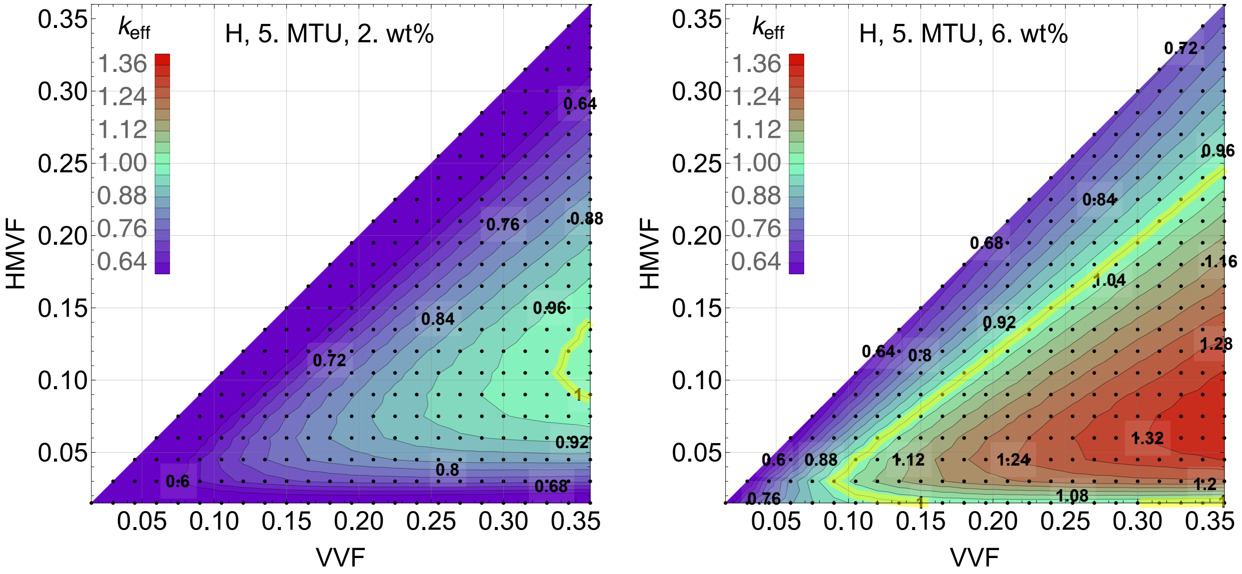

(a) Homogeneous, 2 wt%

(b) Homogeneous, 6 wt%

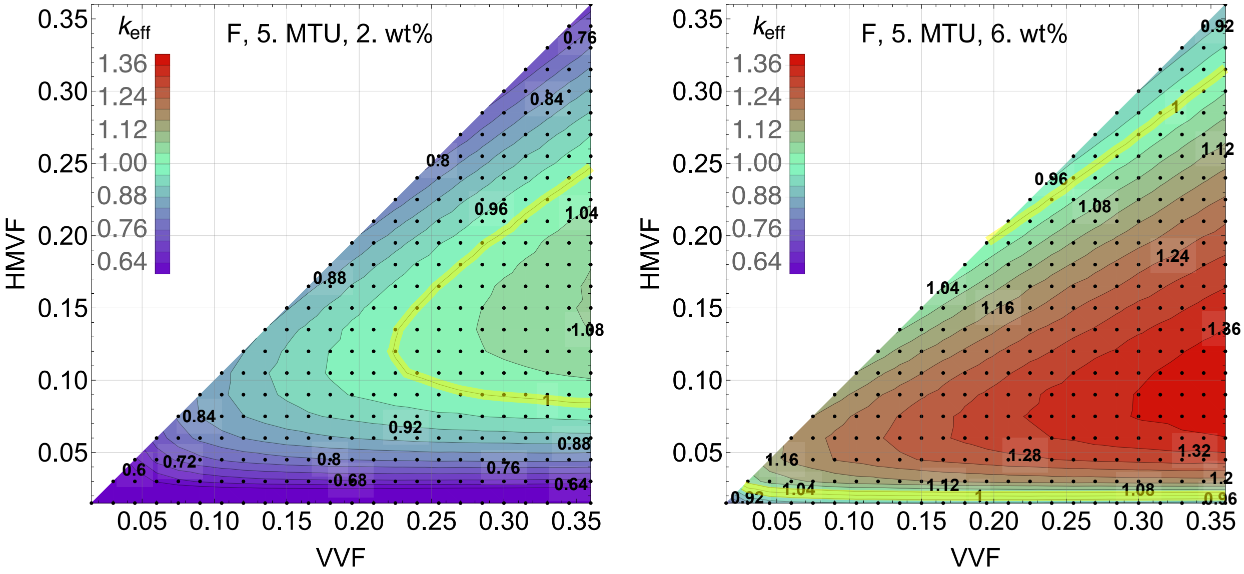

(c) Fractured, 2 wt%

(d) Fractured, 6 wt%

Figure 4.4.12: The effective multiplication factor for the 5 MTU precipitates, where a contour indicating $k_{eff} = 1$ is drawn in yellow.

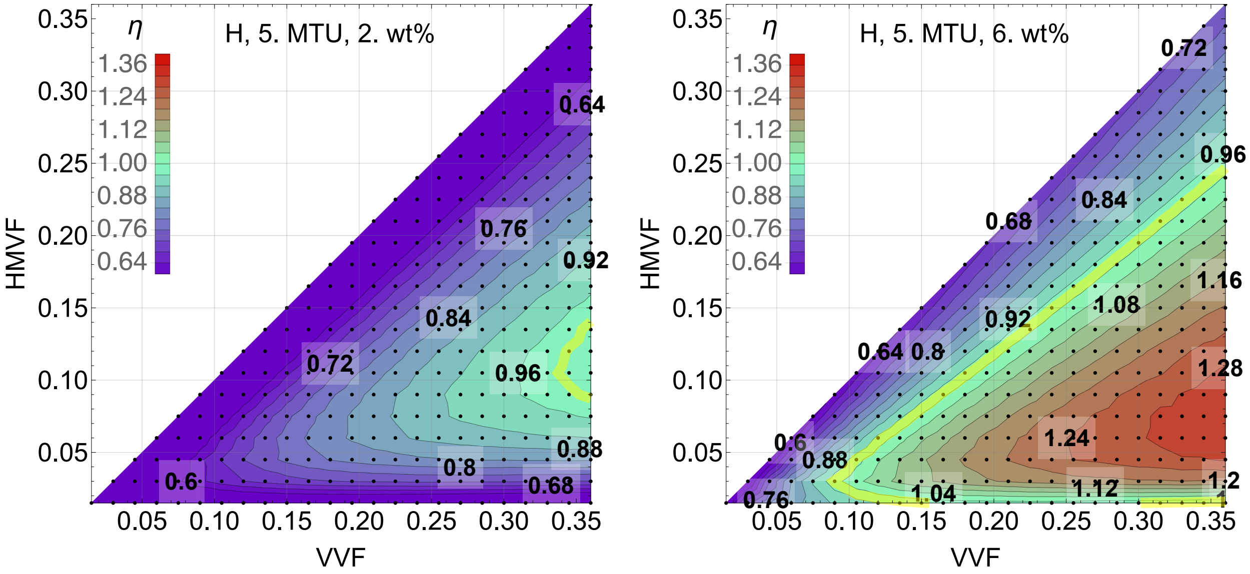

(a) Homogeneous, 2 wt%

(b) Homogeneous, 6 wt%

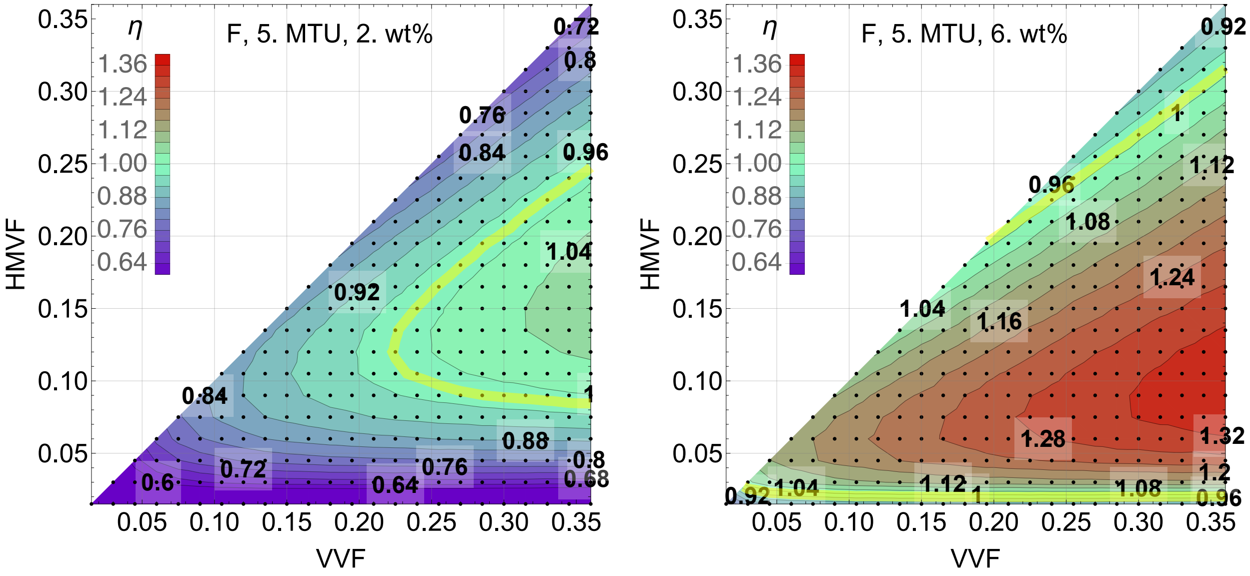

(c) Fractured, 2 wt%

(d) Fractured, 6 wt%

Figure 4.4.13: The factor η for all cells in the 5 MTU precipitates, where a contour indicating $k_{eff} = 1$ is drawn in yellow.

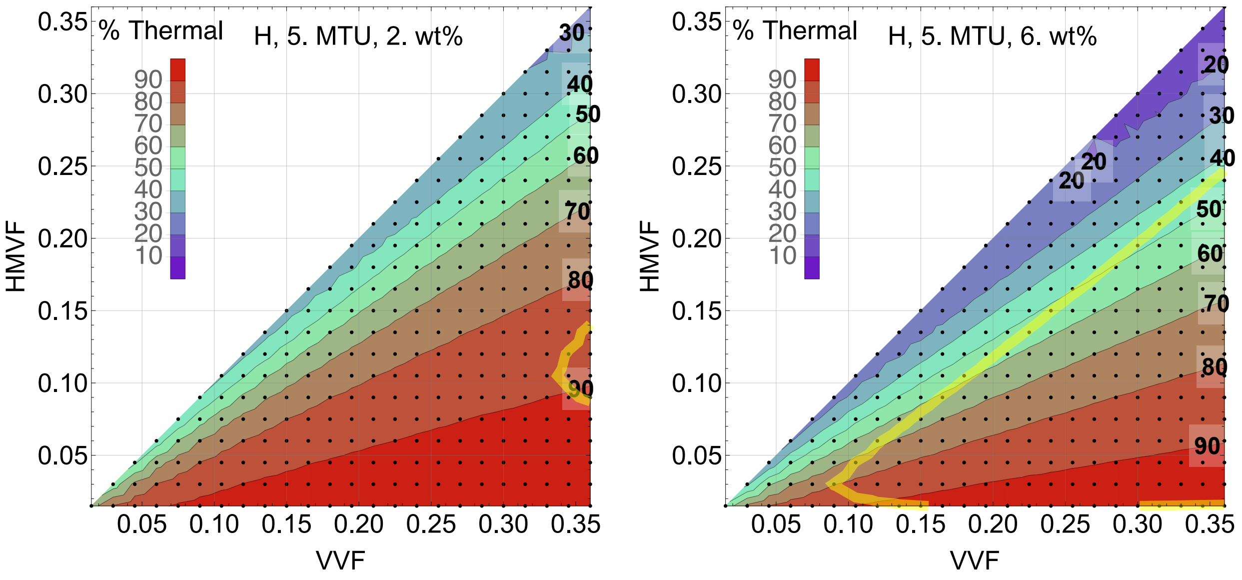

(a) Homogeneous, 2 wt%

(b) Homogeneous, 6 wt%

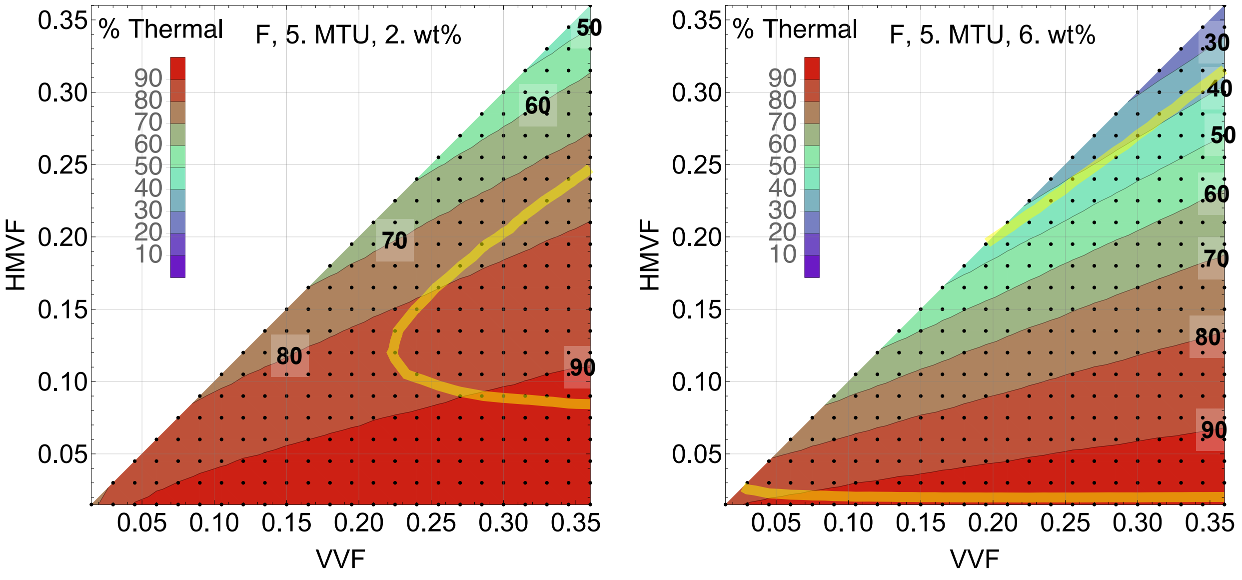

(c) Fractured, 2 wt%

(d) Fractured, 6 wt%

Figure 4.4.14: The percentage of neutrons causing fission in the thermal range ($< 0.625\,eV$) for the 5 MTU precipitates, where a contour indicating $k_{eff} = 1$ is drawn in yellow.

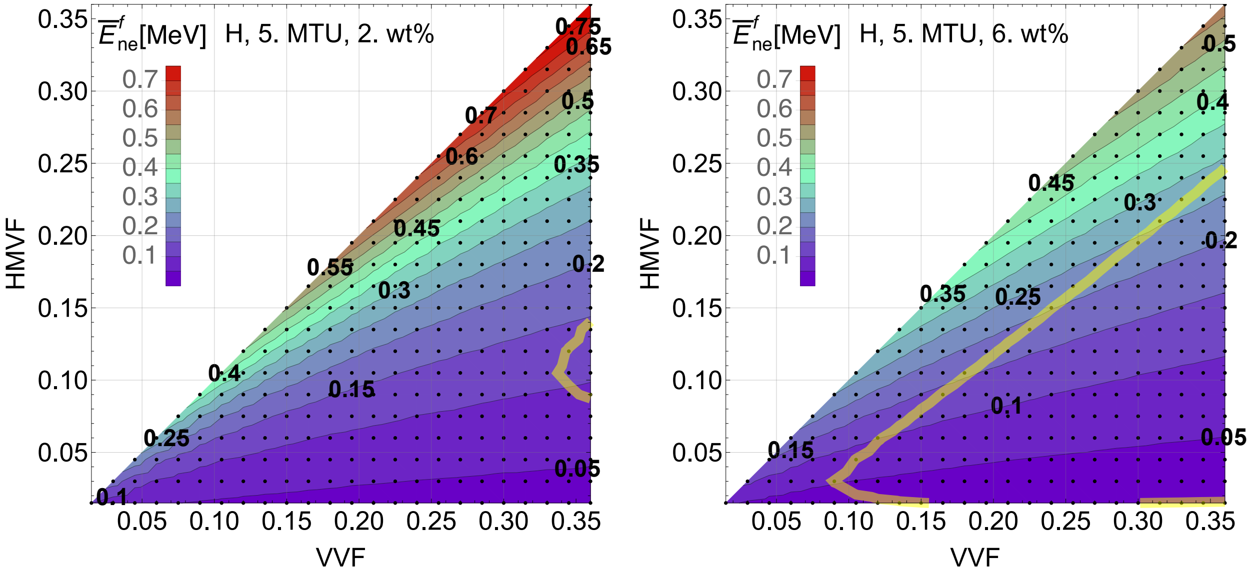

(a) Homogeneous, 2 wt%

(b) Homogeneous, 6 wt%

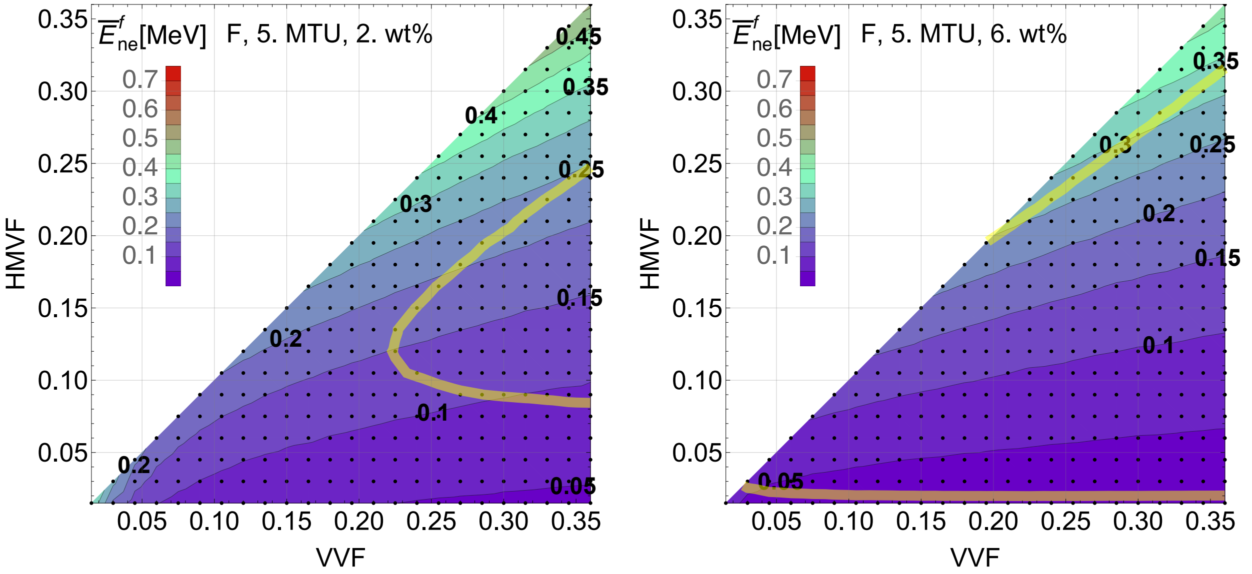

(c) Fractured, 2 wt%

(d) Fractured, 6 wt%

Figure 4.4.15: The average neutron energy $\bar{E}_n$ in MeV for the 5 MTU precipitates, where a contour indicating $k_{eff} = 1$ is drawn in yellow.

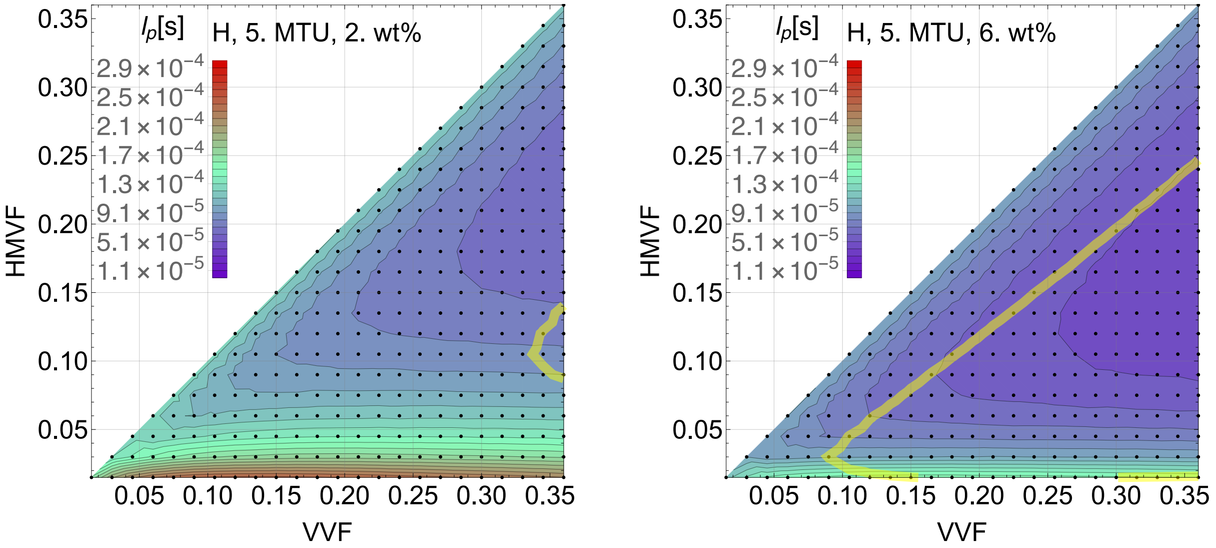

(a) Homogeneous, 2 wt%

(b) Homogeneous, 6 wt%

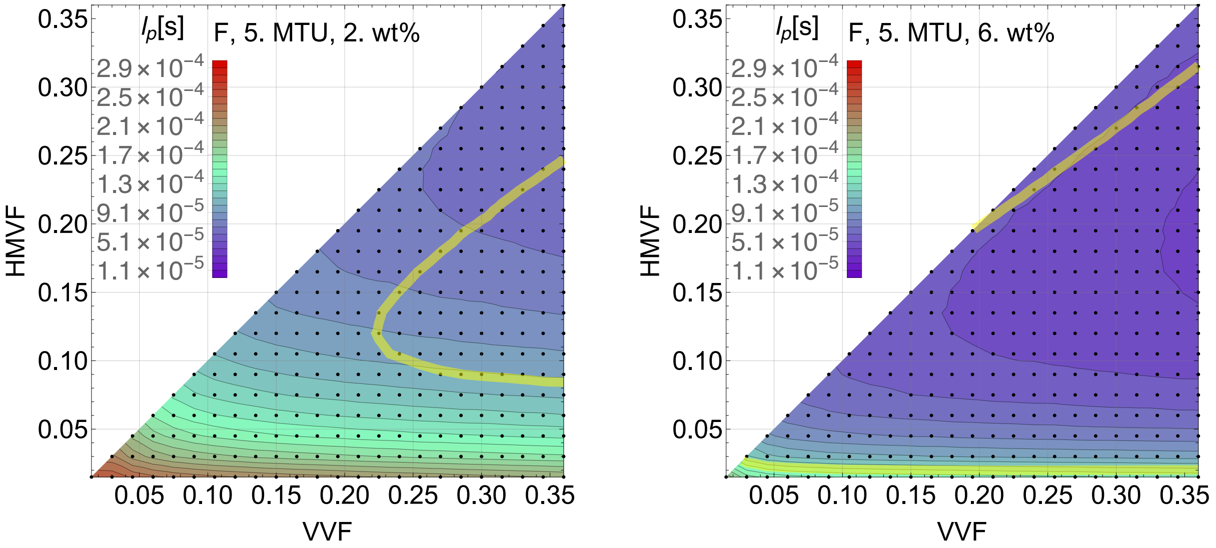

(c) Fractured, 2 wt%

(d) Fractured, 6 wt%

Figure 4.4.16: The prompt removal lifetime l_p in seconds for 5 MTU precipitates, where a contour indicating $k_{eff} = 1$ is drawn in yellow.

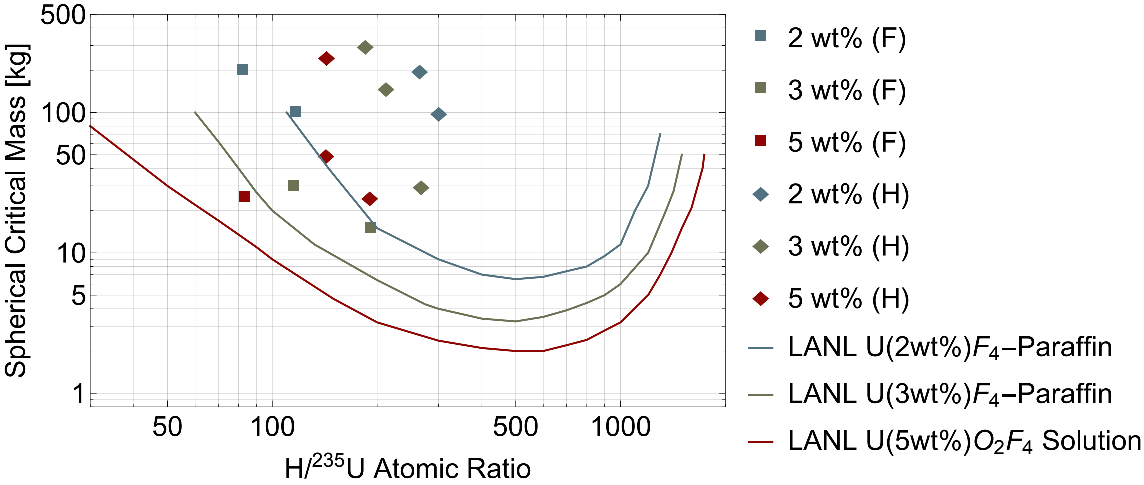

Figure 4.4.17: Comparison of homogeneous (H) and fractured (F) $k_{eff}^{min} = 1$ results with extrapolated Los Alamos criticality data on hydrogen-moderated water-reflected U-235 systems of uranyl fluoride solution or uranium hexafluoride in paraffin wax (C_nH_{2n+2}).

mass from the steady-state enrichment level expected in the precipitate was found to not be feasible. However, the more-enriched compositions corresponding to times before the steady state level exhibit a variety of configurations that reach criticality, with minimum masses fitting the scope of total mass observed in the transport analysis. Results from the two extreme enrichments of two and six weight percent were highlighted to provide an idea on the spread of possible configurations.

Through interpolations of effective multiplication results, limits have been established on the role of the incoming plume of uranium in sustaining criticality. An enriched plume from dissolved UNF in the repository will have limited positive feedback contributions, since at some point, the void space will become undermoderated. This leads to a monotonically decreasing feedback coefficient that can eventually lead the system to subcriticality, depending on the relative addition of U-235. If U-238 dominates the uranium composition, then reactivity contributions are consistently negative, and the feedback coefficient can be modeled as a negative constant.

The moderator defect was analyzed at room temperature to highlight the role of the porewater on sustaining criticality. All minimum critical configurations were observed to be undermoderated, such that decreasing the water saturation from unity to zero results in decreased reactivity. The reactivity drops are more significant for homogeneous configurations and less-enriched precipitates. Prior to an analysis of the Doppler effect on a heat-emitting critical mass, it is necessary to model spatial distributions of the fission power, as such distributions would affect the saturation profile and specific reactivity behavior.

Reactivity changes from de-saturation are expected to dominate those imparted by thermal expansion, since the radial deformation needed for similar drops in reactivity is large and indicative of containment failure. The latter phenomenon can be analyzed external from the dynamics analysis and be used in the performance metric instead. A gradual material failure metric is proposed as opposed to autocatalytic mechanisms of explosively destroying the surrounding host rock. This is suggested since supercritical configurations require increasingly unrealistic volumes of void, and that positive feedback from low-enriched uranium in the direct disposal context is rather limited.

Chapter 5

Depletion analysis

5.1 Overview

From the criticality scoping analysis of chapter 4, representative far-field precipitates were found to correspond to a range of critical radii (see tables 4.4.1 and 4.4.2). These dimensions are commensurate with those of the original canisters (table 3.3.1), which would exclude a point-like treatment of heat and mass transfer from the precipitate prior to a detailed neutronics study. A proper hydrological treatment of these processes requires considerations of the spatial dependence of heat generation, which is liable to be affected by the source term from fission. In order to properly identify the spatial distribution of fission power over time in a critical mass, it is necessary to understand the interplay between the fissile nuclide inventory and neutron-driven transmutation probabilities over time. These reactions are key to understanding the generation of long-lived radioactive fission products (FPs), which serve as the main carriers of dose to the biosphere.

This chapter discusses the evaluation of the nuclide inventory and fission power distribution using an analysis based on the coupling of neutron transport and point depletion for a critical precipitate. Geological time scales will be acknowledged to understand long-term behavior of the nuclide inventory amidst sustained chain reactions. While a proper dose risk assessment is beyond the scope of this study, this information in turn can provide insight on the relative risk of biosphere exposure if fission products are vented from the critical system.

5.2 Background and methodology

5.2.1 Overview

The CINDER depletion module of MCNP is employed for the depletion analysis. This code models each transmutation pathway of significance to the nuclide inventory as Markov chains based on the point depletion equations (5.2.1). [88] For $i = 1, ..., N$ isotopes in the transmutation chain contributing significantly to nuclide densities, the general equation for depletion in terms of the amount n of nuclide i over time is as follows:

$$\dot{n}_i = \dot{S}_i - \lambda_i n_i + \sum_{j \in \hat{i}} \lambda_j n_j + \phi \left(\sum_{j \in \tilde{i}} \sigma_{c,j} n_j + \sum_{j \in \bar{i}} \gamma_{j \to i} \sigma_{f,j} n_j - \sigma_{c,i} n_i - \sigma_{f,i} n_i \right) \tag{5.2.1}$$

where $\hat{i}$ is the set of nuclides that produce nuclide i upon decay, $\tilde{i}$ is the set of nuclides that produce nuclide i upon neutron capture, and $\bar{i}$ the set of fissile nuclides that produce nuclide i upon fission with specific yield $\gamma_{j \to i}$. With regards to other terms, ϕ is a spatially-independent flux, λ is a decay constant, σ is a microscopic cross section for capture (c) or fission (f), and $\dot{S}$ is the source term (which is zero in this analysis). The cross sections are available in a flux-weighted 63 neutron energy group library structure encompassing $10^{-8}\, eV$ to $20\, MeV$. They are considered to be constant and homogeneous for the time step of the calculation.

The overall analysis employs a predictor-corrector approach to determining the nuclide inventory. MCNP calculates fluxes for the 63 neutron energy groups, energy-integrated reaction rates, system-averaged $\bar{\nu}$, and of course the system eigenvalues. [80] Assuming these fluxes and reaction rates remain constant, CINDER calculates isotope densities up to the next half time step as part of the "predictor" step. These densities then allow for steady-state fluxes and collision densities to be determined for the full time steps. Depletion is then run from the initial state with the full time step reaction parameters as part of the "corrector" step.

5.2.2 Power output

The power of a reactor is proportional to the magnitude of the neutron flux, and over time, the flux shape settles to the fundamental node of the Helmholtz equation. The flux profile for a reflected geometry will be different than that of a bare reactor, since the non-multiplying component is employed to reduce neutron leakage. The reflector also tends to flatten the thermal flux profile across the reactor, where the thermal energy group peaks in the reflector region due to the moderation of fast neutrons exiting the surface. The fast flux is highest at the center of the core and decreases outwardly.

For a uniform, bare spherical geometry, the steady-state critical flux profiles can be described as a function of the radius: [22]

$$\phi(r) = A \cdot r^{-1} \sin\left(\frac{\pi r}{\tilde{r}_0}\right)$$

where $\tilde{r}_0$ is the extrapolated diffusion length and A is a proportionality constant based on the operating power level. When a reflector is added to the bare sphere, the continuity of flux and current is applied to the interface when solving the neutron diffusion equation for both media. The reflector can be modeled as very large or interfacing with a vacuum. Either way, when the general solutions are found for either material, the interface boundaries are applied to determine the criticality conditions. These involve an optimization based on the material buckling of the core, diffusion coefficients, diffusion length, and system dimensions, and solutions employing the reflector thickness are shown in Table 3.5 of Ref [89]. The end result is a reduction in the critical radius referred to as a "reflector savings."

Since the flux is dependent on the nuclide density, depletion codes require a special treatment of the neutron flux and power output as part of addressing this inherent nonlinearity of the system of equations. In the zero-order approach of CINDER, it is actually assumed that the flux is not spatially dependent, and the total flux can be calculated by: [88]

$$\phi = \frac{\mathcal{C} \cdot P}{\sum_{j \in TFM} n_j \sigma_j^f E_{f,j}} \tag{5.2.2}$$

where P is the specified system power, n_j is the concentration of fissile nuclide j, σ_j^f is the microscopic fission cross section, $E_{f,j}$ is the useable energy per fission (i.e. no energy contributions from antineutrinos), and $\mathcal{C} = 6.241 * 10^{18} \frac{eV}{J}$. When CINDER is directly coupled with MCNP, the group fluxes need to be modified with multipliers (M) since the calculated collision densities are normalized per source neutron. The total flux passed to depletion is obtained as:

$$\phi_{total} = \phi_{MCNP} M = \phi_{MCNP} \frac{P\bar{\nu}}{k_{eff} Q} \tag{5.2.3}$$

where the Q value is based on the usable energy per prompt fission event $\left(\bar{E}_f\right)$ and a multiplier meant to account for the energy contributions from delayed fission events and gammas released from neutron capture. An underestimate of Q leads to an overestimate of flux, which leads to an overestimate of reactions rates and burnup.

In this study, total thermal power outputs of 0.1 and 1 kW_t were employed to probe general behavior of the fission product distributions. Each time step was specified to cover the full level of power output, as the effects of changing power output would more appropriately analyzed in a dynamics analysis.

Given that critical configurations for low-enriched precipitates can be expected as low as 5 MTU, and limited by transport to approximately 100 MTU, the thermal output specifications would cover a range of specific powers from 1 $\frac{W_t}{MTU}$ up to 200 $\frac{W_t}{MTU}$. The power outputs calculated from the inverse model of Oklo reactor zone 9 in Ref. [29] range from 0.01 to 0.23 kW_t per metric ton of sample. Assuming a maximal uranium mass concentration of 67% in the samples, this power range would correspond to 5-150 $\frac{W_t}{MTU}$. Since the general dimensions of the reactor zone are on the order of ~30 m^3, and the density of high grade ore is on the order of $\approx 9000 \frac{kg}{m^3}$, reactor zone 9 would have approximately 180 MTU. Therefore, the span of specific powers in this study should be relevant to the natural analog.

5.2.3 Computation

The critical configurations analyzed in this study were based on interpolations to $k_{eff} = 1.00$ (see chapter 4). The MCNP template file is used to create an input for this critical mass that includes 15 discrete radial regions of the sphere to capture spatial variability. For each discretization, a material index and volume is specified for each cell containing fuel, although the initial fuel composition is the same for each. Criticality source points are specified in each fuel cell to be collinear with any of the three dimensional cartesian axes. The burnup options are specified based on the volumes of materials containing fuel.

Time steps are specified incrementally from 1 to 10^8 days $(2.7 * 10^5\, yr)$ over a total of 24 full time steps. The approach assumes that the flux shape change between time steps varies linearly; [90, 91] if time steps are too large, this may prove to be invalid given the possibility of considerable flux shape changes with evolving nuclide densities. Given the number of steps relative to the vast time scale. which exceeds those considered for engineered reactors by orders of magnitude, the anticipated propagation of error is expected to be considerable. Therefore, results should be of comparative value rather than an accurate depiction of reality.

After the calculation, the TOUGH2 template input file is modified to include the power distribution in each element over the times implied by the burnup intervals (the GENER card, see chapter 6). The $k_{eff} \pm \delta$ data is gathered in the context of the predictor-corrector approach for both the half and full time steps. The burnup summary results are reaped along with the burnup results by material (the UO_2 within a radial section) over time for the masses and activities of actinides and non-actinides in MCNP Tier 2. No Q-value multipliers (i.e. above unity) are employed when determining the power output per material over time.

There are three burnup tiers that can be used in MCNP, which do not have a clear association with half-life $\left(t_{1/2}\right)$ or cumulative yield (γ_c). The Tier 1 fission products include long-lived Tc-99 $(2.13 * 10^5\, yr)$ and Zr-93 $(1.5 * 10^6\, yr)$, although only the cumulative yield of the former (6.1%) is considerable. Other isotopes include Mo-95, Ru-101, Xe-131 and 134, Cs-133 and 137, Ba-138, Pr-141, and Nd-143 and 145, whose half-lives range from 10 to 100 years. It is questionable whether these half-lives would be applicable to the temporal scope of the consequence analysis. It should be noted that Cs-137 has a high cumulative yield of 6.2% from thermal fission in U-235.

The second tier includes an expanded isotope inventory of the aforementioned elements along with krypton, yttrium, palladium, cadmium, iodine, promethium, samarium, europium, gadolinium, and others within the fission product array in the full MCNP incident neutron cross section directory. Among the especially long-lived isotopes of note include Pd-107 $(6.5 * 10^6\, yr)$, I-129 $(1.5 * 10^7\, yr)$, and Cs-135 $(2.6 * 10^6\, yr)$. High-yield isotopes include Ru-103 (3.1%), I-135 (6.4%), Nd-147 (2.2%), Pm-147 (2.2%) and 149 (1.0%), Sm-149 (1.0%), and Eu-152 (3.2%). Strontium-90, with a cumulative yield of about 5.7% from U-235 fission and a half-life of 29 years, is notably absent from this tier. This isotope is included in the third burnup tier, which is the most inclusive and employs CINDER90 yield information. While this species could be tracked manually by being placed into the fuel material inventories (i.e. with negligible initial fractions) this was not done to limit the scope of the calculation. Isotopes with atom fractions below a threshold of 10^{-10} are no longer tracked in the calculation and do not appear in the results since the transmutation chain is terminated.

5.3 Results

5.3.1 Fission power distribution

The steady-state fission power profiles ($\mathcal{F}_p$) in the critical masses conform to a truncated Gaussian distribution (equation (5.3.1)) that peaks at or just before the surface of the sphere, as shown in figures 5.3.1 and 5.3.2 for the 2 and 6 wt%-enriched homogeneous precipitates. The power peak occurs closest to the surface at early times (on the day scale) before moving inwards at steady state. This can be seen clearly for the 5 MTU, 2 wt% configuration at $1\,kW_t$ in figure 5.3.1b. Use of this fitting overestimates the power contributions of the innermost portions of the critical mass.

$$\mathcal{F}_p(f_r) = \frac{f_0}{\sigma\sqrt{2\pi}} e^{-\frac{(f_r-\mu)^2}{2\sigma^2}},\ 0 < f_r \leq 1 \tag{5.3.1}$$

This type of power distribution is expected since the fuel volumes increase with the inner/outer radii, which leads to more probable fission absorptions relative to the neutron mean free path. Fast neutrons generated at the center of the sphere are unlikely to result in fission since moderation from the pore water is outpaced by resonance absorption. Since reflected boundary conditions are applicable around the sphere, fast neutrons leaving the surface will thermalize in the reflector, and some will scatter back into the core (more likely in the outer annuli) to impart a higher rate of thermal fission absorptions. The strong role of the thermal spectrum for fission reactions in just-critical configurations (80-90%) was highlighted in figure 4.4.14 on page 87, implying that fast fission plays a smaller role in determining k_{eff} and that reflection is an important aspect of the system.

For smaller critical masses, the flux of fast neutrons passing to the shale is higher, so power peaking occurs closer to the surface due to the proportionally higher role of reflected neutrons in determining the fission reaction rate. Conversely, the larger critical masses have less leakage, and pore-water moderation is adequate enough to make the distribution more centered. The differences in the steady-state distributions for various power outputs in the same mass is negligible.

The 6 wt% precipitate is capable of achieving relatively smaller critical masses, and figure 5.3.2 shows the effects of applying the same power levels as the larger critical masses in the 2 wt% precipitate. For the 0.1 MTU critical mass, power peaks at the surface of the sphere, and this is most heavily biased at early times (days to months). This once again implying the strong role of the reflector for small critical radii. The 5 MTU results mirror those in figure 5.3.1, although there is a notch in $\mathcal{F}_p$ near the surface. This may be caused by competing effects of neutrons thermalized in the pore-water of the precipitate versus

Geometry	$\tilde{e}\,[wt\%]$	$M_c\,[MTU]$	$r_c\,[cm]$	$P_t\,[kW_t]$	f_0	μ	σ	R^2
H	2	5	105.6	0.1	0.083	0.773	0.290	0.999
				1	0.084	0.783	0.292	0.999
		100	301.8	0.1	0.074	0.693	0.251	0.999
				1	0.074	0.695	0.250	0.999
	6	0.1	38.0	0.1	0.113	0.943	0.352	0.998
				1	0.153	1.088	0.411	0.996
		1	93.8	0.1	0.097	0.857	0.332	0.996
				1	0.099	0.870	0.334	0.997
		5	160.3	0.1	0.085	0.782	0.300	0.997
				1	0.085	0.787	0.300	0.997
F	2	5	101.0	0.1	0.083	0.770	0.289	0.999
				1	0.084	0.781	0.291	0.999
		100	286.7	0.1	0.074	0.695	0.250	0.999
				1	0.074	0.700	0.250	0.999
	6	0.1	34.6	0.1	0.116	0.954	0.358	0.998
				1	0.164	1.122	0.426	0.995
		1	86.7	0.1	0.091	0.826	0.317	0.997
				1	0.094	0.842	0.321	0.998
		5	165.9	0.1	0.077	0.728	0.268	0.999
				1	0.078	0.739	0.271	0.999

Table 5.3.1: Gaussian fits for the time-averaged fission power distribution in various critical masses.

those thermalized in the shale. The higher enrichment may allow for more probable fission reactions directly at the surface. Otherwise, this is likely a numerical effect.

The profiles of the 2 wt% and 6 wt% precipitates in the fractured geometry overlap those of the homogeneous configuration per given masses due to similar material volumes and U-235 content. The strong similarity is evident in the time-averaged fit parameters for these two cases, and results can be simplified by focusing on the different enrichments. Fit parameters are listed in table 5.3.1, where they appear to vary linearly with the critical mass. There is also a minor dependence on the power level, which is especially apparent for smaller critical masses. As mentioned, μ decreases with increasing radius because the power profile becomes more centered, and σ decreases because there is a consistently higher fission density away from the surface. To use these regressions in chapter 6, averages of these parameters will be made over all power outputs available per mass in the results. Linear interpolations can be used for masses that may fall in between the evaluated masses if necessary.

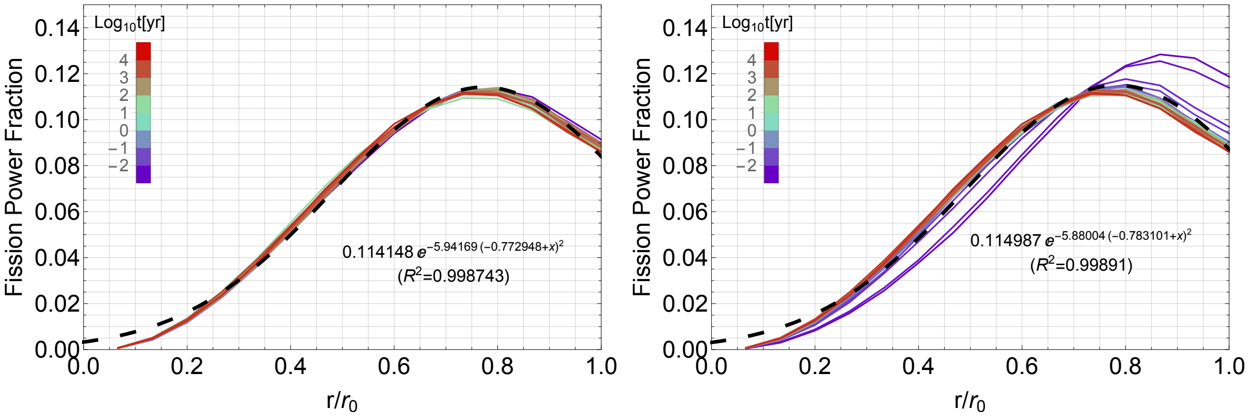

(a) 5 MTU, 0.1 kW_t (b) 5 MTU, 1 kW_t

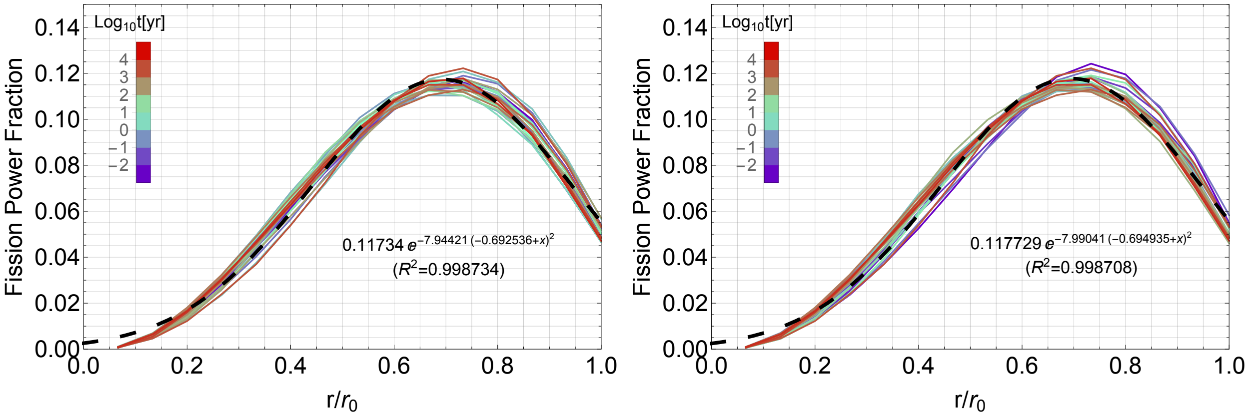

(c) 100 MTU, 0.1 kW_t (d) 100 MTU, 1 kW_t

Figure 5.3.1: Fission power distribution for the 2 wt% precipitate in the homogeneous geometry, shown with a Gaussian fit of the time-averaged data (black, dashed).

5.3.2 Multiplication and burnup

The k_{eff} evaluated at the full time step in the depletion analysis is plotted for the different precipitates in figure 5.3.3. As would be expected, higher power outputs lead to a more-quickly attained subcriticality. For the higher-enriched precipitate, the drop in reactivity is higher over the selected time steps, and relative to the lower-enriched case, the power level is a stronger determinant as to when these reductions in reactivity occur. The results imply that in the absence of a source term of fissile material, lower critical masses are liable to depleted sooner in time, limiting the extent to which fission products are generated.

The behavior of burnup is determined directly by the MCNP calculation parameters, and results are shown for referential purposes. Figure 5.3.4a shows that the cases corresponding to lower critical masses and higher fixed power outputs are, by definition, subject to higher burnup. Since the total power fraction is kept at unity throughout the calculation, the end

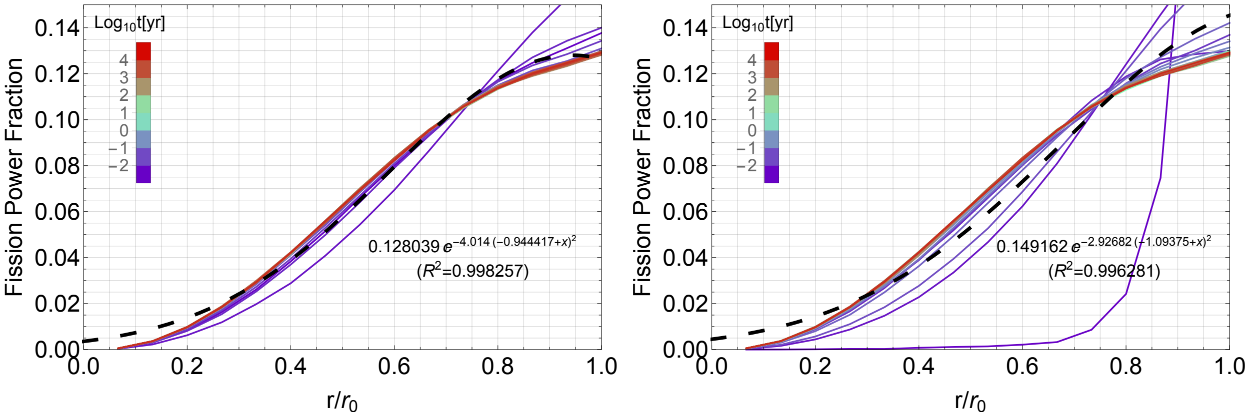

(a) 0.1 MTU, 0.1 kW_t (b) 0.1 MTU, 1 kW_t

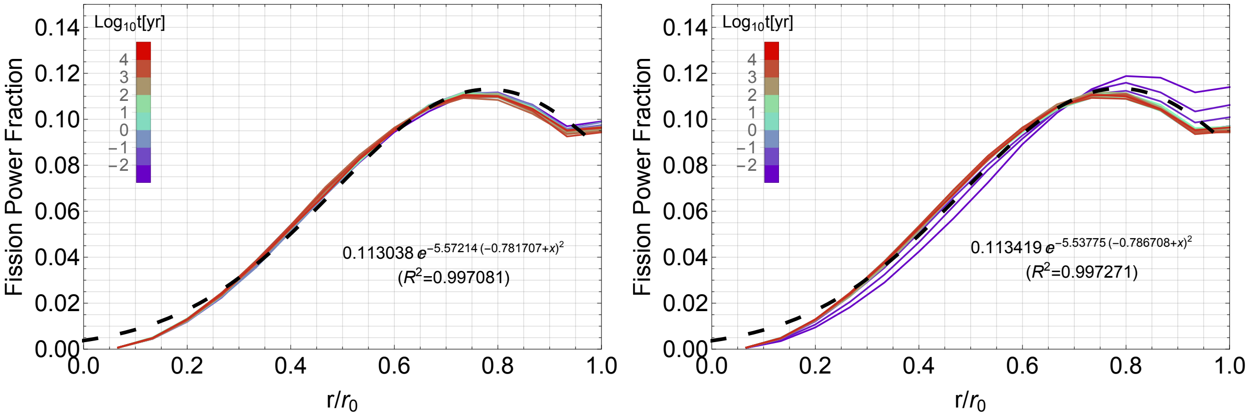

(c) 5 MTU, 0.1 kW_t (d) 5 MTU, 1 kW_t

Figure 5.3.2: Fission power distribution for the 6 wt% precipitate in the homogeneous geometry, shown with a Gaussian fit of the time-averaged data (black, dashed).

result is a linear increase in burnup for each case.

Figure 5.3.4b shows the time-averaged burnup distributions for different critical masses and power outputs. It is clear that burnup is highest in the center of the precipitate and lowest near the surface. This is caused by the lower masses of uranium in smaller annuli near the core of the sphere. That magnitude of these profiles increase with power and decrease with mass, as would be expected.

5.3.3 Fissile content

The fissile isotopes of interest in the highly thermal configurations are U-235 and Pu-239, and the changes in inventory of these isotopes are plotted in figure 5.3.5. The quantity of U-235 is expressed as "depletion," which is defined as the absolute difference in the inventory evaluated at a specific time with the initial loading. As a result of the transport and criticality

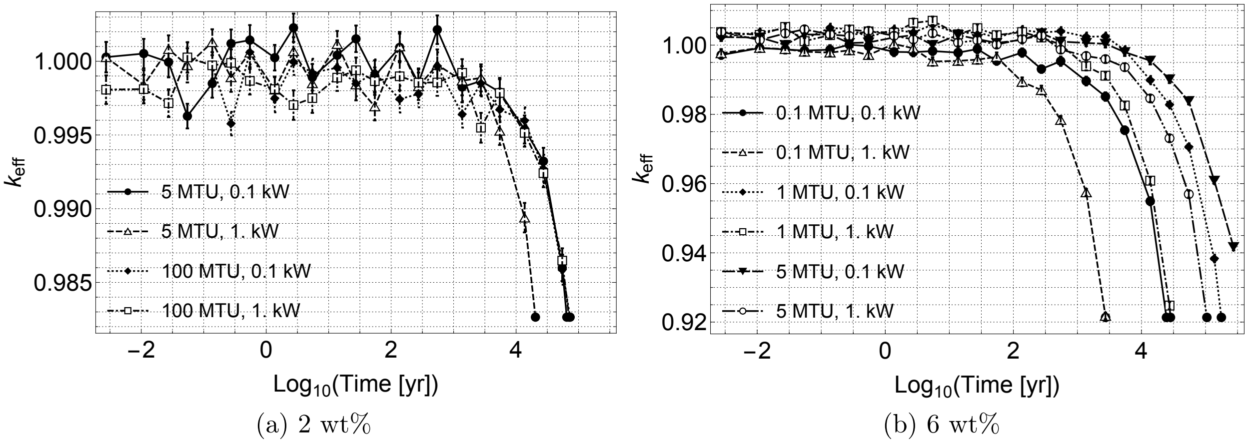

(a) 2 wt%

(b) 6 wt%

Figure 5.3.3: Behavior of the full-step k_{eff} over the $\log_{10}$ of time (years) from initial criticality for different enrichments, shown with error bars.

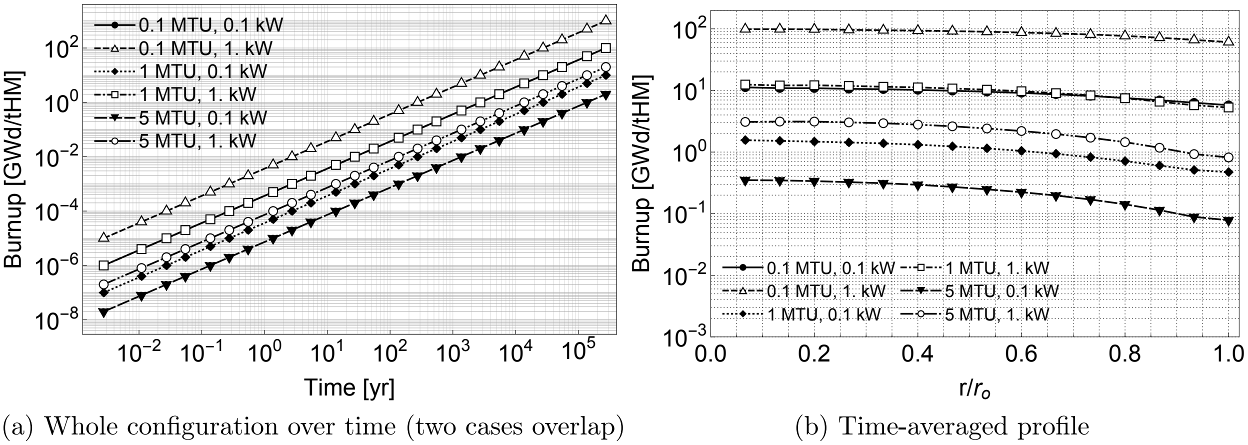

(a) Whole configuration over time (two cases overlap)

(b) Time-averaged profile

Figure 5.3.4: Burnup in the 6 wt% homogeneous critical sphere.

assumptions, there is no initial quantity of plutonium, and all plutonium in the inventory is generated from neutron interactions in the fuel.

It is shown that higher thermal power levels result in greater U-235 depletion and Pu-239 generation, which is expected. However, the time rates of either process are generally congruent for a given critical mass. In the 6 wt% precipitate, the high power case of the smallest critical mass reaches a steady-state level of U-235 depletion (i.e. no further decrease from the initial inventory) which corresponds to a substantial drop in Pu-239 generation. This is caused by the loss of reactivity in the critical mass, which prevents the further generation of Pu-239 from the U-238 precursor, and this is followed by the subsequent decay of this isotope.

In figure 5.3.6, it is shown that while the outer annuli of the sphere consistently contain the highest quantities of plutonium, increasing quantities of Pu-239 are generated over time near the center of the sphere due to absorptions on U-238. For the smaller critical mass (figure 5.3.6a), at long times meeting and exceeding the Pu-239 half-life, the plutonium generation decreases due to the corresponding decrease in reactivity with increasing burnup. The larger critical mass in figure 5.3.6b is not as affected by the loss of reactivity (see figure 5.3.3b), and the Pu-239 content is maintained for a longer period of time. However, the distributions for the prolonged time points do criss-cross as the plutonium content shifts towards the center.

Overall, this spatial behavior directly corresponds to the time-dependent power-peaking behavior observed in section 5.3.1. Roughly speaking, at least for early times, this is reminiscent of the depletion front observed in standing wave reactors, where it is necessary for assemblies with lower depletion in the outer region of the core to swap places with those with higher burnup in the inner region to prolong the operating lifetime at a set electrical output. In this calculation, the power level is imposed via equation (5.2.3), which frames this depletion front principle in terms of the fissile inventory.

5.3.4 Radioactivity

The purpose of the host rock as the natural barrier is to shield the biosphere from radionuclides that could potentially impart a lethal dose. In this study, fission products generated from sustained chain reactions in a critical deposition may pose a radiological risk apart from the heavy metals themselves. Material failure via thermal strain from steady energy release is considered the means of compromising the shale envelope and allowing for venting of FPs through naturally-fractured granite in the far-field. Measuring the actual impact of venting is beyond the scope of the study. However, the burnup simulation includes results on the generation of TRU and significant fission products over time, which can be used to roughly estimate the impact of rock failure.

Actinides

The total activity of the actinides in the homogeneous critical masses is plotted over time in figure 5.3.7, where the time range includes the effects of subcriticality. For one of these critical masses, a nuclide-specific plot is shown in figure 5.3.8 to illuminate the role of certain species. The activity of nuclides in the decay chains of natural uranium (4n+2 and 4n+3) are also included for reference. For the 4n+2 chain ($^{235}U \overset{\cdots}{\rightarrow} {}^{207}Pb$), the 13 short-lived radioactive daughters of Pa-231 leading to Pb-207 were assumed to be secular equilibrium. For the 4n+3 chain ($^{238}U \overset{\cdots}{\rightarrow} {}^{206}Pb$), 12 daughter nuclides of Th-230 leading to Pb-206 (in various pathways) were also assumed to be secular equilibrium, although it should be noted that the first such daughter, Ra-226, is somewhat long-lived with a half-life of 1600 years. The short-lived Pa-234 and its metastable state were also considered to be in secular equilibrium with Th-234, which is also short-lived but nonetheless accounted in the analysis.

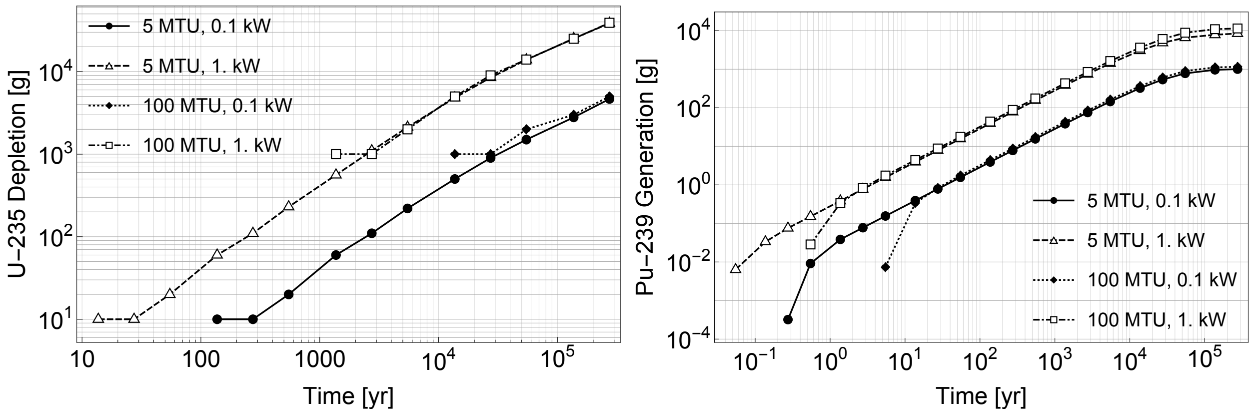

(a) 2 wt%, U-235 (b) 2 wt%, Pu-239

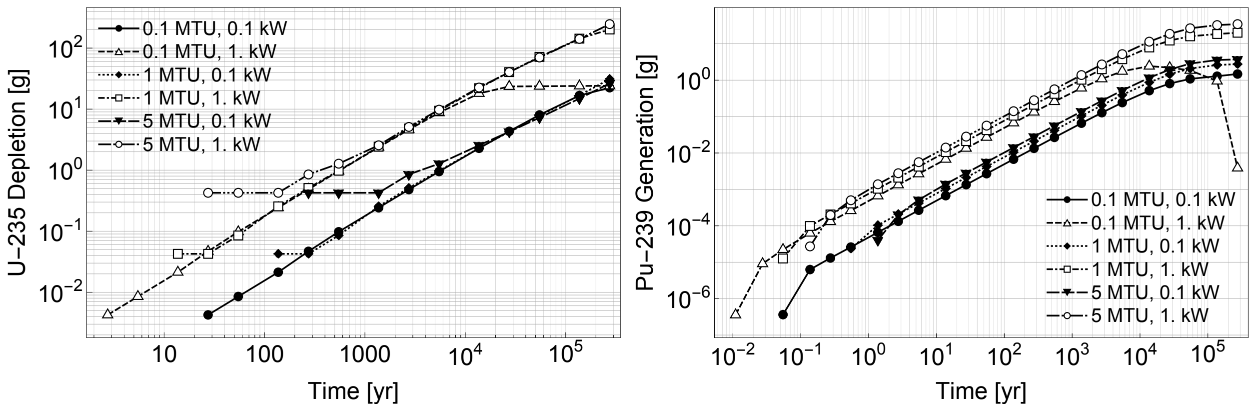

(c) 6 wt%, U-235 (d) 6 wt%, Pu-239

Figure 5.3.5: Behavior of fissile isotopes in the homogeneous precipitate.

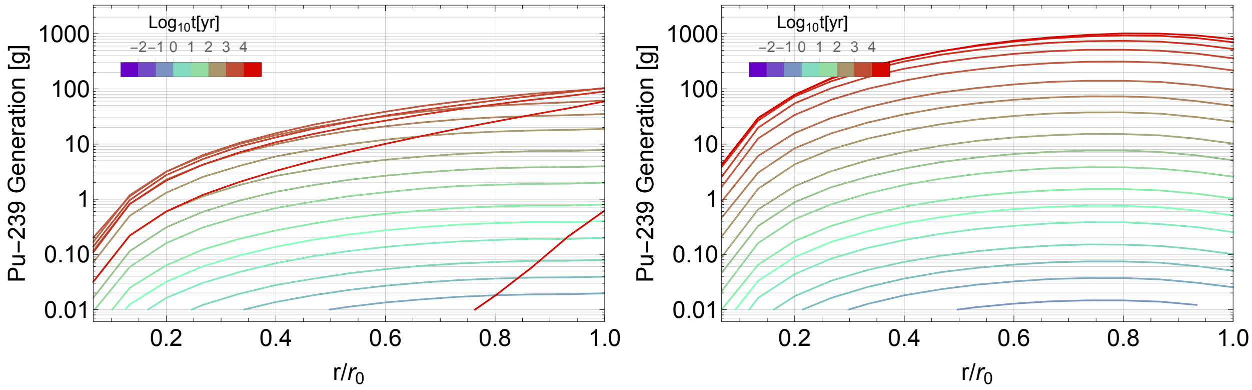

(a) 0.1 MTU (b) 5 MTU

Figure 5.3.6: Profile of Pu-239 generation for 6 wt% critical masses at $1\,kW_t$.

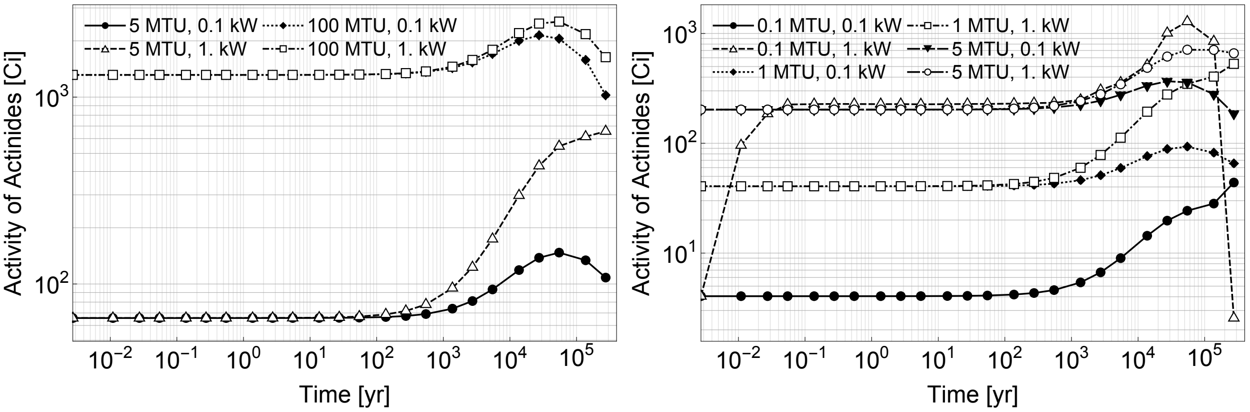

(a) 2 wt%

(b) 6 wt%

Figure 5.3.7: Activity of actinides ($Z \geq 90$) in the homogeneous configuration.

The early radioactivity level is determined by the activities of U-233 and U-234. The first isotope is generated by mobilized TRU during nuclide transport, while the other isotope is in secular equilibrium with U-238. There is a rise in activity at approximately 100 years is caused by the generation of Pu-239, and the subsequent decline is caused by the loss of reactivity and decay in Pu-239. However, there is exceptional behavior in the high power case for the 6 wt% 0.1 MTU precipitate. In this extreme burnup scenario, figure 5.3.8b shows that the total activity level is enhanced by Np-239, which is a beta decay precursor of Pu-239 and most likely generated from neutron capture on U-238 followed by the beta decay of U-239. This is the effect of a higher flux of neutrons that are not able to thermalize effectively, leading to greater absorptions in U-238. The minor contributions of short-lived fissile Pu-241 to this enhanced activity level may be through successive neutron capture on Pu-239 and Pu-240, with a less probable mode based on the immediate generation of U-240 and U-241 followed by beta decay.

Non-actinides

The activity of fission products over time within the second burnup tier of MCNP is plotted in figures 5.3.9 and 5.3.10 for the different enrichments. Total radioactivity increases in proportion to the thermal output, where a maximum of 100 Ci is observed in the 1 kW_t calculations. Decreases in the total reactivity after the maximum are caused by the decay of Cs-137 and Pm-147. Any increases in total activity from the steady level are engendered by Tc-99 or possibly Cs-134, which appears in the extreme burnup case for the smallest 6 wt% critical mass. The extreme burnup case also shows early effects from Ru-103, which has a high U-235 cumulative yield. Therefore, a small critical mass with high power output, while prone to reaching subcriticality sooner in time, will produce the highest activity levels.

In the 2 wt% precipitate, the total activity of the natural uranium is surpassed by that of the fission product inventory only at high power for the smallest critical mass. In the

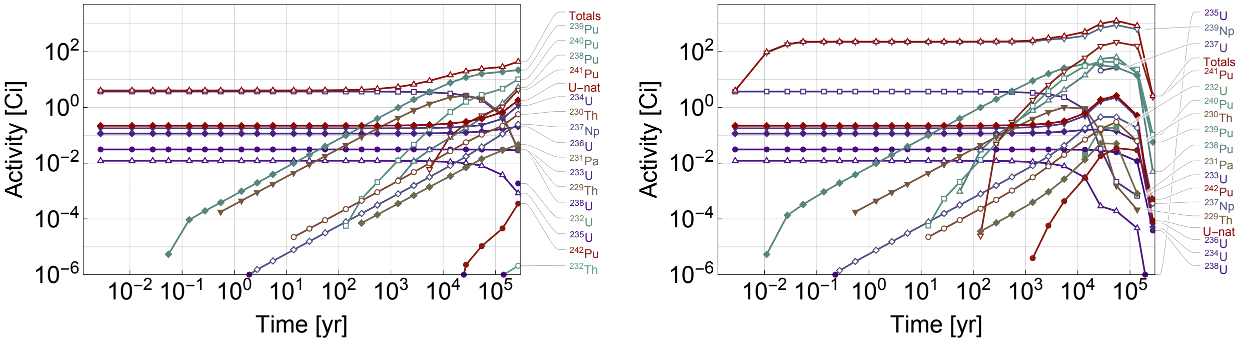

(a) $0.1\,kW_t$ (b) $1\,kW_t$

Figure 5.3.8: The activity over time for nuclides with $Z \geq 90$ in the 0.1 MTU 6 wt% homogeneous precipitate.

higher-enriched precipitate, the U-nat activity is not surpassed in the low power case for the larger critical mass. The strong loss of reactivity leads to a considerable drop in natural uranium activity in figure 5.3.10b. The small divot in total activity in figure 5.3.9c is an effect caused by an isotope (not shown) surpassing the inventory threshold for only one time step.

Effect of heterogeneity

The fission profiles between the homogeneous and heterogeneous geometries are essentially the same. However, the overlay plot in figure 5.3.11 for the 2 wt% precipitate demonstrates transient differences in activity.

For non-actinides (figure 5.3.11a), the steady reactivity level is reached earlier in time for the heterogeneous geometry, and this tendency is especially apparent for the larger critical mass at low power. When comparing figure 5.3.12a with 5.3.9c, it is clear that the early onset of high activity in the fractured case is caused by Cs-137. This isotope surpasses the atom fraction threshold of 10^{-10} to be included in the inventory results for the fractured setup. Since the quantity of Cs-137 will be proportional to the number of fissions, this criterion may be met due to the greater resonance escape probability in the body of the fuel in the heterogeneous layout. Higher fission densities lead to higher yields of nuclides such as cesium.

For actinides, the rise in activity for the smaller critical mass at 1 kW_t occurs sooner for the fractured geometry compared to the homogeneous, while agreement is otherwise good for other cases (see figure 5.3.11b). From figure 5.3.12b, it can be seen that Np-239 determines the total actinide activity level at early times, followed by contributions from Pu-239 much later on. Therefore, it would seem that the generation of Np-239 occurs sooner for the fractured geometry relative to the homogeneous one at the same power level. This would imply that neutron capture reactions on Np-238 and U-238, or else alpha decay from Am-243,

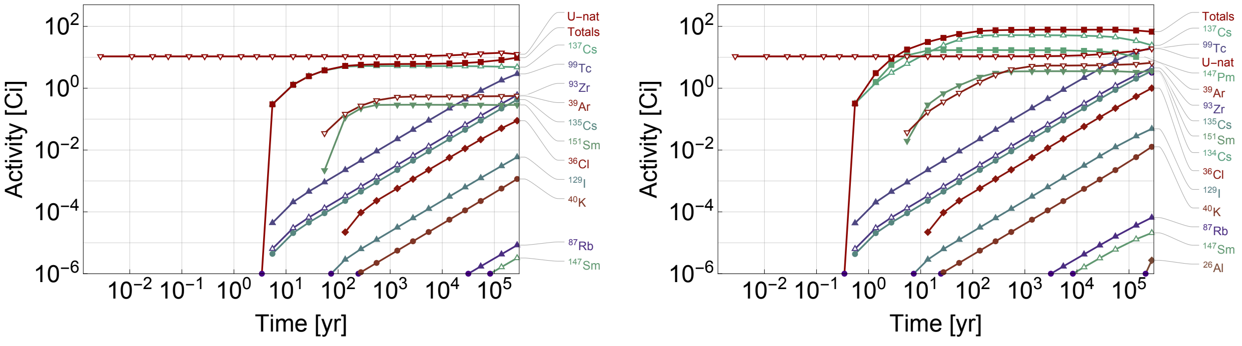

(a) 2 wt%, 5 MTU, 0.1 kW_t (b) 2 wt%, 5 MTU, 1 kW_t

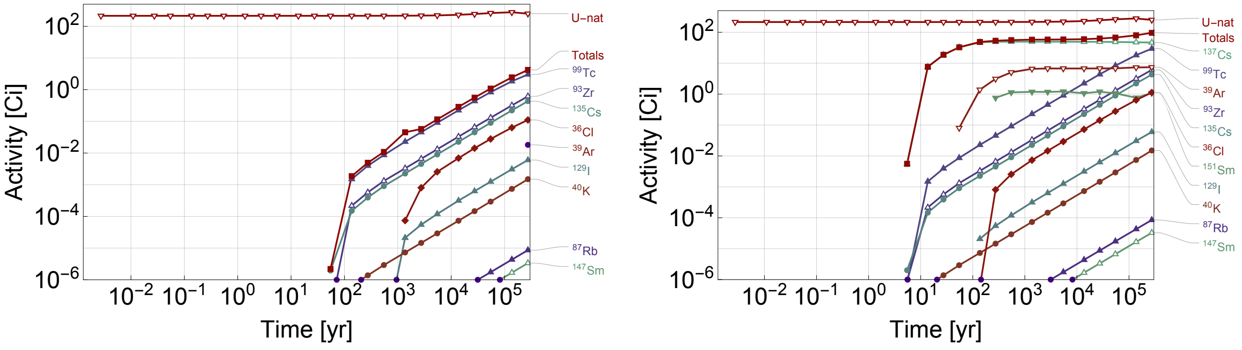

(c) 2 wt%, 100 MTU, 0.1 kW_t (d) 2 wt%, 100 MTU, 1 kW_t

Figure 5.3.9: Activity of non-actinides and isotopes in the natural-uranium decay chains for the homogeneous 2 wt% precipitate.

would need to have higher frequency in this geometry. While it is the case the inner portion of the fuel is shielded from resonance energy neutrons, such that more fission absorptions will take place per given fuel volume, the shielding effect will still lead to resonance absorptions on the fuel slab surfaces. In the homogeneous case, a smaller critical radius and more dispersed pore-water moderator will lead to greater leakage of fast neutrons to the reflector, ultimately leading to fewer resonance absorptions in the core. Therefore, Np-239 generation will occur at a higher frequency in the fractured layout, leading to this isotope surpassing to isotope cutoff sooner in time.

5.3.5 A note on hazard

The radiotoxicity of a radionuclide is a measure of the volume of air or water required for dilution such that the dose rate upon ingestion is no more than 50 mrem per year. It is defined in terms of the maximum permissible concentration (MPC) of the radionuclide as follows:

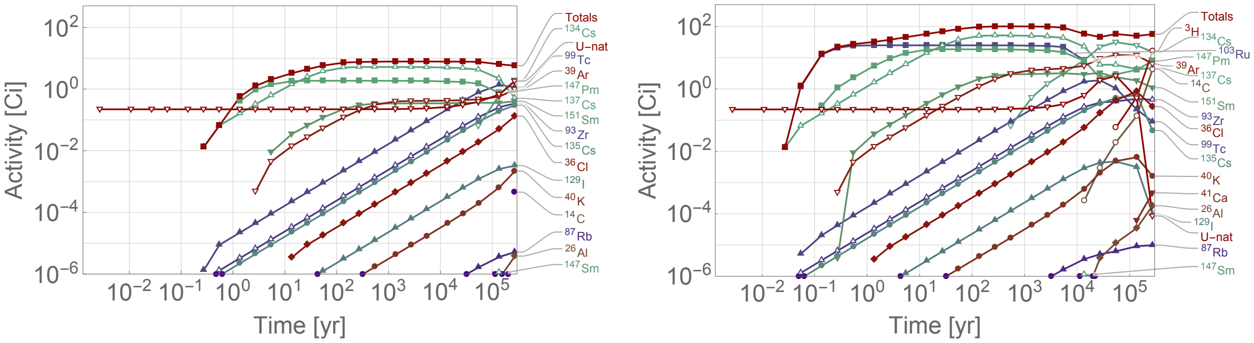

(a) 6 wt%, 0.1 MTU, 0.1 kW_t (b) 6 wt%, 0.1 MTU, 1 kW_t

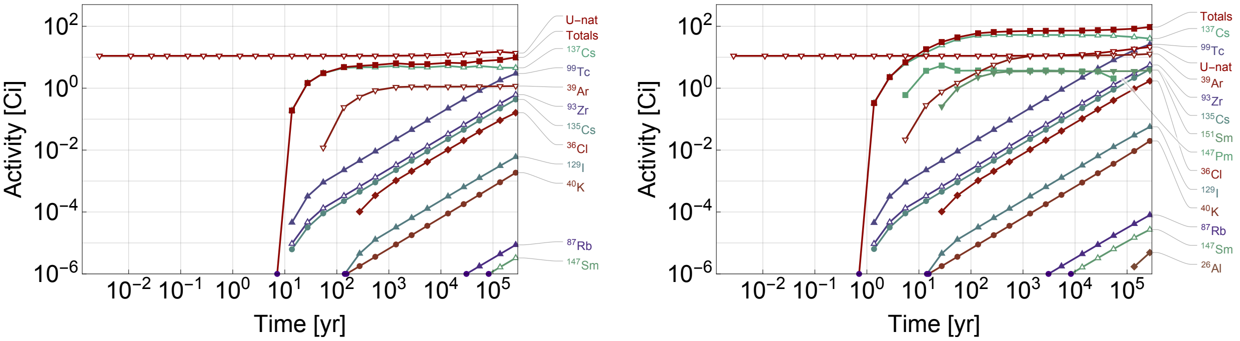

(c) 6 wt%, 5 MTU, 0.1 kW_t (d) 6 wt%, 5 MTU, 1 kW_t

Figure 5.3.10: Activity of non-actinides and isotopes in the natural-uranium decay chains for the homogeneous 6 wt% precipitate.

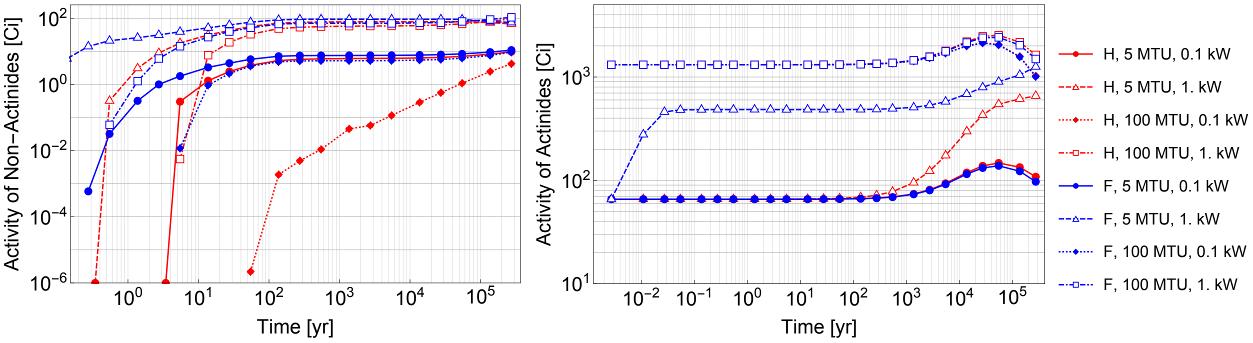

(a) Non-actinides (b) Actinides

Figure 5.3.11: Comparison of activity results for the homogeneous and fractured geometries of the 2 wt% enriched precipitate.

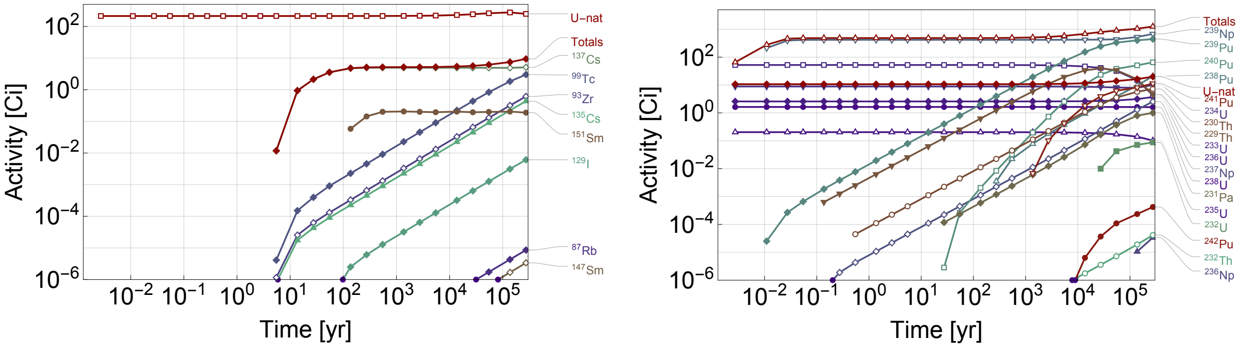

(a) Non-actinides, 100 MTU, 0.1 kW_t

(b) Actinides, 5 MTU, 1 kW_t

Figure 5.3.12: Activity in the 2 wt% fractured geometry.

$$Radiotoxicity_i = \frac{\lambda_i N_i(t)}{MPC_i} = \frac{A_i(t)}{MPC_i} \tag{5.3.2}$$

While it is not appropriate to discuss hazard without a nuclide transport analysis specific to the consequences of criticality, a rough estimation of radiotoxicity can be made assuming chain reactions are sustained to the point where natural barriers fail around 10^5 yr, upon which all nuclides enter the biosphere via fracture water. For the major emitters described in sections 5.3.4 and 5.3.4, the MPC is $4 * 10^{-5} \frac{Ci}{m^3}$ for Zr-93, $6 * 10^{-5} \frac{Ci}{m^3}$ for Tc-99, $10^{-6} \frac{Ci}{m^3}$ for Cs-137, $3 * 10^{-7} \frac{Ci}{m^3}$ for U-234, 235, and 238, $2 * 10^{-5} \frac{Ci}{m^3}$ for Np-239, and $2 * 10^{-8} \frac{Ci}{m^3}$ for Pu-239. [92]

For the smaller 2 wt% critical mass, around $10^5\,yr$ post-formation, an maximum activity of $40\,Ci$ could be expected for Cs-137, leading to a radiotoxicity of $4 * 10^7\,m^3$. Pu-239 would have a maximal radioactivity of $480\,Ci$ and radiotoxicity of $2 * 10^{10}\,m^3$. For the natural uranium decay chains, an activity of about $15\,Ci$ is observed, and if the radiotoxicity can be emulated strongly by uranium isotopes, then about $5 * 10^7\,m^3$ would be required for dilution. This would imply that under conditions of sustained criticality, where reactivity allows for the sustained generation of plutonium, there may be a relatively augmented risk to the biosphere if both actinides and non-actinides are released through fractures. This would be compared to the risk posed by the leachate of the original fuel, which is strongly depleted to U-nat levels.

5.4 Discussion

The behavior of the fission power distribution, fissile inventory, and radioactivity in a critical mass have been illustrated. The power profile was found to be a function of the the critical radius, and some dependence on the power output was evident for smaller critical masses. Peaking behavior was influenced by the role of the shale reflector per given critical radius. Smaller critical masses rely heavily on the reflector for thermalization, and the distribution is centered at or near the spherical surface in these cases. Using regressions based on a Gaussian distribution, the power profiles are portable to the thermo-hydrological analysis for use as the energy source term. Proper spatial consideration of this source term would not be adequately represented by a flat power assumption, as such would clearly not be applicable to the system characteristics based on the results of this chapter.

It has been demonstrated that the production of fission products with high activity is dependent on the enrichment of the precipitate and total power output relative to the critical mass. A critical mass with high burnup characteristics will impart the greatest total reactivity, and this will usually surpass the total activity of species in the natural uranium decay chains. It was found that the combined yield of Tc-99, Cs-137, and Pm-146 is a strong determinant of the total activity level. Given the discrepancies in the Cs-137 and Pm-147 presence above $1\,\mu Ci$ in the results for certain time steps, the activity analysis can be improved by lowering the inventory threshold to perhaps 10^{-15}.

The activity of uranium and TRU is also determined by the power level relative to the critical radius. Higher burnup imposed on smaller critical masses will lead to effects from spectrum hardening, where the level of Pu-239 generation is increased from absorptions on U-238. Either this isotope or its precursor Np-239 controls the total reactivity level. Nonetheless, higher burnup leads to stronger depletion and quicker reductions in reactivity, which eventually leads to a drop in Pu-239 production.

While there is uncertainty in regards to the impact of radionuclides generated from fission during sustained criticality, the results indicate that a considerable hazard should not be eliminated from consideration should extensive venting result from catastrophic failure of the host rock. Given the generation of Pu-239 in the critical sphere, depending on the time scale, attaining the failure criterion in the dynamics analysis can be connected to an actual radiological impact. While a consequence transport analysis is beyond the scope of the study, it is likely that assumptions can be crafted to allow for the activity results presented in this chapter to be strong indicators of total hazard.

Chapter 6

Unsaturated heat and mass transport

6.1 Introduction

The critical mass at the focus of this study is not only a porous medium, but by nature an open nuclear reactor system. There are feedback mechanisms that control the extent of chain reactions and the release of fission energy, while at the same time, there are hydrological mechanisms that control the flux of pore fluid from the system based on capillarity and permeability. The latter consideration is itself a reactivity feedback mechanism by way of controlling both the spatial distribution and density of the moderator. With regards to these physical processes, the range of critical dimensions observed in chapter 4 indicate that the system cannot be treated as a point, such that spatial variation in the pore water content with fission heating must be evaluated to properly assess reactor dynamics.

This chapter will discuss the thermal and hydrological (TH) evaluation of the critical precipitate given their presumed environment of shale of granite in the far-field. In particular, the average temperature and saturation profile in the critical mass will be evaluated within a two-phase unsaturated flow context, given the fission source term investigated in chapter 5.

6.2 Methodology

6.2.1 Overview

The TOUGH2 code is employed to model the heat transfer and multiphase fluid flow from the critical region to the surrounding rock. [93] This code couples the conservation of energy and mass via the integrated finite difference method for discrete, connected elements of partially unsaturated porous media, and employs one of several linear equations solvers for a Newton-Raphson iteration scheme to solve for thermal state parameters at certain time points. It is employed in this report to model the simultaneous changes in temperature and water content given the fission source terms evaluated in chapter 5, as it is ideal for problems involving strongly heat-driven flows. The system in figure 4.3.1 is discretized into individual volume elements that interact with each other at the spherical surface interfaces. The temperature, pressure, saturation, and fluid densities are evaluated for each volume element based on constitutive relations, while the fluxes of heat and fluids are evaluated at the interfaces via the conservation equations.

Conservation laws

Temperature (T) is a measure of the average kinetic energy of randomly-interacting particles in a medium. For a fluid, molecular energy is described in terms of translational motion (from molecular collisions) and internal molecular vibrations and rotations, while for a solid, molecular energy comes in the form of lattice vibrations (phonons) or, for an electrical conductor, the transfer of electrons. [94] Conduction describes the transfer of energy from areas in a medium where particles have higher energy to areas where the energy is lower, assuming there is no bulk motion of particles of said medium. This implies that in the presence of a temperature gradient (∇T), energy transfer via the conduction mode occurs in the direction of decreasing temperature. The energy flux $\mathbf{q}$ $\left[\frac{W}{m^2}\right]$ from this observed phenomenon is described through equation (6.2.1). This relationship is known as Fourier's Law, which assumes that the heat flux can be related to the temperature gradient by way of the thermal conductivity k. It is used to find the heat flux at any point in the medium or on its surface once the temperature distribution is known.

$$\mathbf{q}\left[\frac{W}{m^2}\right] = -k\nabla T \tag{6.2.1}$$

Convection is a heat transfer mode consisting of diffusion, which is the random motion of particles, and advection, which describes the bulk movement of the fluid comprised by the particles. The movement can either be forced, such as from an applied pressure gradient, or natural, where buoyancy acts on local differences in density to move fluid around a cooling object. The heat flux from this energy transfer process is described by a rate equation called Newton's Law of Cooling (6.2.2), where it is assumed that heat is being transferred from the surface of a medium with temperature T_s to the surroundings with ambient temperature T_∞. The rate constant h $\left[\frac{W}{m^2-K}\right]$ is called the heat transfer coefficient, and it is determined through means specific to the problem being analyzed. As will be mentioned in chapter 8, the problem consists of a heat-conducting, stationary control volume that has a convective boundary condition at its surface.

$$\mathbf{q} = h(T_s - T_\infty) \tag{6.2.2}$$

The temperature distribution itself is found through the heat diffusion equation (6.2.3), which is based on the conservation of energy. This describes the time rate of change of thermal energy in the volume and is represented in terms of the source term $\dot{q}(t)$ and the divergence of the thermal conductivity and the temperature gradient, where c_p $\left[\frac{J}{kg-K}\right]$ is the specific heat capacity and $\rho\ \left[\frac{kg}{m^3}\right]$ is the density of the solid. A derivation is discussed in section §E.1.

$$\rho c_p \frac{\partial T}{\partial t} = \dot{q}(t) + \mathrm{div}\left(k \cdot \mathrm{grad}\left(T\right)\right) \tag{6.2.3}$$

Darcy's law is an application of the conservation of momentum (Navier-Stokes) for a porous medium. This law states that the specific discharge Q from a porous medium is proportional to the gradient of the total hydraulic head H or pressure $P\ \left[\frac{kg}{m-s^2}\right]$, which is applicable when the Reynold's number (Re) is less than one for non-turbulent environments. For the non-turbulent one-phase flow of a well-mixed, constant-density, incompressible fluid in a non-deformable, homogeneous solid matrix that is already saturated with fluid, the discharge is modeled in equation (6.2.4), where $K\ \left[\frac{m}{s}\right]$ is the hydraulic conductivity, $\mathcal{K}$ is the intrinsic permeability, $\mu\left[\frac{kg}{m-s}\right]$ is the dynamic viscosity of the fluid, $\rho\ \left[\frac{kg}{m^3}\right]$ is the fluid density, and $g\ \left[\frac{m}{s^2}\right]$ is the acceleration from gravity. This quantity is sometimes referred to as the Darcy velocity or volume flux, but it is different from the actual fluid velocity.

$$\mathbf{Q}\left[\frac{m}{s}\right] = -K\nabla H = -\frac{\mathcal{K}}{\mu}\left(\nabla P + \rho\mathbf{g}\right) \tag{6.2.4}$$

For a two-phase system, the advective mass flux is based on Darcy's law and modified for the relative permeability $\mathcal{K}_r$ and density ρ of phases β:

$$\mathbf{F}_\beta\left[\frac{kg}{m^2 - s}\right] = -\mathcal{K}\frac{\mathcal{K}_{r\beta}\rho_\beta}{\mu_\beta}\left(\nabla P_\beta + \rho_\beta\mathbf{g}\right) \tag{6.2.5}$$

The body forces acting upon the phase are represented by the sum of the reference phase pressure P and the capillary pressure:

$$P_\beta = P + P_{cap,\beta} \tag{6.2.6}$$

Darcy's law is assumed to be applicable since the system begins at full saturation, flow is steady, and the fractured geometry is approximated as a continuum. For a given volume V_n of n total elements and $\kappa = 1...N_k$ mass components (i.e. the water and air in the pore space), the time rate of change of the volume-integrated mass density M is expressed in terms of the surface integral of the fluxes $\mathbf{F}$ and a source term W, as shown in equation (6.2.7). W is zero in this study because there is no injected source of water. The mass density and flux components are summed over all phases, where the contributions from a specific phase are dependent on the saturation S_β, density ρ_β, and the relative fraction of the mass component dissolved/evaporated in the particular phase (e.g. gaseous versus dissolved air). Since the expression is applicable the whole volume, these values in turn are modified by the porosity ϵ, which indicates the volume fraction available to fluid (FVF).

$$\frac{d}{dt}\int_{V_n} M_\kappa\, dV_n = \int_{S_n} \mathbf{F}_\kappa \cdot \mathbf{n}\, dS_n + \int_{V_n} W_\kappa\, dV_n \tag{6.2.7}$$

A integral form of equation (6.2.3) can be made in the same manner as equation (6.2.7), whereupon the κ index is expanded by one to include a heat component ($\kappa = 1...N_\kappa + 1$). The heat version of M is an energy density described in terms of the thermal properties of the solids and fluid phases, namely the heat capacity (c_p) and internal energy (u), as shown in equation (6.2.8).

$$M_{N_\kappa+1}^{(heat)} = (1-\epsilon)\,\rho_s c_p^s T + \epsilon S_l \rho_l u_l + \epsilon\,(1-S_l)\,\rho_g u_g \tag{6.2.8}$$

The heat flux term includes conductive effects via Fourier's law and convective effects from the advection of fluids using their specific enthalpies $h\,\left[\frac{J}{kg}\right]$:

$$\mathbf{F}_{N_\kappa+1}^{(heat)} = -k\nabla T - \sum_\beta h_\beta \mathcal{K} \frac{\mathcal{K}_{r\beta}\rho_\beta}{\mu_\beta}\left(\nabla P_\beta + \rho_\beta \mathbf{g}\right) \tag{6.2.9}$$

The volume integrals of equation (6.2.7) are replaced by the volumes of the discrete elements and volume averages of the mass and energy densities. The surface integrals are represented as summations of discrete fluxes between adjoining elements with fixed interfacial areas. The distances between the centroids of adjoining volume elements is used to approximate the gradient in the flux terms using averages of properties in the respective elements. The time derivatives are discretized into first-order finite differences.

Motivation for use of the code

The use of this code is ideal for a number of reasons, and the following points will be reiterated:

1. From chapter 4, it is clear that the radii of the critical spheres are large ($> 1\,m$), such that the critical masses cannot be treated as points of spatially-consistent temperatures, pressures, and water contents in a two-phase system.

2. There is a peaked fission power distribution caused by the shale reflector (chapter 5), which prohibits the use of a flat flux in modeling. The critical mass is modeled as a natural reactor, and much like an engineered reactor, there is spatial variation in power, flux, etc across the core.

3. The effects of capillary pressure and the air-entry value cannot be dismissed when evaluating mass transport in the critical sphere, as the reactor is part of an open system. Mass transport of air into the void space is limited by this capillary effect and Darcy's Law, which are handled effectively by this code.

4. At some point in the far-field, there will be an unsaturated region (perhaps the vadose zone) that will serve as a reservoir for fluids expelled from the saturated region. The effects of this region as a boundary condition must be taken into account.

5. The low permeability of the clay minerals surrounding the critical mass will inhibit water exfiltration as temperature and pressure evolve, which in turn will affect reactor dynamics.

The geometric approaches that have been considered for the minimal critical mass have fallen at two extremes that would not occur in a natural system, and the lack of realism is compounded by the use of a spherical reflector as a bounding region. A natural deposition would likely occur with an intermediate level of heterogeneity influenced by random and fractal-like fissures of varying aperture, and the total deposition would occur in a relatively flat and elongated manner as determined by the stratigraphy of the rock. The abstracted nature of the formation and configuration of the critical mass precludes a simulation of reality, although TOUGH2 and reactive transport codes like PFLOTRAN have certainly been used in a simulation context for waste management studies. The level of detail included in this application should be sufficient to demonstrate fundamental behavior of heat and mass transfer in the critical mass.

The fractured geometry is treated as an effective continuum, where it is assumed that the rock, metal, and fluid in the individual repeating units can be represented with the same average thermodynamic properties. There is limited value and added complication to representing the fractured configuration with a dual-porosity and/or dual-permeability model. In this approach, mass transfer from the shale planes would be significantly delayed compared to the fracture region given the differences in porosity and hydraulic conductivity, such that the fractures serve as the main conduit for fluid flow while the rock matrix provides secondary fluid flow. The most strongly differentiating factors between the homogeneous and fractured geometries are the critical radii and fluid volume fractions. Per given mass and enrichment, the fractured geometry typically requires less volumetric water content to achieve initial criticality due to the reflective properties of the fracture rocks, and the initial mass of fluid available for transport will be lower. Therefore, the drop in reactivity from reducing water content in the 10 vol% of the shale laminates is expected to be small, and there is limited value to modeling fine-scale effects of fracture rock saturation.

It should be noted that applications of TOUGH2 for modeling multiple interacting continua with coupled fluid and heat flows are meant to simulate fluid flow on a reservoir scale. Matrix blocks are created that represent the intersection of solid rock with fractures, and these blocks are internally discretized to properly model the temperature and pressure gradients at the interfaces. It is not clear whether this method would remain accurate given the elongated fractures of this system, the geometric complication imposed by the spherical reflector, and the added heterogeneity of the UO_2 layer, where it would seem appropriate that the source term of heat would be modeled as strictly emanating from the metal before steady-state. While the shale and UO_2 layers can be homogenized to simplify the system for such an application, this would obviously pose a discrepancy with the neutronics analysis.

The high-level study in this chapter should be adequate to describe basic fluid behavior during sustained criticality. In chapter 7, the average temperature of the repeating cell is used for the rock, metal, water, and air. The main approach calls for the saturation of the shale in the fracture units to be held constant despite any effects from heating, while the average saturation of the cell is treated through a modification of water and air volume in the fracture. However, a secondary approach will be employed that will take the average saturation level for the cell and apply that directly to the shale in the fracture rock, which assumes there is no dual-porosity effect and mass transport is equal for both media.

6.2.2 Problem setup

The problem setup utilized in chapters 4 and 5 and visualized in figure 4.3.1 is carried over to this TH study, although the surrounding void is replaced with an infinite extent of unsaturated granite. Each region in the system is discretized into fifteen spherical annuli to capture spatial variation, where a liquid saturation of 99.9%,[1] temperature of $20.45°C$ (the same used for the "80c" cross sections in chapter 4) and pressure of 15 MPa are employed as the system-wide initial conditions.[2] Water and air are modeled as the fluid constituents of pore space, and the third equation-of-state module (EOS 3) of TOUGH2 is used to evaluate the constitutive relations at each time step for all 45 elements.

As mentioned, this system is surrounded by an extremely large volume of rock modeled as granite. This region serves as the heat sink and a reservoir of pore water moving out of the system via capillary effects. The volume is specified as $10^{34}\,m^3$ to maintain a constant thermodynamic state in the code, and its role in the material balances is precluded by specifying a specific heat of 1100 $\frac{J}{kg-K}$. The saturation of this surrounding region, S_l^{env}, is tested at 10% and 0.1% to conservatively probe a lower bound of water content for the critical mass at steady-state, as it is anticipated that strong reductions in saturation will yield stronger reactivity feedback effects in chapter 7. For crystalline granite in the far-field, these levels of saturation are not representative of the actual vadose zone, and the saturated granite layer would likely be $\approx 400\,m$ thick as opposed to the small $10\,m$ thickness employed in this study. The water table will likely be close to the surface of the rock, with the vadose zone being about $100\,m$ thick or less. It is plausible that over geological time, the capillary fringe in the host rock surrounding the repository will lower to fall in line with the assumptions of this study, which are chosen to maximize desaturation.

The critical region is modeled as being far more pervious than the shale or host rock, with a permeability ($\mathcal{K}$) of 1 milli-Darcy ($1\,D \approx 10^{-12}\,m^2$) compared to 1 μD. These quantities are chosen to reflect the highly porous or fractured nature of the critical configurations from tables 4.4.2 and 4.4.1, along with their interaction with shale as a clay-like mass transport barrier. Indeed, 1 μD would be an upper bound value of permeability for shale and chosen to promote the exfiltration of water from the critical mass. [95] Choice of permeability affects the pressure gradient and mass fluxes, but steady-state temperatures appear to be relatively insensitive to the quantity.

---

[1] The problem cannot be initialized with 100% saturation since two phases are modeled in the code.

[2] Using 15 MPa over the hydrostatic stress of 4.9 MPa extends the temperature region of the liquid phase, which will allow for Doppler broadening to be factored into more unsaturated system states in chapter 7.

Permeability is treated isotropically (i.e. there is no fast channel in the transverse direction) and the effects of the gravitational acceleration vector are turned off. The effect of the relative orientation of the problem cells to the gravitational acceleration vector can be handled on a element-by-element basis. However, in order to make the results independent of direction in the dynamics analysis. Nonetheless, it should be noted that given the magnitude of radii for critical masses evaluated in this study, buoyancy effects in the critical sphere are likely to be non-negligible. Darcy's law will call for more fluid to exfiltrate in the direction of the gravitational acceleration vector, particularly as the critical mass increases in temperature. A lopsided distribution of water content will cause an insulating effect to the upper regions, where the fluid densities will decrease at a different rate with increasing temperature. With these density differences, lower density fluid will be transported upwards to form a convection current. Treating these phenomena would require further discretization of the critical sphere into angular sections, which would complicate the simulation. Furthermore, it is questionable whether the results from these effects would be extensible to the point-like treatment in the QSS analysis. Nevertheless, this must be mentioned since buoyancy can be factored into the heat transfer relationships discussed in chapter 8.

The van Genuchten-Mualem model is employed to model the relative permeability of water (equation (6.2.10)) and air (equation (6.2.11)) in the pore space. [96] These functions are based on parameters S^* and $\hat{S}$, which are functions of the liquid saturation S_l. The residual saturations of water (S_{lr}) and air (S_{gr}) are 5% and 1%, respectively. These values represent the fluid content retained in the porous medium through intermolecular effects with the rock grains that are strong enough to overcome gravitational forces. A value of $S_{ls} = 1$ is used to ensure that both the liquid and gas phases are mobile for a given change in pressure, i.e. such that air is not stagnant. The fitting parameter was chosen to be $\lambda = 0.5$ to emulate a middle-ground between clay-like and fractured behavior.

$$\mathcal{K}_{rl} = \begin{cases} \sqrt{S^*}\left[1 - \left(1 - (S^*)^{1/\lambda}\right)^{\lambda}\right]^2 & S_l < S_{ls} \\ 1 & S_l \geq S_{ls} \end{cases} \tag{6.2.10}$$

$$\mathcal{K}_{rg} = \begin{cases} 1 - \mathcal{K}_{rl} & S_{gr} = 0 \\ \left(1 - \hat{S}\right)^2 \left(1 - \hat{S}^2\right) & S_{gr} > 0 \end{cases} \tag{6.2.11}$$

$$S^* = \frac{S_l - S_{lr}}{S_{ls} - S_{lr}} \tag{6.2.12}$$

$$\hat{S} = \frac{S_l - S_{lr}}{1 - S_{lr} - S_{gr}} \tag{6.2.13}$$

The water retention curve determines the relationship between the pressure head and the moisture content, and the shape of this curve depends on the assortment of particle sizes within the porous medium. Media like sand contain a diverse assortment of grain shapes and sizes, which makes retention of water in the pores strongly determined by capillary effects. However, in clay, there is usually a more uniform assortment of grain sizes, and body forces are have a more dominant role in the ability for water to overcome intermolecular forces imposed by the grains.

To model capillary pressure in TOUGH2, an model associated with the relative conductivity, shown in equation (6.2.14), is employed with a fitting parameter of $\lambda = 0.5$, an air-entry value of $P_0 = 200\,kPa$, and a lower bound of -0.1 GPa. In this particular relationship, the residual water saturation is modeled as 1% to maintain realistic capillary behavior when the liquid phase becomes immobile.

$$P_{cap} = -P_0\left(\left(S^*\right)^{-1/\lambda} - 1\right)^{1-\lambda}, \; -P_{max} \leq P_{cap} \leq 0 \tag{6.2.14}$$

Parametric plots of equation (6.2.10) and equation (6.2.14) are shown in figure 6.2.1, where the evolution of either quantity with S_l is strongly influenced by the λ parameter. In figure 6.2.1b, smaller values of λ are associated with clay and clay-containing soils, where water molecules are more closely bound in the mineral structure, which requires higher potentials to remove water. Higher values of λ are associated with looser, sandy soils, where water retention is based mostly on capillary effects. In this study, these functions are applied globally to all rocks in the model. For granite, this selection would correspond the macroscopic effect of the fracture network. The sensitivity of results related to the choice of λ is discussed in appendix C.

When water completely drains from a porous medium, it is usually the case that a stronger pressure head is required for water to re-infiltrate the pore space to a given saturation level. This is evident in the shift of the water retention curve for the primary wetting path compared to the primary drying path, leading to an overall nonlinear effect manifested in “scanning curves” between these two bounds for successive wetting and drying in partially unsaturated media. This effect is referred to as hysteresis, and it is caused by variations in the pore diameters of the medium. Water retreating from a wider pore channel into a thinner pore channel will experience less capillary forces compared to water trying to infiltrate the wider pore from the thinner; this is because the surface tension of the water is significantly stronger to overcome in the latter scenario. In this study, this phenomenon is not modeled for any re-wetting of the pore space that may occur in the approach to steady-state, i.e. the drying and wetting curves are one and the same. There are, however, applications of TOUGH2 that acknowledge hysteresis through a modification of S^* and λ in equation (6.2.14).

6.2.3 Material parameters

The system configuration is carried over from the neutronics analysis in chapter 4, where the material properties are shown in table 6.2.1. These values are used when devising the parameters in the ROCKS card within the TOUGH2 input deck, where the porosity is modeled by the critical FVF as the UO_2 is considered stationary and insoluble. For highly enriched

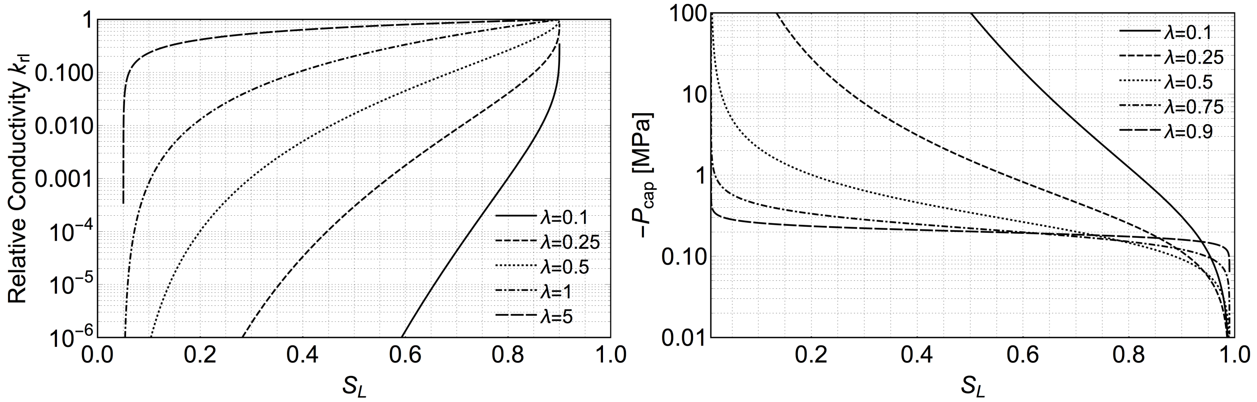

(a) Relative conductivity of the liquid phase, where $S_{ls} = 0.9$ is used for demonstration purposes.

(b) Negative of the capillary pressure.

Figure 6.2.1: Saturation-dependent models employed in the code.

minimum critical masses that do not require water in the pore space or otherwise have extremely low FVFs, a minimum 1% porosity is artificially employed. The compressibility and expansivity of the materials are ignored in this study to maintain results at constant volume, as deformation of the critical sphere is treated as part of the performance metric. As mentioned in chapter 4, the thermal conductivity (k), density, and specific heat (c_p) of the precipitate are average values calculated from the composition script, which are based on the VVF and HMVF of the area of interest. (The HMVF is set to zero for the shale and the granite.) Shale is the only rock that is given a fixed tortuosity factor of 1; the other rocks have τ calculated from a model based on the porosity and phase saturation.

Fluid properties of water and air at 15 MPa are shown in table 6.2.2, where $\mathcal{U}$ is the internal energy, $\mathcal{H}$ is the enthalpy, $\mathcal{S}$ is the spontaneity, β is the cubic thermal expansion coefficient, and μ is the dynamic viscosity. The water properties shown here are automatically tabulated in TOUGH2 using the ASME steam tables, which are based on relations established by the 1967 International Formulation Committee. [97] These tables are available up to $1500°F$ ($815.6°C$), although two-phase flow is only applicable to a fraction of the entire range. Although supercritical at this pressure level, air is represented as an ideal gas, and the quantity of air in the liquid phase is handled through Henry's Law (although these fractions are rather small). Although the presence of dissolved air in the water would demonstrate a voiding effect in the water laminate for the fractured geometry in a manner reminiscent to a BWR, for simplicity, these results will not be employed for the water compositions in chapter 7. In that chapter, it will be assumed that the two phases contain single molecular components, i.e. the liquid phase is represented completely by H_2O. Thermal expansion in air is assumed to be modeled according to $\beta = \frac{1}{T}$, if at all needed.

In the two phase calculation, the code has difficulty handling system parameters after the phase change of water, which occurs at $342.155°C$. [98–100] For this reason, in order to

Material	$\mathcal{K}\,[m^2]$	$k\,\left[\frac{W}{m-K}\right]$		$c_p\left[\frac{J}{kg-K}\right]$	$\rho_s\left[\frac{g}{cm^3}\right]$	τ	ϵ [%]	E [GPa]	B [GPa]	UTS [MPa]
		Dry	Wet							
Precipitate	10^{-15}	varies				0	FVF (1% min)	-	-	-
UO_2	-	7	7	260	10.95	-	-	180	165	-
Shale	10^{-18}	1.8	2.9	795	2.8	1	10	35	10	2-22
Granite	10^{-18}	2.79	3.2	840	2.75	0	1	20-50	50	4-25
Sandstone	10^{-15}	1.9	3.8	825	2.65	0	10	10-20	0.7	7-25

Table 6.2.1: Material properties used to guide inputs for MCNP composition scripts, TOUGH2, and strain model. Here, $\mathcal{K}$ is the intrinsic permeability, τ is a tortuosity correction factor, ϵ is the porosity, E is the elastic modulus, B is the bulk modulus, and UTS is the ultimate tensile strength.

Fluid	T [$°C$]	$\rho\left[\frac{kg}{m^3}\right]$	k$\left[\frac{W}{m-K}\right]$	$c_p\left[\frac{kJ}{kg-K}\right]$	$c_v\left[\frac{kJ}{kg-K}\right]$	$\beta\ [K^{-1}]$	$\mathcal{S}\left[\frac{kJ}{kg-K}\right]$	$\mathcal{H}\left[\frac{kJ}{kg}\right]$	$\mathcal{U}\left[\frac{kJ}{kg}\right]$	$\mu\ [Pa-s]$
Water	20.45 (l)	1005	0.60611	4.1400	4.1043	2.325E-04	0.29958	99.797	84.869	9.87E-04
	342.155 (sl)	603.52	0.46401	8.5132	3.0837	7.505E-03	3.6846	1610.2	1585.4	6.94E-05
	342.155 (sg)	96.727	0.11533	12.967	3.5826	1.698E-02	5.3106	2610.7	2455.6	2.28E-05
	815.6 (g)	30.62	0.11892	2.5196	1.9512	1.046E-02	7.2400	4130.4	3640.5	4.18E-05
Air	20.45 (sc)	177.7	0.034	1.241	0.7507	-	2.337	390.27	305.87	2.19E-05
	342.155 (sc)	79.99	0.0498	1.093	0.7757	-	3.171	750.23	562.71	3.27E-05
	815.6 (sc)	45.91	0.0735	1.167	0.8736	-	3.813	1285	957.98	4.65E-05

Phases: g=gas, l=liquid, sl=saturated liquid, sg=saturated gas, sc=supercritical

Table 6.2.2: Fluid properties at 15 MPa used to guide inputs for MCNP composition scripts and TOUGH2 results. [98–100]

broaden the temperature data available for the dynamics analysis, an assumption is made that the detailed mass transport of gas from the critical mass can be ignored past the phase transition. This is because the low-densities of the gas across the sphere are not likely to result in considerable changes to the average neutron collision density, and any absorptive qualities can be considered negligible. Any fine-scale effects of gas density in the shale reflector are likely to be superseded by the simultaneous effect of Doppler broadening.

While a two-phase pore fluid would have significant heat transfer effects, what matters most for the neutron economy is the density of the pore fluid. The density will fall in a continuum between the saturated values in table 6.2.2 based on the steam quality. Nonetheless, if the pressure is maintained at a steady-state level, the need to acknowledge the two-phase region as the temperature rises will be limited. Therefore, the assumption at hand will neglect a continuum of densities in the two-phase region above the single-phase gas density, although this level of detail should be not be necessary in the first place.

6.2.4 Source term

The source term of the problem is the energy generated from sustained chain reactions, which can be modeled according to the fission power distributions in critical sphere as analyzed in chapter 5. Given the dependence of the power profiles on the critical mass, averages of

Parameter	Mass [MTU]			
	0.1	1	5	100
f_0	0.13636	0.09522	0.08243	0.07387
μ	1.02706	0.84865	0.76785	0.69563
σ	0.38714	0.32598	0.28758	0.25040

Table 6.2.3: Average fit parameters of equation (5.3.1) for critical masses in the analysis.

the fit parameters for the truncated Gaussian distribution (equation (5.3.1)) were made per critical mass over all powers, enrichments, and configurations. These averages are shown in table 6.2.3 for the studied masses. Parameters for masses that may fall between those in the table are obtained through linear interpolation, while the nearest values are chosen for masses that may exceed the table boundaries.

The power fractions are obtained via equation (5.3.1) for each fractional radius evaluated at the middle of each discrete annulus of the critical sphere, which are then re-normalized. These fractions are then further normalized to the total power output being investigated and then inserted into the GENER portion of the input deck. This procedure is justified by the fact that the fuel-containing materials in MCNP and the volume elements in TOUGH2 were discretized, evaluated, and post-processed in the same manner, which allows f_r to be a portable means of assigning the fraction of the total power in the sphere.

The power distribution was found in chapter 5 to reach steady-state behavior, so rather than modeling time dependent power fractions from the depletion study, the time-averaged regression is employed for a constant total power output. This power level is found through an iterative procedure to meet a temperature near the liquid-gas phase transition, which will be described in the next section. At the moment, there is no understanding of the reactivity feedback that would influence total fission power output, and time-dependent effects from depletion are handled more appropriately in the consequence analysis. Therefore, this analysis concerns a reactor operating at a steady-state power level, where the power defect is counteracted through changes in the external reactivity feedback mechanisms.

6.2.5 Computation

In a manner similar to the treatment with MCNP in the previous chapters, an input file was employed where the material characteristics, thermal properties, initial conditions, dimensions, discretization, and heat distributions could be updated for each problem using a template. The parameters for the relative permeability and capillary pressure relationships were kept fixed in the template file along with time points for data printing, convergence criteria, time steps, and solver options. Fifty five time points were listed to capture both fine-scale and long-term behavior. A post-processing script was written that organized data for each element in a convenient format along with the specification of extreme values (e.g. of temperature and pressure) for parametric evaluation.

A TOUGH2 execution ends when a clear steady-state is reached, when convergence fails after a set number of iterations, or when steam table data are not available for constitutive parameters in a volume element. Only the first scenario is considered a successful calculation, and results will only be presented for these conditions. The conservatism of this particular study promotes the full scope of precipitate de-saturation with heating; therefore, the saturation point of water is used as an upper limit goal for achieving a maximal steady-state temperature. This will allow the Doppler feedback study to acknowledge a diverse range of unsaturated moderator distributions.

For a given critical volume, an iterative approach is utilized to find the power-output corresponding to a maximal steady-state temperature of $342.155 \pm 0.1\,°C$ via the bisection method. Power distributions are created from tested total power levels using the aforementioned interpolation procedure, where $q_o = 1\,kW_t$ is used as an initial guess. A factor of 20 is used to adjust bounds on the total power based on the results for the maximum temperature, in which case q_0 becomes the lower bound or upper bound when devising the next test value. In the event q_0 is the upper bound, 50 kW_t is the lower bound, and for opposite scenario, 100 kW_t is used as the upper bound. For tests falling below the temperature goal, the test value becomes the lower bound, and the new test value is increased to the midpoint of the upper and lower bounds. In the event the test falls above the temperature goal, the test value becomes the upper bound. A failed calculation is taken to imply that the total power is too high, since it is likely the solver cannot find steam table parameters for the rapid changes imparted by the test value. The bisection method continues until a successful calculation reaches the temperature goal within the margin of error.

6.3 Results

6.3.1 Optimal power levels

The total power (q_{opt}) required to achieve a maximum temperature (T_{max}) of $342.155 \pm 0.1°C$ is shown in tables 6.3.1 and 6.3.2 for two different values of S_l^{env}, along with minimal values of average saturation and liquid density observed in the critical mass $\left(S_{l,min}^{crm} \text{ and } \rho_{l,min}^{crm}\right)$. The simulation ceases when the average temperature of any volume element reaches this criterion, which likely corresponds to one volume element of the heat-emitting sphere. Therefore, the average temperatures (T_{avg}) of the critical masses are lower than this criterion, where the most considerable discrepancies are observed in smaller critical masses. Due to this procedure, the saturation of the critical mass cannot approach zero. Nonetheless, when evaluating k_{eff} in the integrated neutronics analysis, the fine-scale effects on the choice of water content between $S_{l,min}^{crm}$ and 0% are not expected to be significant.

The values of q_{opt} lie on the order of hundreds of watts and vary mostly linearly with the radii of the critical spheres, as shown in figure 6.3.1. For power levels meeting the fixed temperature difference with the environment of $\Delta T_{opt} = T_{max} - T_{\infty} = 342.155°C - 20.45°C = 321.71°C$, this behavior should be expected. Imagine a critical sphere of radius r_i can be

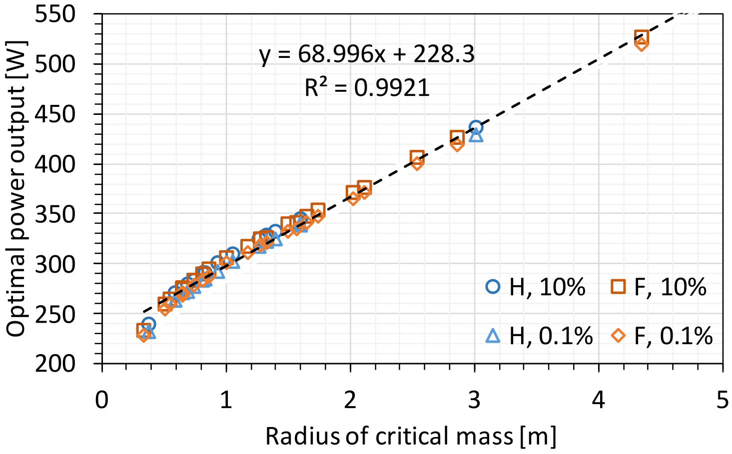

Figure 6.3.1: Power output needed to reach liquid-gas phase boundary as a function of the critical radius.

treated with a lumped temperature equal to T_{max} and constant power generation q_{opt}, and that this sphere is surrounded by a much larger solid volume with outer radius r_o, thermal conductivity k, surface temperature T_∞, and no heat generation from fission. Assuming steady-state heat transfer, no angular dependence on conduction, and a temperature-independent thermal conductivity, Fourier's law (6.2.1) can be represented as:

$$q = -k(4\pi r^2)\frac{dT}{dr}$$

The differentials can be separated, and the lefthand side can be integrated over the radii bounding the large annulus and the righthand side over the corresponding surface temperatures:

$$q\int_{r_i}^{r_o}\frac{dr}{r^2} = -4\pi k\int_{T_{mas}}^{T_\infty} dT$$

In the solution, the thermal resistance (R) is defined as the term relating the heat rate and the change in temperature, and this will vary with the inverse of the difference in radii. Since the outer shell is significantly larger, the effect is that q_{opt} scales proportionally with the radius of the critical mass, as shown in equation (6.3.1).

$$q^m_{opt} = \frac{\Delta T_{opt}}{R_m} = \frac{\Delta T_{opt}}{\frac{1}{4\pi k}\left(\frac{1}{r_{i,m}} - \frac{1}{r_{o,m}}\right)} = 4\pi k\Delta T_{opt}\frac{r_{o,m}r_{i,m}}{r_{o,m}-r_{i,m}} \propto \Delta T_{opt}r_{i,m},\; r_{o,m} \gg r_{i,m} \quad (6.3.1)$$

The thermal power levels of 100 and 1000 W_t assumed in chapter 5 encompass the range of q_{opt}, making the range of results from that study applicable to this scenario. For a given critical radius, the power required to reach the phase boundary is a few watts lower when the heat sink is drier, and the corresponding time to steady-state is also reduced. In the simulation, steady-state is achieved on the order of 50,000 years, which is plausible when comparing the critical radii, which are on the order of meters, with the relatively low power levels, which could be found in a computer graphics card or an electric bicycle.

6.3.2 Temperature and saturation

Tables 6.3.1 and 6.3.2 demonstrate that the use of a lower S_l^{env} corresponds to a reduction in the minimum average saturation observed in the critical mass, where $S_{l,min}^{crm}$ is about 25% for $S_l^{env} = 10\%$ and 15% for $S_l^{env} = 0.1\%$. This is expected as the magnitude of P_{cap} is larger for lower values of S_l (see figure 6.2.1b), and increased capillary suction will drive water out of the saturated rock into the dry neighboring pores more strongly.

The behavior of temperature and saturation over time is shown in figure 6.3.2 using the critical dimensions of the highly-enriched homogeneous precipitate as an example. As the system begins heating, the average temperatures rise steadily while the system remains saturated. This rise in temperature is higher for smaller precipitates, which appear to reach what vaguely resembles a steady-state. After a short period near steady-state, around ten years, dT/dt increases substantially, and the temperature increases until the final steady-state level is reached.

The saturation begins to decrease around 500 years into the simulation when average temperatures begin to exceed approximately $100°C$. The fall from $S_l = 1$ to 0 over time is exponential (linear on the log-scale plot) between $100°C$ and the saturation temperature. A linear, inverse relationship between temperature and saturation is highlighted in figure 6.3.3 for discrete regions in the critical mass in the dry environment, where the threshold temperature appears to lie between $75°C - 100°C$. The linear trend in $S_l(T)$ is less consistent for the smaller critical masses. It is clear that per given temperature, the corresponding saturation is lowest at the surface of the sphere, and that this difference is much wider for smaller precipitates. This irregular distribution of moderator is liable to harden the neutron spectrum at the surface of the sphere, and since the fast fission factor is not appreciable, the role of the reflector will be especially important.

When the saturation of the far-field rock is greater, figure 6.3.4 shows that the threshold temperature for the drop in saturation is larger, lying between $200°C - 250°C$. This is caused by increased resistance to water exfiltration to the environment, and results in a more drastic reduction in saturation as the temperature increases to the phase boundary. In these plots, a gradual decline in the initial saturated state can be observed before the threshold temperature. Altogether, the results imply that a critical mass formed in wetter environments will have consistently more water moderator available as temperature increases, which will likely allow criticality to be sustained for longer provided the effects from Doppler broadening are not too significant.

In terms of the spatial distribution of saturation, figure 6.3.5 shows that variation is strongest in the rock layers surrounding the critical mass. There is not appreciable variation

Set	M_c	$r_c\,[m]$	FVF	$S_l^{env} = 10\%$						$S_l^{env} = 0.1\%$					
				$q_{opt}\,[W]$	$t\,[yr]$	T_{max}	T_{avg}	$S_{l,min}^{crm}$	$\rho_{l,min}^{crm}$	$q_{opt}\,[W]$	$t\,[yr]$	T_{max}	T_{avg}	$S_{l,CRM}^{min}$	$\rho_{l,min}^{crm}$
2	5	1.056	0.23225	309.77	7.32E+04	342.14	335.16	0.244	630.73	302.23	3.46E+04	342.12	332.68	0.143	639.45
	10	1.334	0.20325	328.32	6.90E+04	342.13	336.10	0.250	627.49	322.75	3.23E+04	342.13	335.71	0.137	628.91
	100	3.018	0.16625	435.94	9.68E+04	342.13	338.85	0.247	617.12	428.52	2.97E+04	342.14	338.21	0.151	619.70
3	1	0.691	0.2215	280.08	8.07E+04	342.13	330.67	0.239	645.66	272.60	3.80E+04	342.11	327.88	0.139	654.43
	5	1.273	0.1405	324.61	7.54E+04	342.14	336.28	0.243	626.77	316.78	3.34E+04	342.09	333.82	0.144	635.64
	10	1.608	0.1215	345.02	1.06E+05	342.13	336.16	0.231	627.39	339.45	3.15E+04	342.13	335.91	0.138	628.27
4	0.5	0.592	0.2035	270.80	8.19E+04	342.13	328.98	0.239	650.87	263.20	3.93E+04	342.08	325.98	0.138	659.97
	1	0.819	0.1615	291.21	5.51E+04	342.13	332.57	0.260	639.55	283.09	3.67E+04	342.06	329.50	0.140	649.58
	5	1.401	0.0955	332.03	7.50E+04	342.13	335.89	0.247	628.32	325.19	3.26E+04	342.11	334.48	0.145	633.39
5	0.5	0.650	0.158	276.37	8.71E+04	342.13	329.87	0.236	648.20	270.80	3.79E+04	342.13	329.10	0.130	650.56
	1	0.832	0.1185	291.21	1.05E+05	342.13	331.71	0.228	642.53	284.83	3.63E+04	342.12	330.11	0.140	647.71
	5	1.603	0.079	345.02	7.99E+04	342.13	336.44	0.244	626.32	338.53	3.16E+04	342.13	335.51	0.137	629.74
6	0.1	0.380	0.31475	239.26	1.22E+05	342.12	318.56	0.225	679.56	232.65	7.21E+04	342.11	316.34	0.125	685.17
	0.5	0.744	0.13575	283.79	1.02E+05	342.13	330.52	0.229	646.28	277.12	3.74E+04	342.06	328.58	0.140	652.41
	1	0.938	0.099	300.49	5.00E+04	342.13	333.49	0.266	636.60	292.78	3.55E+04	342.07	331.02	0.141	644.87
	5	1.603	0.05925	345.02	8.38E+04	342.13	338.71	0.242	626.56	339.45	3.11E+04	342.13	336.25	0.137	627.00

Table 6.3.1: Power levels Q_{opt} of critical homogeneous masses (in MTU) needed to achieve saturation temperature at steady-state based on the saturation of the encapsulating granitic environment (S_l^{env}). Temperatures are in celsius, while liquid densities are shown in units of $\frac{kg}{m^3}$.

Set	M_c	$r_c\,[m]$	FVF	$S_l^{env} = 10\%$						$S_l^{env} = 0.1\%$					
				$q_{opt}\,[W]$	$t\,[yr]$	T_{max}	T_{avg}	$S_{l,min}^{crm}$	$\rho_{l,min}^{crm}$	$q_{opt}\,[W]$	$t\,[yr]$	T_{max}	T_{avg}	$S_{l,min}^{crm}$	$\rho_{l,min}^{crm}$
1	100	2.546	0.121	406.25	8.80E+04	342.13	338.71	0.246	617.68	399.76	2.75E+04	342.14	338.33	0.145	619.19
	500	4.354	0.105	526.86	9.60E+04	342.13	339.50	0.258	614.53	519.43	2.37E+04	342.20	339.64	0.156	613.92
	1000	5.484	0.103	608.50	9.41E+04	342.13	339.63	0.271	614.03	599.22	3.59E+04	342.13	339.43	0.155	614.82
2	5	1.010	0.103	306.05	6.07E+04	342.13	334.12	0.257	634.51	300.49	3.41E+04	342.13	333.43	0.134	636.91
	10	1.277	0.072	324.61	6.31E+04	342.13	335.75	0.255	628.80	319.04	3.22E+04	342.13	335.25	0.135	630.62
	100	2.867	0.037	426.66	8.03E+04	342.13	339.02	0.250	616.45	419.24	2.72E+04	342.14	338.24	0.142	619.55
3	0.5	0.509	0.199	259.67	1.18E+05	342.12	325.26	0.225	661.88	254.28	4.06E+04	342.07	324.09	0.137	665.24
	1	0.653	0.113	276.37	8.86E+04	342.13	329.80	0.236	648.43	270.80	3.79E+04	342.12	328.75	0.130	651.74
	5	1.181	0.018	317.19	7.51E+04	342.13	334.52	0.248	633.21	311.45	3.32E+04	342.10	333.79	0.142	635.73
	10	1.500	**0.010**	339.45	8.25E+04	342.13	336.85	0.240	624.74	332.44	3.15E+04	342.11	335.24	0.144	630.75
4	0.5	0.549	0.102	265.23	1.15E+05	342.12	326.94	0.226	657.10	259.67	3.96E+04	342.08	325.70	0.138	660.76
	1	0.744	0.047	283.79	1.04E+05	342.13	330.50	0.229	646.36	277.93	3.70E+04	342.11	329.19	0.139	650.52
	5	1.333	**0.010**	326.46	4.79E+04	342.07	334.59	0.281	633.02	320.90	3.26E+04	342.08	334.24	0.143	634.22
	10	1.741	**0.010**	353.37	6.68E+04	342.13	336.43	0.256	626.37	346.88	3.09E+04	342.06	335.52	0.145	629.73
5	0.5	0.650	0.069	274.51	1.21E+05	342.12	328.30	0.223	653.11	268.95	3.84E+04	342.07	327.17	0.138	656.54
	1	0.819	0.012	289.41	5.06E+04	342.11	330.61	0.277	646.14	283.96	3.63E+04	342.11	330.08	0.140	647.81
	5	1.569	**0.010**	341.31	4.74E+04	342.06	335.14	0.283	631.08	335.51	3.19E+04	342.06	334.79	0.144	632.34
	10	2.029	**0.010**	371.00	8.86E+04	342.13	336.71	0.243	625.36	364.44	3.02E+04	342.08	335.96	0.146	628.18
6	0.1	0.346	0.237	233.69	1.30E+05	342.11	316.80	0.224	683.92	228.24	5.06E+04	342.07	315.38	0.133	687.48
	0.5	0.651	0.022	275.27	5.21E+04	342.11	328.37	0.276	653.01	269.79	3.81E+04	342.09	327.73	0.138	654.92
	1	0.867	**0.010**	294.92	7.56E+04	342.13	332.91	0.242	638.48	287.73	3.59E+04	342.10	330.52	0.140	646.41
	5	1.659	**0.010**	347.80	9.77E+04	342.13	336.15	0.234	627.36	341.19	3.16E+04	342.09	335.01	0.145	631.54
	10	2.116	**0.010**	376.56	8.61E+04	342.13	336.88	0.244	624.75	371.00	2.90E+04	342.13	336.97	0.138	624.38

Table 6.3.2: Power levels Q_{opt} of critical fractured masses (in MTU) needed to achieve saturation temperature at steady-state based on the saturation of the encapsulating granitic environment (S_l^{env}). Assumed FVF values are shown in bold. Temperatures are in celsius, and liquid densities are shown in units of $\frac{kg}{m^3}$.

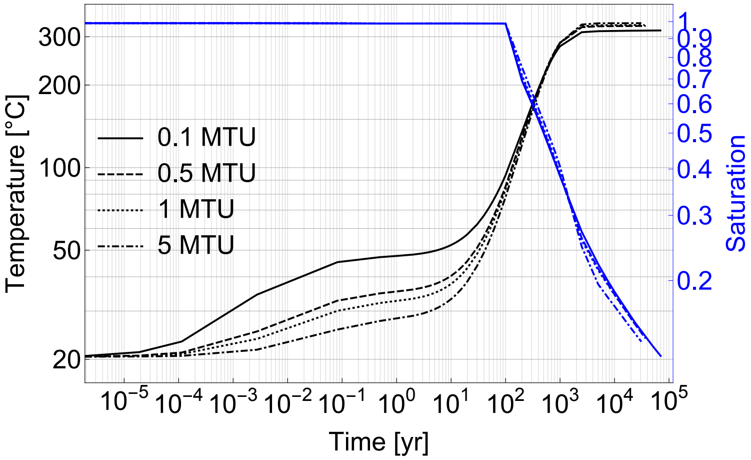

Figure 6.3.2: The spatially-averaged behavior of temperature (black, left axis) and saturation (blue, right axis) over time in the TOUGH2 simulation of the 6 wt% homogeneous critical masses, assuming $S_l^{env} = 0.1\%$.

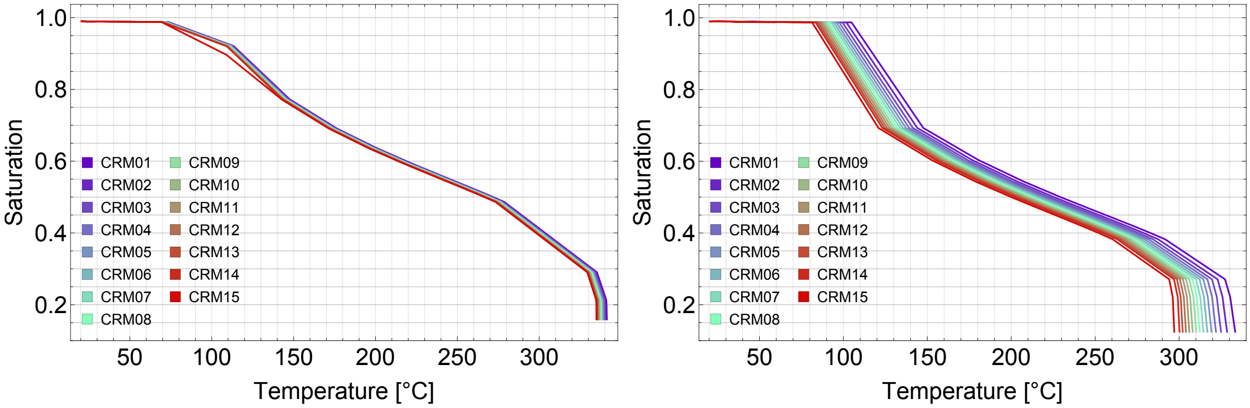

(a) Homogeneous, 2 wt%, 100 MTU

(b) Homogeneous, 6 wt%, 0.1 MTU

Figure 6.3.3: The behavior of saturation with temperature for each discrete region of the critical mass ("CRM") as steady-state is reached for $S_l^{env} = 0.1\%$. The regions are numbered from the core outwards.

in the critical mass itself, although for larger precipitates, the inner core may be significantly more desaturated at steady-state.

6.4 Discussion

The TOUGH2 code has been used to obtain coupled results of system temperature and fluid behavior based on mass and energy balances. These results are necessary to describe the

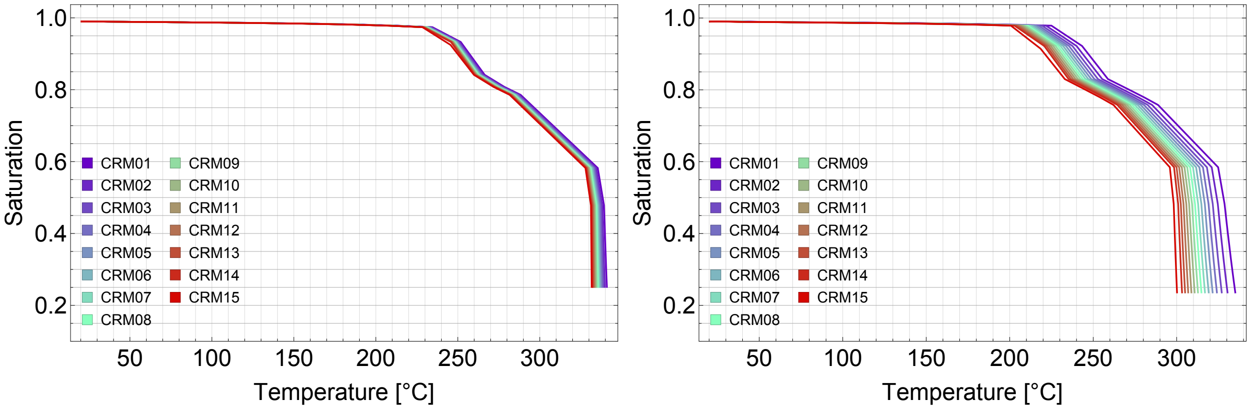

(a) Homogeneous, 6 wt%, 5 MTU (b) Homogeneous, 6 wt%, 0.1 MTU

Figure 6.3.4: The behavior of saturation with temperature for each discrete region of the critical mass ("CRM") as steady-state is reached for $S_l^{env} = 10\%$. The regions are numbered from the core outwards.

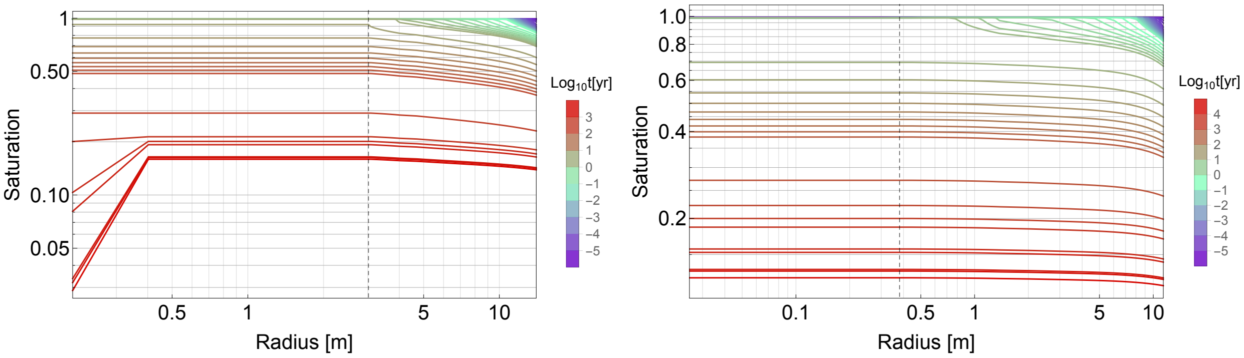

(a) Homogeneous, 2 wt%, 100 MTU (b) Homogeneous, 6 wt%, 0.1 MTU

Figure 6.3.5: The saturation distribution evaluated at the $\log_{10}$ of time for $S_l^{env} = 0.1\%$. The critical radii are indicated with vertical lines.

state of the unsaturated critical system using fundamental heat and mass transfer principles given the onset of heating from fission. Gaussian-type fits based on results from chapter 5 were employed to model the spatial dependence of the source term. In order to maximize the breadth of temperatures and saturations analyzed, and to desaturate the critical mass as much as possible, an iterative method was used to identify the total power outputs in the critical masses that would lead to steady-state temperatures near the liquid-gas phase transition temperature. The power levels were commensurate with the thermal outputs specified in the depletion study, which demonstrates convergence with the data used to describe the fission heat rate.

The results indicate that while the deposition may occur in a saturated medium, the proximity to the vadose zone will demonstrably effect the exfiltration of water as the temperature increases. A formation deep into the saturated zone will be able to retain more water in the critical mass as temperature increases, although a point will be reached where the saturation is reduced drastically. This would be more favorable to sustaining criticality as the system evolves. However, since the ultimate saturation level in this scenario is on par with that of the environment, the complete scope of voiding is not assessed. Therefore, the approach favoring stronger desaturation with a dryer environment is still within the conservative framework.

Inverse behavior was observed between temperature and saturation in the critical mass past a certain temperature threshold. This finding can be used to roughly approximate the effects saturation will have on heat transfer terms in the analysis of chapter 8. It is proposed that a future iterations of this study characterize the initial saturation conditions of the environment beyond the granite layer to vary in a spatially continuous manner. This would represent transitions to the capillary fringe and vadose zone more accurately, as opposed to the extreme case in this study where an interface is imposed between a saturated zone and a zone that is essentially dry. In terms of addressing fine spatial variation of pore water characteristics in the critical mass itself, behavior was observed to be rather uniform, which effectively mirrors the assumptions made in section 4.4.3. If the granite region beyond the shale reflector is modeled within a continuous spectrum of saturation, it is likely that this will cause more radial dependence in water content of the precipitate, which would make for more interesting neutronics calculations. Nonetheless, results for larger precipitates indicated nearly full desaturation at the center of the critical mass at the steady-state temperature.

The analysis was limited in addressing fine-scale behavior at the phase transition of water in the pore-space. In particular, the range of densities of the two-phase mixture were not calculated, and this may impart discontinuities when the system states are devised in chapter 7. The treatment of boiling in porous media is not expected to be very straightforward, and within the scope of this study, such a task would extend too far into a simulation of reality. The most significant aspect that must be carried to the detailed neutronics analysis is whether a specified temperature for a cell has a physical relationship to the presence of pore fluid in its composition. To that end, considering the strong reactivity effects from fluid removal from a just-critical mass (see section 4.4.3), the characterization of fluid densities and volume fractions in the critical mass as it begins heating should provide an adequate level of detail. Altogether, while the study is comprehensive in modeling the combined flow of water and air in the precipitate, the limited breadth in temperatures imposes restrictions on the scope of the dynamics analysis. Therefore, a means of extending the temperature behavior when the critical mass is completely drained of liquid will be proposed in chapter 7.

Chapter 7

Reactivity feedback in unsaturated critical mass

7.1 Introduction

In order to analyze reactivity feedback for a porous medium with heat generation, the temperature-dependent water content of the critical mass must be incorporated into the neutronics evaluation. It is clear from the results of the previous chapter that the behavior of heat and water exfiltration cannot be decoupled for the dimensions of relevance to criticality, and the assumption of spatial dependence is considered to be an innovation on the dynamics treatment.

This chapter will discuss the integration of results from the thermo-hydrological simulation with a neutronics analysis employing the Doppler effect. The study is motivated by the assumption that heat and mass transfer in the reactor cannot be decoupled due to the combined capillary and permeability effects in a porous medium. After incorporating average pore fluid behavior and temperature into the neutronics evaluation, the results can be used to develop analytical relationships for the combined reactivity feedback of heating and desaturation. These models can be applied directly to the QSS analysis in the next chapter.

7.2 Methodology

7.2.1 Computation

The critical system is split into discrete radial units in a manner similar to chapter 5, although the reflector and surrounding granite are also discretized and given their own materials in MCNP. These discrete regions exactly mirror the volume elements employed in chapter 6 except for the infinite extent of granite at the boundary (which is modeled as void). However, it is not anticipated that substantial quantities of neutrons will be moderated in the ten meter-thick granite layer and migrate back to the critical mass. Given the low collision density, spatial variation is modeled mostly out of diligence and to follow the TOUGH2 mirroring scheme in the input deck construction. A Perl script was written to run post-processing calculations of the TOUGH2 results that incorporates the following data for each cell for each time in the problem:

- Density of the pore liquid (water, where dissolved air is ignored)
- Density of the pore gas (air)
- Average temperature of each cell
- Average saturation of each cell

Using the time- and space-dependent saturations and fluid densities from the TOUGH2 results, the average density of each cell is modified in the homogeneous configuration using the rock composition script (see appendix A). As mentioned in chapter 4, the densities of the UO_2 laminates in the fractured geometry are fixed while the fluid densities (ρ_l, ρ_g) are specified for those slabs directly from the results. Two approaches will be described for modeling the densities of the shale slabs. The time component from the unsaturated heat and mass transport simulation is only significant in providing different compositions from TOUGH2 results; it has absolutely no relationship to the time component of the dynamics analysis to follow in chapter 8. The results in this chapter are obtained by creating an MCNP input file for each of these virtual "time points."

The fractured geometry will simulate spatial variation in the saturation by varying the volume fractions of air and water by changing the thickness of their slabs (see figure 4.3.1). In this case, the saturation of each spherical discretization determines the extent which the liquid region extends into the fracture. Figure 7.2.1 shows an example of a geometry plot showing the different components of the heterogeneous critical mass in the radial discretization context. The planes separating water and air vary as determined by the radial bins mirrored in the TOUGH2 calculation, although in this particular plot, due to the spatial uniformity of S_l expected from figure 6.3.5, these planes merge into the same surface. An example of fine scale variation in the planes is shown in appendix B for a system that is just beginning to desaturate. The water laminate is kept in contact with the ore as a conservative measure, although it is not certain how significant this exact placement may be. The average temperatures from the TH results are applied to each material in the repeating unit within the spherical shell region; this implies a smeared treatment for each fracture unit in each annulus. The densities of the fluids are carried over directly from the TH study, and the initial compositions of the ore are held constant and not modified for depletion. There are two approaches for devising the spatial composition variation of the fracture rock laminates:

1. The composition and density of the shale is modified to meet the average saturation and fluid densities of the cell, such that the water content of the shale is displaced by air at the same rate as the fracture opening.

2. The density and composition of shale are held constant to correspond to full saturation with water, regardless of the average temperature of the cell (even for $T > 342.155°C$).

The first approach treats the critical mass in a more global manner and would acknowledge the role of fracture rock in the evolution of multiplication. As mentioned in chapter 6, any dual-porosity effects that would affect the water content of the rock matrix relative to the fracture are ignored in this approach. The uniformity of the saturation level is considered part of the effective continuum assumption, which applies to approach 2 as well. The assumption retains conservatism as a greater amount of water moderator is reduced per change in temperature, which is expected to lead to stronger reactivity feedback.

The second approach assumes that water is effectively trapped in shale due to very low permeability and intermolecular forces, and that water exfiltration from these slabs will be negligible compared to the neighboring open conduit. This allows for an examination of fracture-specific effects when water is withdrawn, and the full moderation effects of the slab as employed in chapter 4 are conserved. This is anticipated to enhance the reactivity levels per given temperature and saturation, although the corresponding feedback effects may not be as negative. In reality, since the rock laminate will de-saturate at a slower rate than the adjoining fracture, the two approaches can provide bounding results on the natural phenomenon.

Although the first time step of the TH simulation is very small and bound to emulate the initial conditions imposed in chapter 4, there is anticipated to be initial reactivity differences engendered either by nuances in the more detailed composition-assignment procedure or else numerical consequences resulting from the deployment of more diverse MCNP materials in the slab/sphere geometry. Therefore, a slightly supercritical configuration was chosen for approach 1 out of diligence, such that $\rho_0 \approx 0.02$ was used as opposed to $\rho_0 \approx 0$. The fractured configurations meeting $k_{eff} \approx 1.02$ are shown in table F.1.2 on page 268, where the radii are very similar to those in table 4.4.2. The similar geometries should make the a direct utilization of the just-critical TOUGH2 data in the supercritical configuration to be excusable and preclude separate TH simulations. Furthermore, the ultimate product of this study is based on the fluctuations of reactivity, not the reactivity levels on their own, so consistency with TH results is the most important consideration.

7.2.2 Extension of temperature results

In chapter 6, the TH simulations were conducted until convergence was reached as close as possible to the saturation point of water at 15 MPa ($342.155°C$). Given the configuration of the problem as two-phase, the code is not able to handle the one-phase mass transport of air. Nonetheless, the flow of air and changes in its density with temperature are not expected to be of importance to a neutronics evaluation since the densities are far too low to substantially affect absorptions.

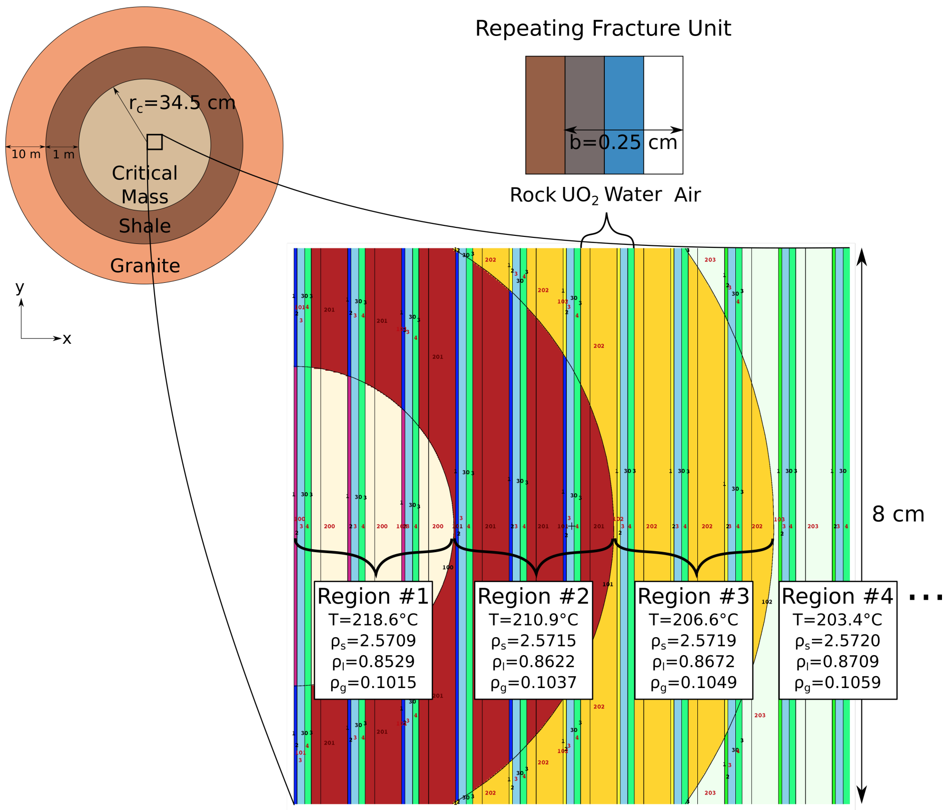

Figure 7.2.1: An xy cross section of the MCNP input geometry for the partially unsaturated 0.1 MTU 6 wt% fractured configuration colored by material number, where spherical shell discretization is shown for four regions 8 cm from the origin. Numbered labels appear in red for materials and black for surfaces. The saturation is approximately 54% throughout the system at 400 years into the TOUGH2 simulation, driven at $q_{opt} = 228\,W$. The densities of shale, water, and air all vary by shell, and are shown in units of $\frac{g}{cm^3}$.

To expand the scope of the Doppler feedback analysis and the upper bound temperature of the consequence analysis, the assumption is made that beyond the boiling point (T_{BP}), a simple heat transfer circuit model can be applied to extrapolate temperature points up to a point below the representative shale melting point ($T_{MP} = 1300°C$). This would allow for completely de-saturated results to be obtained for the system. It must be noted that at extremely high temperatures above $\approx 800°C$, the effects of silica crystallization described in the Bowen's Reaction Series are ignored. Also, the effects from the transition of smectite to illite in the clay component of shale above $\approx 100°C$ are also ignored. Either of these considerations would affect the density and chemical composition of either component.

The system components are labeled in a sequence of elements i that are indexed radially outward. In the extrapolation procedure, the heat fluxes q_i in each element are employed from the last evaluated time point in TOUGH2, which correspond to steady-state. The saturation S_l of each element is a based on a linear interpolation between the steady-state value and 0 using the boiling point of water:

$$S_{l,i} = \begin{cases} S_{l,i-1} + \left(\frac{S_{l,i-1}}{T_{i-1}-T_{BP}}\right)(T_{BP} - T_i) & T_i \leq T_{BP} \\ 0 & T_i > T_{BP} \end{cases} \tag{7.2.1}$$

While another approach could involve extrapolation of the $S_l(T)$ behavior for $T > T_{BP}$, the rapid changes in S_l as the $T \rightarrow T_{BP}$ observed in figure 6.3.3 on page 125 are supportive of this strict cut-off. The thermal conductivity uses the known dry and wet densities calculated from the composition scripts as a function of liquid saturation:

$$k_i = k_{dry}(1 - S_{l,i}) + k_{wet}(S_{l,i}) \tag{7.2.2}$$

Once thermal conductivity is known, as mentioned in section 6.3.1, the thermal resistance R for the spherical annulus can be obtained using the inner and outer radius of the annulus (r_{in} and r_o, respectively) in equation (7.2.3). This relationship is applicable for steady state.

$$R_i = \frac{r_o - r_{in}}{r_o r_{in}} \frac{1}{4\pi k_i} \tag{7.2.3}$$

This resistance is used to to calculate the temperature difference in the element, which in turn provides the average temperature T_i:

$$\Delta T_i = q_i R_i \Rightarrow T_i = T_{i-1} + \Delta T_i \tag{7.2.4}$$

The temperature of the innermost element is arbitrarily chosen based on increments that increase from the last-calculated centerline temperature all the way to 1250°C. The air density is determined using the ideal gas law in equation (7.2.5), where $\mu_{air} = 28.96 \frac{g}{mol}$, P_0 is 15 MPa (or whichever steady-state pressure was calculated in TOUGH2) and $\mathcal{R}$ is the ideal gas constant.

$$\rho_{g,i} = \frac{P_0 \mu_{air}}{\mathcal{R}\,(T_i + 273.15)} \tag{7.2.5}$$

The water density is altered using the coefficient of thermal expansion, $\beta_l = 2.7{*}10^{-4}\,K^{-1}$, and the temperature change, according to equation (7.2.6).

$$\rho_{l,i} = \frac{\rho_{l,i-1}}{1 + \beta_l\,(T_i - T_{i-1})} \tag{7.2.6}$$

7.2.3 Doppler broadening

Effects of resonance absorption have been discussed in some detail in the preceding chapters. The Doppler effect concerns the changes in neutron interaction probability when temperature elevates the average molecular motion of target nuclei, which is particularly significant among the sharp peaks of resonance regions. Doppler broadening describes the smearing effect of peaked resonances when averaging is applied to account for the relative speed of the target nucleus, such that the cross section peak drops but otherwise spreads in energy. The latter aspect is more significant and the energy range over which absorption can occur is increased. This decreases the energy self-shielding and flux depression in the fuel around the resonance energies, leading to greater net resonance absorption and reductions in fission reaction rates.

The On-The-Fly Doppler Broadening (OTFDB) code built into MCNP6.1 is used to simulate the Doppler effect with the evolving temperature distribution of the critical mass. [101] For all nuclides specified in the problem materials, the code uses ENDF data at different temperatures to create an interpolated energy grid based on a temperature range with set intervals. When a collision is scored in the Monte Carlo simulation, the code employs the user-specified cell temperature to alter both the collision kinematics and absorption cross sections based on the Cullen and Weisbin exact Doppler broadening equation. [102]

A script was written to run the OTFDB code and create interpolations for the every nuclide present in any material of the simulation based on a range of temperatures from 0 to $1300°C$. The interpolations are made in $10°C$ intervals over the temperature range using an energy grid based on $100°C$ bins. A text file is created with all processed nuclides that can be read and directly inserted into as the OTFDB data card deck in the MCNP input. All interpolation files are housed in an independent directory, and all directories where calculations need this code have symbolic links to the these files.

7.2.4 Regression

In order for the results of this study to be portable to the consequence analysis, the reactivity curves should ideally be representable as continuous functions of temperature. This would allow for the feedback coefficients to also be modeled as continuous functions. Although these coefficients will be employed numerically, it is anticipated that this methodology would lead to more stable results. Furthermore, future studies can use these solutions to develop tailored analytical approximations.

In an engineered reactor, when the fuel is treated adiabatically, the reactivity feedback coefficient from the Doppler effect is known to take the form of a power law, such as that shown in equation (7.2.7). The power x is about 0.5 for thermal reactors and 1.0 for fast reactors, and the magnitude of α_T is much larger in the former because thermal neutrons are more likely to interact with resonances. [103] Therefore, it is hypothesized that configurations lending to spectrum hardening will see reductions in the temperature feedback coefficient.

$$\alpha_T(T) = \frac{\alpha_T^0}{T^x} \tag{7.2.7}$$

From chapter 4, it was shown that the moderator defect is a lot stronger for the homogeneous geometry compared to the fractured geometry. Furthermore, the exfiltration of water from the critical mass due to heating was confirmed in chapter 6. Therefore, it is expected that there may be discontinuous behavior in results for the homogeneous sphere depending on the relative impact of Doppler broadening. These results may not demonstrate conformance to power-law behavior for the full scope of temperatures, and different regressions will be proposed to handle this expected behavior.

7.3 Results

For each configuration, reactivity data was calculated for every time point of the TOUGH2 simulation and the appended figures from the circuit model. The results for reactivity versus temperature were obtained for both the homogeneous and fractured geometries. The temperatures indicated in the plots are the average temperatures of the critical masses, hence the $342.155°C$ transition may not be explicit.

7.3.1 Homogeneous

The behavior of reactivity versus average system temperature is shown in figure 7.3.1. While the effects from Doppler broadening are not very noticeable when the critical mass contains most of its water, the increase in temperature eventually leads to a reduction in reactivity. There is a decrease in reactivity when desaturation begins to take place at a threshold temperature of $100°C$, and this is closely followed by a discontinuity in behavior around T_{BP}, when liquid is completely evacuated from the pore space.

Before this discontinuity, behavior is reminiscent of the reactivity behavior observed in the uniform exfiltration study (see figure 4.4.6 on page 74). When pore water is removed from the 5 MTU critical mass, the reactivity is observed to drop to -1.0 for the 6 wt% composition and -2.0 for the 2 wt% composition. From table 4.4.1, the moderator defect was observed to be -0.8 and -1.6 for either of those precipitates, respectively. Therefore, while it is clear that the Doppler effect is appreciable during the desaturation process, the effect from moderator removal is ultimately the strongest.

After T_{BP}, the reactivity decreases monotonically but at a much more gradual rate, where changes come purely through Doppler broadening in the heated fuel and, to a presumably lesser extent, the rock. The drops in reactivity are lower for more highly enriched precipitate compositions because fewer neutrons are absorbed in the resonances of fertile U-238. The decreases in ρ are also more significant for smaller critical masses because of greater neutron leakage.

In figure 7.3.2, the percentage of neutrons causing fission is plotted versus temperature based on thermal, epithermal, and fast energy ranges. As the system starts heating, the lower-enriched precipitates retain the most thermal character. However, when the system is depleted of water, the effects of spectrum hardening are substantial for these compositions, where a quarter of all fissions are caused by neutrons above $100\,keV$ in the 2 wt% precipitate. This signifies that neutrons cannot effectively moderate past resonance energies in the rock. Conversely, the role of thermal and epithermal neutrons are relatively stronger in the highly enriched compositions of the dry region.

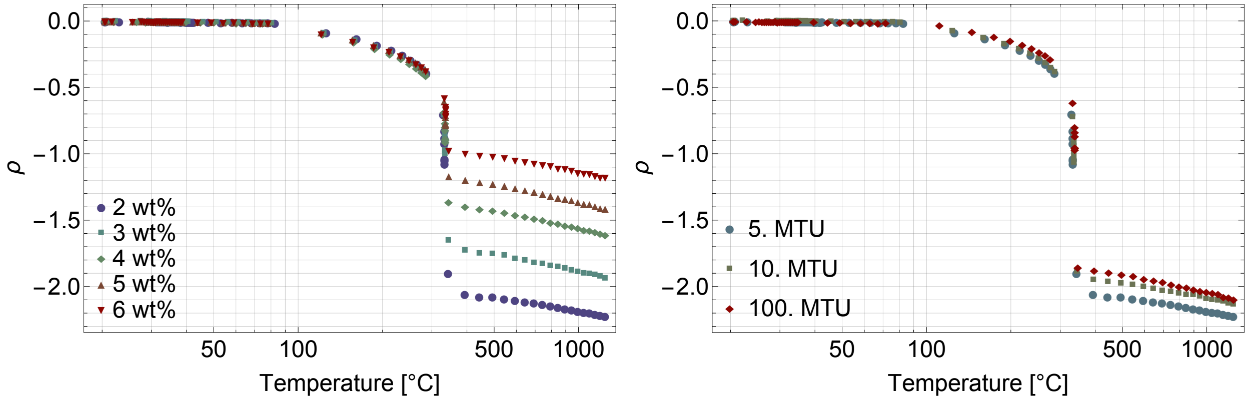

(a) 5 MTU, by enrichment.

(b) 2 wt%, by mass.

Figure 7.3.1: Reactivity feedback with increasing average temperature of configurations in the homogeneous approach.

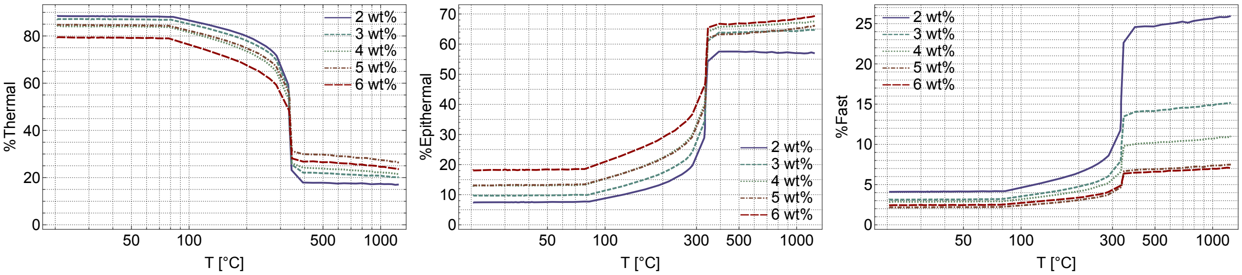

(a) $< 0.625\,eV$

(b) $0.625\,eV - 100\,keV$

(c) $> 100\,keV$

Figure 7.3.2: Percentage of neutrons causing fission in various energy ranges as determined by the enrichment.

7.3.2 Fractured

The fractured geometry is first analyzed with globally varying saturation in both the fracture and shale slabs. The results in figure 7.3.3 are similar to the homogeneous geometry, although per given mass and enrichment the total reductions in reactivity are not as substantial. This implies that moderation in continuous regions of shale adjacent to the ore is substantial enough to keep the reactivity elevated with higher temperatures and less pore water. Also, the reactivity level at the beginning of the sharp drop is less negative for more highly enriched precipitates, while it is essentially common for precipitates of the same enrichment. The loss of pore water combined with the Doppler effect is once again stronger than removing water alone. For the 2 wt% 100 MTU deposition, reactivity drops to approximately -1.5 when water is removed from the critical mass, which is substantial compared to the -0.0355 drop observed in the study fixed at room temperature in chapter 4.

In the second approach, when employing shale laminates with fixed densities and 100%

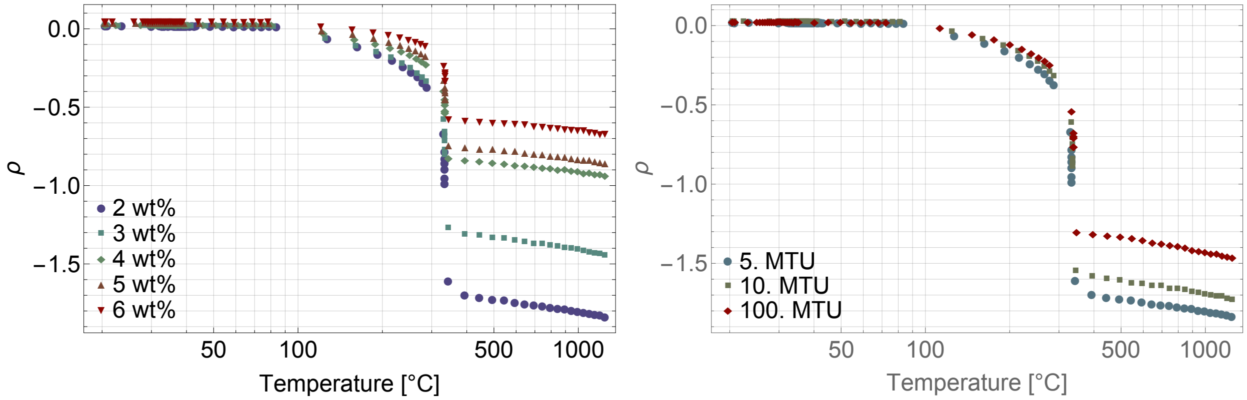

(a) 5 MTU, by enrichment.

(b) 2 wt%, by mass.

Figure 7.3.3: Reactivity feedback with increasing average temperature of configurations in the first fractured geometry approach.

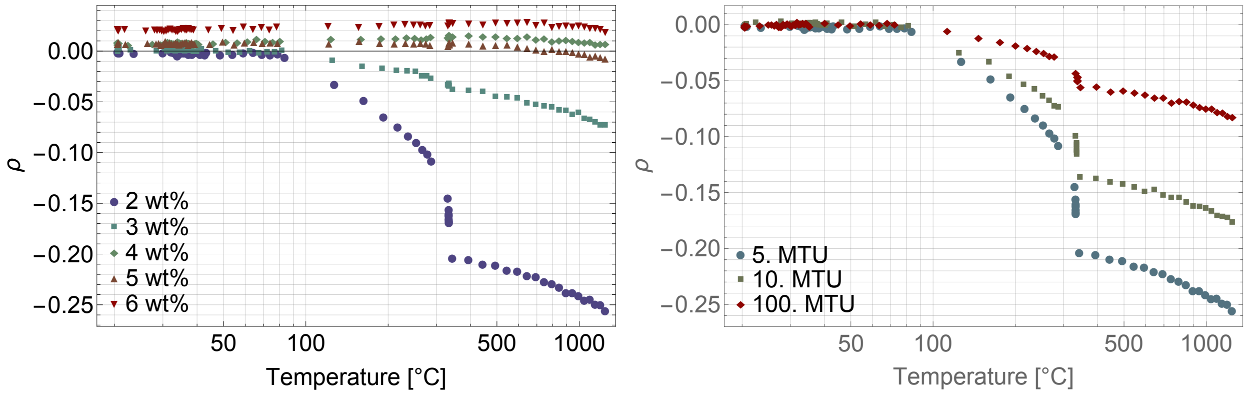

(a) 5 MTU, by enrichment.

(b) 2 wt%, by mass.

Figure 7.3.4: Reactivity feedback with increasing average temperature of configurations in the second fractured geometry approach.

saturation, the overall decrease in reactivity is substantially lower than the previous approach. The discontinuities around T_{BP} are not as pronounced, and the behavior ρ is increasing more continuous with temperature as the enrichment or the mass of the precipitate increases. For these cases, the neutron spectrum remains rather uniform and dominated by the thermal range over the span of temperatures analyzed, which can be explained from the consistent presence of water trapped in the shale. The flat profiles indicate α_T that essentially zero, and mildly positive feedback is actually observed for the 5 MTU precipitates at 4-6 wt%. This is caused by spectrum hardening, as there is an increasing role of fast neutrons above resonance energies in the fission reaction rate.

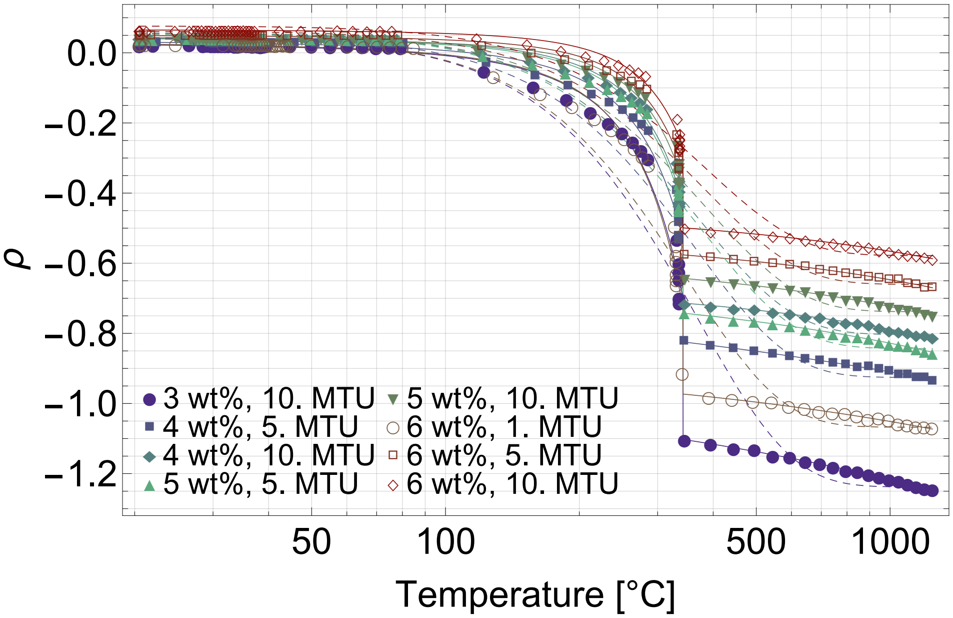

Figure 7.3.5: Reactivity feedback with increasing average temperature of configurations with $FVF \leq 1\%$ in the first fractured geometry approach, shown with color-coded piecewise exponential/power law fits (solid lines) and Gaussian fits (dashed lines).

7.3.3 Dry critical configurations

Based on the behavior observed in figure 7.3.4a, fractured configurations in either approach were identified with $0 \leq FVF \leq 1\%$. The reactivity evaluations for these "dry" critical masses are plotted in figures 7.3.5 and 7.3.6. The existence of water in the 10% porosity of the shale planes allow dry results in approach 1 to conform the behavior of figure 7.3.3. It is clear that positive feedback is limited to certain precipitates within the constant density treatment of approach 2, although the span of reactivity levels is very slim (±0.04). Given the very gradual climbs in ρ with T, the positive feedback coefficients are expected to be very small.

7.3.4 Regression

In this study, the goal is to make the reactivity feedback data portable to the dynamics analysis in the next chapter. Based on the behavior observed in the previous sections, there are three functional forms proposed to model the discontinuities in the results with continuous relationships.

In statistics, the normal (or Gaussian) distribution has the functional form of equation (7.3.1), where μ and σ are the mean and standard deviation of data. Its peaked behavior may be able to capture the high values of reactivity at low temperatures and the decline to relatively steady reactivity levels at higher temperatures.

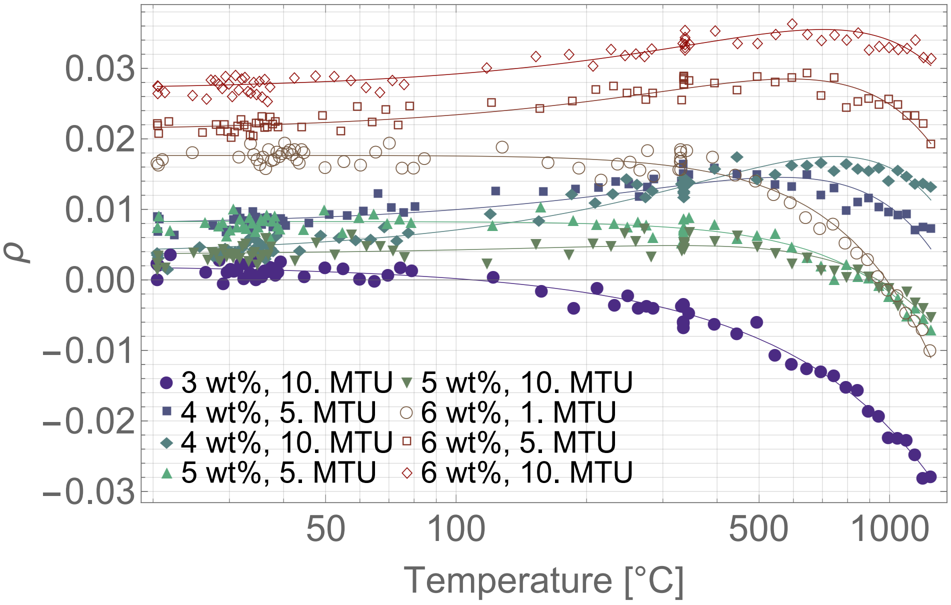

Figure 7.3.6: Reactivity feedback with increasing average temperature of configurations with $FVF \leq 1\%$ in the second fractured geometry approach, shown with color-coded polynomial fits.

$$\mathcal{N}(\mu,\sigma) \sim \frac{1}{\sqrt{2\pi\sigma^2}} e^{-\frac{(T-\mu)^2}{2\sigma^2}},\ \sigma > 0 \tag{7.3.1}$$

To facilitate fitting, the fudge factors α_0 and α_1 are introduced to equation (7.3.1) as follows:

$$\rho(T) = \alpha_0 + \frac{\alpha_1}{\sqrt{2\pi\sigma^2}} e^{-\frac{(T-\mu)^2}{2\sigma^2}} \tag{7.3.2}$$

The derivative of equation (7.3.2) with respect to temperature is shown in equation (7.3.3), where the functional form conforms to the first Hermite polynomial. This would serve as the temperature feedback coefficient $\alpha_T(T)$.

$$\left.\frac{\partial\rho}{\partial T}\right|_T = \alpha_T(T) = -\alpha_1 \frac{T-\mu}{\sqrt{2\pi}\sigma^3} e^{-\frac{(T-\mu)^2}{2\sigma^2}} \tag{7.3.3}$$

To account for kurtosis in equation (7.3.1), which would make the distribution more narrow or broad, the generalized normal distribution is shown in equation (7.3.4), where $\Gamma(x) = \int_0^\infty y^{x-1}e^{-y}\,dy$ is the gamma function (an extension of the factorial function to the complex plane). This version of the distribution assumes the power of 2 in equation (7.3.1) can be replaced with a power of s. [104] When σ and μ are fixed, increasing s eventually makes the distribution flatter near the mean, or platykurtic, like the top of a loaf of bread, while decreasing s makes the peak sharper. For these properties, this distribution is employed as the second functional form for regression, and fitting factors are introduced in the same manner as before in equation (7.3.5). If the term $\frac{T-\mu}{\sigma}$ can be assumed to be positive, the feedback coefficient can be represented in equation (7.3.6).

$$\mathcal{N}_g\left(\mu,\sigma\right) \sim \frac{s}{2\sigma\Gamma\left(1/s\right)} e^{-\left|\frac{T-\mu}{\sigma}\right|^s} \tag{7.3.4}$$

$$\rho(T) = \alpha_0 + \frac{\alpha_1 s}{2\sigma\Gamma\left(1/s\right)} e^{-\left|\frac{T-\mu}{\sigma}\right|^s} \tag{7.3.5}$$

$$\left.\frac{\partial\rho}{\partial T}\right|_T = \frac{\alpha_1 s^2\left(\frac{T-\mu}{\sigma}\right)^{s-1}}{2\sigma^2\Gamma\left(1/s\right)} e^{-\left(\frac{T-\mu}{\sigma}\right)^s},\ \frac{T-\mu}{\sigma} > 0 \tag{7.3.6}$$

Finally, the third set of regression functions handles the discontinuity with a piecewise function. The partially unsaturated region is modeled with a relationship incorporating an exponentially-decaying term. The dry region, where the system is completely evacuated of water and only the fuel and rock are heated, is modeled with a power law as mentioned in section 7.2.4 albeit with a scaling term. The functions and their derivatives are represented in equations (7.3.7) and (7.3.8), respectively. In the numerical analysis, a version of this expression can be used where the piecewise function pivots at the intercept of the two reactivity functions. This intercept can be found through preliminary numerical solving, and would allow for less drastic jumps in ρ, although the jump in α_T would still be appreciable.

$$\rho(T) = \begin{cases} \alpha_0 - \alpha_1 e^{-\alpha_2 T+\alpha_3} & 0 < S_l \leq 1 \\ \alpha_0 + \frac{\alpha_1}{T^x} & S_l = 0 \end{cases} \tag{7.3.7}$$

$$\left.\frac{\partial\rho}{\partial T}\right|_T = \begin{cases} \alpha_1\alpha_2 e^{-\alpha_2 T+\alpha_3} & 0 < S_l \leq 1 \\ -\frac{\alpha_1 x}{T^{1+x}} & S_l = 0 \end{cases} \tag{7.3.8}$$

The use of these functions in regression is plotted on a log-linear scale in figure 7.3.7a for a critical configuration with discontinuous behavior. The piecewise function performs very well in representing the two regions. However, it can be seen in figure 7.3.7b that there is a vast divide in the temperature feedback coefficient between the partially-unsaturated region and the dry region. This suggests that if positive feedback is strong as the system begins heating, the countering effect from Doppler broadening will be lost if all pore fluid is driven from the critical mass. In turn, this could lead to an unfettered energy release of energy. The fitting results for the piecewise function are shown in section F.2.1.

The Gaussian fit strongly represents both temperature bounds of the analysis, but it does not adequately model the transition to dry conditions observed near the phase boundary. The reactivity is underestimated for the partially-unsaturated region and overestimated for much of the dry region. In figure 7.3.7b, this is shown to result in a feedback coefficient that is overly negative for temperatures up to $100°C$ (the onset of desaturation observed in chapter 6). Although the minimum occurs at this transition point, the magnitude is far less than what the actual coefficient would be (when compared to the well-fitted exponential

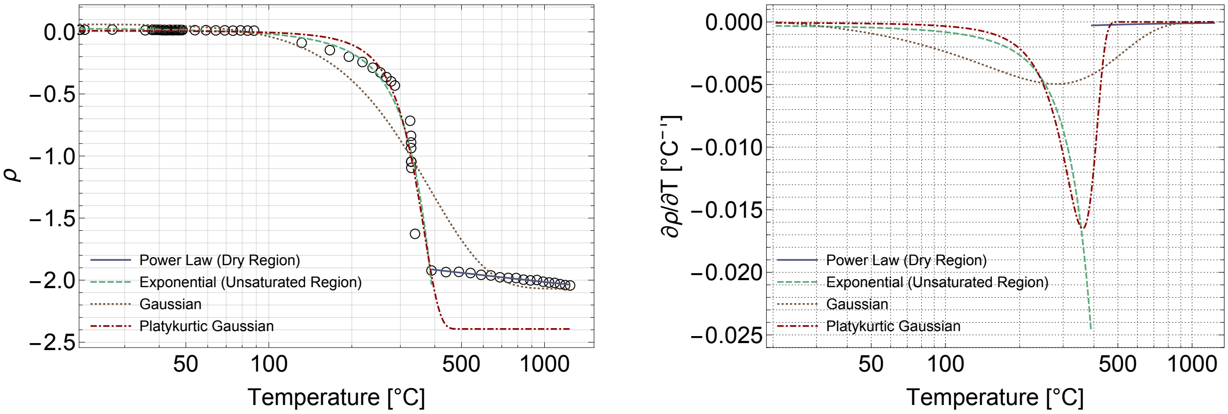

(a) $\rho(T)$ (b) $\frac{\partial \rho}{\partial T}$

Figure 7.3.7: Different fittings for the reactivity results of the 1 MTU 3 wt% fractured configuration (approach #1).

solution), which runs against the conservatism of the model. Nonetheless, the gaussian fit overestimates the magnitude of α_T for the dry region, which would have a balancing effect. Regression results are shown in section F.2.2, where $\mu = 20.45°C$ is clearly imposed on the fit.

The platykurtic Gaussian curve is very sensitive to fitting, and the parameters needed to conform to the broad shape of the partially-unsaturated region result in an underestimate of reactivity for the dry region. Since the curve is not very tailed, the reactivity of the dry region is essentially flat, which leads to a feedback coefficient that is zero. This would imply that heating of the dry fuel will have no impact on affecting the reactivity balance, which is a bad estimate. However, the regression shows middle-ground in representing α_T at the transition temperature, as behavior falls between the observed magnitudes of the exponential and Gaussian fits.

Using the fractured #1 results for dry configurations, the feedback coefficients obtained when using of the piecewise fit are shown in figure 7.3.8. There is an order of magnitude difference in α_T between the partially unsaturated and saturated regions. Smaller and less-enriched precipitates are usually observed to have the most consistently negative coefficients as temperature evolves, with an exception of the anomalous 6 wt%, 1 MTU precipitate. This observation is carried over to figure 7.3.9, where coefficients obtained from a Gaussian regression are plotted. As discussed, while the use of this functional form provides continuity in α_T over the two saturation regimes, the most negative values of the coefficient are not as negative as those observed in figure 7.3.8a. Since the Gaussian fit overestimates the magnitude of α_T in the dry region, it is not yet certain which approach would have the strongest effects in the dynamics analysis.

The dry configurations of the second fractured geometry data are essentially continuous and can be modeled with a simple polynomial fit of maximum order 2, as shown in

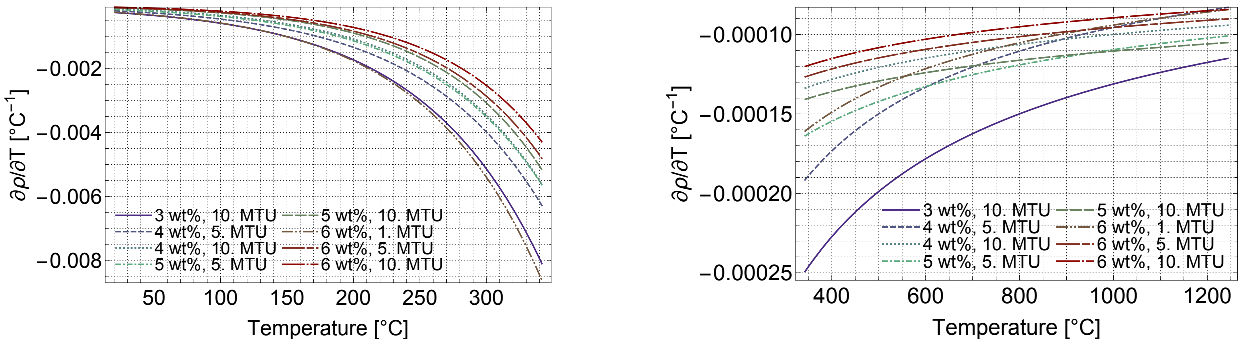

(a) Partially unsaturated

(b) Dry

Figure 7.3.8: Feedback coefficients for the dry critical configurations in the first fractured geometry approach, split into two regions to demonstrate application of equation (7.3.8)..

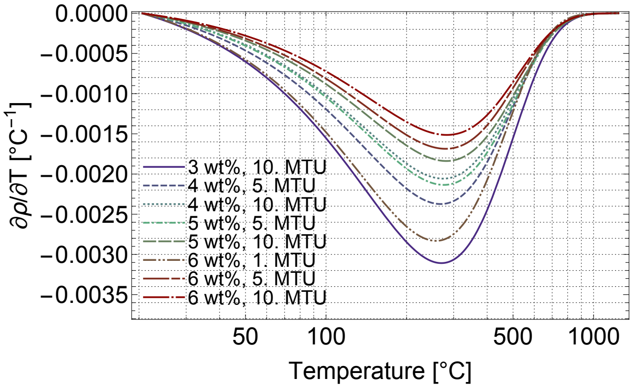

Figure 7.3.9: Feedback coefficients for the dry critical configurations in the first fractured geometry approach using the gaussian solution in equation (7.3.3)..

equation (7.3.9). Regression results are shown in section F.2.3. The use of a second order model allows for feedback coefficients to be represented as linear functions in temperature, as indicated in equation (7.3.10) and plotted in figure 7.3.10. It is observed the feedback is indeed positive for temperatures up to $300°C$ for the 5 MTU, 5 wt% deposition and $750°C$ for the 10 MTU, 4 wt% deposition. Positive temperature feedback would amplify the role of neutron poisoning from the U-238 influx in bringing the reactivity to zero. If non-fission absorptions do not have an appreciable effect, the temperature may be free to climb unhindered. However the magnitude of α_T is much less than the values observed in figures 7.3.8a and 7.3.9, which marginalizes the consideration.

$$\rho(T) = \alpha_0 + \alpha_1 T + \alpha_2 T^2 \tag{7.3.9}$$

$$\left.\frac{\partial \rho}{\partial T}\right|_T = \alpha_1 + 2\alpha_2 T \tag{7.3.10}$$

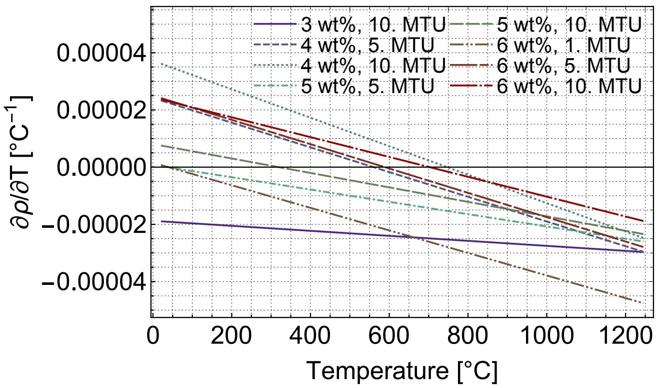

Figure 7.3.10: Feedback coefficients for the dry critical configurations of the second fractured geometry approach.

7.3.5 Temperature defect

The temperature defect D_T can be defined as the change in reactivity when the critical mass is heated from temperature T_0 to T_1, as shown in equation (7.3.11). In an engineered reactor, T_1 is the temperature when the core is brought to full power, and is mostly determined from the coolant temperature and fuel-to-moderator ratio. [22] In this study, D_T is evaluated via numerical integration at two different temperature ranges: from room temperature to the phase transition temperature, and then after the phase transition temperature up to $1250°C$.

In table 7.3.1, D_T is observed to be consistently stronger for the homogeneous configuration compared to the fractured. The FVF in the latter configuration is usually lower per given mass of heavy metal, so this behavior is expected from less neutrons being moderated to resonance energies. Per given mass, D_T decreases with enrichment because a higher concentration of fissile material allows for less neutrons to be absorbed in the fertile material. Per given enrichment, the defect is usually stronger for smaller critical masses, with this discrepancy evidently stronger at higher enrichments. For example, in the 6 wt% composition in the homogeneous geometry, $D_T = -2.42$ for the 0.5 MTU deposition and -0.90 for the 5 MTU deposition, while D_T ranges between -1.85 and -1.38 for the 2 wt% precipitate at 5 and 100 MTU, respectively. This may be caused by the larger fluid volume fractions needed for smaller critical radii, which allows for more neutron interactions with resonance energies. The anomalous case of the smallest 6 wt% precipitate is observed to have an extreme value at full desaturation due to neutron leakage effects.

The defects in the dry temperature range are substantially smaller, as would be expected from the results. Significant drops in reactivity should not be expected as the critical mass proceeds into dryout, so if negative feedback during desaturation does not bring an end to chain reactions, the system will rely on neutron poisoning to reach subcriticality. Overall, the magnitudes of D_T make the supercritical assumption for fractured approach 1 excusable.

Set	$M_c\,[MTU]$	$D_T:\ 20.45^\circ C \rightarrow 342.155^\circ$		$D_T:\ 342.155^\circ \rightarrow 1250^\circ C$	
		H	F	H	F
1	100	-	-1.16179	-	-0.17230
	500	-	-1.16179	-	-0.17749
	100	-	-1.16901	-	-0.18721
2	5	-1.85099	-1.57402	-0.32710	-0.22976
	10	-1.70324	-1.42132	-0.25412	-0.18496
	100	-1.38623	-1.03820	-0.24450	-0.16196
3	0.5	-	-1.91903	-	-0.10854
	1	-1.79588	-1.66114	-0.17223	-0.13329
	5	-1.56280	-1.22101	-0.28935	-0.17919
	10	-1.41846	-1.01890	-0.25361	-0.14266
4	0.5	-	-1.62733	-	-0.11353
	1	-1.77047	-1.35310	-0.17926	-0.11649
	5	-1.60530	-0.79818	-0.21232	-0.11502
	10	-1.27699	-0.67397	-0.25140	-0.09947
5	0.5	-	-1.46880	-	-0.12482
	1	-1.55895	-1.19886	-0.18243	-0.12507
	5	-1.37736	-0.71672	-0.18538	-0.11715
	10	-1.07060	-0.59652	-0.24714	-0.10732
6	0.1	-2.42438	-2.38054	-0.13243	-0.08211
	0.5	-1.44637	-1.25611	-0.19982	-0.12190
	1	-1.23796	-0.93941	-0.20278	-0.09440
	5	-0.90347	-0.56574	-0.20255	-0.09344
	10	-	-0.47931	-	-0.09009

Table 7.3.1: The temperature defects in two separate temperature ranges, where fractured data correspond to the first approach with shale laminate desaturation. The initial reactivity of the homogeneous geometry was close to zero, while that of the fractured geometry was around 0.02.

$$D_T = \int_{T_0}^{T_1} \frac{\partial \rho}{\partial T} dT \tag{7.3.11}$$

7.3.6 Effective cross sections

Tallies were obtained for the neutron flux $\left(\frac{\#}{cm^2}\right)$ averaged over each cell containing U-235. An identical set was employed with multipliers for the total, capture, and fission reaction rates. In either of these sets, the tallies were summed for all cells in the critical mass.

The multiplier set was then normalized to the total flux to generate effective cross sections according to equation (7.3.12), where $\mathcal{C} = 1$.

$$\sigma_{i,eff} = \frac{\mathcal{C} \int \sigma_i(E)\phi(E)dE}{\int \phi(E)dE} \tag{7.3.12}$$

Figure 7.3.11 shows the effective fission and capture cross sections for the fractured geometry where global densities vary with temperature. As would be expected, more highly enriched precipitates have larger values of σ_f. The cross section is mostly constant for the first $100°C$ until the pore water begins to exfiltrate. This implies that the Doppler effect is weak when neutrons thermalize in the fracture water and avoid resonance energies when they interact with the fuel. As temperatures reach the phase transition temperature, the fission probabilities decrease and reach steady-state level. A slight monotonic decrease is observed for those that are most highly-enriched, but the effect is barely observable. This behavior is expected, as the rock becomes the only medium that can effectively moderate neutrons, and the final energy of neutrons causing fission should be rather uniform.

The capture probability behaves roughly in the similar manner before the phase transition, although the overall magnitude appears rather uniform over the range in temperatures, especially for the highly enriched precipitates. While there is a drop in σ_c at the phase boundary, it eventually begins to increase with higher temperature a direct result of Doppler broadening. The rise is noticeably stronger for more highly enriched precipitates. The 0.1 MTU, 6 wt% precipitate behaves anomalously because neutron leakage is exacerbated by the desaturation of the shale reflector. The behavior of the homogeneous configuration behaves similarly, although the magnitudes of σ obviously drop due to mixing. The steady-state σ_f also appear to be more tightly spaced, as the reduced self-shielding prevents resonance escape and less fission absorptions regardless of the actual quantity of fissile material; this would cause the fission probabilities to be smeared across total mass and enrichment.

Cross sections behave much more differently for the heterogeneous configurations utilizing constant fracture rock densities and saturations, as shown in figure 7.3.12. The magnitude of σ_f certainly decreases over the range in temperatures, but with a much smaller net difference. It is not as drastically effected by the loss of moderator. Some configurations have a flat or slightly monotonic increase in σ_c over temperature. Overall, σ_f is consistently higher than σ_c for precipitates above 1.5 wt%, which allows room for water removal to pose a positive feedback mechanism. That is, the absorptive character of water could be amplified with Doppler broadening, such that water exfiltration allows for increase in reactivity due to reduced absorptions.

7.4 Discussion

The behavior of reactivity with increasing temperature has been evaluated where the effects on both saturation and fluid densities have been directly coupled. The fluid content and average atomic densities were modeled according to a discrete spherical shells based on

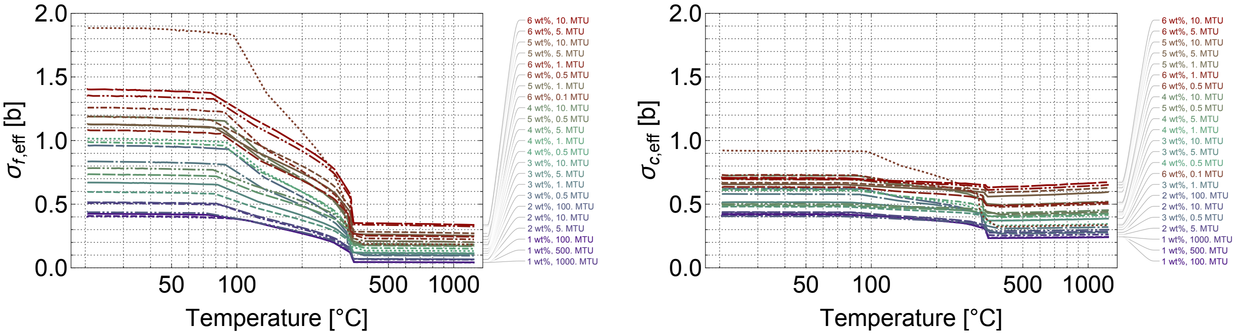

(a) Fission (b) Capture

Figure 7.3.11: Effective microscopic cross sections in fractured critical configurations (approach 1).

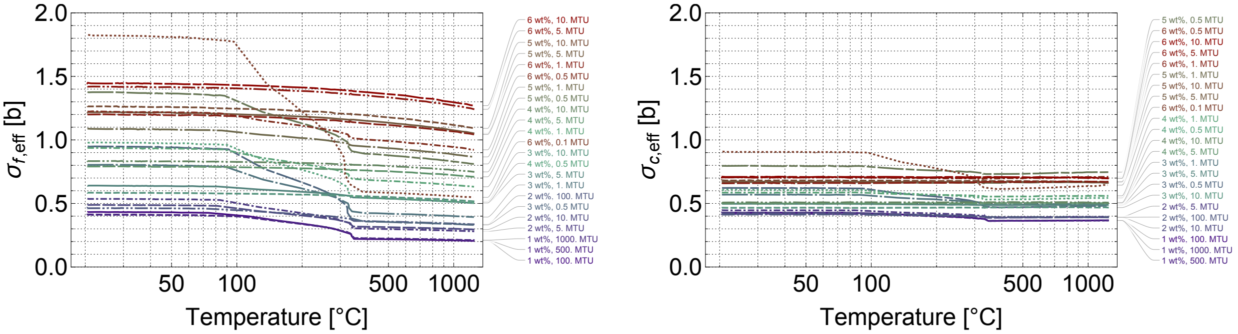

(a) Fission (b) Capture

Figure 7.3.12: Effective microscopic cross sections in fractured critical configurations (approach 2).

results from the study in chapter 6, and cross sections were broadened in energy based on the average temperature of each region. The volumetric water content was assumed to fall to zero as temperatures exceeded the liquid-gas phase transition, and an upper bound temperature of $1250°C$ was imposed as a practical limit for the investigation.

Prior to the major onset of desaturation around $100°C$, the Doppler effect is not noticeable within the scope of larger reactivity reductions in the system. However, for the partially-unsaturated temperature region, the declining behavior observed for the moderator defect study in chapter 4 reappeared, where the additional impact of Doppler broadening was observed to augment the drop in the reactivity as the system approached dry conditions. When the pore space is dried out, there is a steady increase in neutron capture probability that leads to continuing reductions in reactivity, although these differences are less dramatic and indicate weaker temperature feedback than the partially-unsaturated context.

The reductions in reactivity with temperature are stronger in the homogeneous geometry compared to the fractured, as Doppler broadening is compounded with the lack of separation between fuel and moderating components, which lead to a decreased self-shielding effect. This allows the fertile component of the fuel to absorb neutrons more frequently and stronger drops in ρ as the moderator is driven out of the system. Smaller critical masses and those with lower enrichments are also succumb to negative temperature feedback more substantially due to leakage and/or the competition between fissile and fertile material. Anomalous behavior was observed for the smallest critical mass of the 6 wt% composition, where despite the very high effective cross section for fission during the initial temperature climb, the interaction probability drastically decreases when water is exfiltrated due to significant neutron leakage. This corresponds to a major temperature defect and negative temperature feedback coefficient, which implies that although a small critical mass may be feasible given the strong mobilization of transuranics in nuclide transport, the Doppler effect may be very strong in these depositions and will counteract sustained chain reactions.

A second heterogeneous configuration was proposed to isolate the role of water removal strictly to the fracture conduits, where water in the fracture rock slabs was modeled at constant density and full saturation. Results at low mass and enrichment in this modeling context are similar to before in terms of general behavior, although the drops in the reactivity are substantially lower. As enrichment increases, the discontinuity around the phase boundary is less pronounced as the role of fracture water becomes less important with lower fluid volume fractions needed for the critical configuration. In some cases, there is essentially zero temperature feedback, where the 10% saturated porosity of the shale laminates is enough to sustain criticality. Indeed, the effective fission cross section remains rather uniform over the span of temperatures due to continued presence of a neutron moderator in the rock. For configurations that are critical under very low or zero FVF, there may be weakly positive feedback if fast neutrons above the resonance region play a more prominent role in fission. Altogether, the results from the two heterogeneous models should present bounds on reactivity behavior, as in reality the shale will desaturate at a incongruent rate with the fracture. A repeat of the study is recommended using findings from a thermo-hydrological simulation that incorporates a dual porosity approach for the heterogeneous precipitate.

A normal distribution was proposed as a continuous function to analytically model the temperature feedback coefficient given discontinuous behavior of the results. This was meant to facilitate smoother numerical solving in the dynamics analysis. However, this approach was found to have limitations in modeling behavior expected near the phase transition. The disadvantage of using equation (7.3.2) is the poor approximation of reactivity both at the onset of desaturation and the monotonic decrease in reactivity in the dry-out regime. The magnitude of the resulting feedback coefficient is underestimated in the partially unsaturated zone and overestimated in the dry region region. A modification of the Gaussian was also considered that is used in statistics to handle kurtosis, or broadening of the peak in the distribution. Although this model was found to more tightly fit the behavior observed at the phase transition, the feedback coefficient was brought to zero in the high temperature zone.

Reactivity was found to be more accurately represented by a regression model comprised of an exponential coupled with a power law in a piecewise function. With the exponential function, the magnitude of α_T is represented at its highest in the partially-unsaturated region, while the power law leads to very small coefficients in the dry region. This leads to a major discontinuity in α_T, and implies that temperature feedback is insubstantial when the critical mass is dry. For comparison, when the functional form of the normal distribution is employed, the profile of α_T is depressed but allows for appreciable feedback when the system is depleted of water. Therefore, it is not yet certain which regression type would have the strongest impact in the dynamics analysis.

Chapter 8

Dynamics of critical mass at quasi-steady-state

8.1 Introduction

Various mechanisms have been discussed that may affect the reactivity of the far-field critical mass. In chapter 4, the role of the incoming plume of uranium was evaluated using two-dimensional interpolations of reactivity figures in the scope of void and heavy metal volume fractions. The decline in reactivity from the uniform expulsion of pore water was assessed for both the homogeneous and fractured geometries. The role of thermal expansion in reducing reactivity was also simulated by simultaneously increasing the volume of the critical mass and reducing the atomic density. In chapter 7, the combined role of heating and de-saturation was investigated in an analysis that incorporated effects from Doppler broadening with increasing temperatures. It is now necessary to combine all phenomena into a unified analysis in order to assess the dynamic temperature evolution of the system.

This chapter will describe the application of a quasi-steady-state (QSS) approach to modeling the interplay between heat transfer and reactivity feedback via a system of equations involving point depletion. This borrows from the methodology of Ref. [105] and related publications, which has been successfully utilized to simulate reactor zones at the Oklo natural analog. [16, 70] The goal of this study is to model the evolution of the steady-state system temperature given the various feedback mechanisms, which are incorporated in the form of analytical regression curves. The results in this chapter will be based on the parametrization of different components of the theoretical model to illustrate sensitivity. Of particular importance is the role of the source term of fissile and non-fissile uranium from the repository.

8.2 Model

8.2.1 Scenario

The scenario concerns a gradual release of heat from a just-critical mass of uranium mixed evenly with water and rock. Chain reactions are sustained beyond prompt criticality by an influx of uranium from the repository canisters, where heavy metal fills the void space occupied by fluid. It is assumed that the rate of fission energy release is low enough to be in equilibrium with the rate of heat transfer to the shale, and that the mass flux of fissile material is slow. This allows the system to be considered at quasi-steady-state, where there are no large, sudden release of energy such as the autocatalytic scenarios hypothesized in previous studies (see Ref. [8,12,13,106–108]). After a slow release of energy from an increase in reactivity, the system is hypothesized to reach subcritical conditions given a sufficient increase in temperature due to negative reactivity feedback mechanisms mainly from the Doppler effect. If these negative feedback mechanisms do not bring the system back to ambient temperature, then the system may reach temperatures that expand the spherical region and cause sub-criticality via changes in volume. If not, the system will continue to heat and eventually fail via thermal strain.

In summary, the approach revolves around the following framework:

1. At time $t = 0$, the precipitate has just reached criticality ($\rho = 0$)
2. Thermally fissile material from the repository arrives to the critical mass via radionuclide transport (the source term), which raises the reactivity above critical ($\rho > 0$)
3. Fission power is generated
   a) TFM is depleted or generated depending on capture and fission cross sections
   b) Neutron poisons are generated as fission products
   c) Temperature increases at a rate determined by the specific heat (energy storage) and heat transfer coefficient (convection)
4. The temperature increase from fission reactions corresponds to an increase in resonance absorptions from Doppler broadening, which counteracts the rise in reactivity
5. Heat is transferred to the surroundings according to Newton's law of cooling
6. Steady state is achieved when the rate of heat generation by fission is approximately equal to that lost by transfer to surroundings
7. If steady state is not achieved, the process may continue until
   a) TFM stops arriving from the dissolving UNF, or
   b) A sub-critical state is reached ($\rho < 0$), or

c) Water in the pore space is completely displaced by fissile nuclides, or

d) Critical strain of the host rock is reached as a point of system failure

The failure metric in 7d is treated in chapter 9. The next sections will describe the mathematical models meant to analyze these effects in order to solve for the system temperature over time. As a major departure from the approaches of the previous chapters, the system temperature is represented as a lumped quantity, where spatial dependence can be ignored. This is supported by plots of the temperature distributions in the critical mass over time in the TH study, where at steady state there is negligible difference in the temperature between the center of the sphere and the surface.

8.2.2 Reactivity balance

The time rate of change of total system reactivity ($\bar{\rho}$) is constrained to zero as different aspects of the system change. The changes to reactivity result from depletion and generation of isotopes, changes in temperature ($T\ [^{\circ}C]$), changes in saturation (S_l), and changes in the system volume as determined by the radius ($r\ [m]$). The inventory $n_i\ [mol]$ of $i = 1 \ldots N$ nuclides is governed by the point depletion equation (5.2.1). The reactivity balance is represented in equation (8.2.1), which is featured in some form in many reactor physics textbooks.

$$\frac{\partial \bar{\rho}}{\partial t} = \sum_{i=1}^{N} \frac{\partial \rho}{\partial n_i} \frac{\partial n_i}{\partial t} + \frac{\partial \rho}{\partial T} \frac{\partial T}{\partial t} + \frac{\partial \rho}{\partial S_l} \frac{\partial S_l}{\partial t} + \frac{\partial \rho}{\partial r} \frac{\partial r}{\partial t} = 0 \qquad (8.2.1)$$

The symbol α is used to denote the reactivity feedback coefficients for the various mechanisms, and the equation is modified as:

$$\frac{\partial \bar{\rho}}{\partial t} = \sum_{i=1}^{N} \alpha_i \frac{\partial n_i}{\partial t} + \alpha_T \frac{\partial T}{\partial t} + \alpha_{S_l} \frac{\partial S_l}{\partial t} + \alpha_R \frac{\partial r}{\partial t} = 0 \qquad (8.2.2)$$

One of the major assumptions employed in this study is that the behavior of saturation in the critical mass is directly coupled to temperature. Therefore, reactivity feedback from desaturation (α_{S_l}) is removed from the equation and assumed to be accounted for through $\frac{\partial T}{\partial t}$. While it was apparent in chapter 4 that the reactivity effects of water exfiltration are much stronger than thermal expansion, the $\alpha_R\ [m^{-1}]$ term is included for diligence. It is based on the relative change in radius from thermal expansion (as discussed in section 4.4.6) which in turn is dependent on the temperature. Using the volumetric coefficient of thermal expansion β and the original critical volume V_0 and radius r_0, the evolving radius r can be calculated as:

$$V\ \left[m^3\right] = V_0 \left(1 + \beta \Delta T\right) \Rightarrow r\ [m] = \sqrt[3]{\frac{3}{4\pi} V_0 \left(1 + \beta \Delta T\right)} = \sqrt[3]{r_0^3 \left(1 + \beta \Delta T\right)} \qquad (8.2.3)$$

The change in radius with respect to the temperature change is thus:

$$\frac{dr}{d\Delta T}\left[\frac{m}{K}\right]=\frac{r_0^3\beta}{3}\left[r_0^3\left(1+\beta\Delta T\right)\right]^{-2/3}=f_R\left(\Delta T\right) \tag{8.2.4}$$

The change in reactivity from the change in radius can thus be approximated as:

$$\frac{\partial\rho}{\partial t}\left[s^{-1}\right]\approx\alpha_R f_R\left(\Delta T\right)\frac{\partial T}{\partial t} \tag{8.2.5}$$

The main nuclides of interest are U-235 (n_{25}) and U-238 (n_{28}). The first nuclide serves as the fuel, both in the original critical mass and the quantity continually arriving from the repository that allows for criticality to be sustained. The second is a fertile nuclide that dominates the precipitate composition and mainly absorbs neutrons in resonances. The governing equations for each nuclide are shown in 8.2.6 and 8.2.7, respectively, where $\dot{S}$ is the source term, λ is the decay constant, and σ is a cross section for neutron capture (c) or absorptions resulting in fission (f). The role of thermal fissions in U-238 is considered negligible, and the treatment overall is monoenergetic (thermal).

$$\dot{n}_{25}=\dot{S}_{25}-\lambda_{25}n_{25}+\phi\left(-\sigma_c^{25}n_{25}-\sigma_f^{25}n_{25}\right) \tag{8.2.6}$$

$$\dot{n}_{28}=\dot{S}_{28}-\lambda_{28}n_{28}+\phi\left(-\sigma_c^{28}n_{28}\right) \tag{8.2.7}$$

Given the fertile nature of U-238, equation (8.2.8) can be used if the generation of Pu-239 is accounted for via the neutron capture mechanism $\left({}^{238}_{92}U\xrightarrow{\sigma_\gamma}{}^{239}_{92}U\xrightarrow{\beta^-}{}^{239}_{93}Np\xrightarrow{\beta^-}{}^{239}_{94}Pu\right)$. This would require the precursor term $\lambda_{49}n_{49}$ to be added in equation (8.2.6). Although plutonium precursors played a major role in the transport study, a majority uranium accumulation was assumed as plutonium quantities were considered too small at the precipitate location to warrant a direct calculation, especially given the context of the direct disposal scenario. Therefore, there would be no initial quantity or source term of Pu-239 if equation (8.2.8) is used.

$$\dot{n}_{49}=-\lambda_{49}n_{49}+\phi\left(\sigma_c^{28}n_{28}-\sigma_c^{49}n_{49}-\sigma_f^{49}n_{49}\right) \tag{8.2.8}$$

If certain neutron poisons (p) such as Xe-135 and Sm-149 are included to amplify non-fission absorptions, equations in the form of 8.2.9 can be used to model buildup determined by their cumulative fission yield γ_c from all TFM. These species would naturally have no initial quantity, and no source term can be provided since the transport study was restricted to uranium and TRU.

$$\dot{n}_p=-\lambda_p n_p+\phi\left(\gamma_{c,p}^{25}\sigma_f^{25}n_{25}+\gamma_{c,p}^{49}\sigma_f^{49}n_{49}\right) \tag{8.2.9}$$

The reactivity feedback from the U-235 plume (α_{25} $[mol^{-1}]$) is a function of net increase in mass ($n_{25}-n_{25}^0$) as derived from the study in section 4.4.4. Although the study acknowledged reactivity changes related to the filling of a completely empty void space with heavy metal, the functions will be applied as-is to purposefully acknowledge the full spectrum of positive α_{25} before it becomes negative due to undermoderation. The values of α_{25} were obtained from reactivity functions modeled as polynomials of order 6, and these reactivity values were based on initial configurations meeting $k_{eff} = 1$ or $k_{eff} = 1.02$. Regression models are shown in section §F.1.

The negative feedback effects from the addition of pure U-238 are accounted for in the coefficient α_{28} $[mol^{-1}]$, and this behavior was discussed in section 4.4.5. Since reactivity was a linear function of the change in U-238 infiltrating the void space, the feedback coefficients will be assumed to be constant. Given the similarity in α_{28} between the different enrichment levels and geometries, an average value of $-5.19 * 10^{-11}$ $[mol^{-1}]$ is employed.

While there are many fission products with strong absorptive properties, there was no isolated parametric study of reactivity based on increasing specific poison concentrations. Therefore, to remove the arbitrariness of α_p from the analysis, fission products will be ignored. If the feedback coefficient of Pu-239 is neglected, the functional form of equation 8.2.2 is therefore represented as:

$$\frac{\partial \bar{\rho}}{\partial t} = 0 =$$

$$\alpha_{25}\left(n_{25} - n_{25}^{0}\right)\frac{\partial n_{25}}{\partial t} + \alpha_{28}\frac{\partial n_{28}}{\partial t} + \cancel{\alpha_p \frac{\partial n_p}{\partial t}} + \alpha_T(T)\frac{\partial T}{\partial t} + \alpha_R\left(\frac{r - r_0}{r_0}\right) f_R\left(\Delta T\right)\frac{\partial T}{\partial t} \quad (8.2.10)$$

The thermal expansion coefficient is chosen to be the steepest of those observed in section 4.4.6 (the 5 MTU result) which is shown in equation (8.2.11). This expression is simplified into a function of the temperature change using the thermal expansion coefficient. This version of the feedback equation is shown in equation (8.2.12). A value of $\beta = 3.0 * 10^{-5}\, K^{-1}$ is chosen to be representative of sandstone. [109]

$$\alpha_R\left(\frac{r - r_0}{r_0}\right) = -0.274 - 0.806\left(\frac{r - r_0}{r_0}\right) \quad (8.2.11)$$

$$\alpha_R\left(\Delta T\right) = -0.274 - 0.806\left[\frac{\sqrt[3]{r_0^3\left(1 + \beta\Delta T\right)}}{r_0} - 1\right] \quad (8.2.12)$$

The working reactivity feedback equation is thus:

$$\frac{\partial \bar{\rho}}{\partial t} = \alpha_{25}\left(n_{25} - n_{25}^{0}\right)\frac{\partial n_{25}}{\partial t} + \alpha_{28}\frac{\partial n_{28}}{\partial t} + \alpha_T(T)\frac{\partial T}{\partial t} + \alpha_R\left(\Delta T\right) f_R\left(\Delta T\right)\frac{\partial T}{\partial t} = 0 \quad (8.2.13)$$

8.2.3 Power

The feedback equation is coupled to the point depletion equations (see 5.2.1 on page 93) for the nuclides of interest to comprise a system of $N + 1$ equations. To remove nonlinearity from the system, the magnitude of the neutron flux $\left(\phi \, \frac{\#}{cm^2 s}\right)$ is assumed to be proportional to the power generated from fission (P_f $[W]$), as part of the QSS assumption. This relationship is shown in equation (8.2.14), where N_A is Avogadro's number, n_i is the quantity of the thermally-fissile isotope, $E_{f,i}$ is the useable energy from fission (i.e. no neutrino contributions), and $\sigma_{f,i}$ is the fission cross section.

$$P_f(T,t) = \phi(T,t) N_A \sum_{i \in TFM} E_{f,i} \sigma_{f,i} n_i(t) \tag{8.2.14}$$

The flux is dependent on temperature since this effects neutron velocities and cross sections. However, the temperature dependence can be ignored in this relationship, as temperature effects can be handled through the Doppler feedback coefficient. From the one-dimensional heat diffusion equation in spherical geometry (E.1.14), the time rate of change of thermal energy in the medium per unit volume in the system is defined in equation (8.2.15). However, if radial variation of the temperature in the sphere is considered to be negligible, the gradient may be canceled.

$$\rho c_p \frac{\partial T}{\partial t} = \dot{q}(t) + \cancel{\frac{k}{r^2} \frac{\partial}{\partial r} \left(r^2 \frac{\partial T}{\partial r} \right)} \tag{8.2.15}$$

The volumetric heat generation source term $\dot{q}\left[\frac{W}{m^3}\right]$ is exclusively from fission and is shown in equation (8.2.16), which is based on equation (8.2.14). The quantity $V(t)$ is the volume of the critical mass over time.

$$\dot{q}(t) = \frac{\phi(t)}{V(t)} N_A \sum_{i \in TFM} E_{f,i} \sigma_{f,i} n_i(t) \tag{8.2.16}$$

While thermal expansion is acknowledged in the feedback equation, overall changes are expected to be small, and the volume can be roughly modeled as a constant V_0. In 4 on page 57, the role of fast fissions in the critical mass were determined to be low, so the effects of U-238 fission can continue to be ignored. Assuming U-235 and Pu-239 are the only thermally fissile materials in the system, equation (8.2.16) is expressed explicitly in equation (8.2.17).

$$\dot{q}(t) = \frac{\phi(t) N_A}{V_0} \left(E_f^{25} \sigma_f^{25} n_{25}(t) + E_f^{49} \sigma_f^{49} n_{49}(t) \right) \tag{8.2.17}$$

8.2.4 Lumped capacitance approach

A lumped thermal capacitance approach is utilized, such that the critical mass is essentially treated as a point source and the radial variation in T can be ignored. In this approach, it is assumed that resistance to conduction in the sphere is much lower than resistance to convection on the surface. [94] Therefore, conduction of heat from fission across the UO_2 is much more rapid than the transfer of heat to the surrounding host rock. For this to be plausible, a low value of the dimensionless quantity called the Biot number is required. This quantity defines the ratio of thermal resistances on the inside and at the surface of the

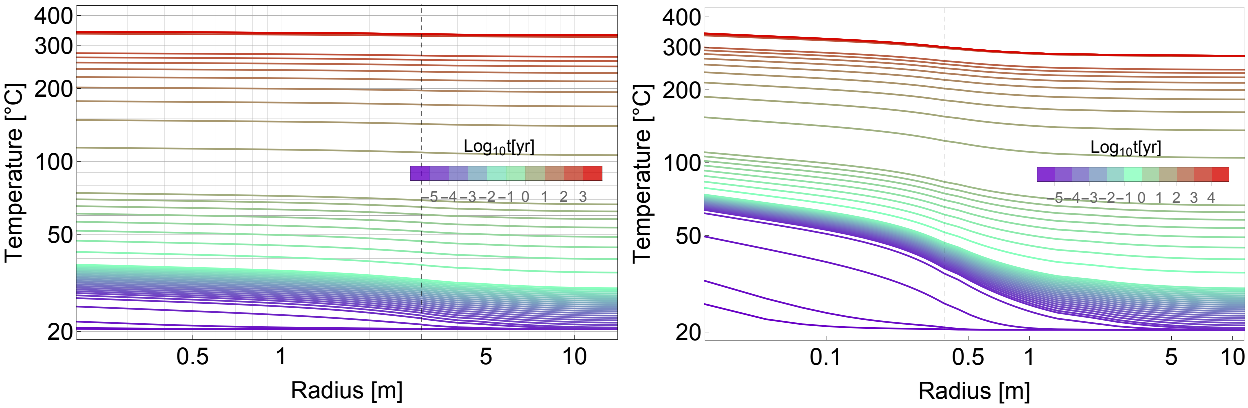

(a) Homogeneous, 2 wt%, 100 MTU (b) Homogeneous, 6 wt%, 0.1 MTU

Figure 8.2.1: The temperature distribution in the system as time progresses, with the critical radius indicated with the vertical line.

sphere, and is defined in equation (8.2.18) in terms of the heat transfer coefficient h, thermal conductivity of the *solid* k, and characteristic length L_c, which is equal to the volume-to-surface ratio. For the lumped capacitance approach to be valid, a Bi much less than one is ideal.

$$Bi = \frac{hL_c}{k} = \frac{h(\frac{\cancel{4}}{3}\cancel{\pi}r_c^3)}{k\,(\cancel{4\pi}r_c^2)} = \frac{hr_c}{3k} \ll 1 \tag{8.2.18}$$

The results of the TH study in chapter 6 indicate that, relative to the scope of the temperatures analyzed, the differences in temperature between the center of the sphere and its surface are negligible at steady-state. Figure 8.2.1 shows the temperature distributions in two critical masses with extreme radii. In terms of transient behavior, the difference in temperatures from the inner core to the outer shell of the critical mass is appreciable and much more dramatic in the smaller critical mass. As time progresses, these differences are still stronger for the smaller mass, but the ultimate temperature difference does not warrant a treatment of $\frac{\partial T}{\partial r}$ in the precipitate at steady-state. Therefore, mild inaccuracies are accepted for smaller volumes and shorter time scales. Furthermore, given the dimensions of the critical spheres (meters) relative to the much larger extent of host rock in the far-field (kilometers), this treatment of the critical mass should be satisfactory and the lumped temperature T can be considered the instantaneous average temperature of system.

The assumptions for lumped capacitance cancel the temperature gradient in equation (8.2.15) and the heat equation can no longer be applied to the system. A new energy balance is applied to solve for the temperature difference between the heat-emitting sphere and the surrounding host rock. The rate of change of internal energy stored within the sphere is related to energy generated from fission and the energy lost to the surrounding rock.

$$\dot{E}_{stored} = \dot{E}_{gen} - \dot{E}_{out} \tag{8.2.19}$$

Heat transfer in the host rock consists of both conduction in the rock matrix and convection from the pore fluid. The heat transfer coefficient is applied to equation (8.2.19) based on Newton's law of cooling (6.2.2), where A is the area of the sphere and T_∞ is the temperature of the surrounding rock. The heat storage term and source term from equation (8.2.15) are further applied to the energy balance to yield equation (8.2.20).

$$\rho c_p \frac{dT}{dt} = \dot{q}(t) - \frac{hA}{V_0}(T - T_\infty) \tag{8.2.20}$$

To further simplify, let $\Delta T = T - T_\infty$, and since T_∞ is a constant, $\frac{dT}{dt} = \frac{d\Delta T}{dt}$. Therefore:

$$\dot{q}(t) = \rho c_p \frac{d\Delta T}{dt} + \frac{hA}{V_o}\Delta T \tag{8.2.21}$$

The source term $\dot{q}(t)$ in equation (8.2.20) is replaced with the righthand side of equation (8.2.17), and when both sides are multiplied by V_0, equation (8.2.22) shows the energy balance expressed in terms of the individual fission sources.

$$\phi(t) N_A \left(E_f^{25} \sigma_f^{25} n_{25}(t) + E_f^{49} \sigma_f^{49} n_{49}(t) \right) = \rho c_p V_0 \frac{d\Delta T}{dt} + hA\Delta T \tag{8.2.22}$$

The energy storage term is restated in terms of the properties of the individual components of the critical mass (CM) in equation (8.2.23), where f is a volume fraction (e.g. VVF, HMVF) and the summed masses m and heat capacities c_p of the i components are M and C_p, respectively.

$$\rho c_p V_0 = V_0 \sum_{i \in CM} f_i \rho_i c_{p,i} = \sum_{i \in CM} m_i c_{p,i} = M C_p \tag{8.2.23}$$

The VVF can be re-symbolized as the porosity ϵ, and the HMVF and FVF can be represented as ϵ_m and ϵ_f, respectively. Within the parametrization of the larger study, the total mass and average heat capacity are calculated in equations 8.2.24 and 8.2.25 using the saturation S_l to acknowledge effects of liquid (l) water and air (a).

$$M = V_c \left[\rho_m \epsilon_m + \rho_s (1 - \epsilon) + \rho_l S_l \epsilon_f + \rho_a \epsilon_f \left(1 - S_l\right) \right] \tag{8.2.24}$$

$$C_p = \frac{V_c}{M} \left[c_{p,m} \rho_m \epsilon_m + c_{p,s} \rho_s (1 - \epsilon) + c_{p,l} \rho_l S_l \epsilon_f + c_{p,a} \rho_a \epsilon_f \left(1 - S_l\right) \right] \tag{8.2.25}$$

The density and isobaric specific heat capacity figures for the water and air are obtained from linear interpolations of the steam tables at 15 MPa tabulated between $20°C - 1250°C$ in $5°C$ increments (some values are shown in table 6.2.2). The density of the solid rock matrix is kept constant at 1900 $\left[\frac{kg}{m^3}\right]$, and the heat capacity is modeled according to a temperature dependent relationship in Ref. [65], which is shown in equation (8.2.26). The reference heat capacity $c_{p,ref}$ is taken from sandstone at $T_{ref} = 20°C$, which is listed in the reference as $775\,\frac{J}{kg-K}$.

$$\begin{gathered} c_{p,n}(T) = 8.95 * 10^{-10}T^3 - 2.13 * 10^{-6}T^2 + 0.00172\,T + 0.716 \\ c_{p,s}(T)\,\left[\tfrac{J}{kg-K}\right] = c_{p,ref}\left(\tfrac{c_{p,n}(T)}{c_{p,n}(T_{ref})}\right) \end{gathered} \tag{8.2.26}$$

For the UO_2 deposition, ρ_m is kept at the full theoretical density of 10.950 $\left[\frac{kg}{m^3}\right]$. The specific heat capacity is obtained from a fit of experimental data in Ref. [110] shown in equation (8.2.27), where μ_{UO_2} is the molar mass of the deposition. The result of this function at room temperature is $230\,\frac{J}{kg-K}$, which is close to the maximum value from table 6.2.1.

$$\begin{gathered} c_{p,m}(\tau)\,\left[\tfrac{J}{kg-K}\right] = \tfrac{10^3}{\mu_{UO_2}}\left(52.1743 + 87.951\tau - 84.2411\tau^2 + 31.523\tau^3 - 2.6334\tau^4 - 0.71391\tau^{-2}\right) \\ \tau = \tfrac{T+273.15}{1000},\; 25°C \leq T \leq 2847°C \end{gathered} \tag{8.2.27}$$

Provided these definitions, equation 8.2.22 can be stated to provide the energy balance between fission generation, heat transfer, and energy storage:

$$\phi(t)N_A\left(E_f^{25}\sigma_f^{25}n_{25}(t) + E_f^{49}\sigma_f^{49}n_{49}(t)\right) = MC_p\frac{d\Delta T}{dt} + hA\Delta T \tag{8.2.28}$$

8.2.5 Heat transfer

Conduction

The typical validity criterion for lumped capacitance is that $Bi < 0.1$. Therefore, the heat transfer coefficient is bounded as follows:

$$\frac{h_b r_c}{3k} \leq 0.1 \Rightarrow h_b \leq \frac{3k}{10r_c} = \frac{3k}{5D}\left[\frac{W}{m^2 - K}\right] \tag{8.2.29}$$

The thermal conductivity must represent the effects of all thermal resistances in the constituents of the critical mass. A heat transfer analysis for a homogenized system is discussed in section §E.2, where there are different extremes for representing the effective thermal conductivity of the system. A solution capturing average behavior between these extremes was derived by Maxwell, who modeled electrical conductivity of a compound consisting of a solid matrix embedded with small spherical inclusions of a second component. [111] The thermal analogy is relevant to heat transfer in a porous medium, and the solution for effective conductivity k_e is shown in equation (8.2.30) for the solid component (s) and fluid component (f), which is applicable when ϵ is a small fraction. This condition was considered necessary to avoid interference in the electrical analog by reducing the embedded spherical radii relative to their separation distances. A threshold of 0.25 is suggested by Ref. [94], which accounts for the VVF of most critical masses in this study but will be applied to all configurations regardless.

$$k_e = k_s \frac{k_f + 2k_s - 2\epsilon\left(k_s - k_f\right)}{k_f + 2k_s + \epsilon\left(k_s - k_f\right)},\ \epsilon \lesssim 0.25 \tag{8.2.30}$$

To incorporate the effect of resistances caused by metal, water (l), and air (a) in the space occupied by fluid, it is proposed that k_f be modified to include k_m, k_l, and k_a. If the thermal resistances of the pore components can be modeled in parallel, then the pore space conductivity can be described in equation (8.2.31), where S_l is the liquid saturation. The values of k_l and k_a are obtained from linear interpolations of the steam tables at $15\,MPa$ tabulated between $20°C - 1250°C$ in $5°C$ increments (some values are shown in table 6.2.2).

The solid conductivity k_s is based on a relationship for acidic rocks (high silica content) from Ref. [112] via Ref. [113]. This empirical relationship is shown in equation (8.2.32), where k_s varies inversely with temperature. At room temperature, $k_s(20.45°C) = 2.82\ \left[\frac{W}{m-K}\right]$, which is on par with the wet values used in chapter 6 for shale and sandstone (table 6.2.1). However, since k_s needs to represent solid conductions without porewater, this would serve as an overestimate. Nonetheless, the monotonic decrease in temperature should compensate for this overestimate.

The value of k_m is borrowed from the temperature dependent relationship found in Ref. [114], and is shown in equation (8.2.33) for temperatures in Celsius. It is assumed that the model is still applicable for the small discrepancies in temperatures down to $20.45°C$ $(293.6\,K)$ and up to $1250°C$ $(1523.5\,K)$. At this temperature, this equation yields $k_m = 9.92\ \left[\frac{W}{m-K}\right]$, which exceeds the upper-bound value of $7\,\frac{W}{m-K}$ used for UO_2 in chapter 6 (as inspired by the figures in Ref. [115]). Nonetheless, this should be compensated by the considerable decline as temperature evolves. Altogether, k_f, and thus k_e, are represented as functions of temperature and saturation.

$$k_f = \frac{\epsilon_m k_m + \epsilon_f S_l k_l + \epsilon_f\left(1 - S_l\right)k_a}{\epsilon} \tag{8.2.31}$$

$$k_s\left(T\right)\left[\frac{W}{m-K}\right] = 807 + 0.64\left(350 + T\right)^{-1},\ 0°C \leq T \leq 1400°C \tag{8.2.32}$$

$$k_m(T)\left[\frac{W}{m-K}\right] = \left[2.997 * 10^{-2} + \left(T + 273.15\right)\left(2.414 * 10^{-4}\right)\right]^{-1},$$
$$26.85°C \leq T \leq 1226.85°C \tag{8.2.33}$$

For demonstration, assume a radius $1.5\,m$ (on par with the 5 MTU critical masses), a VVF of 25%, and an HMVF of 10%. Using the dry values in table 6.2.1 for UO_2 $\left(7\,\frac{W}{m-K}\right)$ and shale $\left(1.8\,\frac{W}{m-K}\right)$, and the room temperature values in 6.2.2 for water $\left(0.61\,\frac{W}{m-K}\right)$ and air $\left(0.03\,\frac{W}{m-K}\right)$, at full saturation, $k_f = 3.16\,\frac{W}{m-K}$ and $k_e = 2.09\,\frac{W}{m-K}$. This suggests a heat transfer coefficient bound at $0.357\,\frac{W}{m^2-K}$. This also implies that the heavy metal plays a strong role in determining the pore conductivity, and the less-conductive rock matrix has a diluting effect, which makes the simplification of keeping . When the saturation is reduced to 10%, the pore conductivity drops significantly to $k_f = 2.85\,\frac{W}{m-K}$, while the effective conductivity is only slightly reduced to $k_e = 2.03\,\frac{W}{m-K}$. When the HMVF is reduced to 6% in the 10% saturated case, $k_f = 1.75\,\frac{W}{m-K}$ and $k_e = 1.79\,\frac{W}{m-K}$, implying a stronger role of the rock matrix in determining conductivity with poorly-conducting pores. Given the importance of UO_2 in determining conductivity, the contributions from the incoming plume of UO_2 will be factored until metal displaces all pore water ($\epsilon_f \rightarrow 0$, $\epsilon_m \rightarrow \epsilon$).

From section 6.3.2, the behavior of saturation with temperature was observed to vary roughly linearly after a certain threshold temperature, which can be referred to as T_{th}. It was also observed that desaturation of the critical mass led to poorer heat transfer characteristics, causing an increase in average temperatures in the critical mass. Given the anticipated effects of S_l on equation (8.2.31), a simple piecewise relationship is employed in equation (8.2.34) to model the saturation. This can be used to simplify thermal conductivity dependence to temperature only. A T_{th} of $100°C$ can be used to describe the onset of desaturation, based on results shown in figure 6.3.2 and figure 6.3.3.

$$S_l(T) = \begin{cases} 1 & T < T_{th} \\ 1 - \frac{T - T_{th}}{T_{BP} - T_{th}} & T_{th} \leq T < T_{BP} \\ 0 & T \geq T_{BP} \end{cases} \tag{8.2.34}$$

Convection

From chapter 3, groundwater was modeled as flowing across the repository within a variation of velocities. In chapter 6, the outward flow of water from the critical mass was observed due to capillary effects even in the absence of heating. Therefore, the heat transfer term in the model should ideally include effects from the porewater. Within the scope of this particular study, there may be forced convection or natural convection of pore water as potential heat transfer phenomena of interest. Forced convection deals with the flux of groundwater around the surface of the sphere driven by a hydraulic gradient, while natural convection describes the buoyant movement of pore water about the critical mass driven by variations in the density and gravitational acceleration. In either case, the convective boundary layers are formed that transfer heat from the surface of the sphere to the surroundings.

The Nusselt number is typically used to assign heat transfer coefficients for forced and natural convection scenarios. It describes the eminence of convective heat transfer over conductive heat transfer at the surface of the sphere, and acts as a dimensionless temperature gradient at the interface between the critical mass and the surrounding rock. The global value of the Nusselt number, $\bar{Nu}$, is defined in terms of the heat transfer coefficient, thermal conductivity of the *porewater*, and characteristic length:

$$\bar{Nu} = \frac{hL_c}{k_l} = \frac{h\,(2r_c)}{k_l} \tag{8.2.35}$$

In the forced convection context, consider a volume-averaged uniform groundwater velocity v, and a radial angle θ in the sphere relative to the direction of uniform flow. The h term in local value of the Nusselt number, Nu_θ, is defined by the heat flux and difference in temperatures between the spherical surface and surroundings. For a heat emitting sphere interacting with an infinite porous medium, a correlation for Nu_θ is shown in equation (8.2.36) using the local Péclet number (Pe_θ) assuming an isothermal sphere. [116] As discussed briefly in chapter 3 in the mass transport context, the Péclet number describes the ratio of advective flow over diffusive flow (equation (8.2.37)). It is defined in terms of the uniform velocity, characteristic length, and thermal diffusivity $\alpha = \frac{k}{\rho c_p} \left[\frac{m^2}{yr}\right]$. In forced convection about spheres and cylinders, the characteristic length in Pe_θ is defined as the arc $r_c\theta$. Equation (8.2.36) is therefore valid when the flow boundary thickness is much smaller than the radius of the sphere, i.e. when $r_0\sqrt{Pe_\theta} < r_0$, or when $Pe_\theta^{1/2} \gg 1$. The global value is obtained from averaging the heat flux and is expressed in terms of the typical Péclet number where the characteristic length is the spherical diameter. [117]

$$Nu_\theta = \frac{q''\left(2r_c\right)}{k_l\left(T_s - T_\infty\right)} = 0.564 \cdot Pe^{1/2}\sqrt{\frac{3\theta}{2}} sin^2\theta \left(cos^3\frac{\theta}{3} - cos\theta + \frac{2}{3}\right)^{1/2},\ Pe^{1/2} \gg 1 \quad (8.2.36)$$

$$Pe = \frac{vL_c}{\alpha} = \begin{cases} \frac{(2r_c)vc_p\rho}{k} & \text{global} \\ \frac{(r_c\theta)vc_p\rho}{k} & \text{local} \end{cases} \quad (8.2.37)$$

$$\bar{Nu} = 1.128 \cdot Pe^{1/2} \quad (8.2.38)$$

In the natural convection context, consider a radial angle θ in the sphere relative to the gravitational acceleration vector. The Nusselt number for boundary layer convection around an isothermal sphere in an infinite porous medium is shown in equation (8.2.39) in terms of the Rayleigh number (Ra). [116] The average value is shown in equation (8.2.40).[1] [117]

$$Nu_\theta = 0.444 \cdot Ra^{1/2}\sqrt{\frac{3\theta}{2}} \frac{sin^2\theta}{\sqrt{\frac{1}{3}cos^3\theta - cos\theta + \frac{2}{3}}},\ Ra \gg 1 \quad (8.2.39)$$

$$\bar{Nu} = 0.724 \cdot Ra^{1/2} \quad (8.2.40)$$

The Rayleigh number is the product of the Grashof and Prandtl numbers. The Prandtl number (Pr, equation (8.2.41)) describes the ratio between the momentum diffusivity (or kinematic viscosity, $\nu \left[\frac{m}{yr}\right]$) to the thermal diffusivity in a fluid. The viscosity describes the viscous diffusion rate, which concerns to the resistance of a fluid to deformation from stress relative to fixed surfaces. The thermal diffusivity measures the rate of heat transfer from

---

[1] There is a factor of 2 difference in the coefficient between references [117] and [118]. The most recently published value is used in the analysis.

the hot portion of a material to the cold portion, and thus the "inertia" of the movement of heat. Therefore, Pr demonstrates the effectiveness of the diffusive transfer of momentum in the boundary layer.

$$Pr = \frac{\rho c_p \nu}{k} = \frac{\nu}{\alpha} \tag{8.2.41}$$

The Grashof number (Gr, equation (8.2.42)) is described in terms of the thermal expansion coefficient β $\left[\frac{1}{K}\right]$, the acceleration due to gravity g $\left[\frac{m}{yr}\right]$, and the temperature difference of the spherical surface and the surroundings. It describes the ratio of buoyancy forces and viscous forces acting on a fluid. As buoyancy forces emerge from changes in density via heating, the viscous forces of the fluid counteract the movements caused by those density changes, which are important characteristics in defining the onset of natural convection.

$$Gr = \frac{g\beta L_c^3}{\nu^2}(T_s - T_\infty) \tag{8.2.42}$$

As the product of Pr and Gr (equation (8.2.43)), the Rayleigh number describes the ratio of buoyancy and viscosity forces multiplied by the ratio between fluid momentum and thermal diffusivity. It is used to characterize the onset of convection in the system, as there is a critical value of Ra above which fluid motion is liable to occur. Below this critical value, heat transfer will occur primarily through conduction.

$$Ra = Pr \cdot Gr = \frac{g\beta L_c^3}{\nu\alpha}(T_s - T_\infty) \tag{8.2.43}$$

A separate version of this quantity relevant to the Nu correlation in equation (8.2.40) is shown in equation (8.2.44) that incorporates the permeability of the surrounding rock ($\mathcal{K}$) for fluid flow applicable to Darcy's law.

$$Ra = \frac{\mathcal{K} g\beta\,(2r_c)}{\alpha\nu}\,(T_s - T_\infty) = \frac{\mathcal{K} g\beta\,(2r_c)\,\rho c_p}{k\nu}\,(T_s - T_\infty) \tag{8.2.44}$$

Therefore, it is clear that the magnitude of h would largely be determined by the relative magnitudes of Pe and Ra. For Pe, an average groundwater velocity of $50\,\frac{m}{yr}$ can be assumed. An example can be made of the 5 MTU 2 wt% homogeneous critical mass, which has a radius of $1.06\,m$, a VVF (ϵ) of 33.7%, and HMVF (ϵ_m) of 10.5%. Just for reference, at full saturation, the pore-filling conductivity of this precipitate would be $k_f = 2.60\,\frac{W}{m-K}$ with an overall conductivity of $k_e = 2.04\,\frac{W}{m-K}$. Also, based on the parameters in table 6.2.1 and table 6.2.2, an average heat capacity of $872\,\frac{J}{kg-K}$ is obtained via equation (8.2.25) and an average density of $2640\,\frac{kg}{m^3}$ from $\rho = M/V_c$ in equation (8.2.24).

The calculation of Pe is based on properties of the pore fluid itself:

$$Pe = \frac{(2r_c)\,v c_p \rho}{k} = \frac{(2 * 1.06\,m)\left(50\,\frac{m}{yr} * 3.17 * 10^{-8}\,\frac{yr}{s}\right)\left(4140\,\frac{J}{kg-K}\right)\left(1005\,\frac{kg}{m^3}\right)}{0.606\,\frac{W}{m-K}} = 23$$

The square root of this quantity is 4.8, which satisfies the boundary layer criterion. When calculating the Rayleigh number, a temperature difference based on the phase boundary transition can be used: $T_s - T_\infty = 615.305\,K - 293\,K = 322.305\,K$. The kinematic viscosity is obtained as $\nu = \frac{\mu}{\rho}$. Using a permeability of $1\,\mu D \approx 10^{-18}\,m^2$, the resulting Ra is very low:

$$Ra = \frac{\left(10^{-18}\,m^2\right)\left(9.81\,\frac{m}{s^2}\right)\left(2.325*10^{-4}\,\frac{1}{K}\right)\left(2.12\,m\right)\left(4140\,\frac{J}{kg-K}\right)\left(1005\,\frac{kg}{m^3}\right)}{\left(0.606\,\frac{W}{m-K}\right)\left(9.87*10^{-4}\,\frac{kg}{m-s}\right)/\left(1005\,\frac{kg}{m^3}\right)} 322.305\,K$$
$$= 1.1*10^{-5}$$

This would not be applicable to the natural convection relationship of equation (8.2.40). Therefore, to confirm the role of natural convection in the system, the Grashof number can be compared with the Reynold's number (Re), which is defined as:

$$Re = \frac{\rho v (2r_c)}{\mu} = \frac{\left(1005\,\frac{kg}{m^3}\right)\left(50\,\frac{m}{yr}*3.17*10^{-8}\,\frac{yr}{s}\right)\left(2.12\,m\right)}{\left(9.87*10^{-4}\,\frac{kg}{m-s}\right)} = 3.4$$

This quantity is used to define the ratio of inertial to viscous forces in a fluid, which is important when characterizing flow as laminar or turbulent. It is also multiplied with the Prandtl number to given the Péclet number. The Grashof number can be restated to account for permeability:

$$Gr = \frac{\mathcal{K} g \beta (2r_c)}{\nu^2}(T_s - T_\infty) = \frac{\left(10^{-18}\,m^2\right)\left(9.81\,\frac{m}{s^2}\right)\left(2.12\,m\right)\left(2.325*10^{-4}\,\frac{1}{K}\right)\left(322.305\,K\right)}{\left[\left(9.87*10^{-4}\,\frac{kg}{m-s}\right)/\left(1005\,\frac{kg}{m^3}\right)\right]^2}$$
$$= 1.6*10^{-6}$$

Since Gr is typically held to be the square of Re in buoyancy-driven flow problems, the ratio is evaluated as:

$$\frac{Gr}{Re^2} = 1.4*10^{-7} \ll 1$$

This signifies that free convection effects in the porous medium can be ignored. [94] Assuming the forced convection relationship can be applied with the derived value of Pe, the Nusselt number is evaluated as $\bar{Nu} = 5.42$. This would imply a heat transfer coefficient of

$$\bar{Nu} = \frac{h\,(2r_c)}{k_l} \Rightarrow h = \frac{\bar{Nu} \cdot k_l}{2\,(r_c)} = 5.42 \frac{0.606\,\frac{W}{m-K}}{2.12\,m} = 1.55\,\frac{W}{m^2-K}$$

From equation (8.2.29), the bound on h required for the lumped parameter treatment is:

$$h_b \leq \frac{3k_e}{10r_c} = \frac{3\left(2.04\,\frac{W}{m-K}\right)}{10\,(1.06\,m)} = 0.385\,\frac{W}{m-K}$$

This implies the existence of a bound on groundwater velocities for the forced convection model to be applicable to the lumped parameter approach:

$$h_b \geq \frac{1.128 \cdot k_l}{2\,(r_c)}\left(\frac{(2r_c)\,v c_{p,l}\rho_l}{k_l}\right)^{1/2} \Rightarrow v \leq 1.571\frac{h_b^2 r_c}{\rho_l c_{p,l} k_l} = 3.10\,\frac{m}{yr}$$

For the precipitate, this would correspond to $Pe^{1/2} = 1.2$, which is not large enough to ensure that the convection boundary layer is smaller than the critical radius. Therefore, the effects of convection cannot be realistically modeled in the methodology, and the heat transfer coefficient is instead defined at the upper limit ($h = h_b$) to compensate for this limitation. Since h_b is a function of k_e, this term is employed as a function of temperature and time in the numerical solver.

8.2.6 Integration

Now that the heat transfer and energy storage terms are defined, the system of equations can be finalized. The dotted notation can be used for the time derivative, and the critical mass temperature can be restated in terms of the temperature difference such that $\frac{dT}{dt} = \frac{d}{dt}\left(T - T_\infty\right) = \frac{d\Delta T}{dt} = \dot{\Delta T}$. The neutron flux can be described in equation (8.2.45) in terms of the lumped mass M, the total specific heat capacity C_p, and the change in temperature, which are all implicitly functions of time.

$$\phi(t) = \frac{MC_p\dot{\Delta T} + hA\Delta T}{N_A\left(E_f^{25}\sigma_f^{25}n_{25}(t) + E_f^{49}\sigma_f^{49}n_{49}(t)\right)} \tag{8.2.45}$$

The $N = 3$ isotopes of the system are comprised of fissile U-235 (n_{25}) and Pu-239 (n_{49}) along with fertile U-238 (n_{28}), and equation (8.2.13) is used to provide the set of $N + 1$ equations as follows:

$$\left\{\begin{array}{c} \dot{n}_{25} = \dot{S}_{25} - \lambda_{25}n_{25} + \lambda_{49}n_{49} + \phi\left(-\sigma_c^{25}n_{25} - \sigma_f^{25}n_{25}\right) \\ \dot{n}_{49} = -\lambda_{49}n_{49} + \phi\left(\sigma_c^{28}n_{28} - \sigma_c^{49}n_{49} - \sigma_f^{49}n_{49}\right) \\ \dot{n}_{28} = \dot{S}_{28} - \lambda_{28}n_{28} + \phi\left(-\sigma_c^{28}n_{28}\right) \\ \alpha(n_{25} - n_{25}^0)\dot{n}_{25} + \alpha_{28}\dot{n}_{28} + \alpha_T(T_\infty + \Delta T)\dot{\Delta T} + \alpha_R\left(\Delta T\right) f_R\left(\Delta T\right)\dot{\Delta T} = 0 \end{array}\right. \tag{8.2.46}$$

The source term is assumed to be temporally limited by the volume of pore space available in the critical mass. This implies that heavy metal must displace pore water in order to affect reactivity, as opposed to accumulating on the surface. If the total source term is defined as the sum of the incoming plumes of U-235 and U-238, $\dot{S}\left[\frac{mol}{yr}\right] = \dot{S}_{25} + \dot{S}_{28}$, then the time required to fill the pore space is defined using the density ρ_{UO_2} and molar mass μ_{UO_2} of the incoming material:

$$t_{fill=}\frac{V_0\epsilon_f^0\rho_{UO_2}}{\mu_{UO_2}\dot{S}} \tag{8.2.47}$$

Therefore, the source term is given a banded representation in equation (8.2.48), where constant flux values are employed before t_{fill}. The TTB fluxes are in units of $\frac{mol}{m^2-yr}$, and they are multiplied by the total surface area of the critical mass to obtain a mass influx rate. Although the fluxes of nuclides in figure 3.4.7 evolve over time, the behaviors at time-points relevant to attaining a critical mass are relatively steady, so the treatment of chapter 3 results observed at these time points as constants is defensible. Although it would seem apt to modify equation (8.2.48) using the Bateman solutions since λ is included in equation (8.2.46), the magnitude of t_{fill} is expected to be much less than the half-life of either nuclide, so it is not entirely necessary. However, at least a first-member decay term should be employed if there is a source of a short-lived nuclide.

$$\dot{S}_i(t) = \begin{cases} \dot{S}_i e^{-\lambda_i t} & t < t_{fill} \\ 0 & t \geq t_{fill} \end{cases} \tag{8.2.48}$$

As metal fills the pore space, the fluid volume fraction slowly approaches zero and the heavy metal volume fraction approaches the full porosity. These considerations can be modeled via equations 8.2.49 and 8.2.50. These relationships replace the static fractions in equations 8.2.24, 8.2.25, and 8.2.31, which make M, C_p and k_f (and, by association, h) functions of both time and temperature. Examples of C_p and h are shown in figure 8.2.2 for the initial volume fractions, where effects at T_{th} and T_{BP} may be noticeable.

$$\epsilon_f'(t) = \begin{cases} \epsilon_f^0 - \frac{\dot{S}\mu_{UO_2}}{\rho_{UO_2}V_0}t & t < t_{fill} \\ 0 & t \geq t_{fill} \end{cases} \tag{8.2.49}$$

$$\epsilon_m'(t) = \begin{cases} \epsilon_m^0 + \frac{\dot{S}\mu_{UO_2}}{\rho_{UO_2}V_0}t & t < t_{fill} \\ \epsilon & t \geq t_{fill} \end{cases} \tag{8.2.50}$$

The decay terms of U-235 and U-238 are ignored due to extremely long half-lives that exceed the scope of the nuclide transport results. A dummy source term for Pu-239 $\left(\dot{S}_{49} = 0\right)$ can be employed for future reference. Thus, when the QSS flux approximation of equation (8.2.45) is employed in equation (8.2.46), the final working set of equations for this study is:

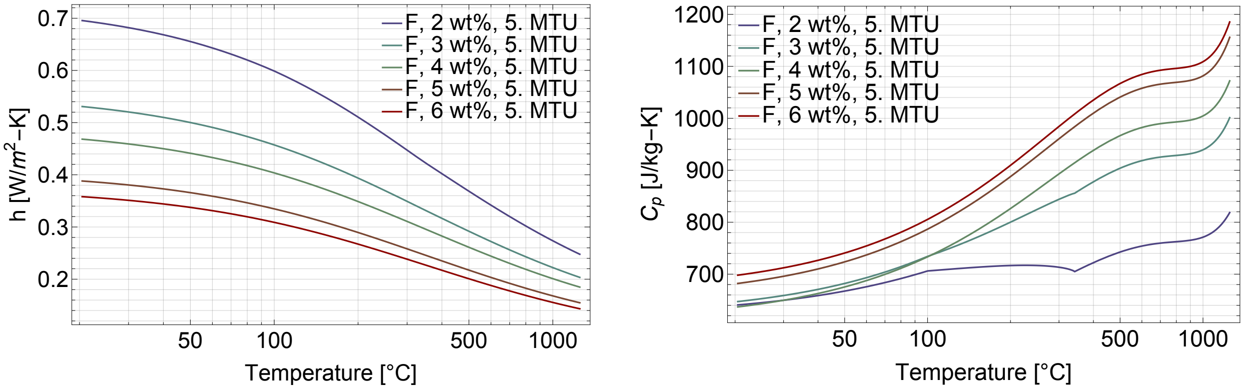

(a) h (b) C_p

Figure 8.2.2: Examples of temperature-dependent heat transfer terms using initial volume fractions.

$$\begin{cases} \dot{n}_{25} = \dot{S}_{25} - \cancel{\lambda_{25} n_{25}} + \lambda_{49} n_{49} + \frac{M C_p \Delta \dot{T} + h A \Delta T}{N_A \left(E_f^{25} \sigma_f^{25} n_{25} + E_f^{49} \sigma_f^{49} n_{49} \right)} \left(-\sigma_c^{25} n_{25} - \sigma_f^{25} n_{25} \right) \\ \dot{n}_{49} = \left[\dot{S}_{49} \right] - \lambda_{49} n_{49} + \frac{M C_p \Delta \dot{T} + h A \Delta T}{N_A \left(E_f^{25} \sigma_f^{25} n_{25} + E_f^{49} \sigma_f^{49} n_{49} \right)} \left(\sigma_c^{28} n_{28} - \sigma_c^{49} n_{49} - \sigma_f^{49} n_{49} \right) \\ \dot{n}_{28} = \dot{S}_{28} - \cancel{\lambda_{28} n_{28}} + \frac{M C_p \Delta \dot{T} + h A \Delta T}{N_A \left(E_f^{25} \sigma_f^{25} n_{25} + E_f^{49} \sigma_f^{49} n_{49} \right)} \left(-\sigma_c^{28} n_{28} \right) \\ \alpha (n_{25} - n_{25}^0) \dot{n}_{25} + \alpha_{28} \dot{n}_{28} + \alpha_T (T_\infty + \Delta T) \Delta \dot{T} + \alpha_R \left(\Delta T \right) f_R \left(\Delta T \right) \Delta \dot{T} = 0 \end{cases} \tag{8.2.51}$$

Given the functional forms of the feedback coefficients, the source terms, and heat transfer terms, this system of equations requires numerical solving. In appendix D, assumptions are made to modify the governing equations to provide analytical solutions for simplified systems.

8.2.7 Initial conditions

The initial conditions for equation (8.2.51) are as follows:

1. The initial mass of U-235, n_{25}^0, is derived from the enrichment and critical mass: $n_{25}(t = 0) = n_{25}^0 \approx M_c \tilde{e}$, where the presence of U-233 is ignored. The quantity is converted to moles.
2. The initial mass of U-238, n_{28}^0, is derived from the critical mass and the complement of the enrichment: $n_{28}(t = 0) = n_{28}^0 \approx M_c \left(1 - \tilde{e}\right)$, where the isotopes U-234 and U-236 are ignored. The quantity is converted to moles.
3. There is no initial quantity or source term of any other nuclide, and the effects of the generation of poisonous fission products like Sm-149 are ignored.

4. The initial temperature difference with the surroundings is zero: $T(t=0) = T_\infty \Rightarrow \Delta T(t=0) = 0$.
5. The source term of U-235, $\dot{S}_{25}(t)$, is obtained from the 50% quantile in the mixed sampling case from the transport calculation in chapter 3, based on the characteristics observed at the time when the total critical mass is met. The use of the 75% and 90% quantiles may be possible to probe extreme behavior.
6. The source of U-238, $\dot{S}_{28}(t)$, is obtained similarly to $\dot{S}_{25}$ in item .

Given the highly thermal spectrum corresponding to criticality, ENDF-B/V.II cross sections at 2200 m/s are employed in the equations. In this report, these cross sections are not modified with the temperature increase, as Doppler broadening effects are handled through α. However, an approximation would be possible by following the Maxwellian curve. The effective cross sections of chapter 7 are not transferred to this analysis since it is apparent from equation (8.2.51) that the ratios of the various σ values re most important. Furthermore, the competition between the various nuclides in parasitically absorbing neutrons cannot be directly determined from the effective capture cross section.

The unknowns n_{25}, n_{28}, n_{49}, and ΔT, along with their time derivatives, are solved over time using the *NDSolve* differential equations solver in Mathematica, where the default method involves switching between various methods adaptively depending on stiffness. [67]

8.3 Results

8.3.1 TTB source terms

The superposed mass fluxes from the nuclide transport study are multiplied by the total surface areas of the critical masses. The fluxes are then applied to the governing equations based on the mass of the precipitate, regardless of enrichment. Within this approach, the fluxes of U-233 were found to be negligible, so there is no need to modify equation (8.2.51) to include these contributions. It was observed early on that a strong dependence exists between the magnitude of ΔT and $\dot{S}$. Therefore, flux values were chosen at the 90% quantile to conservatively overestimate temperature. The study is bounded to a hundred million years to correlate with the assumptions in chapter 3.

The temperature difference between the critical mass and the far-field rock is shown in figure 8.3.1 in terms of enrichment for different geometries. The corresponding plots of reactivity were shown in figures 7.3.1a and 7.3.3a in chapter 7, and the $\alpha_T(T)$ models obtained from regression are shown in figure 8.3.2. It is observed that for a given mass, precipitates with the lower enrichments lead to higher temperature differences. Lower-enriched precipitates require a greater amount of void space and heavy metal (see figure 4.4.5), which increases the critical radius per given mass. This decreases the heat transfer coefficient due to inverse proportionality with the radius, while the rock interface area increases with the square of the radius. This leads to the hA term increasing proportional to the radius, so for a given amount of heat from fission, a greater temperature difference will be realized from Newton's law of cooling. This would be compounded by the increased volumetric content of UO_2, which has a lower c_p than the rock, reduces C_p, and further affects the energy balance. Despite the two geometries having similar critical dimensions (see section 4.4.2), the fractured geometry exhibits relatively higher temperatures because its temperature feedback coefficients are slightly less negative per given enrichment level.

Within the scope of the plots, the temperature does not exceed the phase transition and the system remains in the partially-unsaturated region. In this context, the Gaussian fit leads to temperatures that are consistently less than the those of the exponential fit given the differences in $|\alpha_T|$ that are evident in figure 8.3.2. It can be seen that the gaussian regressions lead to greater $|\alpha_T|$ within the first $\approx 180°C$ of heating in the critical mass, before being outpaced by the exponential curves. The time scale for the onset of high temperatures is a million years from the formation of the critical mass, and maximal temperatures of $200°C - 225°C$ are ultimately observed. The extremely negative effects from the piecewise plot can therefore not be realized,

For the 2 wt% precipitates, the dependence of mass on the temperature change was investigated and plotted in figure 8.3.3. The larger critical masses have lower maximum heat transfer coefficients due to the $\frac{1}{r_c}$ proportionality, and h also decreases with temperature since k_e does as well. Since these precipitates have relatively lower porosities and heavy metal volume fractions, they have a higher proportion of rock relative to the UO_2 and fluid. This causes the value of C_p to be lower in the partially unsaturated region, since the strong contributions of water to the mass average are reduced. From chapter 7, α_T was observed to be less negative for higher masses, so with this aspect, combined with the behavior of the heat transfer terms, the plotted temperatures of the larger masses are consistently higher. Nonetheless, it should be noted that results for the 5 and 10 MTU masses behave very similarly. Also, after the critical mass is desaturated, the average heat capacity of the larger mass will be higher than those of the smaller masses because the heat capacity of the rock matrix is higher than that of the ceramic, which will alter the energy balance.

An extreme case is presented with the 1.5 wt% precipitates of the fractured geometry in figure 8.3.4. The feedback coefficients in these massive precipitates closely overlap, which leads to string similarities in ΔT behavior. Per given time, the temperatures achieved in these precipitates are higher than those in the 2 wt% category, as expected. However, the difference is not substantial enough to allow these unrealistic configurations to represent the worst case scenario in terms of ΔT.

It is generally clear that per enrichment, the extent of temperature evolution is dependent on an interplay between h, C_p, and the magnitude of α_T. In chapter 7, it was shown that, with some exceptions (i.e. the minimal 6 wt% precipitates), that α_T is more strongly negative for lower-enriched precipitates of greater critical radius. From the methodology employed in this report, the higher enriched precipitates will have less pore water available for the uranium plume to displace, and in some cases ϵ_f is zero. Therefore, temperature rises from the added fissile material will be much more limited, such that temperature feedback, despite being of

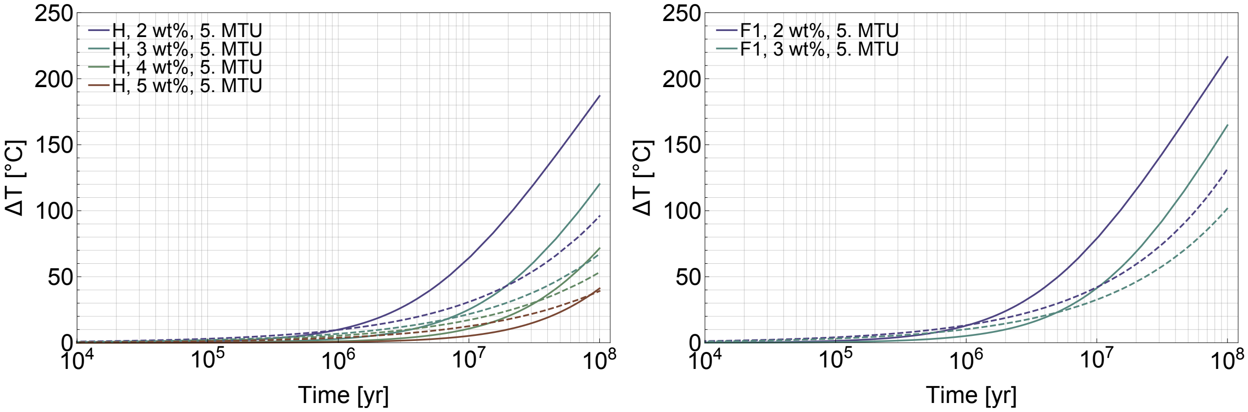

(a) Homogeneous, 5 MTU

(b) Fractured, 5 MTU

Figure 8.3.1: The evolution of ΔT over time for 5 MTU precipitates using the 90% quantile source terms from chapter 3, where α_T is modeled as a piecewise function (solid) or Gaussian (dashed).

lower magnitude, will be able to offset the contributions rather easily. In order to investigate maximal temperatures, the focus should be shifted to accumulations of lower enrichment and higher mass, since there is greater flexibility over time for the different mechanisms to interact.

The less-realistic approach #2 for the fractured geometry featured much lower α_T and cases of mildly positive feedback for some highly enriched precipitates. The dry cases with approximately zero or positive feedback had non-convergent solutions except for the 10 MTU, 3 wt% case, which reached a steady-state temperature of $130°C$ (as all the pore space was filled). For the wet cases at lower enrichment, the ΔT solutions for 2 and 3 wt% at 5 MTU reached $200°C$ at $2 * 10^7\, yr$ in manner similar to the approach #1, but afterwards the temperature rise was observed to increase exponentially. Upon closer inspection, this was tied to a drastic increase in the flux due to unfettered positive feedback from U-235, the quantity of which is observed to rise in this region. This comes as a numerical consequence of unrealistically low α_T and high $\alpha_{25}\dot{n}_{25}$. Therefore, when compounded with the unrealistic geometry, these results will not be considered indicative of runaway reactions. However, from the methodology of the model, it is safe to assume that for a system with low Doppler feedback coefficients and a large pore space available for UO_2 to drop out of solution, very strong temperature rises may still be observed.

8.3.2 Modified source terms

Given the limited extent of $\Delta T(t)$ from the source terms based on the TTB results, a study was undertaken to modify $\dot{S}_i$ parameters to explore possible changes in temperature evolution. While these results are dissociated from the specific details of the transport

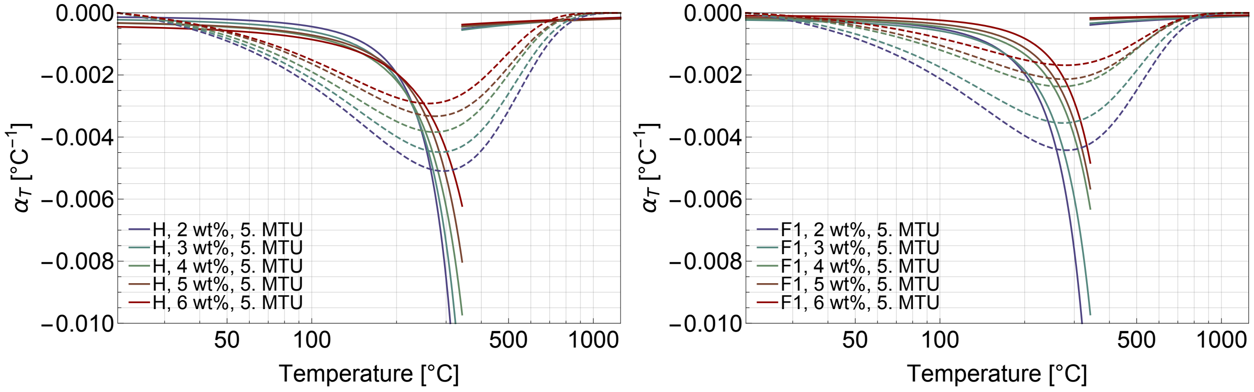

(a) Homogeneous, 5 MTU

(b) Fractured, 5 MTU

Figure 8.3.2: Temperature feedback coefficient (α_T) for the 5 MTU precipitates derived from reactivity modeled as a piecewise function (solid) or Gaussian (dashed).

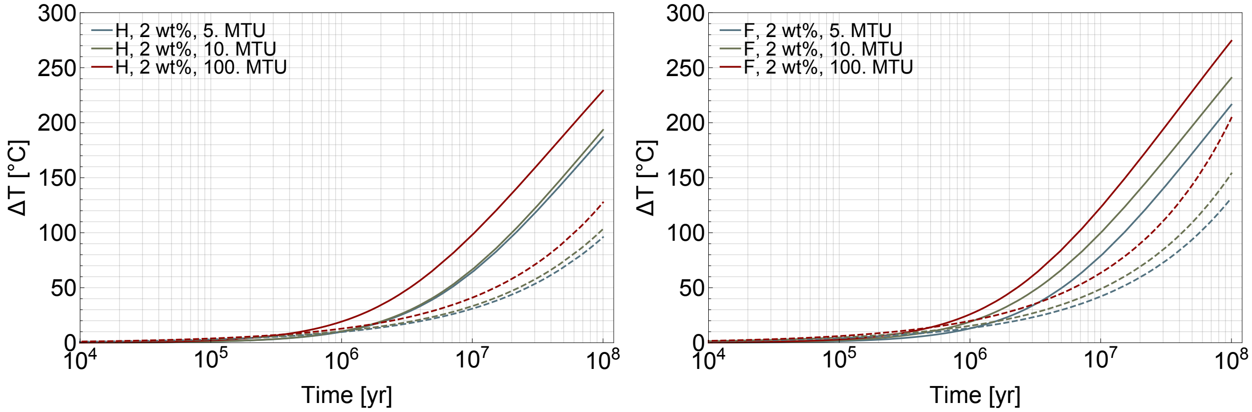

(a) Homogeneous, 2 wt%

(b) Fractured, 2 wt%

Figure 8.3.3: The evolution of ΔT over time for 2 wt% precipitates using the 90% quantile source terms from chapter 3, where α_T is modeled as a piecewise function (solid) or Gaussian (dashed).

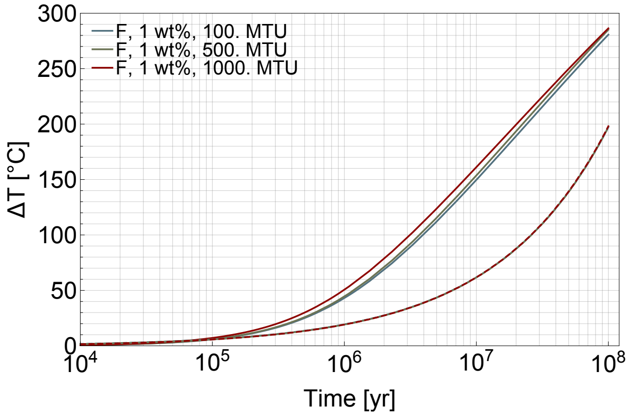

Figure 8.3.4: The evolution of ΔT over time for 1.5 wt% fractured geometry precipitates using the 90% quantile source terms from chapter 3, where α_T is modeled as a piecewise function (solid, top) or Gaussian (dashed, bottom).

study, they can be indicate behavior for critical masses hypothesized in studies with liberal scenarios. The 5 MTU, 2 wt% homogeneous critical mass is examined for closer inspection, where $\dot{S}_{25} = 7.8 * 10^{-8} \frac{mol}{yr}$ and $\dot{S}_{28} = 5.5 * 10^{-6} \frac{mol}{yr}$. The behavior described in this section was observed to be extensible to other low-enriched configurations.

Enriched uranium plume

The uranium source term is increased in log-scale increments between 10^{-7} and 10^{-1} moles per year, where the relative proportions of U-235 and U-238 are approximated by the enrichment of the precipitate. For simplicity, it is presumed that the modeled quantity of U-235 can account for the effects of additional fissile material presented by U-233. In figure 8.3.5, the results of $\Delta T(t)$ are shown in the context of this parametrization, where $10^{-5} \frac{mol}{yr}$ line most closely approximates the TTB results. The temperature rise is observed to peak before falling to a steady level, and as $\dot{S}$ is increased, these peaks occur proportionately sooner in time. The peaks correspond to reductions in flux and Pu-239 production caused by the U-235 feedback coefficient reaching the negative (undermoderated) region, while the steady-levels are caused by the pore-water being completely displaced by uranium. In the model, since α_{25} is based on the net difference in U-235, the flux and radioactive decay are not high enough to engender further depreciation in n_{25} to affect the reactivity balance. Since the poisoning effects of α_{28} are too small relative to $\dot{S}_{28}$, the temperature remains constant as equation (8.2.13) remains balanced.

The use of a Gaussian regression results in a higher peak and steady-state ΔT, since in this case α_T is less negative at temperatures near the phase transition. Altogether, a maximal ΔT of $540°C$ is observed for the Gaussian fit and $360°C$ for the piecewise. The latter temperature is clearly indicative of the average temperature of the system as it becomes completely desaturated, and this is attained as the feedback becomes considerably weaker

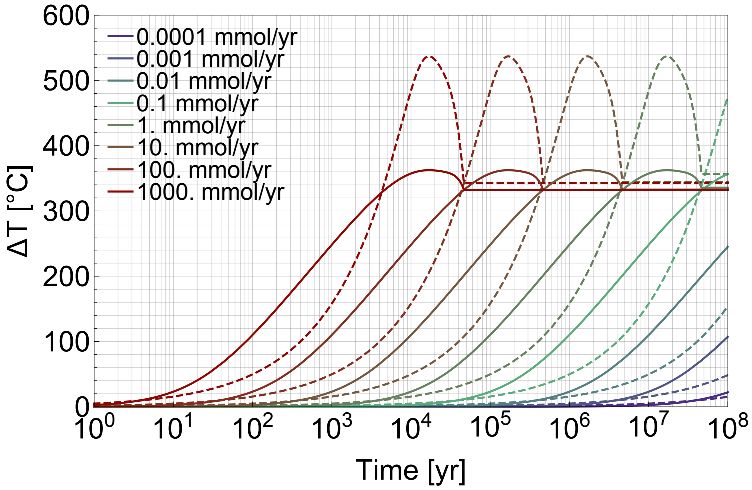

Figure 8.3.5: The effect of increasing the total uranium source term $\left[\frac{mmol}{yr}\right]$ in the 5 MTU, 2 wt% precipitate in the homogeneous geometry for piecewise (solid) and Gaussian (dashed) treatments of α_T.

when the system is dry. The underestimate in α_T for the continuous function leads to the higher temperature, and it is therefore proposed that the real system temperature will lie between these two bounds.

For comparison, the parametrization for 1 MTU configurations of the homogeneous and fractured geometries is shown in figure 8.3.6. In either of these cases, the void space and HMVF required for criticality is lesser than the configurations at 2 wt%, and the fractured geometry requires lower volume fractions compared to the homogeneous. Although the temperature feedback coefficients are expected to be less negative, the α_{25} for more-enriched geometries reaches the undermoderated (negative) region for relatively smaller changes in the heavy metal volume fraction, which will limit the positive feedback contributions from the arriving fissile material before Doppler feedback brings reactivity back down. For this reason, the maximum temperature observed in the piecewise model is slightly suppressed to $320°C$. For the Gaussian model, the fractured geometry yields a maximum temperature of $480°C$ while the homogeneous geometry yields $400°C$. Due to lower porosities, a shorter time period is needed for the pore space to fill and for ΔT to reach a steady state, and the fractured geometry presents an extreme example of this tendency.

Enhanced U-235 plume

A study is conducted where the TTB source terms are augmented by an additional source of pure U-235 oxide, which is tested from $10^{-8}\,\frac{mol}{yr}$ to $10^{-3}\,\frac{mol}{yr}$ in log-scale increments. This would represent a scenario with strong mobility of TRU precursors that would amplify the mass flux of U-235 over that of U-238. In 3, such imbalances were observed at early times before the main plume of uranium originating from the used fuel eventually dominates, as

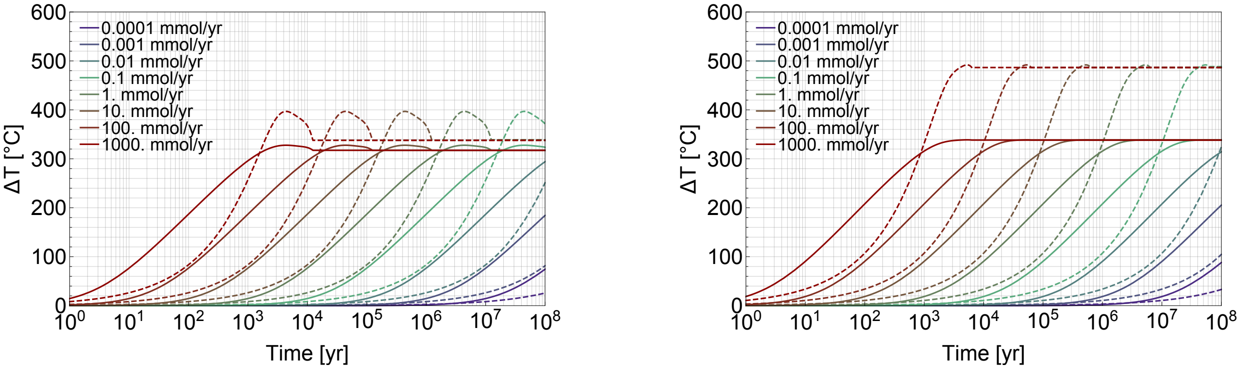

(a) Homogeneous (b) Fractured

Figure 8.3.6: The effect of increasing the total uranium source term $\left[\frac{mmol}{yr}\right]$ in 1 MTU, 3 wt% configurations for piecewise (solid) and Gaussian (dashed) treatments of α_T. The original source terms from TTB are $\dot{S}_{25} = 1.5 * 10^{-8}\ \frac{mol}{yr}$ and $\dot{S}_{28} = 1.1 * 10^{-6}\ \frac{mol}{yr}$.

indicated in figure 3.4.7. Figure figure 8.3.7 shows that when $\dot{S}_{25}$ is parametrized, the same peak temperatures are observed as before in figure 8.3.5, although there are no steady-state levels after the maximum temperatures. This is due to the negative region of α_{25} being fully attainable from the additional fissile material (Δn_{25}), which causes the system to be undermoderated. Since U-238 does not occupy significant portions of the pore space, and all positive feedback mechanisms disappear, the system is brought to subcriticality.

It is assumed that the α_{25} derived from the section 4.4.4 methodology, which involved an enriched source, is applicable to a pure source. A study is recommended to evaluate reactivity changes directly in MCNP as pure ${}^{235}UO_2$ displaces volumes of H_2O in the pore space. It is anticipated that feedback will be consistently positive with little to no undermoderation effect. However, this type of source term may be unrealistic for the time scales needed to attain a critical mass. Furthermore, the amplification of $\dot{S}_{25}$ that would be expected with the direct co-disposal of highly-enriched uranium is not likely, as that material would likely be down-blended and used in LWRs or MOX reactors.

Addition of Pu-239 with high level of U-235

Given the role of Pu-239 as fissile material, a product of fertile absorption, and the precursor to U-235, a study was performed assuming a source of pure Pu-239 from the repository. This would physically represent contributions from highly mobile transuranics emanating from the portion of the repository closest to the observation point. The largest of the mass fluxes considered may be realizable provided co-disposal with mixed-oxide fuel or, in the most extreme case, weapons-grade plutonium. The U-235 is assumed to be fixed at $10^{-4}\ \frac{mol}{yr}$, and the U-238 is once again fixed at the TTB levels. The mass flux of Pu-239 initially matches that of U-235 but is then incremented on a logarithmic scale to $1\ \frac{mol}{yr}$. Three different nuclides

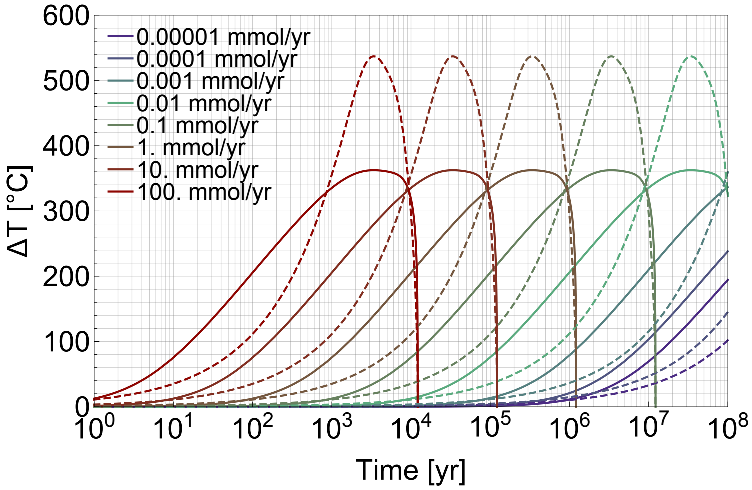

Figure 8.3.7: The effect of selectively increasing the source term of U-235 $\left[\frac{mmol}{yr}\right]$ in the 5 MTU, 2 wt% precipitate in the homogeneous geometry while maintaining the U-238 influx fixed at the original TTB value, where α_T is determined by piecewise (solid) and Gaussian (dashed) functions.

are filling the pore space at different rates, and for simplicity, Pu-239 oxide is assumed to be modeled with the same theoretical density of UO_2.

For the high influx cases of $10^{-1}\,\frac{mol}{yr}$ and $10^{0}\,\frac{mol}{yr}$, where $\dot{S}_{49}$ vastly exceeds $\dot{S}_{25}$ by orders of magnitude, figure 8.3.8 shows that there is enough precursor decay to amplify the quantity of U-235 significantly, which amounts to approximately a factor of 1.75 above n_{25}^{0} before the ΔT peak is reached. This brings α_{25} to negative levels to the extent that the system reaches subcriticality, as was observed in section 8.3.2. In figure 8.3.9, the neutron flux (equation (8.2.45)) is observed to fall to zero when chain reactions cease. The use of a piecewise regression results in flux peaking behavior.

In the middle influx case of $10^{-2}\,\frac{mol}{yr}$, the peak temperature difference is broadened, such that high temperature is maintained for an extended period of time. The temperature rise reaches its peak around 200,000 years, at which time ten half-lives of Pu-239 have passed. This ensures that all contributions to n_{25} from the incoming precursor have been realized. However, these contributions do not bring α_{25} substantially into the negative regime, and ΔT only decreases slightly until $\dot{S}_{25}$ can increase the rate of change. At four million years, the heavy metal fills the pore space, leading to a steady-state temperature. In figure 8.3.9, the flux is likewise observed to reach a steady level.

For the low influx cases of $10^{-4}\,\frac{mol}{yr}$ and $10^{-3}\,\frac{mol}{yr}$, the source terms are similar to that of U-235, such that behavior largely mirrors the corresponding plot line in figure 8.3.7. For the $\dot{S}_{49}$ that is slightly larger, higher temperatures are observable at earlier times relative to the peak because Pu-239 contributes more significantly to $\dot{S}_{25}$ through decay. However, the time at which maximal ΔT is achieved is not observably affected.

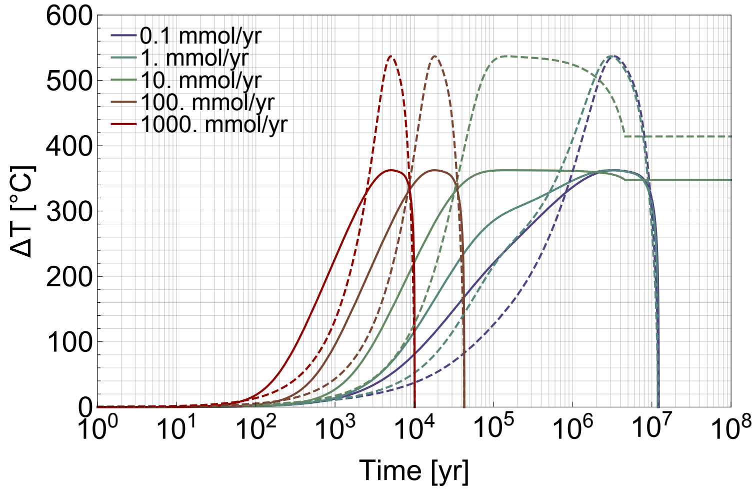

Figure 8.3.8: The effect of selectively increasing the source term of Pu-239 $\left[\frac{mmol}{yr}\right]$ in the 5 MTU, 2 wt% precipitate in the homogeneous geometry while maintaining the mass fluxes of U-235 at $10^{-1}\,\frac{mmol}{yr}$ and $5.5*10^{-6}\,\frac{mol}{yr}$ for U-238, where α_T is determined by piecewise (solid) and Gaussian (dashed) functions.

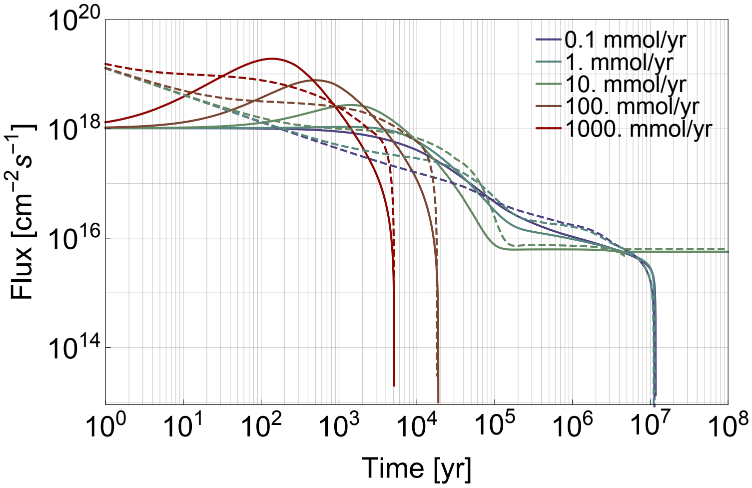

Figure 8.3.9: The neutron flux observed in the 5 MTU, 2 wt% precipitate in the homogeneous geometry when selectively increasing the Pu-239 source term $\left[\frac{mmol}{yr}\right]$, based on mass fluxes fixed at $10^{-1}\,\frac{mmol}{yr}$ for U-235 and $5.5*10^{-6}\,\frac{mol}{yr}$ for U-238, where α_T is determined by piecewise (solid) and Gaussian (dashed) functions.

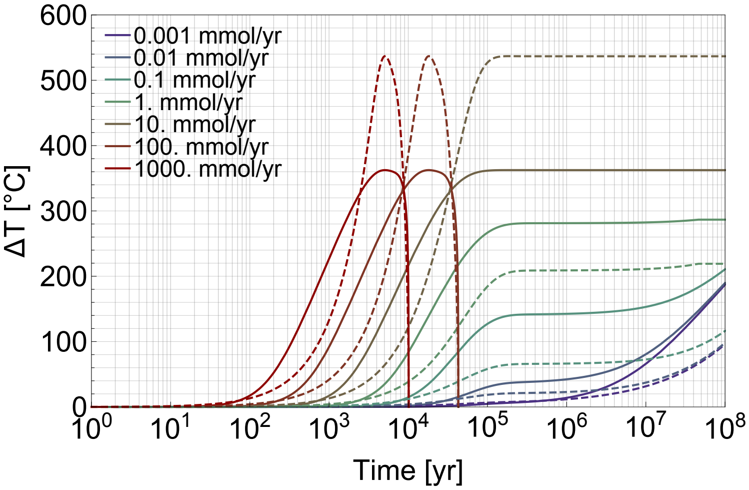

Figure 8.3.10: The effect of selectively increasing the influx of pure Pu-239 $\left[\frac{mmol}{yr}\right]$ in the 5 MTU, 2 wt% precipitate in the homogeneous geometry, based on U-235 and U-238 mass fluxes fixed at TTB values and α_T determined by piecewise (solid) and Gaussian (dashed) functions.

TTB source term with additional Pu-239

Given the effects of Pu-239 on $\Delta T(t)$ observed in the previous section, a last case is proposed that attempts to impart more realism by considering a system with the original TTB uranium fluxes and an additional influx of Pu-239 from the repository. While not quantified in chapter 3, the lower values that are examined are considered to be realizable in a transport analysis as long as the observation distance is not excessively far. The effects of U-233 are still assumed to be negligible.

Figure 8.3.10 shows that for small $\dot{S}_{49}$ that begin to surpass $\dot{S}_U$, the temperature begins to rise earlier in time and reach a steady level, which is caused by decay contributions to the mass of U-235 and positive feedback from α_{25}. This is followed by a rise in ΔT caused by the original source of uranium. For the piecewise regression in figure 8.3.11, a preliminary rise in the flux is observed for small $\dot{S}_{49}$ as Pu-239 begins to decay significantly after $2 * 10^4\, yr$, which is followed by a decrease until the original uranium source term can raise the flux again. The Gaussian regression shows a monotonic decrease until the $\dot{S}_U$ effects are realized.

As $\dot{S}_{49}$ becomes much larger than $\dot{S}_U$, the original uranium plume has diminishing effect on reactivity, and positive feedback is directly imparted by the plutonium contributions. Increasing the plutonium influx increases the maximum ϕ, and a steady-state flux is attained after 200,000 years for $\dot{S}_{49} \leq 10^{-2}\, \frac{mol}{yr}$. When radiogenic U-235 becomes sufficiently large at $\dot{S}_{49} \geq 10^{-1}\, \frac{mol}{yr}$, the system becomes undermoderated, which results in subcriticality. Overall, these results and those of section 8.3.2 confirm the maximum temperatures that would be expected in figure 8.3.1a if $\dot{S}_U$ was larger.

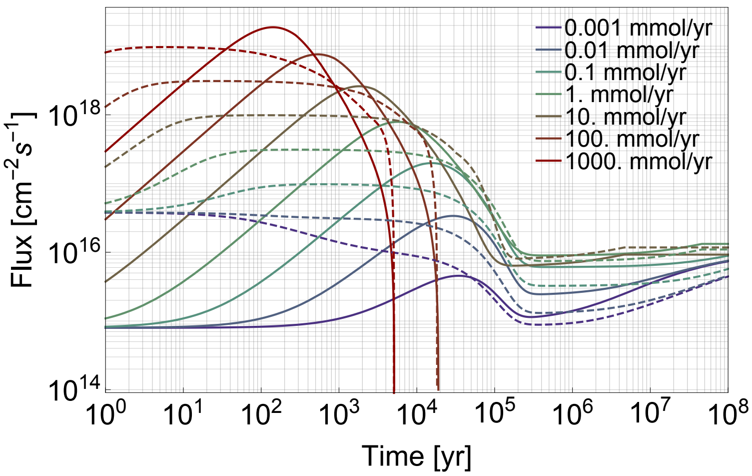

Figure 8.3.11: Neutron flux in the 5 MTU, 2 wt% precipitate in the homogeneous geometry for selected source terms of pure Pu-239 $\left[\frac{mmol}{yr}\right]$, based on U-235 and U-238 mass fluxes fixed at TTB values and α_T determined by piecewise (solid) and Gaussian (dashed) functions.

8.3.3 Limitations

Given the tendencies observed in the fractured geometry in figure 8.3.6b, it would seem apt to test the 2 wt% fractured configuration at 5 MTU for higher peak temperatures with the Gaussian fit using the realistic geometry with global variation in the saturation. However, due to the stiffness of the system of equations, divergent behavior was observed for both regression models in areas that would be expected to peak (see figure 8.3.12). When the piecewise model reaches the phase transition temperature, where $|\alpha_T|$ becomes substantially smaller, the change in temperature spikes, while an exponential rise is observed at the corresponding time point in the Gaussian model. This would imply that positive feedback from the uranium plume is unfettered by undermoderation, the Doppler effect, and thermal expansion, leading to an unhindered rise in temperature. Temperature must be physically bound, since melting of the rock would deform the precipitate into a non-critical configuration. While this behavior may be unrealistic, the results can serve as a worst case scenario of inadequate negative feedback mechanisms in the critical mass. It is recommended that numerical limitations of the solver be investigated, as it may be the case that a sharp peak cannot be resolved in the time steps employed in the default solver method.

8.4 Discussion

The reactivity feedback models were successfully implemented into a quasi-steady-state heat transfer analysis to determine the dynamic evolution of temperature in the critical system over time. When the source terms of uranium from the transport study were applied to the model, the time scales needed for considerable temperature rises were on the order of several

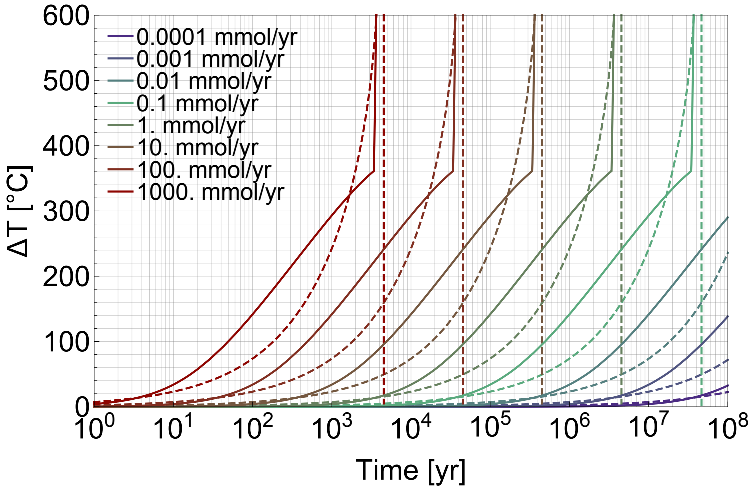

Figure 8.3.12: Divergent behavior observed for the 5 MTU, 2 wt% fractured configuration when increasing the total uranium source term $\left[\frac{mmol}{yr}\right]$ for piecewise (solid) and Gaussian (dashed) treatments of α_T.

millions of years. For reference, the Oklo analog can be inversely modeled to demonstrate criticality on the order of about a million years, and temperature buildups are hypothesized on the order of hundreds of degrees centigrade. [119] Although these time scales are congruent with those needed to obtain critical masses, geological processes that may affect the critical configuration, such as microbial buildup, erosion, fuel oxidation, and seismic fissuring, are liable to take place during such lengthy periods of time. These considerations would impact the heat transfer characteristics of the system or the ability for fissile material to infiltrate the pore space. Therefore, the study was parameterized to gauge the sensitivity of the source term to conservatively evaluate higher temperatures that could be attained in shorter periods of time post-formation.

It was observed that the source term of uranium strongly determines the onset of substantial temperature evolution. There are also substantial effects when a source term of Pu-239 is acknowledged, where the temperature rise is observed at earlier times due U-235 generated from decay and the resulting amplification of positive feedback. This promotes a closer examination of plutonium fluxes in future transport analyses. In direct disposal, since the source terms of U-235 and U-238 will likely be determined on a combined basis with an enrichment level as opposed to pure sources, and since $|\alpha_{28}|$ is very small and negligible, the feedback coefficients of the two isotopes should be merged in future iterations of this analysis. For this reason, the results considering an amplified U-235 source term (section 8.3.2) are inaccurate, since feedback from pure U-235 would be very positive and likely devoid of undermoderation characteristics. The feedback equation can also be considerably improved with the inclusion of α_{49}, and both α_U and α_{49} should evaluated directly in a neutronics calculation without reliance on interpolations of pre-existing data. It is postulated that while

α_U will still have the parabolic behavior observed in section 4.4.4, α_{49} will provide positive feedback until significant decay depreciates the plutonium inventory.

Peak temperatures are observed that correspond to the transition between positive and negative feedback from α_{25} as a function of the incoming fissile material. If the pore space is filled before α_{25} becomes excessively negative, the temperature difference reaches a steady level. Otherwise, the system is brought to subcriticality. The maximum temperatures in the system are determined by the magnitude of $\alpha_T(T_\infty + \Delta T)$, where $\Delta T \approx 360°C$ is observed for the exponential/power law regression due to strongly negative feedback leading up to the phase transition followed by negligible feedback in the dry zone. The Gaussian fit shows maximum differences of $\Delta T \approx 540°C$ since the continuous modeling of α_T about the phase transition is altogether less negative. Given the working melting point of $1250°C$, this temperature is applicable thermal creep, which will be described in the next chapter for evaluation of the failure metric. It is proposed that realistic temperature evolution would lie between these two extremes. The proposed improvements to the TH modeling from chapter 6 are likely to introduce a more continuous and accurate representation of α_T that will in turn produce more reliable results on ΔT.

The behavior examined for optimal temperature can only be confirmed for the globally-desaturated approaches to modeling feedback in the critical mass. In proceeding to the next chapter, it will be stated that the approach to modeling the heterogeneous geometry with constant rock slab saturation will be dismissed as too unrealistic, and system failure will not be evaluated in this context. The 1.5 wt% precipitate in the fractured geometry will be discarded, and the divergent behavior of the 5 MTU, 2 wt% heterogeneous configuration will be employed as worst-case scenario.

Chapter 9

Failure via thermal creep

9.1 Introduction

The temperature evolution of a critical system has been modeled using a quasi-steady-state heat transfer model incorporating heat-driven unsaturated reactivity feedback effects. However, a relationship must be established between this modeled behavior and a performance metric tied to the creation of a biosphere exposure pathway. Another analysis must therefore be undertaken to relate thermal evolution with the integrity of the natural barrier. It was proposed in chapter 4 that given unrealistic void configurations required for supercriticality and high energy (autocatalytic) release, a gradual material degradation process should be analyzed instead for a just-critical formation sustained with an influx of low-enriched fissile material.

Creep is a time-dependent mechanical deformation process occurring at constant stress below the ultimate tensile stress (UTS) of the rock. It takes place from the production and diffusion of vacancies and self-interstitials (point defects) in a material either from the bombardment of neutrons or from high temperatures. In the heat-driven phenomenon, high temperatures result in the creation of equilibrium vacancies. These vacancies are mobilized through grain boundary diffusion or dislocation climb, which is the movement of defects orthogonal to their crystal planes. Technically, both irradiation and thermal creep phenomena are applicable to the critical mass in this study, but the temperature-based mechanism is most readily quantifiable based on the results of the simulations.

This chapter will apply a creep strain model to determine under what circumstances the ΔT results from chapter 8 could indicate excessive plastic deformation of the system and implied failure. Although plastic deformation is isolated as the phenomenon affecting host rock integrity, it is acknowledged that other thermally-driven mechanical processes may be applicable in the far-field scenario as well. For one, the effects of brittle failure (and the ductile-to-brittle transition temperature) are not acknowledged in the model, although brittle failure would be expected in solid quartz, which is the predominate mineral constituent of the host rock. It is also known that increasing temperatures can reduce the fracture strength of the rock through thermally-activated dissolution and precipitation processes from the pore fluid. [120] This could elongate pre-existing rock fractures and eventually provide a pathway of volatile FPs to the biosphere. These considerations, and others such as seismic fault reactivation, are considered beyond the scope of this particular study but would otherwise be important to acknowledge in a full TSPA.

9.2 Methodology

The separation of creep into its primary, secondary, and tertiary regimes is not specifically acknowledged, although phenomenologically the second regime of steady-state creep is most relevant. The temperature range of applicability for creep is usually defined as $T/T_m > 0.3$, where T_m has been assumed to be $1523.15\,K$ ($1250°C$). This implies a threshold of $507\,K$ ($234°C$), which excludes the systems described in section 8.3.1 that are driven by source terms calculated in TTB, as maximal temperatures of only $\approx 225°C$ are resolved within the temporal scope of the investigation. These temperatures come very late post-formation, and are not anticipated to introduce high concentrations of defects in the rock crystals needed for creep. Therefore, only systems with modified source terms that can attain larger ΔT are applicable to the study of failure.

From chapter 8, the piecewise exponential/power-law regression for $\alpha_T(T)$, while accurately representing the reactivity changes of the critical mass over the course of desaturation, resulted in maximal average temperatures of $\approx 360°C$. This result was consistent with various permutations of the source terms. The Gaussian regression was a poorer yet continuous fit that underestimated the maximal $|\alpha_T(T)|$, which led to maximal temperatures of $\approx 540°C$. Therefore, the results stemming from the second functional form will likely be indicative of the worst case scenario for creep deformation. The 5 MTU, 2 wt% precipitate from section 8.3.2 will be used as the test configuration for the analysis of strain failure. Since more highly enriched precipitates will have more limited fluid volume fractions to displace, and since smaller changes in HMVF are needed for α_{25} to become negative (undermoderated), peak temperatures needed for creep are likely to be suppressed. Since the 1.5 wt% fractured configurations are too unrealistic, the analysis of this configuration should be acceptable. The 5 MTU, 2 wt% fractured configuration will be analyzed as a worst-case scenario.

The strain rate $\dot{\epsilon}$ from the power law creep relationship is shown in equation (9.2.1) as a function of the shear stress σ_s, shear modulus G, and an Arrhenius term with activation energy Q, the universal gas constant $\mathcal{R}$, and temperature T $[K]$. The variables n (the stress exponent) and A are material-specific constants, where n is usually found between 3 and 10. The shear modulus is a measure of rock deformation when exposed to a shear force. Q describes the thermal energy needed to activate plastic deformation in a given mass, and in this study, it is assumed to be independent of temperature. The use of this strain relationship is usually acceptable for scenarios where $\sigma_s < 10^{-3}G$. [121, 122] The threshold of $150°C$ is employed to ensure that rock deformation is irreversible (plastic). This is a conservative measure that will allow for the observation of a wider span of behavior, as opposed to the

$234°C$ criterion.

The applied shear stress is considered to be constant and must be below the UTS. If an upper bound UTS of 22 MPa is chosen based on measurements of Green River shale in Ref. [123], and if the shear stress is taken to be 15 MPa as a principal stress difference between the overburden and lateral forces in the host rock, [83] then the shear moduli of $G = 10 - 20\,GPa$ should be acceptable for host rock at 10% porosity. [124, 125] The lower bound value of $10\,GPa$ is chosen out of conservatism to overestimate the stress term.

The other terms in the law are chosen to approximately represent material properties of shale or sandstone. The activation energy was chosen to be $Q = 20\,\frac{kJ}{mol}$, with a lower bound of $10\,\frac{kJ}{mol}$ and upper bound of $75\,\frac{kJ}{mol}$, [126, 127] and a stress exponent of $n = 3.5$ was held to be a representative value. The constant A was adjusted to meet a strain rate of $10^{-9}\,s^{-1}$ at $150°C$, [127] such that $A = 2252\,s^{-1}$. This is considered to be an upper bound value for the strain rate in the geological setting (as opposed to the laboratory).

$$\dot{\epsilon}\left(T(t)\right) = \begin{cases} A\left(\frac{\sigma_s}{G}\right)^n e^{-\frac{Q}{\mathcal{R}T(t)}} & 150°C \leq T < T_m \\ 0 & T < 150°C \end{cases} \tag{9.2.1}$$

To solve for total strain, the $T(t) = \Delta T + 20.45°C$ solution from the QSS model is composited with equation (9.2.1) and numerically integrated over time t according to equation (9.2.2). A metric of $\epsilon = 1.5\%$ is employed to determine if the system has deformed to a point where it likely the host rock is compromised.

$$\epsilon = \int_0^t \dot{\epsilon}\left(T(\tau) + 273.15\right) d\tau \tag{9.2.2}$$

9.3 Results

9.3.1 Enhanced uranium source terms

The integrated strain rates for the 5 MTU, 2 wt% homogeneous configuration are shown in figure 9.3.1, based on elevated source terms of enriched uranium. Only the results related to the Gaussian regression can be resolved on the plot, and the dashed line convention from chapter 8 is maintained. It can be seen that higher $\dot{S}$ do not relate to higher integrated strain levels. Since creep is a time-dependent process, and larger $\dot{S}$ lead to temperature rises that occur earlier post-formation over shorter periods, there is not enough time for the system to appreciably deform. When the arrival rate of uranium is lower, the temperature rises over a more extended period of time, which allows for much more considerable creep deformation. If the uranium arrival rate is $1\,\frac{mmol}{yr}$, the failure metric can be met around $10^7\,yr$. From these results, it appears there is an optimal $\dot{S}$ for meeting a high temperature and high strain while not being too unreasonably large from the nuclide transport perspective. The results for $10^{-6}\,\frac{mol}{yr}$, which are roughly similar to the magnitude of the TTB results, do not

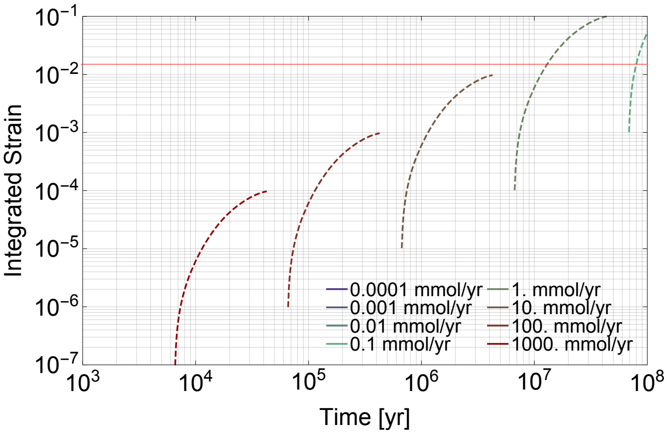

Figure 9.3.1: The integrated strain for various source terms of uranium $\left[\frac{mmol}{yr}\right]$ in the 5 MTU, 2 wt% homogeneous configuration (see figure 8.3.5).

resolve on the plot and are therefore not liable to result in creep failure over the temporal scope of the investigation.

9.3.2 Pu-239 source terms

In section 8.3.2, it was shown that when Pu-239 dominates as the source term, steady temperature levels can be obtained for prolonged periods of time. Figure 9.3.2 shows the results of ϵ for various plutonium arrival rates, where the largest source terms exhibit low strain due to short durations of creep-relevant temperatures. However, an optimal value of $\dot{S}_{49}$ is found at $10\,\frac{mmol}{yr}$, where the strain increases monotonically all the way to failure at $4 * 10^{6}\,yr$. After this rate of influx, lower test values yield steady-state temperatures that are too low for creep to be applicable. Therefore, a window of applicability exists where a specific addition of fissile content from transuranics can lead to elevated and sustained temperatures needed for catastrophic creep deformation.

9.3.3 Worst-case scenario

In section 8.3.3, the 5 MTU, 2 wt% heterogeneous critical mass was observed to have an unfettered rise in temperature due to inadequate negative feedback in the system. Although numerical effects may be the root cause of these solutions, if these results are applied to the strain model as a worst case scenario, large source terms of uranium lead to the melting point of the rock before the model can indicate anything meaningful about creep in the solid-state. Given the time scale of the most severe results, the characterization of the event as autocatalytic (millisecond scale) can be excluded since the ΔT discontinuity is approached on the range of 1,000 years in the piecewise model and the corresponding pre-melt strain behavior, while steep, is still measured on the order of 500 years. Since the strain is on

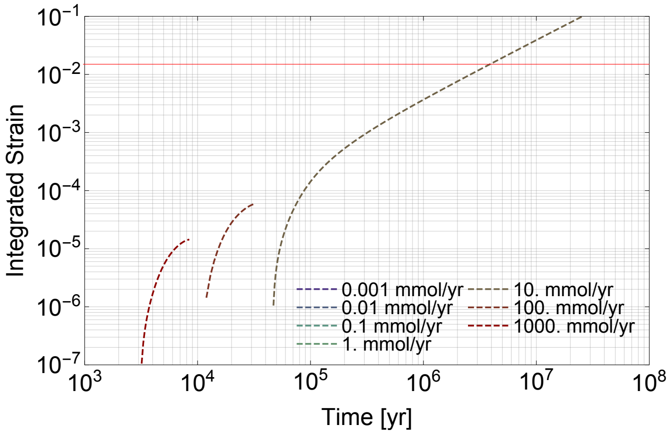

Figure 9.3.2: The integrated strain for source terms of plutonium $\left[\frac{mmol}{yr}\right]$ in the 5 MTU, 2 wt% homogeneous configuration that overlap with those of uranium determined in the TTB calculation (see figure 8.3.8).

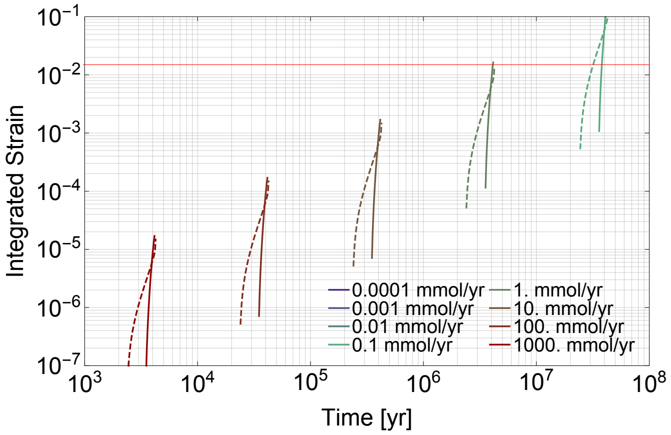

Figure 9.3.3: The integrated strain for various source terms of uranium $\left[\frac{mmol}{yr}\right]$ in the 5 MTU, 2 wt% fractured configuration before the rock melting point (see figure 8.3.12) where the piecewise model is indicated with solid lines and the Gaussian model with dashed lines.

the order of 10^{-5} before the melting point, it may be possible that the critical configuration is compromised from deformation before the temperature excursion. Nonetheless, these results are obviously indicative of catastrophic failure of the system, and although the critical configuration will be compromised, a pathway to the biosphere will likely be created unless fission products are trapped in the resulting glass.

When restricting the scope to the solid state, a source term of $10^{-3}\,\frac{mol}{yr}$ indicates that the critical mass can reach strain failure at $3 * 10^{7}\,yr$, which is on par with the homogeneous results with a bounded $\Delta T(t)$.

9.3.4 Sensitivity

There is uncertainty in the application of the parameters in equation (9.2.1) to a hypothetical critical system, and there is likely to be sensitivity in $\epsilon(t)$ based on the specific choice. Figure 9.3.4 shows permutations of figure 9.3.1 based on alterations of the activation energy, stress exponent, and applied stress, assuming that the original derivation of A is fixed. As the activation energy is decreased, the total strain is increased because less energy is required to cause plastic deformation. This decreases the strain failure time to a approximately a million years. Increases in n yield much lower strain levels, and choosing the lower bound value of 3 decreases the failure period to 250,000 years. If the applied stress on the system is elevated, the total strain expected from creep increases as well. The first two parameters are strongly tied to specific rock material properties, while the third is determined by the far-field environment. Therefore, the applied stress is most liable to engender significant changes in the total integrated strain for a given geology.

The parametric study was performed such that the constant A was adjusted to meet the strain rate criterion at the temperature threshold per given set of test parameters. The results for the stress exponent and applied stress were found to overlap the original results in figure 9.3.1, implying that when the strain rate criterion is enforced, there is little or no sensitivity to the choice of these parameters. For the activation energy, while the initial integrated strain levels are observably the same per parametrization, higher values of Q result in higher ϵ for the temperature region of applicability (see figure 9.3.5). This contradicts the logic observed for the fixed A case, and the behavior directly results from dramatic increases in A needed to meet the criterion ($10^2\,s^{-1} \rightarrow 10^{10}\,s^{-1}$ as Q increases). These larger coefficients are not likely to be realistic. Since lower Q would likely indicate higher strain rates per given temperature, the use of a fixed calibration parameter for A is probably invalid, and these sensitivity effects can be ignored.

9.4 Discussion

A simple model for the application of QSS temperature results to assess a strain failure criterion has been demonstrated. The role of the uranium source term is essential to reaching the strain failure criterion, and it is clear that the original source terms from TTB would never be able to meet the 1.5% metric. If the contributions of plutonium from the repository meet a specific window of mass fluxes, the temperature may reach high steady-state temperatures that allow creep strain to increase monotonically until the failure metric is achieved. This promotes the further investigation of the transport behaviors of plutonium at the far-field exit.

When a worst-case scenario is considered where ΔT is allowed to rise unhindered due to a lack of negative feedback, the system was observed to melt before the failure metric was achieved when employing high rate of uranium influx. Therefore, the applicability of the model to the scenario is limited. Nonetheless, given the rate of strain over time, and compar-

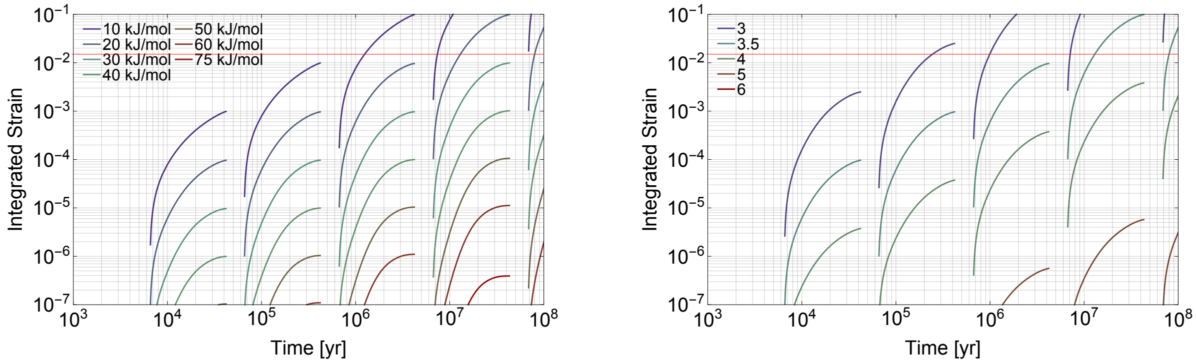

(a) Q

(b) n

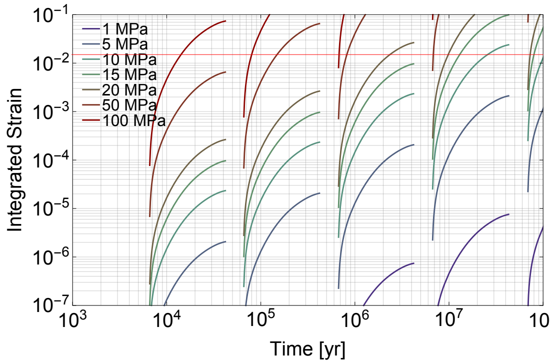

(c) σ

Figure 9.3.4: The effect of adjusting certain parameters in equation (9.2.1) on figure 9.3.1, while maintaining other default parameters.

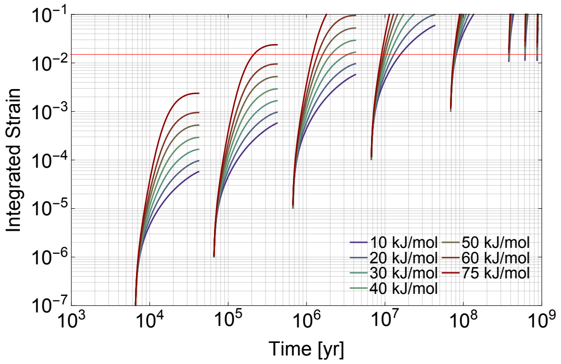

Figure 9.3.5: The effect of adjusting Q in equation (9.2.1) on figure 9.3.1, where A is chosen to calibrate the strain rate to $10^{-9}\,s^{-1}$ at $150°C$.

ing the magnitude of ϵ with the time scales needed to reach the temperature discontinuity, it may be the case that the critical mass is deformed from the critical configuration before the excursion can occur.

There is sensitivity in the final results from the parameters used in the power law creep model. If the activation energy required for plastic deformation is lower, the critical strain is met sooner in time. Since the applied stress is most strongly tied to the state of stress of the far-field host rock, as opposed to the material properties themselves, the applied stress is considered to be the parameter most likely to enhance the total creep strain. If stresses in the far-field are elevated over time, the failure metric will be realized sooner in time. Altogether, many of the parameters are tied to a specific geology or laboratory testing environment, and the inclusion of more detail in this assessment is unwarranted unless the whole study is reframed to a site-specific investigation.

Chapter 10

Integrated conclusions

10.1 Summary

This study has provided an analysis of a series of events leading to the failure of the host rock in the far-field of a repository for UNF, which is presumptive of a release of fission products to the biosphere and system failure. These events occur within a narrow frame of applicability over extremely long periods of time in a worst-case scenario treated with heavily conservative assumptions. While the phenomena of interest have been described in a mechanistic manner, the compounded effect of the assumptions leading to host rock failure is too extreme to merit concern in the engineering of repositories for direct disposal. The time period of applicability surpasses the most stringent current regulatory limits of a million years and approaches geologic time scales that no man-made system can be ensured to withstand. Several important considerations have nonetheless been illuminated that can be valuable to used nuclear fuel management and repository performance assessment.

The transport study represented the repository as an simple square grid of waste emplacements, where extensive corrosion and degradation was assumed for the canister, grid spacers, and used fuel. Nuclide transport was modeled along straight-line pathways directly connecting a each emplacement to a common point in the far-field, with no concentration band limitations posed by adjoining waste forms. It was found that a uranium-dominated precipitate of appreciable magnitude will likely occur beyond a million years and closely emulate the maximum fissile content of the used nuclear fuel measured at the time of failure. Augmentation of the fissile composition will occur in a narrow window of time before this steady-state composition, and this would be due to the mobilization of transuranics from waste packages in the repository nearest to be deposition. These TRU nuclides were shown to be very important in the dynamics portion of the analysis, and it is imperative that future refinements of this study quantity the fluxes of all fissile nuclides (including Pu-239) and uranium precursors in the far-field.

The level of fuel degradation required to meet the larger solubilities acknowledged in the transport calculation would be indicative of inadequate cooling coupled with mechanical perturbations both before emplacement and afterwards. This can be caused by premature disposition leading to inadequate heat disposition in the engineered barriers, which would lead to high temperature degradation modes (like creep) of the fuel. There may also be considerable cycle fatigue from poor shock absorption during road or rail transport from interim storage facility, or via seismicity of the near-field bedrock. Even with these scenarios considered, the heavy metals of interest are well-known to be insoluble species, which is compounded by the natural reducing environment of crystalline granite that inhibits dissolution. A departure to oxidizing conditions would be needed for the near-field rock, which may be possible through a drop in the water table or perhaps seepage of oxidizing agents from future human industrial activities. It is also possible that future generations may be compelled to explore the geology for water or shale gas resources, and the introduction of pumping, drilling, hydraulic fracturing and other disturbances that could affect the geochemistry and natural barriers.

A series of assumptions was made in the criticality study to probe the minimum critical mass. This included a favorable spherical geometry, unrealistically high uranium densities, full saturation of the pore space without acknowledgment of storativity limitations, and the modeling for the surrounding geology as a neutron reflector. If the deposition was modeled as a flat prism or cylinder to emulate the geological strata of the far-field (or the natural analog at Oklo), the critical volumes would be different due to vastly different effects on the neutron leakage. Two extreme geometries were employed to capture the variation in heterogeneity: a homogeneous configuration with all rock, uranium, and fluids mixed together, and a heterogeneous geometry consisting of repeating laminar units of these materials. The latter model was expected to emulate the stratification expected in a highly fractured medium. Using the full theoretical density of uranium oxide, significant differences were found in the porosity and heavy metal content required for criticality in either configuration, and the differences in volume fractions and critical dimensions were key considerations in later stages of the analysis. It should be noted that if the Pu-239 contributions to the far-field are considerable (i.e. from high mobility in the fractures) that the critical radii could be further minimized as more fissile material would reduce the diluting effect of U-238.

A burnup simulation was used to guide the source term model for a simulation of heat and mass transfer in the critical configurations. Given the scope of critical dimensions, the motivation for pursuing such a study was the conviction that the water content and temperature of the system could not be dissociated, and the use of a thermo-hydrological code was considered to be a major innovation on past analyses of the criticality phenomenon. The iterative methodology was focused on achieving steady-state behavior at the phase transition temperature of water, as the boiling of the moderator was considered to be part of the worst case scenario, and the neutronics analysis would not be affected greatly by fine variations in gas transport. Nonetheless, the modeling of the system and surrounding bedrock as fully saturated and the infinite environment as dry led to the most significant space-dependent behavior being observed at the periphery of the system, whereas the temperature and saturation distributions of the critical mass were relatively uniform per given time. Therefore, this approach to modeling the initial state of the system is considered to be overly-conservative.

The major product of the TH study was informing an integrated neutronics analysis for the investigation of coupled reactivity feedback from the Doppler effect and the loss of moderator. Given the lack of spatial variation observed for temperature, it also defended a lumped capacity approach for the dynamics study. While the Doppler effect was found to significantly enhance the reductions in reactivity that would otherwise be found with the moderator defect at room temperature, the integrated neutronics analysis was impacted by the somewhat drastic behavior of water content with temperature. This necessitated two approaches to regression in order to capture discontinuities in the results, as reactivity feedback is based on differential behavior. Therefore, it is imperative that future iterations of the study include assumptions to purposefully introduce more continuous heat and mass transfer effects in order to facilitate reactivity modeling.

A quasi-steady-state heat transfer model was employed to model the dynamic evolution of system temperature using the feedback relationships in a lumped capacity approach. Thermal cross sections were employed for a very simple system comprised of U-235, U-238, and Pu-239. The source term of heavy metal was found to be crucial for the onset of significant temperature evolution, and for a scope of investigation fixed at a hundred million years, the upper bound mass flux results from the transport analysis were found to be inadequate to produce the temperatures needed for a mechanics analysis based on thermal creep. Nonetheless, amplified source terms were found to engender significantly high temperature differences needed for creep. Behavior was observed to be peaked for enhanced plumes of uranium, while the inclusion of Pu-239 was found to engender higher steady-state temperature levels. It is notable that although the inclusion of enrichments as high as 6 wt% allowed for the assessment of lower-bound critical masses and an overall expansion of the study, ultimately the role of the fluid volume fraction was most important in the dynamics analysis given the need for heavy metal to displace the pre-existing pore fluid to impart positive feedback.

Given the time-dependence of the creep phenomenon, there are optimal source terms for meeting the failure metric, where the window of applicability is particularly narrow for Pu-239 dependent systems. When creep failure is actually met, it is usually within a million and ten million years post-formation, which is compounded by the millions of years required to generate the initial critical mass from nuclide transport. If a biosphere exposure pathway is created from this severe deformation of the system, then a biosphere present in a ten million years may be subject to a dose from the fission products that are generated. However, the effects on the biosphere at this period in time (if such a biosphere exists) have not been considered in a regulatory context. Therefore, the ultimate conclusion from this series of worst case assumptions is that criticality in the far-field should not be of concern for direct disposal.

If far-field criticality is retained as a significant event in the scope of the repository performance assessment, the focus should be kept on engineering a robust canister and barrier system, and ensuring adequate interim cooling of the used nuclear fuel. Many front-end considerations can also aid in alleviating long-term concerns. Open fuel cycles incorporating the extensive reduction of fissile nuclides in the final waste form would promote the greatest assurance against far-field criticality events, since the ultimate enrichment of the heavy metal deposition would ultimately mirror the fissile content of the original waste form.

10.2 A proposed canister modification

In chapter 3, it was observed that steady-state enrichment levels in the far-field precipitate mirror the fissile content of the original waste form. This is caused by the eventual dominance of the U-238 flux over that of U-235 and other fissile nuclides. Based on this finding, if the U-238 inventory can be augmented by adding more material with this isotope to each canister, it is hypothesized that the risk of criticality by transport and re-concentration can be further mitigated. It is proposed that depleted uranium, which has an enrichment around 0.2 wt%, can be added to each canister to dilute the average content of U-233 and U-235. If the chemical form of the DU matches that of the fuel, the groundwater leaching process will occur at similar rates for both the UNF and the filler. The mass loading of uranium per waste form will increase, which will affect $m_k(t)$ of equation 3.3.3 on page 26 by increasing the magnitude of the initial uranium release rates (assuming the canister surface area remains constant). The end result should be a much lower enrichment level as precipitate masses are largest.

DU is currently stored above-ground in gas cylinders as uranium hexafluoride $\left({}^{D}UF_6\right)$, where the current inventory is on the order of several hundred thousand metric tons. Since this chemical form is gaseous and corrosive, further processing of the material into ${}^{D}UO_2$ powder would be needed for deployment into the canister as a component of the metallic inserts. ${}^{D}UO_2$ is preferred over the more thermodynamically stable ${}^{D}U_3O_8$ since the goal is to match the redox state of the used fuel. It is proposed that bulk plates of DU can be manufactured through compression of the oxide powder followed by sintering. This is suggested as opposed to the fine powder itself in order to reduce preferential dissolution relative to the used fuel rods given the increased surface area. The dimensions would need to be optimized to match the expected dissolution rates of thermally- and mechanically-comprised fuel from laboratory experiments, as well as considerations to ensure robust material properties during the transport and emplacement phase.

As shown in figure 10.2.1, the depleted uranium plates can then be inserted into slots machined between assembly guides in the canister inserts where transverse dimensions are determined by the assembly grid spacing and longitudinal dimensions are chosen based on material constraints. In order to remove compressive stress on the ceramic, vertical spacers made of cast iron can be placed axially between the ${}^{D}UO_2$ plates. These spacers can also be used to meet limitations on the total canister mass posed by vehicular transport and tunnel emplacement restrictions. Overall, since canister inserts are designed in such a manner to ensure adequate thermal dissipation, criticality safety, and structural integrity, these considerations would also need to be accounted for when determining DU cavity and plate dimensions. Nonetheless, adding ${}^{D}UO_2$ would not introduce increased criticality risk if the spacings from the original design are maintained.

It is proposed that ${}^{D}UO_2$ can be manufactured either as a whole plate or as part of several blocks to meet dimensions of 24.5(L) by 5(W) by 50(H) centimeters (see righthand side figure 10.2.1). A cylindrical PWR canister inspired by concepts from Sweden (Ref. [128]) and Finland (Ref. [129]) is presumed to have an overall height of 4.817 m and a diameter of 1.016 m (see table 3.3.1) with an Alloy 22 shell of 5 cm thickness. The canister insert is made of cast iron with total length 4.717 m and diameter 0.916 m, and four square slots of side 0.230 m are machined at a pitch of 0.150 m to accommodate the used assemblies. Within the space of separation, a cruciform slot of width 0.075 m is machined to accommodate four zones of DU plate emplacements, where the center region is occupied by a metallic truss. Each zone accommodates eight DU plates separated by 1 cm by way of cast iron spacers.

The DU is assumed to have a uniform enrichment of 0.2 wt%, and the density of the finished plate is 10 g/cm^3, leading to a total mass of 61 kg per plate. The total quantity of DU inserted into the canister is thus 1.728 MTU, with a total U-235 mass of 3.45 kg. The average assembly loading for PWR UNF is 435 kg (table 2.3.1), so there is a total of 1.740 MTU worth of used fuel in the canister. At reactor discharge, as shown in table 2.4.1 on page 19, there is an average fissile content of 1.241 wt% in the 1.679 metric tons of heavy metal (U+TRU). This corresponds to a total of 20.8 kg of fissile material in all the UNF in the canister. Therefore, the combined mass of depleted uranium and UNF heavy metal is 3.407 metric tons.

It is postulated that extensive localized corrosion in the repository may cause the infiltration of groundwater into the canister, upon which the cast iron components can be extensively degraded to the point where mass transport limitations to the heavy metal are excluded. The UNF and DU can be assumed to leach and mix thoroughly in solution through diffusion and advection. This would cause the effective enrichment of the equilibrium uranium solute to be 0.713 wt%, which is close to the natural abundance of U-235. Restricting the scope to PWR canisters, this would heavily dampen the steady enrichment levels of the far-field precipitate observed at long times in figure 3.4.2 on page 47 and drastically reduce any potential for criticality. A similar design approach can be applied to BWR used fuel canisters to bring the effective enrichment to a similar level, although different geometries of the ${}^{D}UO_2$ would be needed for the special assembly arrangement and geometry.

10.3 Recommendations for future studies

10.3.1 Site-specific data

Throughout the study, assumptions had to be made in order to approximate the features of the repository, in particular the geochemical and material parameters of the host rock. At times, published data on existing engineered barrier concepts, like those proposed by the Japan Atomic Energy Agency, and European repository concepts like the one at Forsmark were used to inform the assumptions for various models. However, without a consolidated

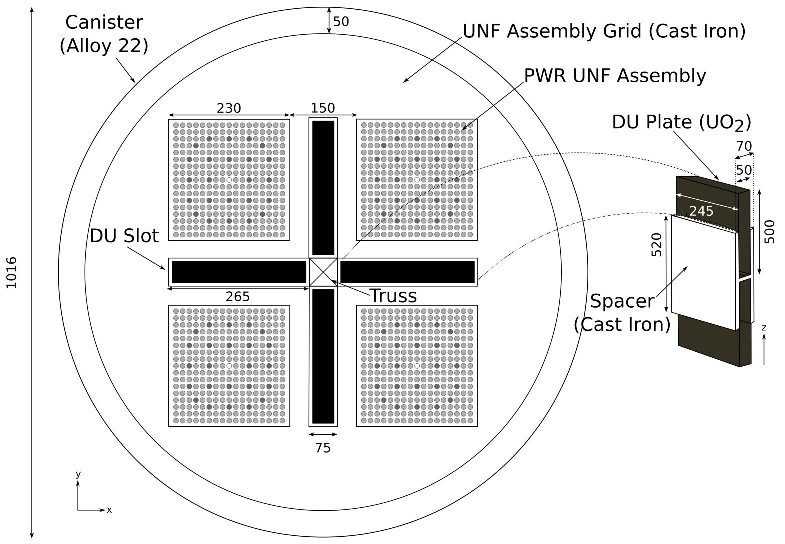

Figure 10.2.1: A mid-length cross section of a proposed canister for used Westinghouse 17 by 17 PWR assemblies, modified with slots for plates of depleted uranium oxide. The dimensions are indicated in millimeters.

database on both the site of interest and working EBS concept (including the canister) the uncertainty inherent in the modeling approach is compounded with a spread of data. It is imperative that enhancements of this study only proceed when such a database is available. This can considerably refine the transport model by bounding the scales of variation in the transport parameters and understanding the hypothesized conditions of the fuel when a specific canister material is compromised. The groundwater velocity can be better approximated with measurements of the hydraulic gradient, and the fracture characteristics can be tied to actual measurements of the fracture density in the field. Finally, the creep analysis can also be informed with laboratory measurements of host rock mechanics and the in-situ strain rate.

10.3.2 Modeling of fractures

A fractured medium will not likely be comprised of the parallel planar fractures employed for the heterogeneous configuration in this study. In reality, the extent of fracturing in a medium like granite is determined as a density, as the sum of all fractures occurs in a geostatistical manner with varying aperture and length. To impart a degree of realism to the transport model, the effect of varying length and aperture can be incorporated into the analysis.

The practice of applying individual transport lengths to individual waste forms in chapter 3 can be re-applied to a single EBS to model variations in fracture length of the adjoining near-field bedrock. In this case, the lengths would based on the fracture density relative to the total rock volume. A one-dimensional model exists for the advective and diffusive transport of radionuclides in arbitrary-length decay chains in heterogeneous geological formations

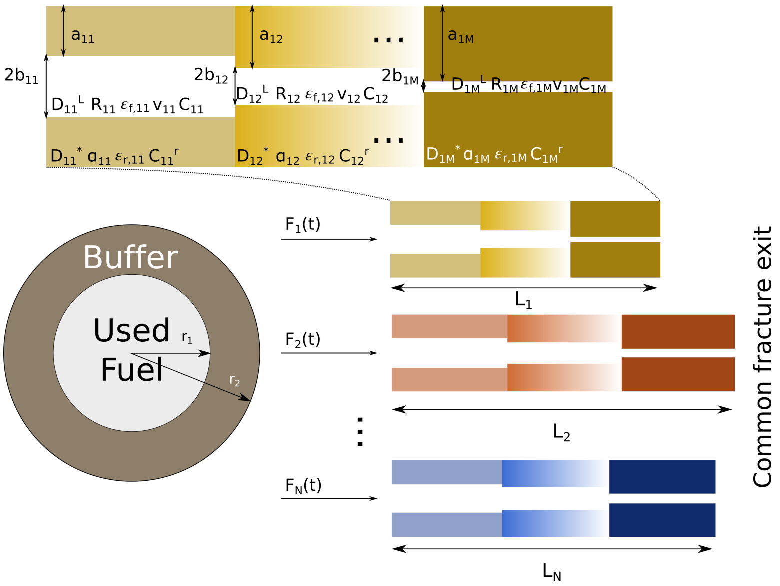

Figure 10.3.1: It is proposed that nuclide transport in the fractures surrounding the EBS can be modeled with N pathways of M heterogeneous segments with varying apertures $2b$ and inlet fluxes $F(t)$ leading to a fixed point of convergence.

that can accommodate porous continua and fracture segments of varying aperture. [9] This model incorporates the spherical EBS source term of TTB, and an expanded version of this model with longitudinal dispersion in the one-dimensional fracture transport pathway exists albeit with a simplified source term. [130] It is proposed that the expanded heterogeneous model be coupled to the spherical EBS source term model. If this proves exceedingly difficult, the effect of dispersion can be emulated by sampling the groundwater velocity, although this would come at a greater computational expense.

A proposed treatment of the problem is diagrammed in figure 10.3.1. The diffusion of nuclides from the surface of a spherical waste form into a layer of buffer material would be modeled as before in chapter 3. The nuclides exiting to the surface of the buffer would infiltrate the entrances of fractures with fluxes $F_i(t)$ based on the relative area of the fracture opening compared to the fracture density. The fracture apertures $(2b_{i,j})$ would first be modeled as beginning with high values at $j = 1$ and terminating at smaller values near the end of the fracture length L_i at $j = M$. However, it is likely that a randomized approach to selecting $(2b_{i,j})$ would be just as adequate for the simulation. Each fracture unit would have its own transport parameters for the fracture and rock matrix (of width $a_{i,j}$), such as the matrix diffusion coefficient $D^*_{i,j}$ and water velocity $v_{i,j}$. The generation of Latin hypercube samples could be applied to one transport pathway, where only the dimensions are varied, or extended to each individual rock and fracture unit to acknowledge an extreme level of heterogeneity. The fluxes of nuclides at the fracture exit would be considered to occur at the same location in the far-field.

10.3.3 Modeling of the unsaturated precipitate

The goal of the TH simulation was to probe effects of spatial variation of the moderator in the critical mass. However, it was found in chapter 6 that the saturation profile across the critical mass does not vary substantially in the radial direction; often, difference in the results of S_l were in the thousandths place. This was found to be a result of modeling the shale and granite directly surrounding the critical mass at full saturation, while imposing an environment that is very dry. This causes radial variation in the water content to vary most significantly in the surrounding rock due to capillary effects. It is proposed that a more realistic approach be undertaken where the initial saturation of the granite is modeled with continuously desaturated levels to model the vadose zone above the critical mass. The shale can be kept at full saturation to remain relevant to the assumptions of the criticality scoping analysis. This procedure would allow for capillary suction to become more appreciable in the critical mass before the steady-state temperature is reached. Furthermore, more realism should be included in modeling the water table expected in a crystalline host rock, as rock saturation should be expected to be consistent for hundreds of meters as opposed to the small ten meter layer considered in the study.

It was found in chapter 7 that the results for the fractured configuration vary based on the treatment of the water content of the fractured rock. When the saturation of the rock components of the critical mass is allowed to vary at the same rate as the adjoining fractures, the impact of the complete desaturation of the medium with heating leads to significant drops in reactivity. This presents a discontinuity in the results at the liquid-gas phase boundary, upon which the heating of the dry rock and fuel leads to a more gradual reduction in reactivity. When the water content of the rock matrix is kept constant, the loss of reactivity is not as significant as a sufficient amount of moderator remains in the shale. In this approach, the temperature feedback coefficients for precipitates of higher mass and enrichment approach zero or a slightly positive value. To bridge these two extremes, a dual porosity approach can be utilized in the TH simulation to model the delay in water exfiltration in the rock matrix relative to the open fracture. It is possible that the reduction in reactivity with increasing temperature will be more gradual such that, for example, a middle-ground could be obtained for figures 7.3.3b and 7.3.4b.

Considering the effects of the phase transition temperature in the peak temperatures observed for certain feedback models in the QSS analysis, fine scale treatment of this region is certainly warranted in future studies. It is postulated that the improvements to the model described above and extension of the calculations to the two-phase region can yield more continuous behavior that will remove the need for a piecewise treatment of ρ. In the dynamics evaluation, this will likely reduce divergent solutions, such as those observed in figure 8.3.12. It is proposed that TOUGH2 or a similar code be re-utilized to handle steam generation within the full scope of temperatures analyzed.

10.3.4 Neutronics

The source points in the MCNP calculations were modeled at fixed points occurring at the centroids of fuel-containing regions intersecting the cartesian axes. In reality, since the source neutrons emanate from the spontaneous fission of U-238 and, to a lesser extent, other isotopes of uranium, there is a both a probability of fission and an energy spectrum of fission neutrons that must be taken into consideration. Therefore, to bring more realism into the model, the calculations can be refined by sampling the number of spontaneous fission neutrons from the Watt spectrum in each cell containing fuel.

The integrated neutronics analysis of chapter 7 can be expanded by including the effects of depletion in the ore materials according to the time steps employed in TOUGH2 figures used to comprise the input files. It is hypothesized that enhanced resonance absorptions in U-238 with temperature will lead to considerable generation of Pu-239, and reactivity will be more strongly determined by competition between fissile/fertile nuclides. Since the amount of Pu-239 was demonstrated to be commensurate with U-235 at steady-state in chapter 5, spectrum hardening at higher temperatures may lead to fewer resonance absorptions and perhaps a larger fast fission factor in both the pre-existing and generated fissile material. This could lead to a suppression of the temperature defect or perhaps positive feedback.

10.3.5 Feedback

The feedback effects of the arriving plume of uranium was investigated using interpolations of parametric criticality data. It is strongly suggested that a full MCNP analysis be conducted to understand the effects of pore water in a critical mass being displaced by certain enrichments of incoming heavy metal. This is necessary to more precisely describe the extent of positive feedback from the source term in the quasi-steady-state model, in particular the onset of undermoderation (if any), since this aspect controls the peaking behavior of temperature.

The roles of Pu-239, fission products, and other poisons in the reactivity feedback balance were not included in chapter 8 due to a lack of studies that isolated their individual effects. While the generation of Pu-239 and second tier fission product were assessed in chapter 5, it was not possible to discern their individual contributions to the k_{eff} data given the dominant effects of uranium in the fuel. For plutonium, a simulation is suggested where pore water in the critical configuration is directly displaced by $^{239}PuO_2$ until the pore space is filled. Although the section 4.4.4 results indicated limits on positive feedback from an enriched uranium plume due to undermoderation, the results for α_{49} may be more consistently positive since the fraction of non-fissile Pu-240 is expected to be low. The study can be conducted with pure fissile content or an enriched plume.

The effect of poisons can be assessed from two perspectives. For soluble packaged poisons like boron, the effect can be modeled by increasing the concentration in the pore water. The effects of fission products like Sm-149 can be modeled as being trapped in the fuel matrix, and assuming binary fission, atoms of U-235 can be directly replaced by two of the isotopes. The relationship in equation (8.2.9) can then be included in the model for the major poisons.

References

[1] U.S. Energy Information Administration, "Nuclear Fuel Data Survey, Form GC-859," 2013.

[2] F. Gauthier-Lafaye, F. Weber, and H. Ohmoto, "Natural fission reactors of Oklo," *Economic Geology*, vol. 84, pp. 2286–2295, Jan. 1989.

[3] M. Harada, P. L. Chambre, M. Foglia, K. Higashi, F. Iwamoto, D. Leung, T. H. Pigford, and D. Ting, "Migration of radionuclides through sorbing media, analytical solutions-I, Rep. no. LBL-10500 (UC-11), Lawrence Berkeley Laboratory," *Univ Calif. Berkeley CA*, 1980.

[4] E. A. Sudicky and E. O. Frind, "Contaminant transport in fractured porous media: Analytical solutions for a system of parallel fractures," *Water Resour. Res.*, vol. 18, no. 6, pp. 1634–1642, 1982.

[5] E. A. Sudicky and E. O. Frind, "Contaminant transport in fractured porous media: Analytical solution for a two-member decay chain in a single fracture," *Water Resour. Res.*, vol. 20, pp. 1021–1029, July 1984.

[6] D. P. Hodgkinson and P. R. Maul, "1-D modelling of radionuclide migration through permeable and fractured rock for arbitrary length decay chains using numerical inversion of Laplace transforms," *Annals of Nuclear Energy*, vol. 15, no. 4, pp. 175–189, 1988.

[7] J. Ahn, "Integrated radionuclide transport model for a high-level waste repository in water-saturated geologic formations," *J Nuc Tec*, vol. 121, no. 1, pp. 24–39, 1998.

[8] J. Ahn, S. Armel, J. Burch, P. L. Chambré, E. Greenspan, and D. A. Roberts, "Underground Autocatalytic Criticality from Fissile Materials Solidified in Borosilicate Glass," *PNC ZA*, vol. 995, pp. 96–001, 1997.

[9] B. P. van den Akker and J. Ahn, "1-D modeling of radionuclide transport via heterogeneous geological formations for arbitrary length decay chains using numerical inversion of Laplace transforms," *Ann. Nucl. Energy*, vol. 63, pp. 763–773, 2014.

[10] P. Behrenz and K. Hannerz, “Criticality in a spent fuel repository in wet crystalline rock,” *KBS Tek. Rapp.*, vol. 108, 1978.

[11] C. D. Bowman and F. Venneri, “Underground supercriticality from plutonium and other fissile material,” *Sci. Glob. Secur.*, vol. 5, no. 3, pp. 279–302, 1996.

[12] W. E. Kastenberg, P. F. Peterson, J. Ahn, J. Burch, G. Casher, P. L. Chambré, E. Greenspan, D. R. Olander, J. L. Vujic, B. Bessinger, and others, “Considerations of Autocatalytic Criticality of Fissile Materials in Geologic Repositories,” *Nucl. Technol.*, vol. 115, no. 3, pp. 298–310, 1996.

[13] W. E. Kastenberg, P. F. Peterson, J. Ahn, J. Burch, G. Casher, P. L. Chambré, E. Greenspan, D. R. Olander, J. Vujic, B. Bessinger, and others, “Mechanisms for autocatalytic criticality of fissile materials in geologic repositories,” Tech. Rep. UCBNE-4214, University of California, Berkeley, Department of Nuclear Engineering, 1996.

[14] X. Liu, J. Ahn, and F. Hirano, “Conditions for criticality by uranium deposition in water-saturated geological formations,” *J. Nucl. Sci. Technol.*, vol. 52, no. 3, pp. 416–425, 2015.

[15] P. N. Smith, R. M. Mason, and R. Cummings, “Understanding Criticality Under Repository Conditions: QSS–A Model for Quasi-Steady-State Criticalities,” tech. rep., Serco Report SA/ENV-0771 Issue 3, 2007.

[16] R. M. Mason, B. D. Turland, and J. K. Martin, “Comparison of the QSS Model with the Oklo Natural Reactors,” Tech. Rep. NPO003927, Nuclear Decommissioning Authority, Apr. 2011.

[17] J. Carter, “Nuclear power policy statement on decisions reached following a review,” *Am. Pres. Proj.*, 1977.

[18] Blue Ribbon Commission on America’s Nuclear Future, *Report to the Secretary of Energy.* United States Department of Energy, 2012.

[19] K. Banerjee, J. M. Scaglione, and R. A. LeFebvre, “Integrated Data and Analysis Tool for Used Nuclear Fuel Management,” *Trans. Am. Nucl. Soc.*, pp. 338–341, 2014.

[20] R. A. Knief, *Nuclear Engineering: Theory and Technology of Commercial Nuclear Power.* American Nuclear Society, 2008.

[21] IAEA, “The Power Reactor Information System (PRIS) and Its Extension to Non-electrical Applications, Decommissioning and Delayed Projects Information,” Tech. Rep. STI/DOC/010/428, International Atomic Energy Agency, Vienna, Austria, 2005.

[22] J. J. Duderstadt and L. J. Hamilton, *Nuclear Reactor Analysis*, vol. 1. Wiley New York, 1976.

[23] I. C. Gauld, S. M. Bowman, J. E. Horwedel, and L. C. Leal, "ORIGEN-ARP: Automatic rapid processing for spent fuel depletion, decay, and source term analysis," *SCALE Modul. Code Syst. Perform. Stand. Comput. Anal. Licens. Eval.*, vol. 1, 2006.

[24] J. M. Scaglione and J. C. Wagner, "Review of Yucca Mountain disposal criticality studies," Oak Ridge National Laboratory (ORNL), 2011.

[25] X. Liu, *Criticality Safety Study for the Disposal of Spent Nuclear Fuel in Water-Saturated Geologic Repository.* PhD thesis, University of California, Berkeley, Berkeley, CA, 2016.

[26] F. J. Dahlkamp, "Uranium ore deposits," 1993.

[27] P. K. Kuroda, *The Origin of the Chemical Elements and the Oklo Phenomenon.* Springer Science & Business Media, 2012.

[28] F. Gauthier-Lafaye, P. Holliger, and P. L. Blanc, "Natural fission reactors in the Franceville basin, Gabon: A review of the conditions and results of a "critical event" in a geologic system," *Geochimica et Cosmochimica Acta*, vol. 60, pp. 4831–4852, Dec. 1996.

[29] R. D. Loss, J. R. De Laeter, K. J. R. Rosman, T. M. Benjamin, D. B. Curtis, A. J. Gancarz, J. E. Delmore, and W. J. Maeck, "The Oklo natural reactors: Cumulative fission yields and nuclear characteristics of Reactor Zone 9," *Earth and Planetary Science Letters*, vol. 89, pp. 193–206, July 1988.

[30] D. G. Brookins, "Radionuclide behavior at the Oklo nuclear reactor, Gabon," *Waste Manag.*, vol. 10, no. 4, pp. 285–296, 1990.

[31] P. L. Chambre, T. H. Pigford, A. Fujita, T. Kanki, A. Kobayashi, H. Lung, D. Ting, Y. Sato, and S. J. Savoshy, "Analytical performance models for geologic repositories," tech. rep., Ernest Orlando Lawrence Berkeley National Laboratory, Berkeley, CA (US), 1982.

[32] J. Ahn, P. L. Chambre, T. H. Pigford, and W. W. L. Lee, "Radionuclide dispersion from multiple patch sources into a rock fracture," *LBL-23425 Lawrence Berkeley Lab. Berkeley CA*, 1986.

[33] J. Ahn, C. L. Kim, P. L. Chambré, T. H. Pigford, and W. W. L. Lee, "Intermediate-field transport of contaminants: Multiple areal sources in fractured rock and point sources in porous rock," *Waste Management*, vol. 11, pp. 11–18, Jan. 1991.

[34] T. H. Pigford, "Migration of Radionuclides Through Sorbing Media Analytical Solutions II," *Lawrence Berkeley Natl. Lab.*, Mar. 2010.

[35] J. Ahn, S. Kuo, D. A. Roberts, and P. L. Chambré, "Release of radionuclides from multiple canisters in a high level waste repository," tech. rep., UCB-NE-4221, 1998.

[36] D. Kawasaki, J. Ahn, P. L. Chambré, and W. G. Halsey, "Congruent Release of Long-Lived Radionuclides from Multiple Canister Arrays," *NT*, vol. 148, pp. 181–193, Nov. 2004.

[37] J. Ahn, D. Kawasaki, and P. L. Chambré, "Relationship Among Performance of Geologic Repositories, Canister-Array Configuration, and Radionuclide Mass in Waste," *NT*, vol. 140, pp. 94–112, Oct. 2002.

[38] D. Kawasaki, *Analyses of Radionuclide Migration in Geologic Media Using Compartment Models.* University of California, Berkeley, 2005.

[39] J. Ahn, "Mass transfer and transport of radionuclides in fractured porous rock," tech. rep., California Univ., Berkeley, CA (USA), Jan. 1988.

[40] K. M. Krupka, D. I. Kaplan, G. Whelan, R. J. Serne, and S. V. Mattigod, "Understanding variation in partition coefficient, Kd, values," *Vol. II Rev. Geochem. Available Kd Values Cadmium Cesium Chromium Lead Plutonium Radon Strontium Thorium Tritium 3H Uranium EPA*, 1999.

[41] D. W. Shoesmith, "Used fuel and uranium dioxide dissolution studies–A review," *Rep. NWMO TR-2007-03 Nucl. Waste Manag. Organ. Tor. ON*, 2007.

[42] C. Joseph, M. Stockmann, K. Schmeide, S. Sachs, V. Brendler, and G. Bernhard, "Sorption of U(VI) onto Opalinus Clay: Effects of pH and humic acid," *Applied Geochemistry*, vol. 36, pp. 104–117, Sept. 2013.

[43] H. Akçay, "Aqueous speciation and pH effect on the sorption behavior of uranium by montmorillonite," *J Radioanal Nucl Chem*, vol. 237, pp. 133–137, Nov. 1998.

[44] B. Allard, H. Kipatsi, and J. O. Liljenzin, "Expected species of uranium, neptunium and plutonium in neutral aqueous solutions," *Journal of Inorganic and Nuclear Chemistry*, vol. 42, pp. 1015–1027, Jan. 1980.

[45] Y. Tachi, Y. Tochigi, T. Suyama, Y. Saito, M. Yui, and M. Ochs, "Development of the sorption and diffusion database system for safety assessment of geological disposal," tech. rep., Japan Atomic Energy Agency, 2009.

[46] Joonhong Ahn, *UCB NE 224 Safety Assessment for Geologic Disposal of Radioactive Wastes.* Berkeley, CA, USA: Department of Nuclear Engineering, University of California, 2010.

[47] J. Bear, *Dynamics of Fluids in Porous Media.* Courier Corporation, 2013.

[48] B. Torstenfelt, K. Andersson, H. Kipatsi, B. Allard, and U. Olofsson, "Diffusion Measurements in Compacted Bentonite," *MRS Online Proc. Libr. Arch.*, vol. 6, 1981/ed.

[49] H. Sato, T. Ashida, Y. Kohara, M. Yui, and N. Sasaki, "Effect of dry density on diffusion of some radionuclides in compacted sodium bentonite," *J. Nucl. Sci. Technol.*, vol. 29, no. 9, pp. 873–882, 1992.

[50] Y. Tochigi and Y. Tachi, "Development of diffusion database of buffer materials and rocks," tech. rep., Japan Atomic Energy Agency, 2009.

[51] "Research and development on geological disposal of high-level radioactive waste: First progress report," Tech. Rep. PNC-TN1410 93-059, PNC (Power Reactor and Nuclear Fuel Development Corporation), Tokyo, Sept. 1992.

[52] R. J. Lemire and F. Garisto, "The solubility of U, Np, Pu, Th and Tc in a geological disposal vault for used nuclear fuel," tech. rep., Atomic Energy of Canada Ltd., 1989.

[53] T. Hamamoto, S. Shibutani, K. Ishida, K. Fujisaki, M. Yamada, and Y. Tachi, "Assessment of sorption and diffusion in the rock matrix in the NUMO safety case," in *Proceedings of EAFORM2017: 6th East Asia Forum on Radwaste Management Conference*, 2018.

[54] I. G. McKinley and D. Savage, "Comparison of solubility databases used for HLW performance assessment," *Journal of Contaminant Hydrology*, vol. 21, pp. 335–350, Feb. 1996.

[55] A. B. Muller, "International chemical thermodynamic data base for nuclear applications," *Radioact Waste Manage Nucl Fuel Cycle*, vol. 6, no. 2, pp. 131–141, 1985.

[56] J. Ahn, E. Greenspan, and P. Chambré, "A preliminary consideration for underground autocatalytic criticality by vitrified high-level waste in water-saturated geologic repository," *J. Nucl. Sci. Technol.*, vol. 37, pp. 465–476, May 2000.

[57] J. Ahn, "Transport of weapons-grade plutonium and boron through fractured geologic media," *Nucl. Technol.*, vol. 117, no. 3, pp. 316–328, 1997.

[58] E. Hakami and E. Larsson, "Aperture measurements and flow experiments on a single natural fracture," *International Journal of Rock Mechanics and Mining Sciences & Geomechanics Abstracts*, vol. 33, pp. 395–404, June 1996.

[59] E. Hakami, *Aperture Distribution of Rock Fractures.* PhD thesis, Royal Institute of Technology Stockholm, Sweden, 1995.

[60] M. D. McKay, R. J. Beckman, and W. J. Conover, "A Comparison of Three Methods for Selecting Values of Input Variables in the Analysis of Output from a Computer Code," *Technometrics*, vol. 21, no. 2, pp. 239–245, 1979.

[61] A. Salazar, M. Fratoni, J. Ahn, and F. Hirano, "Uncertainty analysis of far-field precipitation from used nuclear fuel," (Charlotte, NC, USA), American Nuclear Society, Apr. 2017.

[62] G. Marsaglia, "Xorshift RNGs," *J. Stat. Softw.*, vol. 8, no. 14, pp. 1–6, 2003.

[63] G. Marsaglia and T. A. Bray, "A convenient method for generating normal variables," *Siam Rev.*, vol. 6, no. 3, pp. 260–264, 1964.

[64] "Technical Report on Research and Development for Geological Disposal of High-Level Radioactive Wastes," Tech. Rep. PNC TN 1410 92-08, Power Reactor and Nuclear Fuel Development Corporation, 1992.

[65] D. W. Waples and J. S. Waples, "A review and evaluation of specific heat capacities of rocks, minerals, and subsurface fluids. Part 1: Minerals and nonporous rocks," *Nat. Resour. Res.*, vol. 13, no. 2, pp. 97–122, 2004.

[66] J. Ahn, T. Ikeda, T. Ohe, T. Kanno, Y. Sakamoto, T. Chiba, M. Tsukamoto, S. Nakayama, S. Nagasaki, K. Banno, and T. Fujita, "Quantitative performance allocation of multi-barrier system for high-level radioactive waste disposal," *J Energy Soc Jpn.*, vol. 37, no. 1, 1995.

[67] "Wolfram Mathematica 11.1," 2017.

[68] H. C. Paxton and N. L. Pruvost, "Critical dimensions of systems containing U-235, Pu-239, and U-233," Tech. Rep. LA-10860-MS, Los Alamos National Laboratory (LANL), 1987.

[69] S.-E. Bentridi, B. Gall, F. Gauthier-Lafaye, A. Seghour, A. Pape, and D.-E. Medjadi, "Criticality of Oklo Natural Reactors: Realistic Model of Reaction Zone 9," *IEEE Trans. Nucl. Sci.*, vol. 60, pp. 278–283, Feb. 2013. WOS:000314973200013.

[70] R. M. Mason, J. K. Martin, P. N. Smith, and B. D. Turland, "Comparison of a post-closure transient criticality model with the Oklo natural reactors," *Mineralogical Magazine*, vol. 76, pp. 3145–3153, Jan. 2012.

[71] W. H. Fleming and H. G. Thode, "Neutron and Spontaneous Fission in Uranium Ores," *Phys. Rev.*, vol. 92, pp. 378–382, Oct. 1953.

[72] P. K. Kuroda, "On the infinite multiplication constant and the age of the uranium minerals," *J. Chem. Phys.*, vol. 25, no. 6, pp. 1295–1296, 1956.

[73] P. K. Kuroda, "On the nuclear physical stability of the uranium minerals," *J. Chem. Phys.*, vol. 25, no. 4, pp. 781–782, 1956.

[74] M. A. Molecke, "Waste Isolation Pilot Plant Transuranic Wastes Experimental Characterization Program: Executive Summary," Tech. Rep. SAND78-1356, Sandia Laboratories, Albuquerque, NM, Nov. 1978.

[75] R. A. Van Konynenburg, "Comments on the draft paper written by CD Bowman and F. Venneri (LANL)," *Sci. Glob. Secur.*, vol. 5, no. 3, pp. 303–322, 1996.

[76] A. Salazar, M. Atz, X. Liu, and M. Fratoni, "The criticality safety studies of joonhong ahn," *Trans. Am. Nucl. Soc.*, vol. 112, pp. 110–113, June 2017.

[77] S.-E. Bentridi, B. Gall, F. Gauthier-Lafaye, and A. Seghour, "Monte Carlo based numerical modeling and simulation of criticality conditions occurrence in natural reactor zone 9 in Oklo deposit (Gabon)," *Progr Nucl Sci Technol*, vol. 2, pp. 395–400, 2011.

[78] S.-E. Bentridi, B. Gall, F. Gauthier-Lafaye, A. Seghour, and D.-E. Medjadi, "Inception and evolution of Oklo natural nuclear reactors," *Comptes Rendus Geoscience*, vol. 343, pp. 738–748, Nov. 2011.

[79] D. G. Brookins, "Shale as a repository for radioactive waste: The evidence from Oklo," *Geo*, vol. 1, pp. 255–259, Sept. 1976.

[80] T. Goorley, M. James, T. Booth, F. Brown, J. Bull, L. J. Cox, J. Durkee, J. Elson, M. Fensin, and R. A. Forster, "Initial MCNP6 release overview," *Nucl. Technol.*, vol. 180, no. 3, pp. 298–315, 2012.

[81] J. B. Briggs, L. Scott, and A. Nouri, "The international criticality safety benchmark evaluation project," *Nucl. Sci. Eng.*, vol. 145, no. 1, pp. 1–10, 2003.

[82] H. H. Adler, "Concepts of uranium-ore formation in reducing environments in sandstones and other sediments," *Form. Uranium Ore Depos.*, pp. 141–168, 1974.

[83] J. Sjöberg, U. Lindfors, F. Perman, and D. Ask, "Evaluation of the state of stress at the Forsmark site. Preliminary site investigation Forsmark area-version 1.2," tech. rep., Swedish Nuclear Fuel and Waste Management Co., 2005.

[84] D. H. Yaalon, "Mineral composition of the average shale," *Clay Miner. Bull.*, vol. 5, no. 27, pp. 31–36, 1962.

[85] P. H. Nadeau and D. C. Bain, "Composition of some smectities and diagenetic illitic clays and implications for their origin," *Clays Clay Miner.*, vol. 34, no. 4, pp. 455–464, 1986.

[86] H. Blatt, R. Tracy, and B. Owens, *Petrology: Igneous, Sedimentary, and Metamorphic.* Macmillan, 2006.

[87] J. R. Lamarsh, *Introduction to Nuclear Reactor Theory*, vol. 3. Addison-Wesley Reading, Massachusetts, 1966.

[88] M. L. Fensin, *Development of the MCNPX Depletion Capability: A Monte Carlo Linked Depletion Method That Automates the Coupling between MCNPX and CINDER90 for High Fidelity Burnup Calculations.* University of Florida, 2008.

[89] W. M. Stacey, *Nuclear Reactor Physics.* John Wiley & Sons, 2018.

[90] M. L. Fensin, M. R. James, J. S. Hendricks, and J. T. Goorley, "The new MCNP6 depletion capability," tech. rep., Los Alamos National Lab.(LANL), Los Alamos, NM (United States), 2012.

[91] J. S. Hendricks, "Monte Carlo N-Particle Transport Code System for Multiparticle and High Energy Applications, version 2.6.0," Tech. Rep. LA-UR-08-2216, Los Alamos National Laboratory, 2008.

[92] Nuclear Regulatory Commission, "Standards of Protection against Radiation, 10CFR20," *US Off. Fed. Regist. Wash. DC*, 1991.

[93] UC Regents, "TOUGH2: Transport of Unsaturated Groundwater and Heat w/ T2CG2 Solver Package," July 2011.

[94] T. L. Bergman, F. P. Incropera, D. P. DeWitt, and A. S. Lavine, *Fundamentals of Heat and Mass Transfer.* John Wiley & Sons, 7 ed., Apr. 2011.

[95] R. Haenel, L. Stegena, and L. Rybach, *Handbook of Terrestrial Heat-Flow Density Determination: With Guidelines and Recommendations of the International Heat Flow Commission*, vol. 4. Springer Science & Business Media, 2012.

[96] M. T. Van Genuchten, "A closed-form equation for predicting the hydraulic conductivity of unsaturated soils," *Soil Sci. Soc. Am. J.*, vol. 44, no. 5, pp. 892–898, 1980.

[97] *The 1967 IFC Formulation for Industrial Use : A Formulation of the Thermodynamic Properties of Ordinary Water Substance.* Dusseldorf: IFC Secretariat, 1967.

[98] A. Harvey, W. T. Parry, J. Bellows, J. Gallagher, and R. Harwood, *ASME International Steam Tables for Industrial Use, Third Edition.* ASME Press, 2014.

[99] E. W. Lemmon, M. L. Huber, and M. O. McLinden, "NIST reference fluid thermodynamic and transport properties—REFPROP," *NIST Stand. Ref. Database*, vol. 23, p. v7, 2002.

[100] W. Wagner and A. Pruess, "The IAPWS formulation 1995 for the thermodynamic properties of ordinary water substance for general and scientific use," *J. Phys. Chem. Ref. Data*, vol. 31, no. 2, pp. 387–535, 2002.

[101] W. Martin, "Implementation of On-the-Fly Doppler Broadening in MCNP5 for Multiphysics Simulation of Nuclear Reactors," Final Report for Project 10-897 DE-AC07-05ID14517, Battelle Energy Alliance, LLC, Ann Arbor, MI, Nov. 2012.

[102] D. E. Cullen and C. R. Weisbin, "Exact Doppler broadening of tabulated cross sections," *Nucl. Sci. Eng.*, vol. 60, no. 3, pp. 199–229, 1976.

[103] K. O. Ott and R. J. Neuhold, *Introductory Nuclear Reactor Dynamics.* La Grange Park, Illinois: American Nuclear Society, 1985.

[104] S. Nadarajah, "A generalized normal distribution," *J. Appl. Stat.*, vol. 32, pp. 685–694, Sept. 2005.

[105] P. N. Smith and R. M. Mason, "Modeling of Consequences of Hypothetical Criticality: User Guide for the Quasi Steady State Model," Tech. Rep. RWM005140, AMEC, Februrary 2013.

[106] J. Ahn, E. Greenspan, D. A. Roberts, and P. L. Chambré, "Possibility of underground autocatalytic criticality by actinides in vitrified HLW," in *International Conference on Future Nuclear Systems. Challenge towards Second Nuclear Era with Advanced Fuel Cycles. Proceedings*, 1997.

[107] J. Ahn, "Criticality Safety Assessment for a Conceptual High-Level-Waste Repository in Water-Saturated Geologic Media," *NT*, vol. 126, pp. 303–318, June 1999.

[108] J. Ahn, "Criticality Safety of Geologic Disposal for High-Level Radioactive Wastes," *Nucl. Eng. Technol.*, vol. 38, no. 6, pp. 489–504, 2006.

[109] E. C. Robertson, "Thermal properties of rocks," tech. rep., US Geological Survey,, 1988.

[110] J. K. Fink, "Thermophysical properties of uranium dioxide," *Journal of Nuclear Materials*, vol. 279, pp. 1–18, Mar. 2000.

[111] J. C. Maxwell, *A Treatise on Electricity and Magnetism.* Cambridge: Oxford University Press, 2 ed., 1904.

[112] G. Zoth and R. Haenel, "Appendix 10: Thermal Conductivity," in *Handbook of Terrestrial Heat-Flow Density Determination*, Solid Earth Sciences Library, pp. 449–468, Springer, Dordrecht, 1988.

[113] C. Clauser and E. Huenges, "Thermal Conductivity of Rocks and Minerals," in *Rock Physics & Phase Relations* (T. J. Ahrens, ed.), pp. 105–126, American Geophysical Union, 1995.

[114] C. G. S. Pillai and A. M. George, "Thermal conductivity of uranium dioxide," *Journal of Nuclear Materials*, vol. 200, pp. 78–81, Mar. 1993.

[115] IAEA, "Thermal Conductivity of Uranium Dioxide," Tech. Rep. STI/DOC/10/59, International Atomic Energy Agency, Vienna, Austria, Apr. 1965.

[116] P. Cheng, "Mixed convection about a horizontal cylinder and sphere in a fluid-saturated porous medium," *International Journal of Heat and Mass Transfer*, vol. 25, pp. 1245–1246, Aug. 1982.

[117] D. A. Nield and A. Bejan, *Convection in Porous Media*. Springer Science & Business Media, Dec. 2006.

[118] A. Bejan and A. D. Kraus, *Heat Transfer Handbook*, vol. 1. John Wiley & Sons, 2003.

[119] P. K. Kuroda, "The pre-Fermi natural reactor: A note on the periodic mode of operation," *Journal of Radioanalytical and Nuclear Chemistry, Articles*, vol. 142, pp. 113–118, Sept. 1990.

[120] D. A. Lockner, "Rock failure," *Rock Phys. Phase Relat. Handb. Phys. Constants*, vol. 3, pp. 127–147, 1995.

[121] M. C. Tsenn and N. L. Carter, "Upper limits of power law creep of rocks," *Tectonophysics*, vol. 136, pp. 1–26, May 1987.

[122] G. S. Was, *Fundamentals of Radiation Materials Science: Metals and Alloys*. Springer, 2016.

[123] M. E. Chenevert and C. Gatlin, "Mechanical Anisotropies of Laminated Sedimentary Rocks," *Soc. Pet. Eng. J.*, vol. 5, pp. 67–77, Mar. 1965.

[124] M. W. Lee, *Proposed Moduli of Dry Rock and Their Application to Predicting Elastic Velocities of Sandstones*. US Department of the Interior, US Geological Survey, 2005.

[125] C. MacBeth, "A classification for the pressure-sensitivity properties of a sandstone rock frame," *GEOPHYSICS*, vol. 69, pp. 497–510, Mar. 2004.

[126] K. Kawabata, H. Tanaka, Y. Kitamura, and K.-F. Ma, "Apparent activation energy and rate-limiting process estimation from natural shale deformed by pressure solution in shallow subduction zone," *Earth and Planetary Science Letters*, vol. 287, pp. 57–63, Sept. 2009.

[127] M. H. H. Hettema, C. J. De Pater, and K. H. Wolf, "Effects of temperature and pore water on creep of sandstone rock," in *The 32nd US Symposium on Rock Mechanics (USRMS)*, American Rock Mechanics Association, 1991.

[128] L. Werme, P. Sellin, and N. Kjellbert, "Copper canisters for nuclear high level waste disposal. Corrosion aspects," tech. rep., Swedish Nuclear Fuel and Waste Management Co., Stockholm (Sweden), 1992.

[129] H. Raiko, "Disposal canister for spent nuclear fuel-design report," *Posiva Rep.*, vol. 2, p. 61, 2005.

[130] B. van den Akker, "Laplace Transformed Analytical Solution of Aqueous Radionuclide Transport via Heterogeneous Geological Formations for Arbitrary Length Decay Chain," (Charlotte, NC, USA), American Nuclear Society, Apr. 2017.

Appendix A

Material composition development

A.1 Input

The material compositions for MCNP were devised using a script that considered constituent compounds, atoms, and isotopes. An example of a material composition input file is shown here for the uranium ore in the 1.5 wt%-enriched fractured configuration, which includes shale as the rock component. While only the ore portion of the deck is relevant to the final material composition in the input, the shale and fluids are used to devise average densities, thermal conductivities, and heat capacities. For reference, the homogeneous precipitate employs sandstone (90% SiO_2, 10% $KAlSi_3O_8$) instead of shale, and all components are included in the final material.

The structure of the input is as follows:

- Compound, density $\left[\frac{g}{cm^3}\right]$, volume fraction, thermal conductivity $\left[\frac{W}{m-K}\right]$, heat capacity $\left[\frac{J}{kg-K}\right]$
  - Element, atomic number, atomic fraction in enclosing compound
    - Isotope mass number or ”00” for ENDF natural abundance libraries, molar mass of isotope, isotope fraction

```
#Ore  10.95  0.10  7.00  258.0
U       92      1/3
236     236.045568        0.007300
233     233.0396355       0.000680
238     238.0507882       0.977270
234     234.0409521       0.000230
235     235.0439299       0.014520
O       8         2/3
16      15.99491462  1
```

```
#Shale 2.80 0.70 2.9 795.0 1.8
O        8        6.33789629E-01
16       15.9994  1
Si       14       2.00428809E-01
28       28.0855  1
Ti       22       2.23739097E-04
48       47.867   1
Al       13       8.55295937E-02
27       26.9815  1
Fe       26       2.72797093E-02
56       55.845   1
Mn       25       3.44213996E-05
55       54.938   1
Mg       12       4.71573175E-03
24       24.305   1
Ca       20       1.60172107E-02
40       40.078   1
Na       11       4.13056795E-04
23       22.9897  1
K        19       6.18826755E-03
39       39.0983  1
P        15       1.37685598E-04
31       30.9738  1
S        16       3.44213996E-05
32       32.065   1
Sr       38       9.20772440E-03
88       87.62    1
C        6        1.60000000E-02
00       12.0107  1
#Water 1.005 0.195 0.605 4104
H        1      2/3
1      1.0079        1
O        8      1/3
16     15.9994       1
#Air 0.001777 0.005 0.034 1242
N      7       7.60E-01
14       14.0067   1
O      8       2.33E-01
16       15.9994   1
Ar     18      6.48E-03
40       39.948    1
C      6       2.75E-04
```

```
00        12.0107   1
Ne    10       6.37E−06
20        20.1797   1
He    2        3.64E−07
4         4.0026    1
Kr    36       2.04E−08
84        83.8      1
H     1        1.82E−06
1         1.0079    1
Xe    54       2.07E−09
131       131.293   1
I     53       2.69E−06
127       126.9045  1
```

A.2 Script

The Perl script used to create MCNP atomic compositions and average material properties from the input file is shown here.

```perl
# Script to calculate isotope fractions for unsaturated homogeneous compound
#
# REQUIRES
#    enr.inp
#
# Alex Salazar
# University of California, Berkeley
# Department of Nuclear Engineering
# salazar@berkeley.edu
# February 1, 2018

#MODULES
use warnings;
use strict;
use Cwd;

#CONSOLE READ
my $FINP=$ARGV[0];     #SCRIPT INPUT FILE
my $g5= $ARGV[1];      #xs library designator
my $por= $ARGV[2];     #porosity
my $g3= $ARGV[3];      #heavy metal volume fraction
my $sat= $ARGV[4];     #saturation
my $dw= $ARGV[5];      #density of water
```

```
my $dg= $ARGV[6];      #density of gas

my $DOR=0; #DENSITY OVERRIDE
if($ARGV[5]||$ARGV[6]){
      $DOR=1;
}

my $href="Ore";       #for "heavy metal" in solid material
my $lref="Water";     #for pore-filling liquid
my $gref="Air";       #for pore-filling gas
my @fl=($lref,$gref); #pore fluids

if($g3>$por){
      print "ERROR: HMVF must be less than or equal to porosity!\n";
      exit;
}
if($sat>1||$sat<0){
      print "ERROR: SAT ranges from [0,1]!\n";
      exit;
}
my $g2=($por-$g3)*$sat;     #water volume fraction
my $g4=($por-$g3)*(1.0-$sat); #gas volume fraction

#INPUT READ
#my $FINP="enr.inp";
my $DIR=getcwd;
my $header;
my $suffix;
if($FINP=~/\.inp/){
      my @dat=($FINP=~m/(.*)\./g);
      $header=$dat[0];
}else{
      $header=$FINP;
}
$suffix="inp";

open (my $inp0,"<","$DIR/$header.$suffix")or die "Cannot find ore component
    input!\n";
chomp(my @inp = <$inp0>);
close $inp0;
my @cinp=@inp;  #copy

#READ FRACTION
sub frac{
```

```
     my $inp = shift;
     my $res;
     if($inp=~/\//){
          my @left= ($inp=~m/(\d+)\//) ;
          my @right= ($inp=~m/\/(\d+)/) ;
          my $left=$left[0]*1.00;
          my $right=$right[0]*1.00;
          $res=$left/$right;
     }else{
           $res=$inp*1.000;
     }
     return $res;
}
#UNIQUE VALUES
sub uniq{
  my %seen;
  return grep { !$seen{$_}++ } @_;
}
#TRIM
sub ltrim { my $s = shift; $s =~ s/^\s+//;  return $s };
sub rtrim { my $s = shift; $s =~ s/\s+$//;  return $s };
sub trim { my $s = shift; $s =~ s/^\s+|\s+$//g; return $s };

#SCI FORMAT
sub sci{
     my ($num,$d,$de)=@_;
     my $form=sprintf("%.".$d."e",$num);
     my $prefix=($form=~m/(.+)e/g)[0];
     my $pow=($form=~m/e(.+)/g)[0];
     my $sign=($pow=~m/[+-]/g)[0];
     my $dig= ($pow=~/[+-]\K\d+/g)[0];
     my $pwr=sprintf("%0".$de."d",$dig);
     my $res=$prefix."E".$sign."".trim($pwr);
     return $res;
}

#DATA
my @md=();
#molecule data
     #0 file index
     #1 name
     #2 density
     #3 volume
     #4 element arrays
```

```
          #0 name
          #1 atomic number
          #2 atom fraction of element in *molecule*
          #3 isotope
               #0 mass number
               #1 molar mass
               #2 atom fraction of isotope in *element*
               #3 isotope identifier
               #4 mass fraction of isotope in *element*
               #5 atom fraction of isotope in *compound*
     #5 mass fraction of molecule in compound
     #6 atom fraction of molecule in compound
my $mm1=-1; my $mm2=-1; my $mm3=-1;
my $mr1=0;
my @el;    #ELEMENTS
my @is;    #ISOTOPES
my @is1;   #ISOTOPES MCNP FORMAT
my $ele;   my $atn;
print "-----------------REPORT-----------------\n";
my $trackmat;
foreach my $i(0..$#inp){
     my $line=$inp[$i];
     if(substr($line,0,1) eq "#"){
          $mm1++;
          $mm2=-1;

          my @dat = ($line =~ m/#\K([\w\s]+)/g);
          my $name=$dat[0];
          $md[$mm1][0]=$i;
          $md[$mm1][1]=$name;
          $trackmat=$name;
          if($i>0){
               print "----------------------------------------\n";
          }
          print "Molecule $md[$mm1][1] found on index $i\n";
          $mr1=1;
          next;
     }
     if($mr1==1){
          my @dat = $line =~ m/(\d+(?:\.\d+)?)/g ;
          my $d=$dat[0];
          my $v=$dat[1];
          my $kw=$dat[2];
          my $cp=$dat[3];
```

```
        my $kd=$dat[4];
        if($DOR){
            if($trackmat eq $lref){
                $d=$dw;
            }elsif($trackmat eq $gref){
                $d=$dg;
            }
        }
        $md[$mm1][2]=$d;
        $md[$mm1][3]=$v;
        printf ("%s%.5f%s%.5f%s","Density: ",$md[$mm1][2]," g/cc, Volume
          fraction: ",$md[$mm1][3]," \n");
        if($dat[2]){
            $md[$mm1][5]=$kw;
            printf ("%s%.5f%s%s","Thermal conductivity (wet):
              ",$md[$mm1][5]," W/m-K"," \n");
        }
        if($dat[3]){
            $md[$mm1][6]=$cp;
            printf ("%s%.5f%s%s","Specific heat: ",$md[$mm1][6]," J/kg-K","
              \n");
        }
        if($dat[4]){
            $md[$mm1][7]=$kd;
            printf ("%s%.5f%s%s","Thermal conductivity (dry):
              ",$md[$mm1][7]," W/m-K"," \n");
        }elsif($dat[2]){
            $md[$mm1][7]=$kw;
        }
        $mr1=0;
        next;
    }
    if(substr($line,0,2)=~/[A-Za-z]+/){
        $mm2++;
        $mm3=-1;
        my @dat=($line=~m/([A-Za-z]+)\s+(\d+)/g);
        $ele=$dat[0];
        $atn=$dat[1];
        @dat=
        $line=~m/[A-Za-z]+\s+\d+\s+\K(\d+\/\d+)|(\d+\.\d+(?:[Ee][+-]\d+)?)/g;
        my $fr;
        if($line=~/\//){
            $fr=$dat[0];
        }else{
```

```
            $fr=$dat[1];
        }
        $fr=frac($fr);
        push @el, $ele;
        $md[$mm1][4][$mm2][0]=$ele;
        $md[$mm1][4][$mm2][1]=$atn;
        $md[$mm1][4][$mm2][2]=$fr;
        printf ("%s%.3e%s","~Element $md[$mm1][4][$mm2][0]
           \($md[$mm1][4][$mm2][1]\)~ with molecule fraction
           ",$md[$mm1][4][$mm2][2],"\n");

        next;
    }
    if(substr($line,0,3)=~/[\d+]+/){
        $mm3++;
        my @dat=$line=~m/(\d+(?:\.\d+)?)/g;
        my $iso=$dat[0];
        my $imm=$dat[1];
        my $iaf=$dat[2];
        $md[$mm1][4][$mm2][3][$mm3][0]=$iso;
        $md[$mm1][4][$mm2][3][$mm3][1]=$imm;
        $md[$mm1][4][$mm2][3][$mm3][2]=$iaf;
        my $nuc=$ele."-".$iso;
        my $nuc1= trim(sprintf("%3d%03d%s%s",$atn,$iso,".",$g5));
        #convention for metastable isotope: AAA=(AAA+300)+(m*100), where m is
           the metastable level and m=1, 2, 3, or 4.
        $md[$mm1][4][$mm2][3][$mm3][3]=$nuc1;
        push @is, $nuc;
        push @is1, $nuc1;
        printf ("%s%.5f%s%.5f%s","Isotope $nuc: molar mass
           ",$md[$mm1][4][$mm2][3][$mm3][1]," g/mol, element fraction
           ",$md[$mm1][4][$mm2][3][$mm3][2]*100," at%\n");
        next;
    }
}
print "----------------------------------------\n";
@el=uniq(@el);
@is=uniq(@is);
@is1=uniq(@is1);
my $tmp0=$#md+1;
my $tmp1=$#el+1;
my $tmp2=$#is+1;
print "Found $tmp0 molecules, $tmp1 unique elements, $tmp2 unique isotopes\n";
```

```
#CHECK USER INPUTS FOR CORRECT NORMALIZATION
#VOLUME FRACTIONS
print "----------------------------------------\n";
print "Checking volume fractions...\n";
my $vsum=0;
foreach my$i(0..$#md){
     my $v=$md[$i][3];
     $vsum=$vsum+$v;
}
#RENORMALIZE VOLUME FRACTIONS IF NEEDED
my $vsum1=0;
if($vsum!=1){
     print "Bad checksum for volume fractions: $vsum\n";
     foreach my$i(0..$#md){
          my $vo=$md[$i][3];
          my $vn=$vo/$vsum;
          $vsum1=$vsum1+$vn;
          printf ("%s%s%s%.3f%s","New volume fraction for ",$md[$i][1],":
              ",$vn,"\n");
          $md[$i][3]=$vn;
     }
}

#MOLECULE FRACTIONS
print "----------------------------------------\n";
print "Checking molecule and element fractions...\n";
foreach my$i(0..$#md){
     my $len1 = $#{$md[$i][4]} ;
     my $mfsum=0;
     foreach my $j(0..$len1){
          my $mf=$md[$i][4][$j][2];
          $mfsum=$mfsum+$mf;

          my $len2 = $#{$md[$i][4][$j][3]} ;
          my $efsum=0;
          foreach my $k(0..$len2){
               my $ef=$md[$i][4][$j][3][$k][2];
               $efsum=$efsum+$ef;
          }
          if($efsum!=1){
               printf ("%s%f%s","--->Bad checksum for $md[$i][4][$j][0]:
                   ",$efsum,"\nAdjusting...\n");
               foreach my $k(0..$len2){
                    my $efo=$md[$i][4][$j][3][$k][2];
```

```
                    my $ef=$efo/$efsum;
                    $md[$i][4][$j][3][$k][2]=$ef;
                    printf ("%s%.6e%s","New fraction for
                        $md[$i][4][$j][3][$k][3]: ",$ef," \n");
               }
          }
     }
     if($mfsum!=1){
          printf ("%s%f%s","--->Bad checksum for $md[$i][1]:
              ",$mfsum,"\nAdjusting...\n");
          foreach my $j(0..$len1){
               my $mfo=$md[$i][4][$j][2];
               my $mf=$mfo/$mfsum;
               $md[$i][4][$j][2]=$mf;
               printf ("%s%.6e%s","New fraction for $md[$i][4][$j][0]: ",$mf,"
                   \n");
          }
     }
}

#MAKE A COPY OF THE ORIGINAL DATA BEFORE ALTERING
my @cp=@md;

#CHECK FOR ORE
my $orepres=0;
foreach my $i(0..$#cp){
     my $mat =$cp[$i][1];
     if($mat eq $href){
          $orepres=1;
          last;
     }
}

#FIND OLD POROSITY FROM INPUT
my $fsum=0;
my $fvfo;  #old fluid volume fraction
my $wvfo;  #old water volume fraction
my $gvfo;  #old gas volume fraction
my $hmvfo; #old heavy metal volume fraction
foreach my $i(0..$#cp){
     my $mol=$cp[$i][1];
     foreach my $f(0..$#fl){
          my $fluid=$fl[$f];
          if($mol eq $fluid){
```

```
               my $f=$cp[$i][3];
               $fsum=$fsum+$f;
               if($mol eq $lref){
                    $wvfo=$f;
               }
               if($mol eq $gref){
                    $gvfo=$f;
               }
               last;
          }
     }
     if($mol eq $href){
          $hmvfo=$cp[$i][3];
     }
}
$fvfo=$fsum; #old fluid volume fraction
print "----------------------------------------\n";
print "Total fraction of fluids: $fsum\n";

print "----------------------------------------\n";
print "Modifications to input file:\n";
printf ("%s%.3f%s","Porosity: ",$por,"\n");
printf ("%s%.3f%s","Saturation: ",$sat,"\n");
printf ("%s%.3f%s","WVF:     ",$g2,"\n");
printf ("%s%.3f%s","GVF:     ",$g4,"\n");
printf ("%s%.3f%s","HMVF:    ",$g3,"\n");


#FIND OLD WATER VOLUME FRACTION FROM INPUT AND REPLACE
print "----------------------------------------\n";
print "Adjusting for user-specified water volume fraction...\n";

my $svfo;       #old volume fraction of non-water
my $svf=1-$g2;  #new volume fraction of non-water
foreach my $i(0..$#cp){
     my $mol=$cp[$i][1];
     if($mol eq $lref){
          $svfo=1-$wvfo;
          printf ("%s%.3f%s","Old water volume fraction: ",$cp[$i][3],"\n");
          $cp[$i][3]=$g2;
          printf ("%s%.3f%s","New water volume fraction: ",$cp[$i][3],"\n");
          my $windex=$i;
          foreach my $i(0..$#cp){
               if($i==$windex){
```

```
                      next;
                }
                my $vo=$cp[$i][3];
                my $vn=$vo*($svf/$svfo);
                $cp[$i][3]=$vn;
                printf ("%s%s%s%.3f%s","New volume fraction for ",$cp[$i][1],":
                    ",$cp[$i][3],"\n");
           }
     }
}
#UPDATE KEY COMPONENTS FOR NEXT STEP
foreach my $i(0..$#cp){
     my $mol=$cp[$i][1];
     my $f=$cp[$i][3];
     if($mol eq $lref){
          $wvfo=$f;
     }
     if($mol eq $gref){
          $gvfo=$f;
     }
     if($mol eq $href){
          $hmvfo=$f;
     }
}

#FIND OLD GAS VOLUME FRACTION FROM INPUT AND REPLACE
print "----------------------------------------\n";
print "Adjusting for user-specified gas volume fraction...\n";
$svf=1-$g2-$g4;  #new volume fraction of non-gas
foreach my $i(0..$#cp){
     my $mol=$cp[$i][1];
     if($mol eq $gref){
           $svfo=1-$gvfo-$wvfo;
           printf ("%s%.3f%s","Old gas volume fraction: ",$cp[$i][3],"\n");
           $cp[$i][3]=$g4;
           printf ("%s%.3f%s","New gas volume fraction: ",$cp[$i][3],"\n");
           my $windex=$i;
           foreach my $i(0..$#cp){
                my $mol=$cp[$i][1];
                if($i==$windex||$mol eq $lref){
                      next;
                }
                my $vo=$cp[$i][3];
                my $vn=$vo*($svf/$svfo);
```

```
                $cp[$i][3]=$vn;
                printf ("%s%s%s%.3f%s","New volume fraction for ",$cp[$i][1],":
                    ",$cp[$i][3],"\n");
            }
        }
}
#UPDATE KEY COMPONENTS FOR NEXT STEP
foreach my $i(0..$#cp){
        my $mol=$cp[$i][1];
        my $f=$cp[$i][3];
        if($mol eq $lref){
            $wvfo=$f;
        }
        if($mol eq $gref){
            $gvfo=$f;
        }
        if($mol eq $href){
            $hmvfo=$f;
        }
}

#FIND OLD HEAVY METAL FRACTION FROM INPUT AND REPLACE
print "---------------------------------------\n";
print "Adjusting for user-specified heavy metal volume fraction...\n";
$svf=1-$por; #new volume of gangue
foreach my $i(0..$#cp){
        my $mol=$cp[$i][1];
        if($mol eq $href){
            $svfo=1-$hmvfo-$wvfo-$gvfo;
            printf ("%s%.3f%s","Old HMVF: ",$cp[$i][3],"\n");
            $cp[$i][3]=$g3;
            printf ("%s%.3f%s","New HMVF: ",$cp[$i][3],"\n");
            my $windex=$i;
            foreach my $i(0..$#cp){
                my $mol=$cp[$i][1];
                if($i==$windex||$mol eq $lref||$mol eq $gref){
                    next;
                }
                my $vo=$cp[$i][3];
                my $vn=$vo*($svf/$svfo);
                $cp[$i][3]=$vn;
                printf ("%s%s%s%.3f%s","New volume fraction for ",$cp[$i][1],":
                    ",$cp[$i][3],"\n");
            }
```

```
     }
}

#CALCULATING ATOM FRACTIONS FOR EACH ISOTOPE
print "----------------------------------------\n";
print "Calculating atom fractions of isotopes in the compound...\n";
my $v=1;       #virtual volume, cc, for normalizing
my $ac=0;
my $ac2=0;
my $kds=0;
my $cps=0;
my $kws=0;
my @acd=();    #array of number of atoms of isotope
my @smacd=();  #array of total atoms for each molecule
my @smcd=();   #array of total masses for each molecule
#MOLECULE
foreach my $i(0..$mm1){
     my $nam=$cp[$i][1];

     print "--------------------\n";
     print "Molecule $nam\n";
     my $den =$cp[$i][2]; #density of molecule
     my $vof =$cp[$i][3]; #volume fraction of molecule
     my $kw =$cp[$i][5];  #saturated thermal conductivity
     my $cp =$cp[$i][6];  #specific heat
     my $kd =$cp[$i][7];  #unsaturated thermal conductivity
     my $vol =$vof*$v;    #simulated volume of molecule
     my $mass=$vol*$den;  #simulated mass of molecule

     my $mc=0;      #running mass total for molecule from isotopes
     my @mcd=();    #array of ^
     my $mac=0;     #running atom total for molecule from isotopes
     my $ac1=0;

     #ELEMENT
     my $len1 = $#{$cp[$i][4]} ;
     foreach my $j(0..$len1){
          my $emf=$cp[$i][4][$j][2];
          #ISOTOPES
          my $len2 = $#{$cp[$i][4][$j][3]} ;
          my $ic=0;
          my @icd=();
          foreach my $k(0..$len2){
               my $imm=$cp[$i][4][$j][3][$k][1]; #molar mass
```

```
            my $iaf=$cp[$i][4][$j][3][$k][2]; #at% in element
            my $emc=$imm*$iaf;            #mass contribution of isotope to
               element
            $icd[$k]=$emc;
            $ic=$ic+$emc;                 #running mass of isotopes in element

            my $imf=$emf*$iaf;            #at% of isotope in whole molecule
            my $imc=$imm*$imf;            #mass contribution of isotope to
               molecule
            $mcd[$j][$k]=$imc;
            $mc=$mc+$imc;                 #running mass of isotopes in
               molecule
        }
        #REVISIT ISOTOPE
        foreach my $k(0..$len2){
            my $imass=$icd[$k];  #mass contribution of isotope to element
            my $mfrac=$imass/$ic; #enrichment of isotope in element by weight
            $cp[$i][4][$j][3][$k][4]=$mfrac;
            printf ("%s%.5f%s","Enrichment of $cp[$i][4][$j][3][$k][3] in
               $cp[$i][4][$j][0]: ",$cp[$i][4][$j][3][$k][4]*100," wt%\n");
        }
    }

    #REVISIT ELEMENT
    foreach my $j(0..$len1){
        #ISOTOPES
        my $len2 = $#{$cp[$i][4][$j][3]} ;
        foreach my $k(0..$len2){
            my $imm=$cp[$i][4][$j][3][$k][1]; #molar mass of isotope
            my $imc=$mcd[$j][$k];         #mass contribution of isotope to
               molecule
            my $iwt=$imc/$mc;             #mass fraction of isotope in
               molecule
            my $wmc=$iwt*$mass;           #actual mass of isotope in molecule
            my $iac=$wmc/$imm;            #atom contribution of isotope to
               compound (save for later)
            $acd[$i][$j][$k]=$iac;
            $ac=$ac+$iac;                 #running atom total for compound
            $mac=$mac+$iac;               #running atom total for molecule
            $ac1=$ac1+$wmc;               #running mass of isotopes in
               molecule
            $ac2=$ac2+$wmc;               #running mass of isotopes in
               compound
        }
```

```
          }

          if($cp[$i][5]){
                $kws=$kws+$mac*$kw;
          }
          if($cp[$i][6]){
                $cps=$cps+$ac1*$cp;
          }
          if($cp[$i][7]){
                $kds=$kds+$mac*$kd;
          }

          $smcd[$i] =$ac1;
          $smacd[$i]=$mac;
    }
    $kws=$kws/$ac;
    $cps=$cps/$ac2;  #Kopp's Law for specific heats
    $kds=$kds/$ac;

    #REVISIT MOLECULE
    print "--------------------\n";
    printf ("%s%.3f%s","Effective density of compound: ",$ac2," g/cc\n");
    printf ("%s%.3f%s","Effective wet thermal conductivity of compound: ",$kws,"
       W/m-K\n");
    printf ("%s%.3f%s","Effective specific heat of compound: ",$cps," J/kg-K\n");
    printf ("%s%.3f%s","Effective dry thermal conductivity of compound: ",$kds,"
       W/m-K\n");
    foreach my $i(0..$#cp){
    print "--------------------\n";
          my $mwtfrac=$smcd[$i]/$ac2;
          my $matfrac=$smacd[$i]/$ac;
          $cp[$i][5]=$mwtfrac;
          $cp[$i][6]=$matfrac;
          printf ("%s%.5f%s%.5f%s","Fraction of $cp[$i][1] in compound:
             ",$cp[$i][6]*100," at%, ",$cp[$i][5]*100," wt%\n");

          my $len1 = $#{$cp[$i][4]} ;
          foreach my $j(0..$len1){
                my $len2 = $#{$cp[$i][4][$j][3]} ;
                foreach my $k(0..$len2){
                      my $iac=$acd[$i][$j][$k];
                      my $iat=$iac/$ac;
                      $cp[$i][4][$j][3][$k][5]=$iat;
                      printf ("%s%10s%s%.5e%s","Atom fraction of
```

```
                    ",$cp[$i][4][$j][3][$k][3]," within $cp[$i][1] in compound:
                    ",$cp[$i][4][$j][3][$k][5]," \n");
            }
        }
}

#ORE GRADE
my $ssum=0;  #sum of solid atoms
my $numerator;
if($orepres){
        print "----------------------------------------\n";
        print "Determining ore grade...\n";
        foreach my $i(0..$#cp){
                my $mat =$cp[$i][1];
                if($mat eq $lref||$mat eq $gref){
                        next;
                }
                my $atoms=$smacd[$i];
                if($mat eq $href){
                        $numerator=$atoms;
                }
                $ssum=$ssum+$atoms;
        }
        my $grade=$numerator/$ssum;
        printf ("%s%.3f%s","Grade of $href in solid components: ",$grade*100,"
            at%\n");
}

#COMBINE FRACTIONS OF COMMON ISOTOPES
print "----------------------------------------\n";
print "Combining atom fractions of unique isotopes...\n";
open (my $out,">","$DIR/$header.out") or die "Cannot create MCNP input for ore
    composition!\n";
my @output=();
my @idata=();
foreach my $ii(0..$#is1){
        my $nuke=$is1[$ii];
        $idata[$ii][0]=$nuke;
        my $card;
        if($ii==0){
#               $card="$mat\t"; #old version
                $card="";  #for easier use by the shells.pl script
        }else {
#               $card="\t";
```

```
        $card="";
    }
#    printf $out "$card$nuke\t";
    my $sum=0;
    foreach my $i(0..$mm1){
        my $len1 = $#{$cp[$i][4]} ;
        foreach my $j(0..$len1){
            my $len2 = $#{$cp[$i][4][$j][3]} ;
            foreach my $k(0..$len2){
                my $iso=$cp[$i][4][$j][3][$k][3];
                if($iso eq $nuke){
                    my $iat=$cp[$i][4][$j][3][$k][5];
                    $sum=$sum+$iat;
                    last;
                }
            }
        }
    }
    printf ("%s%10s%s%.4e%s","Atom fraction of ",$nuke," in whole compound:
        ",$sum,"\n");
    $idata[$ii][1]=$sum;
    my $end;
    if($ii==$#is1){
        $end=" ";
    }else{
        $end="\n";
    }
    if($sum>0){
#        printf $out ("%.6e%s",$sum,$end);
        printf $out ("%s%10s%s%s%s",$card,$nuke," ",sci($sum,4,2),$end);
        my $lineout= sprintf("%s%s%s%.8f%s",$card,$nuke,"\t",$sum," ");
        push @output, $lineout;
    }
}
close $out;

my $fr;
open($fr,">","density");
printf $fr $ac2;
close $fr;
open($fr,">","kwet");
printf $fr $kws;
close $fr;
open($fr,">","cpav");
```

```
printf $fr $cps;
close $fr;
open($fr,">","kdry");
printf $fr $kds;
close $fr;
```

Appendix B

MCNP Input

An example of an MCNP input is shown for the unsaturated analysis with the OTFDB code from chapter 7. It represents the 0.1 MTU precipitate in the 6 wt% fractured geometry with a system state determined at 20 years into the TOUGH2 simulation at $q_{opt} = 233.69\,W$. In accordance with modeling approach 1, the densities of the rock component in the reactor are determined by the same average saturation level determining the relative volumes of water and air in the fracture. The BURN card is shown commented for reference. Some material listings are truncated with vertical ellipses (⋮).

```
Critical mass in fractures with reducing sediment in granitic medium
c Template for coupled criticality, burnup, and feedback studies
c Alex Salazar III
c University of California, Berkeley
c salazar@berkeley.edu
c 07/16/2018
c
c DESCRIPTION
c Sphere of fractured ore body consisting of repeated laminar units of
c    Shale rock
c    Pure uraninite (UO2) vein
c    Fracture space filled with water and air depending on saturation
c Surrounding spherical annulus of shale as reducing sedimentary rock
c Surrounding spherical annulus of water-saturated granite
c Granite is surrounded by void
c
c --------------------------------CELL CARDS-----------------------------------
c ~FRACTURETARGET~
100  100 -10.95000  1 -2 U=100 VOL=3.0042175E+00 TMP=3.0479842E-08 IMP:N=1
200  200  -2.61677  -1:4 U=100 VOL=3.4661374E+01 TMP=3.0479842E-08 IMP:N=1
300    3  -0.97782 2 -30 U=100 VOL=1.3312489E+01 TMP=3.0479842E-08 IMP:N=1
400    4  -0.14373 30 -4 U=100 VOL=1.6373614E-01 TMP=3.0479842E-08 IMP:N=1
```

```
101  101 -10.95000  1 -2 U=101 VOL=2.1442747E+01 TMP=2.9902998E-08 IMP:N=1
201  201  -2.61717  -1:4 U=101 VOL=2.4262962E+02 TMP=2.9902998E-08 IMP:N=1
301    3  -0.98185 2 -31 U=101 VOL=9.3105857E+01 TMP=2.9902998E-08 IMP:N=1
401    4  -0.14655 31 -4 U=101 VOL=1.1441956E+00 TMP=2.9902998E-08 IMP:N=1
102  102 -10.95000  1 -2 U=102 VOL=5.8302839E+01 TMP=2.9580365E-08 IMP:N=1
202  202  -2.61739  -1:4 U=102 VOL=6.5856611E+02 TMP=2.9580365E-08 IMP:N=1
302    3  -0.98401 2 -32 U=102 VOL=2.5258352E+02 TMP=2.9580365E-08 IMP:N=1
402    4  -0.14817 32 -4 U=102 VOL=3.1014588E+00 TMP=2.9580365E-08 IMP:N=1
103  103 -10.95000  1 -2 U=103 VOL=1.1357898E+02 TMP=2.9340114E-08 IMP:N=1
203  203  -2.61754  -1:4 U=103 VOL=1.2824708E+03 TMP=2.9340114E-08 IMP:N=1
303    3  -0.98557 2 -33 U=103 VOL=4.9242381E+02 TMP=2.9340114E-08 IMP:N=1
403    4  -0.14939 33 -4 U=103 VOL=6.0363526E+00 TMP=2.9340114E-08 IMP:N=1
104  104 -10.95000  1 -2 U=104 VOL=1.8727030E+02 TMP=2.9139675E-08 IMP:N=1
204  204  -2.61767  -1:4 U=104 VOL=2.1143438E+03 TMP=2.9139675E-08 IMP:N=1
304    3  -0.98684 2 -34 U=104 VOL=8.1121798E+02 TMP=2.9139675E-08 IMP:N=1
404    4  -0.15043 34 -4 U=104 VOL=9.9193388E+00 TMP=2.9139675E-08 IMP:N=1
105  105 -10.95000  1 -2 U=105 VOL=2.7937679E+02 TMP=2.8961727E-08 IMP:N=1
205  205  -2.61779  -1:4 U=105 VOL=3.1541851E+03 TMP=2.8961727E-08 IMP:N=1
305    3  -0.98795 2 -35 U=105 VOL=1.2095609E+03 TMP=2.8961727E-08 IMP:N=1
405    4  -0.15136 35 -4 U=105 VOL=1.4752982E+01 TMP=2.8961727E-08 IMP:N=1
106  106 -10.95000  1 -2 U=106 VOL=3.8989845E+02 TMP=2.8797998E-08 IMP:N=1
206  206  -2.61789  -1:4 U=106 VOL=4.4019945E+03 TMP=2.8797998E-08 IMP:N=1
306    3  -0.98894 2 -36 U=106 VOL=1.6874768E+03 TMP=2.8797998E-08 IMP:N=1
406    4  -0.15223 36 -4 U=106 VOL=2.0512958E+01 TMP=2.8797998E-08 IMP:N=1
107  107 -10.95000  1 -2 U=107 VOL=5.1883529E+02 TMP=2.8643747E-08 IMP:N=1
207  207  -2.61798  -1:4 U=107 VOL=5.8577723E+03 TMP=2.8643747E-08 IMP:N=1
307    3  -0.98986 2 -37 U=107 VOL=2.2449673E+03 TMP=2.8643747E-08 IMP:N=1
407    4  -0.15306 37 -4 U=107 VOL=2.7197817E+01 TMP=2.8643747E-08 IMP:N=1
108  108 -10.95000  1 -2 U=108 VOL=6.6618730E+02 TMP=2.8496219E-08 IMP:N=1
208  208  -2.61807  -1:4 U=108 VOL=7.5215182E+03 TMP=2.8496219E-08 IMP:N=1
308    3  -0.99073 2 -38 U=108 VOL=2.8820419E+03 TMP=2.8496219E-08 IMP:N=1
408    4  -0.15385 38 -4 U=108 VOL=3.4797899E+01 TMP=2.8496219E-08 IMP:N=1
109  109 -10.95000  1 -2 U=109 VOL=8.3195448E+02 TMP=2.8353688E-08 IMP:N=1
209  209  -2.61816  -1:4 U=109 VOL=9.3932324E+03 TMP=2.8353688E-08 IMP:N=1
309    3  -0.99155 2 -39 U=109 VOL=3.5987468E+03 TMP=2.8353688E-08 IMP:N=1
409    4  -0.15463 39 -4 U=109 VOL=4.3267126E+01 TMP=2.8353688E-08 IMP:N=1
110  110 -10.95000  1 -2 U=110 VOL=1.0161368E+03 TMP=2.8215121E-08 IMP:N=1
210  210  -2.61824  -1:4 U=110 VOL=1.1472915E+04 TMP=2.8215121E-08 IMP:N=1
310    3  -0.99233 2 -40 U=110 VOL=4.3950268E+03 TMP=2.8215121E-08 IMP:N=1
410    4  -0.15539 40 -4 U=110 VOL=5.2660619E+01 TMP=2.8215121E-08 IMP:N=1
111  111 -10.95000  1 -2 U=111 VOL=1.2187344E+03 TMP=2.8079915E-08 IMP:N=1
211  211  -2.61832  -1:4 U=111 VOL=1.3760566E+04 TMP=2.8079915E-08 IMP:N=1
311    3  -0.99307 2 -41 U=111 VOL=5.2713487E+03 TMP=2.8079915E-08 IMP:N=1
411    4  -0.15615 41 -4 U=111 VOL=6.2890682E+01 TMP=2.8079915E-08 IMP:N=1
```

```
112  112 -10.95000  1 -2 U=112 VOL=1.4397471E+03 TMP=2.7947726E-08 IMP:N=1
212  212  -2.61840  -1:4 U=112 VOL=1.6256185E+04 TMP=2.7947726E-08 IMP:N=1
312    3  -0.99379 2 -42 U=112 VOL=6.2273362E+03 TMP=2.7947726E-08 IMP:N=1
412    4  -0.15689 42 -4 U=112 VOL=7.4041184E+01 TMP=2.7947726E-08 IMP:N=1
113  113 -10.95000  1 -2 U=113 VOL=1.6791749E+03 TMP=2.7818552E-08 IMP:N=1
213  213  -2.61847  -1:4 U=113 VOL=1.8959772E+04 TMP=2.7818552E-08 IMP:N=1
313    3  -0.99447 2 -43 U=113 VOL=7.2630240E+03 TMP=2.7818552E-08 IMP:N=1
413    4  -0.15762 43 -4 U=113 VOL=8.6057747E+01 TMP=2.7818552E-08 IMP:N=1
114  114 -10.95000  1 -2 U=114 VOL=1.9370180E+03 TMP=2.7692136E-08 IMP:N=1
214  214  -2.61854  -1:4 U=114 VOL=2.1871327E+04 TMP=2.7692136E-08 IMP:N=1
314    3  -0.99513 2 -44 U=114 VOL=8.3784218E+03 TMP=2.7692136E-08 IMP:N=1
414    4  -0.15834 44 -4 U=114 VOL=9.8930704E+01 TMP=2.7692136E-08 IMP:N=1
c
c ~UNITTARGET~
1000 0 5 -6 7 -8 LAT=1 FILL=100 U=10000 TMP=2.3547E-08 IMP:N=1
1001 0 5 -6 7 -8 LAT=1 FILL=101 U=10001 TMP=2.3547E-08 IMP:N=1
1002 0 5 -6 7 -8 LAT=1 FILL=102 U=10002 TMP=2.3547E-08 IMP:N=1
1003 0 5 -6 7 -8 LAT=1 FILL=103 U=10003 TMP=2.3547E-08 IMP:N=1
1004 0 5 -6 7 -8 LAT=1 FILL=104 U=10004 TMP=2.3547E-08 IMP:N=1
1005 0 5 -6 7 -8 LAT=1 FILL=105 U=10005 TMP=2.3547E-08 IMP:N=1
1006 0 5 -6 7 -8 LAT=1 FILL=106 U=10006 TMP=2.3547E-08 IMP:N=1
1007 0 5 -6 7 -8 LAT=1 FILL=107 U=10007 TMP=2.3547E-08 IMP:N=1
1008 0 5 -6 7 -8 LAT=1 FILL=108 U=10008 TMP=2.3547E-08 IMP:N=1
1009 0 5 -6 7 -8 LAT=1 FILL=109 U=10009 TMP=2.3547E-08 IMP:N=1
1010 0 5 -6 7 -8 LAT=1 FILL=110 U=10010 TMP=2.3547E-08 IMP:N=1
1011 0 5 -6 7 -8 LAT=1 FILL=111 U=10011 TMP=2.3547E-08 IMP:N=1
1012 0 5 -6 7 -8 LAT=1 FILL=112 U=10012 TMP=2.3547E-08 IMP:N=1
1013 0 5 -6 7 -8 LAT=1 FILL=113 U=10013 TMP=2.3547E-08 IMP:N=1
1014 0 5 -6 7 -8 LAT=1 FILL=114 U=10014 TMP=2.3547E-08 IMP:N=1
c
c ~CELLTARGET~
100000 0      -100 FILL=10000 VOL=5.1161E+01 TMP=2.3547E-08 IMP:N=1 $ CRM 1
100001 0  100 -101 FILL=10001 VOL=3.5812E+02 TMP=2.3547E-08 IMP:N=1 $ CRM 2
100002 0  101 -102 FILL=10002 VOL=9.7205E+02 TMP=2.3547E-08 IMP:N=1 $ CRM 3
100003 0  102 -103 FILL=10003 VOL=1.8929E+03 TMP=2.3547E-08 IMP:N=1 $ CRM 4
100004 0  103 -104 FILL=10004 VOL=3.1208E+03 TMP=2.3547E-08 IMP:N=1 $ CRM 5
100005 0  104 -105 FILL=10005 VOL=4.6556E+03 TMP=2.3547E-08 IMP:N=1 $ CRM 6
100006 0  105 -106 FILL=10006 VOL=6.4974E+03 TMP=2.3547E-08 IMP:N=1 $ CRM 7
100007 0  106 -107 FILL=10007 VOL=8.6462E+03 TMP=2.3547E-08 IMP:N=1 $ CRM 8
100008 0  107 -108 FILL=10008 VOL=1.1102E+04 TMP=2.3547E-08 IMP:N=1 $ CRM 9
100009 0  108 -109 FILL=10009 VOL=1.3865E+04 TMP=2.3547E-08 IMP:N=1 $ CRM10
100010 0  109 -110 FILL=10010 VOL=1.6934E+04 TMP=2.3547E-08 IMP:N=1 $ CRM11
100011 0  110 -111 FILL=10011 VOL=2.0311E+04 TMP=2.3547E-08 IMP:N=1 $ CRM12
100012 0  111 -112 FILL=10012 VOL=2.3994E+04 TMP=2.3547E-08 IMP:N=1 $ CRM13
```

```
100013 0  112 -113 FILL=10013 VOL=2.7985E+04 TMP=2.3547E-08 IMP:N=1 $ CRM14
100014 0  113 -114 FILL=10014 VOL=3.2282E+04 TMP=2.3547E-08 IMP:N=1 $ CRM15
c --------------------
200000 2000 -2.618648 114 -200 VOL=1.2050E+05 TMP=2.7479460E-08 IMP:N=1 $ SHL 1
200001 2001 -2.618765 200 -201 VOL=1.6654E+05 TMP=2.7267129E-08 IMP:N=1 $ SHL 2
200002 2002 -2.618846 201 -202 VOL=2.2002E+05 TMP=2.7109776E-08 IMP:N=1 $ SHL 3
200003 2003 -2.618906 202 -203 VOL=2.8094E+05 TMP=2.6988531E-08 IMP:N=1 $ SHL 4
200004 2004 -2.618952 203 -204 VOL=3.4932E+05 TMP=2.6892189E-08 IMP:N=1 $ SHL 5
200005 2005 -2.618990 204 -205 VOL=4.2514E+05 TMP=2.6813943E-08 IMP:N=1 $ SHL 6
200006 2006 -2.619021 205 -206 VOL=5.0840E+05 TMP=2.6748969E-08 IMP:N=1 $ SHL 7
200007 2007 -2.619046 206 -207 VOL=5.9912E+05 TMP=2.6694249E-08 IMP:N=1 $ SHL 8
200008 2008 -2.619064 207 -208 VOL=6.9728E+05 TMP=2.6647543E-08 IMP:N=1 $ SHL 9
200009 2009 -2.619086 208 -209 VOL=8.0288E+05 TMP=2.6607214E-08 IMP:N=1 $ SHL10
200010 2010 -2.619098 209 -210 VOL=9.1594E+05 TMP=2.6571969E-08 IMP:N=1 $ SHL11
200011 2011 -2.619119 210 -211 VOL=1.0364E+06 TMP=2.6540946E-08 IMP:N=1 $ SHL12
200012 2012 -2.619130 211 -212 VOL=1.1644E+06 TMP=2.6513457E-08 IMP:N=1 $ SHL13
200013 2013 -2.619140 212 -213 VOL=1.2998E+06 TMP=2.6488898E-08 IMP:N=1 $ SHL14
200014 2014 -2.619151 213 -214 VOL=1.4426E+06 TMP=2.6466924E-08 IMP:N=1 $ SHL15
c --------------------
300000 3000 -2.732419 214 -300 VOL=2.3921E+07 TMP=2.6366963E-08 IMP:N=1 $ BED 1
300001 3001 -2.732423 300 -301 VOL=4.6396E+07 TMP=2.6286821E-08 IMP:N=1 $ BED 2
300002 3002 -2.732425 301 -302 VOL=7.6318E+07 TMP=2.6241925E-08 IMP:N=1 $ BED 3
300003 3003 -2.732426 302 -303 VOL=1.1369E+08 TMP=2.6213488E-08 IMP:N=1 $ BED 4
300004 3004 -2.732426 303 -304 VOL=1.5850E+08 TMP=2.6194013E-08 IMP:N=1 $ BED 5
300005 3005 -2.732427 304 -305 VOL=2.1077E+08 TMP=2.6180139E-08 IMP:N=1 $ BED 6
300006 3006 -2.732427 305 -306 VOL=2.7047E+08 TMP=2.6169884E-08 IMP:N=1 $ BED 7
300007 3007 -2.732427 306 -307 VOL=3.3763E+08 TMP=2.6162129E-08 IMP:N=1 $ BED 8
300008 3008 -2.732428 307 -308 VOL=4.1223E+08 TMP=2.6156269E-08 IMP:N=1 $ BED 9
300009 3009 -2.732317 308 -309 VOL=4.9428E+08 TMP=2.6151788E-08 IMP:N=1 $ BED10
300010 3010 -2.731948 309 -310 VOL=5.8378E+08 TMP=2.6148427E-08 IMP:N=1 $ BED11
300011 3011 -2.731676 310 -311 VOL=6.8072E+08 TMP=2.6145928E-08 IMP:N=1 $ BED12
300012 3012 -2.731450 311 -312 VOL=7.8511E+08 TMP=2.6144118E-08 IMP:N=1 $ BED13
300013 3013 -2.731236 312 -313 VOL=8.9695E+08 TMP=2.6142998E-08 IMP:N=1 $ BED14
300014 3014 -2.731013 313 -314 VOL=1.0162E+09 TMP=2.6142481E-08 IMP:N=1 $ BED15
c --------------------
400000 0 314 TMP=2.3547E-08 IMP:N=0
c ---blank line delimiter follows---

c -------------------------------SURFACE CARDS---------------------------------
c
c Fracture units (fixed per given VVF, HMVF, and SAT)
1   px 0.000    $Beginning plane of fracture
2   px 0.0465116279069767   $End of ore deposit
3   px 0.25    $End of water
```

```
4   px 0.25    $End of fracture
5   px -0.387596899224806 $Left extreme of ore
6   px 0.387596899224806  $Right extreme of ore
7   py -100000.0 $Lower extreme of repeating unit
8   py 100000.00 $Upper extreme of repeating unit
c
c ~PLANETARGET~
30 px 0.24752762
31 px 0.24752965
32 px 0.24753169
33 px 0.24753576
34 px 0.24754186
35 px 0.24754797
36 px 0.24755610
37 px 0.24756424
38 px 0.24757238
39 px 0.24758256
40 px 0.24759070
41 px 0.24760087
42 px 0.24760901
43 px 0.24761715
44 px 0.24762529
c
c ~SURFACETARGET~
100 so  2.302940
101 so  4.605880
102 so  6.908820
103 so  9.211760
104 so 11.514700
105 so 13.817640
106 so 16.120580
107 so 18.423520
108 so 20.726460
109 so 23.029400
110 so 25.332340
111 so 27.635280
112 so 29.938220
113 so 32.241160
114 so 34.544100
c --------------------
200 so 41.210767
201 so 47.877433
202 so 54.544100
203 so 61.210767
```

```
204 so 67.877433
205 so 74.544100
206 so 81.210767
207 so 87.877433
208 so 94.544100
209 so 101.210767
210 so 107.877433
211 so 114.544100
212 so 121.210767
213 so 127.877433
214 so 134.544100
c --------------------
300 so 201.210767
301 so 267.877433
302 so 334.544100
303 so 401.210767
304 so 467.877433
305 so 534.544100
306 so 601.210767
307 so 667.877433
308 so 734.544100
309 so 801.210767
310 so 867.877433
311 so 934.544100
312 so 1001.210767
313 so 1067.877433
314 so 1134.544100
c --------------------
c
c ---blank line delimiter follows---

c --------------------------------DATA CARDS-----------------------------------
c
c ----------------------------------------------------------------------------
c                               BURNUP
c ----------------------------------------------------------------------------
c ~BURNUPTARGET~
c BURN TIME=1 3 6 10 30
c     50 100 300 500 1000
c     3000 5000 10000 30000 50000
c     100000 300000 500000 1000000 3000000
c     5000000 10000000 30000000 50000000
c     POWER=0.001
c     MAT=100 101 102 103 104
```

```
c      105 106 107 108 109
c      110 111 112 113 114
c      BOPT=1.0 11 -1
c      MATVOL=3.09553E+00 2.15506E+01 5.80454E+01 1.13794E+02 1.87476E+02
c      2.78921E+02 3.89864E+02 5.19327E+02 6.65722E+02 8.31305E+02
c      1.01710E+03 1.21845E+03 1.43829E+03 1.68081E+03 1.93710E+03
c
c ----------------------------------------------------------------------------
c                                 TALLIES
c ----------------------------------------------------------------------------
c ~TALLYTARGET~
F4:N  100 101 102 103 104 105
      106 107 108 109 110
      111 112 113 114 T
F14:N 100 101 102 103 104 105
      106 107 108 109 110
      111 112 113 114 T
FM14  ( 1 100 1 )
     ( 1 100 -2 )
     ( 1 100 -6 )
c
c ----------------------------------------------------------------------------
c                                  OTFDB
c ----------------------------------------------------------------------------
c ~OTFDBTARGET~
OTFDB  92235.80c 92238.80c 8016.80c
       92234.80c 92233.80c 92236.80c
       1001.80c 6000.80c 7014.80c
       11023.80c 12024.80c 14028.80c
       15031.80c 16032.80c 18040.80c
       19039.80c 20040.80c 22048.80c
       25055.80c 26056.80c 36084.80c
       38088.80c 53127.80c 54131.80c
       13027.80c 2004.80c
c
c ----------------------------------------------------------------------------
c                                MATERIALS
c ----------------------------------------------------------------------------
c
c ENDF/B-VII CROSS SECTION LIBRARIES
c 70c 293.6K     20.45C
c 71c  600K     326.85C
c 72c  900K     626.85C
c 73c  1200K    926.85C
```

```
c 74c  2500K    2226.85C
c
c ENDF/B-VII.1 CROSS SECTION LIBRARIES
c 80c 710nc 293.6K    20.45C
c 81c 711nc  600K     326.85C
c 82c 712nc  900K     626.85C
c 83c 713nc 1200K     926.85C
c 84c 714nc 2500K     2226.85C
c 85c 715nc  0.1K     -273.05C
c 86c 716nc  250K     -23.15
c
c ----------------------------------------------------------------------------
c
c Material 1: High-grade uranium ore vein
c
c ASSUMPTIONS
c UO2 vein in fractured shale
c 15 MPa, 293K, 1.005 g/cc water
c Water is pure H20
c Densities in kg/m^3:
c    Uraninite: 10950
c    Shale:     2800
c    Water:     1005
c
c    U in UO2 S[alpha,beta]
c
c START COMPOUND MATERIAL
M100  92236.80c  5.9801E-03
      92233.80c  1.3100E-03
      92238.80c  3.0690E-01
      92234.80c  9.6668E-05
      92235.80c  1.9050E-02
       8016.80c  6.6667E-01
MT100 u-o2.20t
c --------------------
.
.
.
c --------------------
M114  92236.80c  5.9801E-03
      92233.80c  1.3100E-03
      92238.80c  3.0690E-01
      92234.80c  9.6668E-05
      92235.80c  1.9050E-02
```

```
      8016.80c  6.6667E-01
MT114 u-o2.20t
c --------------------
M200  8016.80c  5.9731E-01
     14028.80c  1.7610E-01
     22048.80c  1.9658E-04
     13027.80c  7.5149E-02
     26056.80c  2.3969E-02
     25055.80c  3.0244E-05
     12024.80c  4.1434E-03
     20040.80c  1.4073E-02
     11023.80c  3.6292E-04
     19039.80c  5.4372E-03
     15031.80c  1.2097E-04
     16032.80c  3.0244E-05
     38088.80c  8.0902E-03
      6000.80c  1.4058E-02
      1001.80c  8.0856E-02
      7014.80c  6.8375E-05
     18040.80c  5.8299E-07
     10020.80c  5.7309E-10
      2004.80c  3.2748E-11
     36084.80c  1.8353E-12
     54131.80c  1.8623E-13
     53127.80c  2.4201E-10
MT200 sio2.20t
c --------------------
.
.
.
c --------------------
M214  8016.80c  5.9673E-01
     14028.80c  1.7571E-01
     22048.80c  1.9615E-04
     13027.80c  7.4983E-02
     26056.80c  2.3916E-02
     25055.80c  3.0177E-05
     12024.80c  4.1342E-03
     20040.80c  1.4042E-02
     11023.80c  3.6212E-04
     19039.80c  5.4252E-03
     15031.80c  1.2071E-04
     16032.80c  3.0177E-05
     38088.80c  8.0723E-03
```

```
       6000.80c  1.4027E-02
       1001.80c  8.2145E-02
       7014.80c  7.2190E-05
      18040.80c  6.1551E-07
      10020.80c  6.0506E-10
       2004.80c  3.4575E-11
      36084.80c  1.9377E-12
      54131.80c  1.9662E-13
      53127.80c  2.5551E-10
MT214 sio2.20t
c --------------------
c END COMPOUND MATERIAL
c
c -----------------------------------------------------------------------------
c
c Material 2: Shale 10% porosity, initially saturated with water
c 15 MPa, 293.6 K, 1.005 g/cc water
c 2800 kg/m^3 solid density shale
c
c     Si in SiO2 S[alpha,beta] data, ENDF/B-VII.1
c     20t   293K   19.9C
c     21t   350K   76.9C
c     22t   400K  126.9C
c     23t   500K  226.9C
c     24t   800K  526.9C
c     25t   1000K 726.9C
c     25t   1200K 926.9C
c
c ~REFLECTORTARGET~
M2000  8016.80c  5.9669E-01
      14028.80c  1.7569E-01
      22048.80c  1.9612E-04
      13027.80c  7.4972E-02
      26056.80c  2.3912E-02
      25055.80c  3.0173E-05
      12024.80c  4.1336E-03
      20040.80c  1.4040E-02
      11023.80c  3.6207E-04
      19039.80c  5.4244E-03
      15031.80c  1.2069E-04
      16032.80c  3.0173E-05
      38088.80c  8.0712E-03
       6000.80c  1.4025E-02
       1001.80c  8.2226E-02
```

```
      7014.80c  7.2491E-05
     18040.80c  6.1808E-07
     10020.80c  6.0759E-10
      2004.80c  3.4719E-11
     36084.80c  1.9458E-12
     54131.80c  1.9744E-13
     53127.80c  2.5658E-10
MT2000 sio2.20t
c --------------------
.
.
.
c --------------------
M2014 8016.80c  5.9653E-01
     14028.80c  1.7558E-01
     22048.80c  1.9600E-04
     13027.80c  7.4925E-02
     26056.80c  2.3897E-02
     25055.80c  3.0154E-05
     12024.80c  4.1310E-03
     20040.80c  1.4031E-02
     11023.80c  3.6184E-04
     19039.80c  5.4210E-03
     15031.80c  1.2061E-04
     16032.80c  3.0154E-05
     38088.80c  8.0661E-03
      6000.80c  1.4016E-02
      1001.80c  8.2596E-02
      7014.80c  7.1925E-05
     18040.80c  6.1325E-07
     10020.80c  6.0284E-10
      2004.80c  3.4448E-11
     36084.80c  1.9306E-12
     54131.80c  1.9590E-13
     53127.80c  2.5458E-10
MT2014 sio2.20t
c --------------------
c
c ---------------------------------------------------------------------------
c
c Material 3: Granite 1% porosity, initially saturated with water
c 15 MPa, 293.6 K, 1.005 g/cc water
c 2750 kg/m^3 solid density granite
c
```

```
c ~BEDROCKTARGET~
M3000  8016.80c  6.1695E-01
      14028.80c  2.1522E-01
      22048.80c  8.9626E-04
      13027.80c  8.6160E-02
      26056.80c  1.2309E-02
      25055.80c  1.4938E-04
      12024.80c  2.1211E-03
      20040.80c  5.4373E-03
      11023.80c  2.2048E-02
      19039.80c  2.4617E-02
      15031.80c  7.1701E-04
       1001.80c  1.3368E-02
       7014.80c  7.2682E-06
      18040.80c  6.1971E-08
       6000.80c  2.6299E-09
      10020.80c  6.0919E-11
       2004.80c  3.4811E-12
      36084.80c  1.9509E-13
      54131.80c  1.9796E-14
      53127.80c  2.5726E-11
MT3000 sio2.20t
c --------------------
.
.
.
c --------------------
M3014  8016.80c  6.1750E-01
      14028.80c  2.1565E-01
      22048.80c  8.9805E-04
      13027.80c  8.6332E-02
      26056.80c  1.2333E-02
      25055.80c  1.4967E-04
      12024.80c  2.1254E-03
      20040.80c  5.4482E-03
      11023.80c  2.2092E-02
      19039.80c  2.4666E-02
      15031.80c  7.1844E-04
       1001.80c  1.1963E-02
       7014.80c  1.2066E-04
      18040.80c  1.0288E-06
       6000.80c  4.3659E-08
      10020.80c  1.0113E-09
       2004.80c  5.7788E-11
```

```
     36084.80c  3.2387E-12
     54131.80c  3.2863E-13
     53127.80c  4.2706E-10
MT3014 sio2.20t
c --------------------
c
c ----------------------------------------------------------------------------
c
c SET FRACTURE MATERIALS (CONSTANT DENSITY APPROACH)
c
c Material 1: Fracture rock at set saturated porosity
c Shale 10% porosity, saturated with water
c 15 MPa, 293.6 K, 1.005 g/cc water
c 2800 kg/m^3 density shale
c
c ~FRACTURE ROCK TARGET~
c M2    8016.80c  5.9606E-01
c      14028.80c  1.7526E-01
c      22048.80c  1.9564E-04
c      13027.80c  7.4789E-02
c      26056.80c  2.3854E-02
c      25055.80c  3.0099E-05
c      12024.80c  4.1235E-03
c      20040.80c  1.4006E-02
c      11023.80c  3.6118E-04
c      19039.80c  5.4111E-03
c      15031.80c  1.2039E-04
c      16032.80c  3.0099E-05
c      38088.80c  8.0514E-03
c       6000.80c  1.3991E-02
c       1001.80c  8.3722E-02
c MT2 sio2.20t
c --------------------
c
c Material 3: Fracture water
c
c    H in H2O; lwtr S[alpha,beta] data ENDF/B-VII
c    20t   293.6K
c    21t   350K
c    22t   400K
c    23t   450K
c    24t   500K
c    25t   550K
c    26t   600K
```

```
c    27t  650K
c    28t  800K
M3     1001.80c    2
       8016.80c    1
MT3    lwtr.20t
c
c ----------------------------------------------------------------------------
c
c Material 4: Fracture air
c
c ~FRACTURE AIR TARGET~
M4     1001.80c  1.8204E-06
       8016.80c  2.3305E-01
       7014.80c  7.6018E-01
      18040.80c  6.4815E-03
       6000.80c  2.7506E-04
      10020.80c  6.3715E-06
       2004.80c  3.6409E-07
      36084.80c  2.0405E-08
      54131.80c  2.0705E-09
      53127.80c  2.6906E-06
c --------------------
c
c
c ----------------------------------------------------------------------------
c                              PHYSICS
c ----------------------------------------------------------------------------
mode n
mphys on
c print 115
c ----------------------------------------------------------------------------
c                              SOURCE
c ----------------------------------------------------------------------------
kcode 5000 1.0 30 150 10000
c BEGIN SOURCE POINTS
ksrc   0.023   0.000   0.000
       0.023   1.151   0.000
       0.023  -1.151   0.000
       0.023   3.454   0.000
       0.023  -3.454   0.000
       0.023   5.757   0.000
       0.023  -5.757   0.000
       0.023   8.060   0.000
       0.023  -8.060   0.000
```

```
.
.
.
      -31.760  10.315   0.000
      -31.760 -10.315   0.000
      -32.535   0.000   0.000
      -32.535   7.520   0.000
      -32.535  -7.520   0.000
      -33.310   0.000   0.000
      -33.310   2.347   0.000
      -33.310  -2.347   0.000
      -34.085   0.000   0.000
c END SOURCE POINTS
c ---blank line terminator follows---
```

Appendix C

TOUGH2 parametric study

Parameters of the TOUGH2 code are tested for sensitivity in the final steady-state results. The default parameters and initial conditions specified in chapter 6 are employed unless otherwise noted. The source term (q_{opt}) is set such that the original steady state temperature is at the liquid-gas phase boundary ($342.155°C$). If the choice of altered parameters does not result in steady-state, results are excluded from the plots.

C.1 Effect of λ

The λ parameter in equations 6.2.10 and 6.2.11 controls the extent of saturation with which the liquid phase is mobile relative to the gas phase. Within the confines of S_{ls} and S_{lr}, larger values of λ allow water to be mobile for a given level of volumetric water content. Conversely, lower values severely hinder water conductivity even when water occupies a sizable fraction of the pore space. When this parameter is exclusively decreased in the simulation, the steady-state temperature steadily decreases as well, as shown in figure C.1.1a. The reduction in T_{max} values for low λ is caused by greater retention of water in the critical mass, which improves heat transfer to the surroundings via equation (6.2.9). Nonetheless, the scale of variation is only on the scale of degrees.

The λ term in equation (6.2.14) affects the pressure needed to reduce the water content in the pore space. Smaller values impart clay-like behavior (homogeneous particle sizes) where water is retained more strongly in the pore space with changes in pressure. Larger values impart sand-like behavior (heterogeneous particle sizes and pore openings) where water is removed more easily near the air entry value. When this parameter is increased from 0.01 (very absorbing clay) to 1 (loose gravel) exclusively in the capillary pressure function, the steady-state temperature level reaches a peak before falling dramatically. On the left hand side of this peak, heat transfer is improved due to greater retention of water in the pore space. On the right hand side, water is removed quickly enough for the system to reach a steady-state with the surroundings before temperature rises to the maximal temperature observed elsewhere.

Since a value of $\lambda = 0.5$ was applied to both functions in chapter 6, a combined test was conducted where the lambda parameter was varied for both the relative conductivity and capillary pressure functions. This approach is physically justifiable as clay-like media would be more commensurate with reducing water mobility with lower S_l, as the clay-water interaction would be stronger than the water-water intermolecular force upon desaturation. Likewise, gravel-like media would allow water to be mobile over a wider range of saturations since the cohesive forces of the water would be stronger than the adhesive forces with the pore walls in the drying path. Figure C.1.1c shows a hybridization of behaviors from the previous two plots, where it is evident that lower values of λ in either function allow for more results reaching steady-state.

The two equations of interest have since been applied on a global scale to all rocks in the system. Figure C.1.2 shows the effect of varying λ in both functions simultaneously for individual regions, while maintaining the default functions in other rocks. When the precipitate is isolated for treatment, figure C.1.2a shows that a sharper peak is obtained relative to figure C.1.1c. Temperatures in excess of T_{BP} are observed for $\lambda > 0.5$ (the original value and the value assumed for shale and granite) since the steady-state pressures are increased up to $15.5\,MPa$. This implies that high values of lambda in the precipitate allow for significant body forces to accumulate in the pore space. This is caused by the strong mobilization water in the heat-emitting region coupled with the fact that it cannot exfiltrate efficiently due to the less permeable surroundings.

When the parameters are changed for shale, figure C.1.2b demonstrates behavior intermediate of figures C.1.1c and C.1.2a. The difference in T_{max} at $\lambda = 0.02$ and $\lambda = 0.75$ is just one or two degrees.

C.2 Effect of the air entry value

The air entry value determines the pressure at which air is able to displace water in the pore space. It is thus an indicator of the ease at which a porous medium can be dried beginning at the saturated state. When P_0 in equation (6.2.14) is parametrized, figure C.2.1 shows that lower values lead to higher maximal pressures observed in the system, along with lower maximum temperatures. With a higher P_0, a stronger pressure drop is needed to bring the system below a given moisture content. This causes the minimum saturation to be higher, since it is more difficult to displace water with air. The increased water content allows for stronger heat transfer and thus lower T_{max}. There is a minimum in P_{max} at $200\,kPa$, the original value, because the choice of q_{opt} likely minimized pressure in the system relative to the corresponding temperature level.

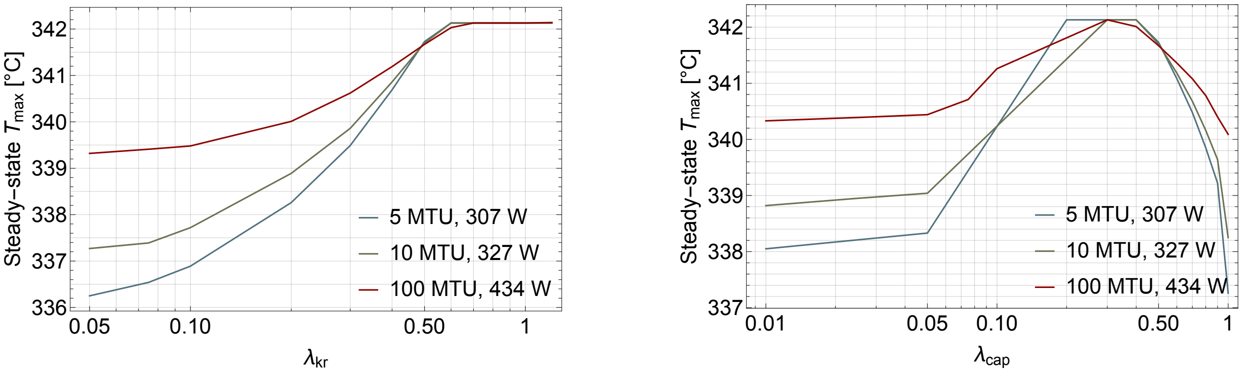

(a) λ in relative permeability function (6.2.10 and 6.2.11).

(b) λ in capillary pressure function (6.2.14).

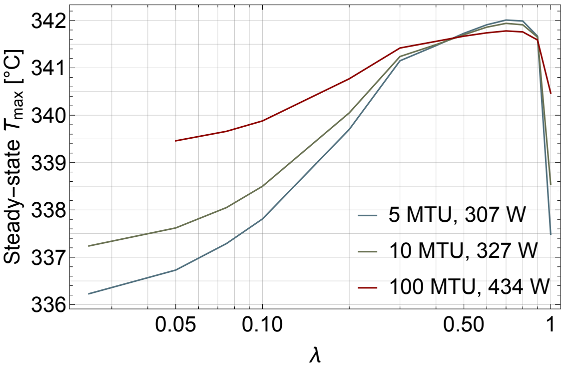

(c) Common λ in either function.

Figure C.1.1: The global effect of varying the λ parameters on the steady-state temperature level for critical depositions in the 2 wt% homogeneous configuration at q_{opt} .

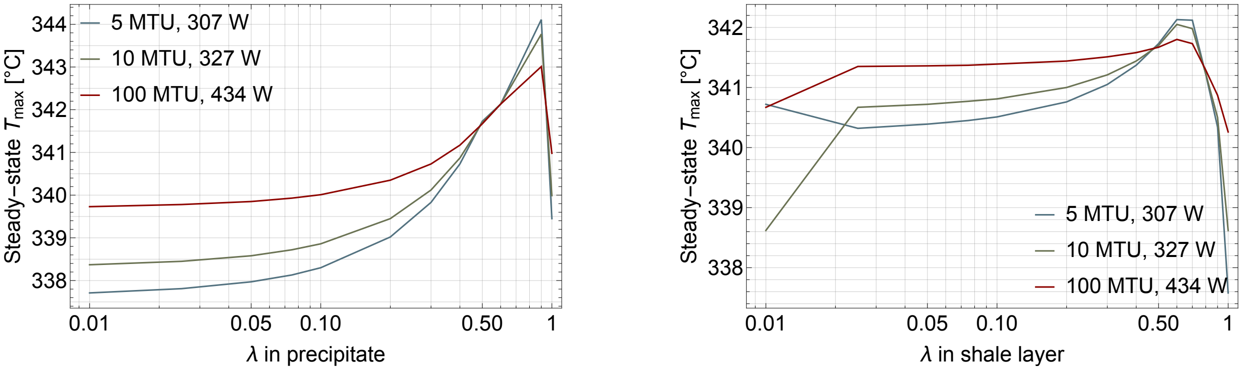

(a) Precipitate

(b) Shale

Figure C.1.2: The effect of varying λ for relative permeability and capillary pressure in certain regions for critical depositions in the 2 wt% homogeneous configuration at q_{opt}.

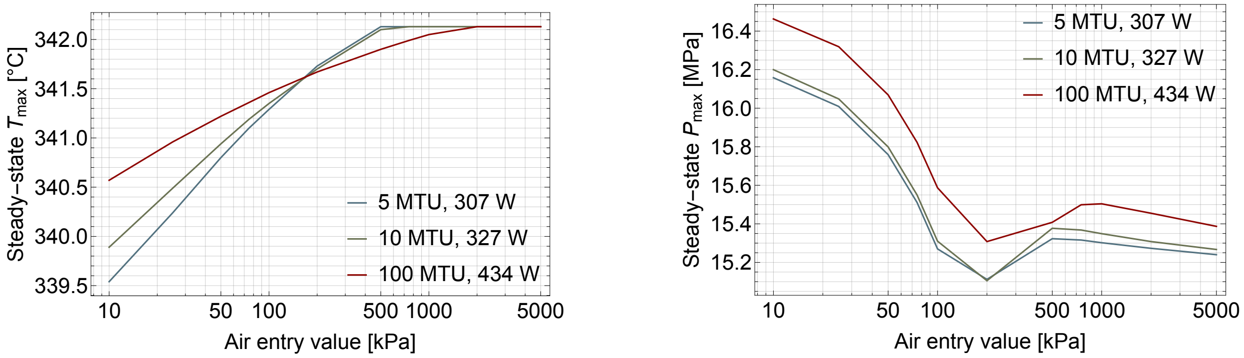

(a) T_{max} (b) P_{max}

Figure C.2.1: Effect of varying the air-entry value in equation (6.2.14) for the critical masses in the 2 wt% homogeneous system at q_{opt}.

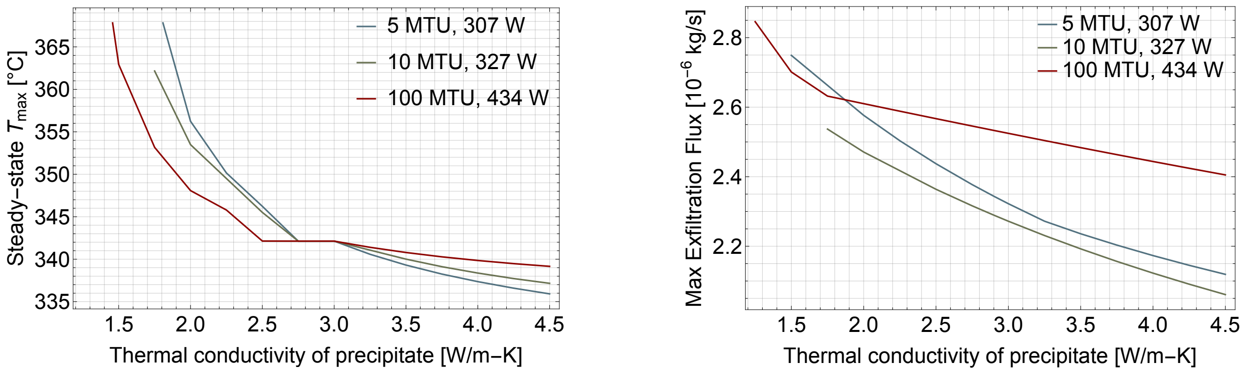

(a) T_{max} (b) Outward mass flux of liquid

Figure C.3.1: Effect of varying the wet thermal conductivity in the 2 wt% homogeneous critical masses for a fixed q_{opt}.

C.3 Effect of thermal conductivity

The thermal conductivity of the precipitate matrix is postulated to have effects on the average temperatures observed throughout the system. Values between 1.25 and 4.5 $\frac{W}{m-K}$ were chosen for the wet conductivity, and the dry conductivity was assumed to be 1 $\frac{W}{m-K}$ less than the wet value. Figure C.3.1a shows that higher values of k_{crm}^{wet} lead to lower maximum temperatures at steady-state, as would be expected. Lower conductivities lead to higher temperatures and pressures in the critical mass resulting from poorer heat transfer. This leads to higher fluxes of the pore fluid out of the system (figure C.3.1b) which leads to strong desaturation.

C.4 Discussion

The parametric study has demonstrated that the choice of λ in the thermo-hydrological evaluation was optimal for reaching high steady-state temperatures in the critical mass without modeling excessive water exfiltration rates. The stagnation of water with the choice of lower lambdas is also avoided. A reduction in the solid conductivity of the precipitate can have remarkable effects on the maximum temperature, as lower conductivity impairs heat transfer relative to a fixed heat flux and raises pressures. This elevates the boiling point and allows for full desaturation of the critical mass. An ultraconservative version of the TH study could purposely underestimate k for the precipitate to probe a broader scope of dry-out. However, these values would not be realistic for the rich ores needed for criticality.

Appendix D

Analytical studies of the QSS model

D.1 System with fuel and lasting poison at steady-state

D.1.1 Introduction

This analysis will cover a simple system comprised of U-235 and a stable neutron poison (Sm-149) in the pore space of a critical mass deposited in an infinite medium of bedrock. The initial inventory of U-235 undergoes fission and releases heat and fission products, while the quantity is replenished with a pure source of the isotope. The increase in temperature induced by fission-heating reduces the reactivity via a negative temperature feedback coefficient. The source of U-235 maintains a positive rate of change in the amount of the isotope, which increases reactivity with an assumed positive reactivity feedback coefficient.

Sm-149 is a stable neutron poison generated through rapid beta decays of the high-yield isotopes Ce-149 and Pr-149, which impart a cumulative fission yield of ~1.0% from U-235. Given its large capture cross section, Sm-149 readily absorbs neutrons and reduces the reactivity. However, the successive neutron absorptions are assumed to have no appreciable effect on the inventory of poisons. Figure (D.1.1) shows the progression of neutron absorptions, with stable isotopes shown in bold. Successive neutron capture results in stable and absorptive isotopes of samarium, or else radioactive samarium isotopes that decay to other stable, absorptive isotopes such as Eu-151 ($\sigma_c = 9184\,b$) and Eu-153 ($\sigma_c = 312\,b$). Therefore, the inventory of neutron poisons can be modeled as continuously growing from U-235 fission, and losses from neutron capture can be ignored.

D.1.2 General assumptions

1. The system is isochoric, such that negative reactivity feedback from thermal expansion is not included
2. The source term does not affect heat transfer as heavy metal accumulates in the pore space

$$ {}^{149}_{58}Ce \xrightarrow{\beta^-} {}^{149}_{59}Pr \xrightarrow{\beta^-} {}^{149}_{60}Nd \xrightarrow{\beta^-} {}^{149}_{61}Pm \xrightarrow{\beta^-} \mathbf{{}^{149}_{62}Sm} $$

$$ \mathbf{{}^{149}_{62}Sm}+n \xrightarrow{4.1e4\,b} \mathbf{{}^{150}_{62}Sm}+n \xrightarrow{1.0e2\,b} {}^{151}_{62}Sm+n \xrightarrow{1.5e3\,b} \mathbf{{}^{152}_{62}Sm}+n \xrightarrow{2.0e2\,b} {}^{153}_{62}Sm+n \xrightarrow{4.2e2\,b} \mathbf{{}^{154}_{62}Sm} $$

$$ {}^{151}_{62}Sm \xrightarrow{\beta^-} \mathbf{{}^{151}_{63}Eu},\ {}^{153}_{62}Sm \xrightarrow{\beta^-} \mathbf{{}^{153}_{63}Eu} $$

Figure D.1.1: Series of nuclear reactions on high-yield Ce-149 and Pr-149 leading to stable neutron absorbers, with stable isotopes in bold and capture cross sections shown in barns.

3. The negative reactivity feedback mechanism of expelling pore water from the critical region is assumed to be accounted in the temperature feedback term
4. The poisonous effects of generating lead via decay are ignored
5. The feedback coefficients can be modeled as constants and independent of temperature or inventory

Furthermore, specifically for this problem:

6. The quantity of poison is not reduced through neutron capture
7. The only source nuclide is U-235
8. No precursors to U-235 or Sm-149 are acknowledged, either from decay or capture
9. The temperature is steady
    a) The unsteady $MC\dot{\Delta T}$ (energy storage) term is ignored
    b) $hA\Delta T$ from Newton's Law of Cooling is the only heat transfer term
10. The critical region is effectively treated as a lumped system with uniform temperature properties per moment in time
11. The reactivity feedback coefficients are constants
    c) The coefficient for U-235 is positive ($\alpha < 0$)
    d) The coefficients for Sm-149 and temperature are negative ($\alpha_p < 0$, $\alpha_T < 0$)
12. The half-life of U-235 is long-enough to ignore the decay term

D.1.3 Initial Conditions

1. Initial mass of U-235: $n(t=0)=n_0$
2. Initial mass of poison: $n_p(t=0)=0$
3. Initial temperature difference: $\Delta T(t=0)=0$
4. Source of U-235: $\dot{S}(t)=\dot{S}$
5. Source of poison: $\dot{S}_p(t)=0$

D.1.4 Governing Equations

For the $N=2$ isotopes, there are $N+1$ coupled equations, where n is U-235 and n_p is Sm-149:

$$\begin{cases} \dot{n}=\dot{S}-\lambda n+\frac{MC\dot{\Delta T}+hA\Delta T}{N_A E_f^{25}\sigma_f^{25} n}\left(-\sigma_c^{25} n-\sigma_f^{25} n\right) \\ \dot{n}_p=\dot{S}_p+\frac{MC\dot{\Delta T}+hA\Delta T}{N_A E_f^{25}\sigma_f^{25} n}\left(-\sigma_c^{p} n_p+\gamma_{25}\sigma_f^{25} n\right) \\ \alpha\dot{n}+\alpha_p\dot{n}_p+\alpha_T\dot{\Delta T}=0 \end{cases} \tag{D.1.1}$$

There is no source of poison other than the isotopes generated from U-235 fission. Since U-235 is very long-lived, the decay term can be neglected, and the behavior of ΔT can be considered steady such that $\frac{d\Delta T}{dt}=0$.

$$\begin{cases} \dot{n}=\dot{S}+\frac{hA\Delta T}{N_A E_f^{25}\sigma_f^{25} n}\left(-\sigma_c^{25} n-\sigma_f^{25} n\right) \\ \dot{n}_p=\frac{hA\Delta T}{N_A E_f^{25}\sigma_f^{25} n}\left(-\sigma_c^{p} n_p+\gamma_{25}\sigma_f^{25} n\right) \\ \alpha\dot{n}+\alpha_p\dot{n}_p+\alpha_T\dot{\Delta T}=0 \end{cases}$$

It can be assumed that neutron capture will not affect the inventory of poisons in the system.

$$\begin{cases} \dot{n}=\dot{S}+\frac{hA\Delta T}{N_A E_f^{25}\sigma_f^{25} n}\left(-\sigma_c^{25} n-\sigma_f^{25} n\right) \\ \dot{n}_p=\frac{hA\Delta T}{N_A E_f^{25}\sigma_f^{25}}\left(\gamma_{25}\sigma_f^{25}\right) \\ \alpha\dot{n}+\alpha_p\dot{n}_p+\alpha_T\dot{\Delta T}=0 \end{cases}$$

Here, it is apparent that the rate of change of U-235 is determined by an interplay between the source term and the change in temperature, while the governing equation for poison is determined exclusively by the change in temperature and U-235 yield. Let $A=\frac{hA(\sigma_c^{25}+\sigma_f^{25})}{N_A E_f^2 5\sigma_f^{25}}\left[\frac{mol}{yr-K}\right]$ and $B=\frac{hA\gamma_{25}}{N_A E_f^{25}}\left[\frac{mol}{yr-K}\right]$ to lump the system knowns and simplify the expressions as follows:

$$\begin{cases} \dot{n}=\dot{S}-A\Delta T \\ \dot{n}_p=B\Delta T \\ \alpha\dot{n}+\alpha_p\dot{n}_p+\alpha_T\dot{\Delta T}=0 \end{cases} \tag{D.1.2}$$

D.1.5 Analysis

Solving for temperature by way of reactivity feedback

Starting with the reactivity feedback relationship from equation (0-5), which describes n, n_p, and ΔT functions of time. Since the feedback coefficients are constants, by integrating both sides with respect to time:

$$\int \left(\alpha\dot{n} + \alpha_p\dot{n}_p + \alpha_T\dot{\Delta T}\right) dt = \alpha n + \alpha n_p + \alpha_T\Delta T + \mathcal{C} = 0$$

Solving for $\mathcal{C}$ by analyzing the system at $t = 0$:

$$\alpha n_0 + \cancel{\alpha n_p(t=0)} + \cancel{\alpha_T\Delta T(t=0)} + \mathcal{C} = 0 \Rightarrow \mathcal{C} = -\alpha n_0$$

$$\therefore \alpha n + \alpha_p n_p + \alpha_T\Delta T - \alpha n_0 = 0$$

Solving for ΔT in terms of n, n_p, and system knowns:

$$\Delta T = \frac{\alpha}{\alpha_T}(n_0 - n) - \frac{\alpha_p}{\alpha_T}n_p \tag{D.1.3}$$

Removing ΔT from the equation for n by way of n_p

Returning to the equation for n, the temperature dependence can be removed by taking advantage of the simplicity of the poison relationship

$$\dot{n}_p = B\Delta T \Rightarrow \Delta T = \frac{\dot{n}_p}{B} \tag{D.1.4}$$

Inserting this into the equation for n:

$$\dot{n} = -A\left(\frac{\dot{n}_p}{B}\right) + \dot{S}$$

Integrating both sides with respect to time:

$$n = -\frac{A}{B}\int \dot{n}_p dt + \int \dot{S} dt = -\frac{A}{B}n_p + \dot{S}t + \mathcal{C}$$

Solving for $\mathcal{C}$ by analyzing the system at initial conditions:

$$n(t=0) = n_0 = \cancel{-\frac{A}{B}n_p(t=0)} + \cancel{\dot{S}\cdot 0} + \mathcal{C} \Rightarrow C = n_0$$

Therefore, n can be written in terms of n_p and knowns:

$$n = -\frac{A}{B}n_p + \dot{S}t + n_0 \tag{D.1.5}$$

Removing n from the reactivity feedback equation

The expression for $n_0 - n$ implied from equation (D.1.5) can be inserted into equation (D.1.3):

$$\Delta T = \frac{\alpha}{\alpha_T}\left(\frac{A}{B}n_p - \dot{S}t\right) - \frac{\alpha_p}{\alpha_T}n_p$$

Note that unless n_p turns out to have dependence on n_0, this part of the analysis has removed temperature dependence on the initial amount of fuel. This can be reconciled by the idea that negative temperature feedback from the initial energy released by the critical mass at $t = 0$ will immediately shut down the reactor since no positive feedback mechanism from replenishing fissile material would exist.

Separating n_p:

$$\Delta T = \left(\frac{A\alpha}{B\alpha_T} - \frac{\alpha_p}{\alpha_T}\right)n_p - \frac{\dot{S}\alpha}{\alpha_T}t$$

Multiplying both sides by B:

$$B\Delta T = \left(\frac{A\alpha}{\alpha_T} - \frac{B\alpha_p}{\alpha_T}\right)n_p - \frac{B\dot{S}\alpha}{\alpha_T}t \tag{D.1.6}$$

This conveniently allows us to replace the LHS with the governing equation for the rate of change of poison.

Removing ΔT from the reactivity feedback equation by way of n_p and then solving for n_p

Taking further advantage of equation (D.1.4), ΔT is removed from equation (D.1.6) as follows:

$$\dot{n}_p = \left(\frac{A\alpha - B\alpha_p}{\alpha_T}\right)n_p - \frac{B\dot{S}\alpha}{\alpha_T}t$$

Moving poison terms to the LHS:

$$\dot{n}_p - \left(\frac{A\alpha - B\alpha_p}{\alpha_T}\right)n_p = -\frac{B\dot{S}\alpha}{\alpha_T}t$$

Assume an integrating factor:

$$IF = \exp\left[-\int\left(\frac{A\alpha - B\alpha_p}{\alpha_T}\right)dt\right] = \exp\left(-\frac{A\alpha - B\alpha_p}{\alpha_T}t\right)$$

This is applied as:

$$\frac{d}{dt}\left[n_p \exp\left(-\frac{A\alpha - B\alpha_p}{\alpha_T}t\right)\right] = \frac{B\dot{S}\alpha}{\alpha_T}\int t\exp\left(-\frac{A\alpha - B\alpha_p}{\alpha_T}t\right)dt$$

It is known that

$$\int x e^{ax} dx = e^{ax}\left(\frac{ax-1}{a^2}\right)$$

so the integral can be solved as:

$$n_p \exp\left(-\frac{A\alpha - B\alpha_p}{\alpha_T}t\right) = \frac{B\dot{S}\alpha}{\alpha_T}\frac{\left(-\frac{A\alpha-B\alpha_p}{\alpha_T}t-1\right)}{\left(-\frac{A\alpha-B\alpha_p}{\alpha_T}\right)^2}\exp\left(-\frac{A\alpha - B\alpha_p}{\alpha_T}t\right)+\mathcal{C}$$

Moving over the exponential term from the LHS to the RHS:

$$n_p = -B\dot{S}\alpha\frac{(A\alpha - B\alpha_p)\,t + \alpha_T}{(A\alpha - B\alpha_p)^2} + \mathcal{C}\exp\left(\frac{A\alpha - B\alpha_p}{\alpha_T}t\right)$$

Solving for $\mathcal{C}$ using that fact that no poison initially exists in the system:

$$n_p(t=0) = 0 = -\frac{B\dot{S}\alpha\alpha_T}{(A\alpha - B\alpha_p)^2} + \mathcal{C} \Rightarrow \mathcal{C} = \frac{B\dot{S}\alpha\alpha_T}{(A\alpha - B\alpha_p)^2}$$

Therefore:

$$n_p = \frac{B\dot{S}\alpha}{(A\alpha - B\alpha_p)^2}\left\{(A\alpha - B\alpha_p)\,t + \alpha_T - \alpha_T\exp\left(\frac{A\alpha - B\alpha_p}{\alpha_T}t\right)\right\} \tag{D.1.7}$$

Solving for n and ΔT using the solution for n_p

Using equation equation (D.1.7) in equation (D.1.5), the equation for n is:

$$n = -\frac{A\dot{S}\alpha}{(A\alpha - B\alpha_p)^2}\left\{(A\alpha - B\alpha_p)\,t + \alpha_T - \alpha_T\exp\left(\frac{A\alpha - B\alpha_p}{\alpha_T}t\right)\right\} + \dot{S}t + n_0$$

Separating the different functions with time in the expression for n, both exponential and linear behavior can be observed:

$$n = \left(\frac{B\alpha_p}{B\alpha_p - A\alpha}\right)\dot{S}\mathbf{t} + \frac{A\dot{S}\alpha\alpha_T}{(A\alpha - B\alpha_p)^2}\exp\left(\frac{A\alpha - B\alpha_p}{\alpha_T}\mathbf{t}\right) + \left(n_0 - \frac{A\dot{S}\alpha\alpha_T}{(A\alpha - B\alpha_p)^2}\right) \tag{D.1.8}$$

Like n, the equation for temperature is now expressed completely in terms of system constants:

$$\Delta T = \left(\frac{A\alpha - B\alpha_p}{B\alpha_T}\right)\frac{B\dot{S}\alpha}{(A\alpha - B\alpha_p)^2}\left\{(A\alpha - B\alpha_p)\,t + \alpha_T - \alpha_T\exp\left(\frac{A\alpha - B\alpha_p}{\alpha_T}t\right)\right\} - \frac{\dot{S}\alpha}{\alpha_T}t$$

Simplifying, it can be seen that the linear term with time cancels out to reveal an expression that may behave like an asymptotic "production with decay" scenario:

$$\Delta T = \frac{\dot{S}\alpha}{A\alpha - B\alpha_p}\left\{1 - \exp\left(\frac{A\alpha - B\alpha_p}{\alpha_T}t\right)\right\} \tag{D.1.9}$$

D.2 Transient system with fuel and lasting poison

D.2.1 Governing equations

The scenario and assumptions from section §D.1 are repeated albeit with an acknowledgement that the transient term from energy storage is not negligible.

$$\begin{cases} \dot{n} = \dot{S} + \frac{MC_p\dot{\Delta T} + hA\Delta T}{N_A E_f^{25}\sigma_f^{25} n}\left(-\sigma_c^{25}n - \sigma_f^{25}n\right) \\ \dot{n}_p = \frac{MC_p\dot{\Delta T} + hA\Delta T}{N_A E_f^{25}\sigma_f^{25} n}\left(\gamma_{25}\sigma_f^{25}n\right) \\ \alpha\dot{n} + \alpha\dot{n}_p + \alpha_T\dot{\Delta T} = 0 \end{cases} \tag{D.2.1}$$

This is expanded as:

$$\begin{cases} \dot{n} = \dot{S} - \frac{hA\Delta T}{N_A E_f^{25}\sigma_f^{25}}\left(\sigma_c^{25} + \sigma_f^{25}\right) - \frac{MC_p\dot{\Delta T}}{N_A E_f^{25}\sigma_f^{25}}\left(\sigma_c^{25} + \sigma_f^{25}\right) \\ \dot{n}_p = \frac{hA\Delta T}{N_A E_f^{25}\sigma_f^{25}}\left(\gamma_{25}\sigma_f^{25}\right) + \frac{MC_p\dot{\Delta T}}{N_A E_f^{25}\sigma_f^{25}}\left(\gamma_{25}\sigma_f^{25}\right) \\ \alpha\dot{n} + \alpha\dot{n}_p + \alpha_T\dot{\Delta T} = 0 \end{cases}$$

Let $A = \frac{hA(\sigma_c^{25}+\sigma_f^{25})}{N_A E_f^2 5\sigma_f^{25}}\left[\frac{mol}{yr-K}\right]$, $B = \frac{MC_p\left(\sigma_c^{25}+\sigma_f^{25}\right)}{N_A E_f^{25}\sigma_f^{25}}\left[\frac{mol}{K}\right]$, $C = \frac{hA\gamma_{25}}{N_A E_f^{25}}\left[\frac{mol}{yr-K}\right]$ (not to be confused with the lumped heat capacity term), and $D = \frac{MC_p\gamma_{25}}{N_A E_f^{25}}\left[\frac{mol}{K}\right]$ to group the system knowns and simplify the expressions as follows:

$$\begin{cases} \dot{n} = \dot{S} - A\Delta T - B\dot{\Delta T} \\ \dot{n}_p = C\Delta T + D\dot{\Delta T} \\ \alpha\dot{n} + \alpha\dot{n}_p + \alpha_T\dot{\Delta T} = 0 \end{cases} \tag{D.2.2}$$

D.2.2 Analysis

Solving for temperature

The expressions for $\dot{n}$ and $\dot{n}_p$ are brought into the expression for reactivity feedback:

$$\alpha\left(\dot{S} - A\Delta T - B\dot{\Delta T}\right) + \alpha\left(C\Delta T + D\dot{\Delta T}\right) + \alpha_T\dot{\Delta T} = 0$$

The temperature terms are then separated:

$$\left(\alpha_T + \alpha_p D - \alpha B\right)\dot{\Delta T} + \left(\alpha_p C - \alpha A\right)\Delta T + \alpha S = 0$$

The higher order temperature term is then isolated:

$$\dot{\Delta T} + \frac{\alpha_p C - \alpha A}{\alpha_T + \alpha_p D - \alpha B}\Delta T + \frac{\alpha S}{\alpha_T + \alpha_p D - \alpha B} = 0$$

Let $E = \frac{\alpha_p C - \alpha A}{\alpha_T + \alpha_p D - \alpha B} \left[\frac{1}{yr}\right]$ and $F = \frac{\alpha S}{\alpha_T + \alpha_p D - \alpha B} \left[\frac{K}{yr}\right]$, such that

$$\dot{\Delta T} + E\Delta T = -F$$

Define an integrating factor $IF = \exp\left(E \int dt\right)$. By chain rule,

$$\frac{d}{dt}\left[\Delta T e^{Et}\right] = -Fe^{Et}$$

Integrating both sides with respect to t:

$$\Delta T e^{Et} = -F \int e^{Et} dt = -\frac{F}{E} e^{Et} + \mathcal{C}$$

Multiplying both sides by e^{-Et}:

$$\Delta T = -\frac{F}{E} + \mathcal{C} e^{-Et}$$

Applying the initial condition for the temperature difference:

$$\Delta T(t = 0) = 0 = -\frac{F}{E} + \mathcal{C} \Rightarrow \mathcal{C} = \frac{F}{E}$$

Therefore, the solution for temperature is:

$$\Delta T = \frac{F}{E}\left(e^{-Et} - 1\right) = \frac{\alpha S}{\alpha_p C - \alpha A}\left[\exp\left(\frac{\alpha A - \alpha_p C}{\alpha_T + \alpha_p D - \alpha B} t\right) - 1\right] \tag{D.2.3}$$

which implies that

$$\dot{\Delta T} = -Fe^{-Et} = -\frac{\alpha S}{\alpha_T + \alpha_p D - \alpha B} \exp\left(\frac{\alpha A - \alpha_p C}{\alpha_T + \alpha_p D - \alpha B} t\right) \tag{D.2.4}$$

In a manner similar to the result in section §D.1, there is no change in temperature without a source of U-235.

Solving for fuel

Since ΔT and $\dot{\Delta T}$ are known, the expression for $\dot{n}$ is determined as

$$\dot{n} = \dot{S} - \frac{AF}{E}\left(e^{-Et} - 1\right) + BFe^{-Et}$$

Integrating both sides with respect to time:

$$\int \frac{dn}{dt}dt = \dot{S}\int dt + BF\int e^{-Et}dt - \frac{AF}{E}\int \left(e^{-Et}-1\right)dt$$

$$n = \left(\dot{S}+\frac{AF}{E}\right)t + \left(\frac{AF}{E^2}-\frac{BF}{E}\right)e^{-Et} + \mathcal{C}$$

Applying the initial condition for the fuel:

$$n(t=0) = n_0 = \frac{AF}{E^2} - \frac{BF}{E} + \mathcal{C} \Rightarrow \mathcal{C} = \frac{BF}{E} - \frac{AF}{E^2}$$

Therefore, the solution for fuel is:

$$n = \left(\dot{S}+\frac{AF}{E}\right)t + \left(\frac{AF}{E^2}-\frac{BF}{E}\right)\left(e^{-Et}-1\right) \tag{D.2.5}$$

where the time derivative is confirmed to be:

$$\dot{n} = \dot{S} + \frac{AF}{E} + \left(BF - \frac{AF}{E}\right)e^{-Et} \tag{D.2.6}$$

Solving for poison

Once again, since ΔT and $\dot{\Delta T}$ are known, the expression for $\dot{n}_p$ is determined as

$$\dot{n}_p = \frac{CF}{E}\left(e^{-Et}-1\right) - DFe^{-Et}$$

Integrating both sides with respect to time results in the solution for poison:

$$\int \frac{dn_p}{dt}dt = \frac{CF}{E}\int \left(e^{-Et}-1\right)dt - DF\int e^{-Et}dt$$

$$n_p = \left(\frac{DF}{E}-\frac{CF}{E^2}\right)e^{-Et} - \frac{CF}{E}t + \mathcal{C}$$

Applying the initial condition for poison:

$$n_p(t=0) = 0 = \frac{DF}{E} - \frac{CF}{E^2} + \mathcal{C} \Rightarrow \mathcal{C} = \frac{CF}{E^2} - \frac{DF}{E}$$

Therefore, the solution for poison is:

$$n_p = \left(\frac{DF}{E}-\frac{CF}{E^2}\right)\left(e^{-Et}-1\right) - \frac{CF}{E}t \tag{D.2.7}$$

where the time derivative is confirmed to be:

$$\dot{n}_p = \left(\frac{CF}{E} - DF\right)e^{-Et} - \frac{CF}{E} \tag{D.2.8}$$

$${}^{135}_{52}Te \xrightarrow{\beta^-} {}^{135}_{53}I \xrightarrow{\beta^-} {}^{135}_{54}Xe \xrightarrow{\beta^-} \mathbf{{}^{135}_{55}Cs}$$

$${}^{135}_{54}Xe + n \overset{2.7e6\,b}{\longrightarrow} \mathbf{{}^{136}_{54}Xe} + n \overset{2.6e{-}1\,b}{\longrightarrow} {}^{137}_{54}Xe \xrightarrow{\beta^-} ...$$

Figure D.3.1: Nuclear reactions involving the burnable poison Xe-135 with long-lived isotopes in bold.

D.3 System with fuel and xenon

D.3.1 Background

This analysis will describe a system comprised of U-235 and the burnable neutron poison Xe-135 in the pore space of a homogeneous critical mass deposited in an infinite medium of bedrock. The initial inventory of U-235 isotopes undergoes fission and releases heat and fission products, while the quantity is replenished with a source. The increase in temperature caused by fission-heating reduces the reactivity due to a negative temperature feedback coefficient. The source of U-235 maintains the rate of change in the amount of U-235 positive, which increases reactivity with an assumed positive reactivity feedback coefficient. The generation of poison serves as a negative feedback effect that depreciates with decay and neutron absorptions.

Xe-135 is a radionuclide generated through rapid beta decays of the high-yield isotopes Te-135 and I-135, which impart a cumulative fission yield of 6.61% from U-235. Given its extremely large capture cross section ($2.7 * 10^6\,b$), Xe-135 readily absorbs neutrons and reduces the reactivity. However, this effect is limited by its 9 hour half-life, upon which it beta decays to long-lived yet non-poisonous Cs-135 $\left(t_{1/2} = 2.3 * 10^6\,yr,\ \sigma_c = 8.6\,b\right)$. Also, neutron absorption results in the stable yet largely non-absorptive Xe-136 ($0.261\,b$), which generates short-lived and non-absorptive isotopes of xenon if successive absorptions do take place.

D.3.2 Governing equations

The assumptions from section §D.2 and D.3 are carried over to burnable poison analysis, but in this case, the loss of poison due to absorption (σ_c^p) cannot be ignored ipso facto. Furthermore, the poison is very short-lived and forces the acknowledgment of the decay term (λ_p). These two added features result in the following set of equations:

$$\begin{cases} \dot{n} = \dot{S} + \frac{MC_p\Delta\dot{T} + hA\Delta T}{N_A E_f^{25}\sigma_f^{25} n}\left(-\sigma_c^{25} n - \sigma_f^{25} n\right) \\ \dot{n}_p = -\lambda_p n_p + \frac{MC_p\Delta\dot{T} + hA\Delta T}{N_A E_f^{25}\sigma_f^{25} n}\left(\gamma_{25}\sigma_f^{25} n - \sigma_c^p n_p\right) \\ \alpha\dot{n} + \alpha_p\dot{n}_p + \alpha_T\Delta\dot{T} = 0 \end{cases} \tag{D.3.1}$$

Expanding the governing equations to group knowns and unknowns:

$$\left\{\begin{array}{c} \dot{n} = \dot{S} - \frac{hA\left(\sigma_c^{25}+\sigma_f^{25}\right)}{N_A E_f^{25}\sigma_f^{25}}\Delta T - \frac{MC_p\left(\sigma_c^{25}\sigma_f^{25}\right)}{N_A E_f^{25}\sigma_f^{25}}\dot{\Delta T} \\ \dot{n}_p = -\lambda_p n_p + \frac{hA\gamma_{25}}{N_A E_f^{25}}\Delta T + \frac{MC_p\gamma_{25}}{N_A E_f^{25}}\dot{\Delta T} - \frac{hA\sigma_c^p}{N_A E_f^{25}\sigma_f^{25}}\left(\frac{n_p}{n}\right)\Delta T - \frac{MC_p\sigma_c^p}{N_A E_f^{25}\sigma_f^{25}}\left(\frac{n_p}{n}\right)\dot{\Delta T} \\ \alpha\dot{n} + \alpha_p\dot{n}_p + \alpha_T\dot{\Delta T} = 0 \end{array}\right. \tag{D.3.2}$$

The known quantities can be defined as:

- $A = \frac{hA\left(\sigma_c^{25}+\sigma_f^{25}\right)}{N_A E_f^{25}\sigma_f^{25}} \left[\frac{mol}{yr\text{-}K}\right]$
- $B = \frac{MC_p\left(\sigma_c^{25}+\sigma_f^{25}\right)}{N_A E_f^{25}\sigma_f^{25}} \left[\frac{mol}{K}\right]$
- $C = \frac{hA\gamma_{25}}{N_A E_f^{25}} \left[\frac{mol}{yr\text{-}K}\right]$
- $D = \frac{MC_p\gamma_{25}}{N_A E_f^{25}} \left[\frac{mol}{K}\right]$
- $E = \frac{hA\sigma_c^p}{N_A E_f^{25}\sigma_f^{25}} \left[\frac{mol}{yr\text{-}K}\right]$
- $F = \frac{MC_p\sigma_c^p}{N_A E_f^{25}\sigma_f^{25}} \left[\frac{mol}{K}\right]$

These parameters compact the equations as follows:

$$\left\{\begin{array}{c} \dot{n} = \dot{S} - A\Delta T - B\dot{\Delta T} \\ \dot{n}_p = -\lambda_p n_p + C\Delta T + D\dot{\Delta T} - E\left(\frac{n_p}{n}\right)\Delta T - F\left(\frac{n_p}{n}\right)\dot{\Delta T} \\ \alpha\dot{n} + \alpha_p\dot{n}_p + \alpha_T\dot{\Delta T} = 0 \end{array}\right. \tag{D.3.3}$$

D.3.3 Analysis

If the first order ΔT terms for energy storage are ignored, the sets of equations in equation (D.3.3) become:

$$\left\{\begin{array}{c} \dot{n} = \dot{S} - A\Delta T \\ \dot{n}_p = -\lambda_p n_p + C\Delta T - E\left(\frac{n_p}{n}\right)\Delta T \\ \alpha\dot{n} + \alpha_p\dot{n}_p + \alpha_T\dot{\Delta T} = 0 \end{array}\right. \tag{D.3.4}$$

By grouping the fuel and poison parameters into the feedback equation:

$$\alpha\left(\dot{S} - A\Delta T\right) + \alpha_p\left(-\lambda_p n_p + C\Delta T - E\left(\frac{n_p}{n}\right)\Delta T\right) + \alpha_T\dot{\Delta T} = 0$$

This is expanded as:

$$\alpha\dot{S} - \alpha A\Delta T + -\alpha_p\lambda_p n_p + \alpha_p C\Delta T - \alpha_p E\left(\frac{n_p}{n}\right)\Delta T + \alpha_T\dot{\Delta T} = 0$$

If it is assumed that the ratio between the density of poisonous nuclides to that of the fuel nuclides will always be very small, then the following simplification can be made:

$$\alpha\dot{S} - \alpha A\Delta T + -\alpha_p\lambda_p n_p + \alpha_p C\Delta T - \cancel{\alpha_p E\left(\frac{n_p}{n}\right)\Delta T}^{\approx 0} + \alpha_T\Delta\dot{T} = 0$$

At this point, only the decay term of the poison is emphasized, since the inventory is neglected. From here, isolating n_p:

$$n_p = \frac{1}{\alpha_p\lambda_p}\left[\alpha\dot{S} + \left(\alpha_p C - \alpha A\right)\Delta T + \alpha_T\Delta\dot{T}\right]$$

Differentiating both sides with respect to time:

$$\frac{dn_p}{dt} = \dot{n}_p = \frac{\left(\alpha_p C - \alpha A\right)}{\alpha_p\lambda_p}\Delta\dot{T} + \frac{\alpha_T}{\alpha_p\lambda_p}\Delta\ddot{T}$$

Now, back to the first order equation for the poison n_p is substituted:

$$\frac{\left(\alpha_p C - \alpha A\right)}{\alpha_p\lambda_p}\Delta\dot{T} + \frac{\alpha_T}{\alpha_p\lambda_p}\Delta\ddot{T} = -\frac{1}{\alpha_p}\left[\alpha\dot{S} + \left(\alpha_p C - \alpha A\right)\Delta T + \alpha_T\Delta\dot{T}\right] + C\Delta T$$

Simplifying:

$$\left(\cancel{-C + C} - \frac{\alpha A}{\alpha_p}\right)\Delta T + \left[\frac{C}{\lambda_p} - \frac{\alpha A}{\alpha_p\lambda_p} - \frac{\alpha_T}{\alpha_p}\right]\Delta\dot{T} + \frac{\alpha_T}{\alpha_p\lambda_p}\Delta\ddot{T} = -\frac{\alpha\dot{S}}{\alpha_p}$$

Isolating second order term:

$$-\frac{\alpha\lambda_p A}{\alpha_T}\Delta T + \left[\frac{C\alpha_p}{\alpha_T} - \frac{\alpha A}{\alpha_T} - \lambda_p\right]\Delta\dot{T} + \Delta\ddot{T} = -\frac{\alpha\lambda_p\dot{S}}{\alpha_T}$$

Lumping the constant coefficients into C_0, C_1, and C^*:

$$\Delta\ddot{T} + C_1\Delta\dot{T} - C_0\Delta T = -C^*$$

For the homogeneous, steady-state solution,

$$\Delta\ddot{T} + C_1\Delta\dot{T} - C_0\Delta T = 0$$

a solution of the form $\Delta T(t) = e^{at}$ can be assumed, where $\Delta\dot{T}(t) = ae^{at}$ and $\Delta\ddot{T}(t) = a^2e^{at}$. Therefore:

$$e^{rt}\left(a^2 + C_1 a - C_0\right) = 0$$

From the quadratic, where solutions are of the form $x = -b \pm \sqrt{\frac{b^2-4ac}{2a}}$, the quantity $b^2 - 4ac \to C_1^2a^2 + 4C_0a^2$ must be greater than zero unless λ_p is very large (for extremely short-lived nuclides). Therefore, the general solution should have two distinct real roots and have the form:

$$\Delta T(t) = R_1 e^{r_1 t} + R_2 e^{r_2 t}$$

where R_1 and R_2 are undetermined, and

$$\dot{\Delta T}(t) = r_1 R_1 e^{r_1 t} + r_2 R_2 e^{r_2 t}$$

If the heat generation rate from fission is essentially constant, then the first order term can be approximated as:

$$\left.\frac{d\Delta T}{dt}\right|_{t=0} \approx \frac{\dot{q}}{\rho c_p} = C_q$$

When $t = 0$,

$$\Delta T(t = 0) = 0 = R_1 + R_2$$

and

$$\dot{\Delta T}(t = 0) = C_q = r_1 R_1 + r_2 R_2$$

$$C_q = R_1\left(r_1 - r_2\right) \Rightarrow R_1 = \frac{C_q}{r_1 - r_2} \Rightarrow R_2 = \frac{C_q}{r_2 - r_1}$$

Therefore:

$$\Delta T(t) = \frac{C_q}{r_1 - r_2}\left[e^{r_1 t} - e^{r_2 t}\right]$$

which means

$$\Delta T(t) = -\frac{C_q}{\sqrt{C_1^2 + 4C_0}}\left(e^{\frac{t}{2}\left(-C_1-\sqrt{4C_0+C_1^2}\right)} - e^{\frac{t}{2}\left(-C_1+\sqrt{4C_0+C_1^2}\right)}\right), t > 0$$

This steady-state result behaves like the χ distribution in neutronics, where a peak is reached followed by a slow approach back to ambient temperature. It also allows n and n_p to be fully determined. The time of the peak temperature change (t_{peak}) is determined as:

$$t_{peak} = \frac{\ln\left[\frac{-2C_0-C_1^2-C_1\sqrt{4C_0+C_1^2}}{2C_0}\right]}{\sqrt{4C_0 + C_1^2}}$$

Appendix E

Heat transfer relationships

E.1 Solid system

Consider a spherical control volume (CV) containing a homogeneous medium having no spatial dependence of material properties and no bulk motion of particles (no convection). Within the CV, there is an infinitesimally tiny differential control volume (DV) described in terms of the radial component r, the polar angle component θ, and the azimuthal angle component φ:

$$dV = r^2 \sin\theta dr d\theta d\varphi \tag{E.1.1}$$

The conduction heat rates orthogonal to each control surface are denoted as q_r, q_θ, and q_φ, which have units of watts. The heat rates at the opposite surfaces can be found using a Taylor Series expansion without the higher-order terms:

$$q_{r+dr} = q_r + \frac{\partial q_r}{\partial r}dr + \cancel{\frac{\partial^2 q_r}{\partial r^2}dr^2} + \cancel{\cdots} \tag{E.1.2}$$

$$q_{\theta+d\theta} = q_\theta + \frac{\partial q_\theta}{\partial \theta}d\theta + \cancel{\frac{\partial^2 q_r}{\partial \theta^2}d\theta^2} + \cancel{\cdots} \tag{E.1.3}$$

$$q_{\varphi+d\varphi} = q_\varphi + \frac{\partial q_\varphi}{\partial \varphi}d\varphi + \cancel{\frac{\partial^2 q_r}{\partial \varphi^2}d\varphi^2} + \cancel{\cdots} \tag{E.1.4}$$

Let E_g $[J]$ be the source/sink term of the CV, which is the net energy generated from fission, exothermic chemical reactions, etc., balanced by endothermic, or heat-absorbing, processes. The rate of energy generated in the CV [J/yr] is described in terms of the volumetric heat generation rate $\dot{q}$ $\left[\frac{W}{m^3}\right]$, which changes over time in the critical mass ($\dot{q}(t)$):

$$\frac{dE_g}{dt} = \dot{q}(t)dV \tag{E.1.5}$$

Let E_{stored} be the total energy stored in the CV. Assuming no phase changes, the rate of energy storage is described in terms of the specific heat capacity $c_p \left[\frac{J}{kg-K}\right]$ and density of the solid $\rho \left[\frac{kg}{m^3}\right]$:

$$\frac{dE_{stored}}{dt} = \rho c_p \frac{\partial T}{\partial t} dV \tag{E.1.6}$$

where the quantity $\rho c_p \left[\frac{J}{m^3-K}\right]$ is referred to as the volumetric heat capacity and is a measure of the medium's ability to store thermal energy. The quantity $\rho c_p \frac{\partial T}{\partial t} \left[\frac{W}{m^3}\right]$ can be understood as the rate of change with respect to time of thermal energy in the medium per unit volume. The conservation of energy is described in terms of the rate of change of energy in the DV as follows:

$$\frac{dE_{stored}}{dt} = \frac{dE_{in}}{dt} - \frac{dE_{out}}{dt} + \frac{dE_g}{dt} \tag{E.1.7}$$

In terms of the quantities defined for the DV, equation (E.1.7) is restated as:

$$\rho c_p \frac{\partial T}{\partial t} dV = \dot{q}(t) dV + q_r + q_\theta + q_\varphi - q_{r+dr} - q_{\theta+d\theta} - q_{\varphi+d\varphi} \tag{E.1.8}$$

Expanding by using the first order Taylor Series expansion from equations E.1.2 through E.1.4:

$$\rho c_p \frac{\partial T}{\partial t} dV = \dot{q}(t) dV - \frac{\partial q_r}{\partial r} dr - \frac{\partial q_\theta}{\partial \theta} d\theta - \frac{\partial q_\varphi}{\partial \varphi} d\varphi \tag{E.1.9}$$

The *gradient* is defined using the nabla notation, and in spherical coordinates it is represented as:

$$\nabla f = \frac{\partial f}{\partial r}\hat{r} + \frac{1}{r}\frac{\partial f}{\partial \theta}\hat{\theta} + \frac{1}{r \sin\theta}\frac{\partial f}{\partial \varphi}\hat{\varphi} \tag{E.1.10}$$

By the definition of the gradient, the individual heat flux vectors from Fourier's Law (6.2.1) in spherical coordinates can be represented as follows, where the thermal conductivity is assumed to be isotropic:

$$q''_r = -k\tfrac{\partial T}{\partial r} \quad q''_\theta = -\tfrac{k}{r}\tfrac{\partial T}{\partial \theta} \quad q''_\varphi = -\tfrac{k}{r \sin\theta}\tfrac{\partial T}{\partial \varphi} \tag{E.1.11}$$

When these heat flux vectors are multiplied by their control surface areas, the conduction rates are found to be:

$$q_r = -kr^2 d\theta d\varphi \sin\theta \tfrac{\partial T}{\partial r} \quad q_\theta = -k \sin\theta dr d\varphi \tfrac{\partial T}{\partial \theta} \quad q_\varphi = -\tfrac{k}{\sin\theta} dr d\theta \tfrac{\partial T}{\partial \varphi} \tag{E.1.12}$$

These values are then employed in equation (E.1.9):

$$\rho c_p \frac{\partial T}{\partial t} dV =$$

$$\dot{q}(t)dV + \frac{\partial}{\partial r}\left(kr^2\frac{\partial T}{\partial r}\right)\sin\theta d\theta d\varphi dr + \frac{\partial}{\partial \theta}\left(k\sin\theta\frac{\partial T}{\partial \theta}\right)drd\varphi d\theta + \frac{\partial}{\partial \varphi}\left(k\frac{\partial T}{\partial \varphi}\right)\frac{1}{\sin\theta}drd\theta d\varphi \tag{E.1.13}$$

Separating out the dV term from both sides reveals the *heat diffusion equation in spherical coordinates*:

$$\rho c_p \frac{\partial T}{\partial t} =$$

$$\dot{q}(t) + \frac{1}{r^2}\frac{\partial}{\partial r}\left(kr^2\frac{\partial T}{\partial r}\right) + \frac{1}{r^2\sin\theta}\frac{\partial}{\partial \theta}\left(k\sin\theta\frac{\partial T}{\partial \theta}\right) + \frac{1}{r^2\sin^2\theta}\frac{\partial}{\partial \varphi}\left(k\frac{\partial T}{\partial \varphi}\right) \tag{E.1.14}$$

In general, the time rate of change of thermal energy in the CV is represented in terms of the source term and the divergence of the thermal conductivity and the temperature gradient:

$$\rho c_p \frac{\partial T}{\partial t} = \dot{q}(t) + \nabla\cdot(k\nabla T) = \dot{q}(t) + \mathrm{div}\left(k\cdot\mathrm{grad}\left(T\right)\right) \tag{E.1.15}$$

E.2 Saturated Porous medium

The heat diffusion equation allows for the temperature field in a control volume given to be determined based on boundary conditions. While the section §E.1 analysis is applicable to a homogeneous system, the porous medium containing the critical mass is a multi-phase system consisting of sandstone as the main solid, a deposition of heavy metal, and pore fluid consisting of water and air. The fluids are liable to dramatically affect heat transfer properties when considering a dry and saturated system, and acknowledging this impact requires a modification of the governing equations. For simplicity, the analysis is considered for a saturated system with water only, and then extended to a partially saturated system including air.

Consider a porous medium with porosity ϵ, which is the volume of void relative to total volume, where the pore space has a fraction ϵ taken up by uranium ceramic (ϵ_m) and the fluid (ϵ_f) such that:

$$\epsilon = \epsilon_m + \epsilon_f$$

The heat equation is applied to both the solid rock matrix (s), heavy metal deposition (m), and fluid (f) components in the whole CV. In reality, the fission source term $\dot{q}(t)$ exists only in the ore component, and the adjoining rock and fluid store and conduct heat from fission. This consideration is non-negligible for heterogeneous configurations like the fractured geometry in figure 4.3.1. However, at steady state, the generation of heat in the sphere can be considered in a global context, so to simplify the analysis, $\dot{q}(t)$ is imagined to exist in each volume fraction with the ultimate goal of approximating the sphere as a homogeneous medium. Thus, the heat diffusion relationships for the solids are listed in equations E.2.1 and E.2.2. It should be emphasized that ρ_s is the *solid* density of the rock, or the microscopic density of the mineral composition, as opposed to the *bulk* density that incorporates void-filling material.

$$(1-\epsilon)\rho_s c_{p,s}\frac{\partial T_s}{\partial t} = (1-\epsilon)\,\dot{q}(t) + (1-\epsilon)\nabla\cdot(k_s\nabla T_s) \tag{E.2.1}$$

$$\epsilon_m\rho_m c_{p,m}\frac{\partial T_m}{\partial t} = \epsilon_m\dot{q}(t) + \epsilon_m\nabla\cdot(k_m\nabla T_m) \tag{E.2.2}$$

If the pore fluid is non-stationary, the advective-diffusive heat equation must be applied. This involves acknowledging the fluid velocity vector $\vec{v} = (v_r, v_\theta, v_\varphi)$, which introduces its own contributions to the heat flux components. It should be noted that $\vec{v}$ contains information on the tortuosity (ω), which is the deviation of a flow path between two points from a straight line. Advection would modify the fluxes from equation (E.1.11) as:

$$q''_r = -k\tfrac{\partial T}{\partial r} + \rho c_p v_r T \quad q''_\theta = -\tfrac{k}{r}\tfrac{\partial T}{\partial \theta} + \rho c_p v_\theta T \quad q''_\varphi = -\tfrac{k}{r\sin\theta}\tfrac{\partial T}{\partial\varphi} + \rho c_p v_\varphi T \tag{E.2.3}$$

This modification of the fluxes results in the following relationship from the conservation of energy (E.1.9) for the pore fluid:

$$\rho c_p\frac{\partial T}{\partial t} = \dot{q}(t) + \frac{1}{r^2}\frac{\partial}{\partial r}\left(kr^2\frac{\partial T}{\partial r} - \rho c_p v_r T\right) + \frac{1}{r^2\sin\theta}\frac{\partial}{\partial\theta}\left(k\sin\theta\frac{\partial T}{\partial\theta} - \rho c_p v_\theta T\right) + \frac{1}{r^2\sin^2\theta}\frac{\partial}{\partial\varphi}\left(k\frac{\partial T}{\partial\varphi} - \rho c_p v_\varphi T\right)$$

This is the convective heat equation, which is simplified as:

$$\rho c_p\frac{\partial T}{\partial t} = \dot{q}(t) + \nabla\cdot(k\nabla T - \rho c_p\vec{v}T) = \dot{q}(t) + \mathrm{div}\,(k\mathrm{grad}T - \rho c_p\vec{v}T) \tag{E.2.4}$$

By distributive property of the divergence, this can also be expressed as:

$$\rho c_p\left[\frac{\partial T}{\partial t} + \nabla\cdot(\vec{v}T)\right] = \dot{q}(t) + \nabla\cdot(k\nabla T) \tag{E.2.5}$$

Within the critical sphere, the advective-diffusion heat equation for the pore liquid is as follows:

$$\epsilon_f \rho_f c_{p,f} \left[\frac{\partial T_f}{\partial t} + \nabla \cdot (\vec{v}_f T_f) \right] = \epsilon_f \dot{q}(t) + \nabla \cdot (k_f \nabla \epsilon_f T_f) \tag{E.2.6}$$

In order to quantify $\vec{v}_l$, the pressure gradient across the sphere would need to be analyzed. Given the low permeability of the sphere, along with low porosity and dependence on the interconnectedness of pores for system-wide convection to be applicable, the conductive properties of the pore fluid are expected far outweigh the advective properties. Therefore, the fluid can be assumed to be stationary, and the advective term can be cancelled:

$$\epsilon_f \rho_f c_{p,f} \left[\frac{\partial T_f}{\partial t} + \cancel{\nabla \cdot (\vec{v}_f T_f)} \right] = \epsilon_f \dot{q}(t) + \nabla \cdot (k_f \nabla \epsilon_f T_f) \tag{E.2.7}$$

Since the porosity is isotropic throughout the critical mass, then

$$\epsilon_f \rho_f c_{p,f} \left[\frac{\partial T_f}{\partial t} + \cancel{\nabla \cdot (\vec{v}_f T_f)} \right] = \epsilon_f \dot{q}(t) + \epsilon_f \nabla \cdot (k_f \nabla T_f) \tag{E.2.8}$$

If the components of the porous, critical sphere conduct heat in parallel within the differential volumes, then $T = T_m = T_l = T_s$ can be assumed, and the individual equations can be combined as:

$$\begin{aligned} &[\epsilon_f \rho_f c_{p,f} + \epsilon_m \rho_m c_{p,m} + (1-\epsilon) \rho_s c_{p,s}] \frac{\partial T}{\partial t} \\ &\qquad = \dot{q}(t) + \nabla \cdot [(\epsilon_f k_f + \epsilon_m k_m + (1-\epsilon) k_s) \nabla T] \end{aligned} \tag{E.2.9}$$

This effectively employs volume averages of the thermal conductivities and specific heats, where the thermal resistances of the porous components are modeled in parallel (see figure E.2.1). This effective thermal conductivity of the parallel system in shown in figure E.2.1, where an arithmetic mean is derived from the volume fractions. This should be applicable to a scenario when the heat flux interacts with the surfaces of all components at a common plane. It must be iterated that the effects of generation in UO_2 are ignored.

$$k_{||} = \epsilon_f k_f + \epsilon_m k_m + (1-\epsilon) k_s \tag{E.2.10}$$

If the heat flux passes through one component before others, then the thermal resistances would be modeled in series, as shown in figure E.2.2. If the source term effects in UO_2 continue to be ignored, the overall thermal conductivity can be modeled as a harmonic average for this scenario:

$$k_+ = \left[\frac{1-\epsilon}{k_s} + \frac{\epsilon_m}{k_m} + \frac{\epsilon_f}{k_f} \right]^{-1} \tag{E.2.11}$$

The values $k_{||}$ and k_+ show maxima and minima of the effective thermal conductivity, respectively. Using an analog between electrical and thermal conductivity, a more realistic

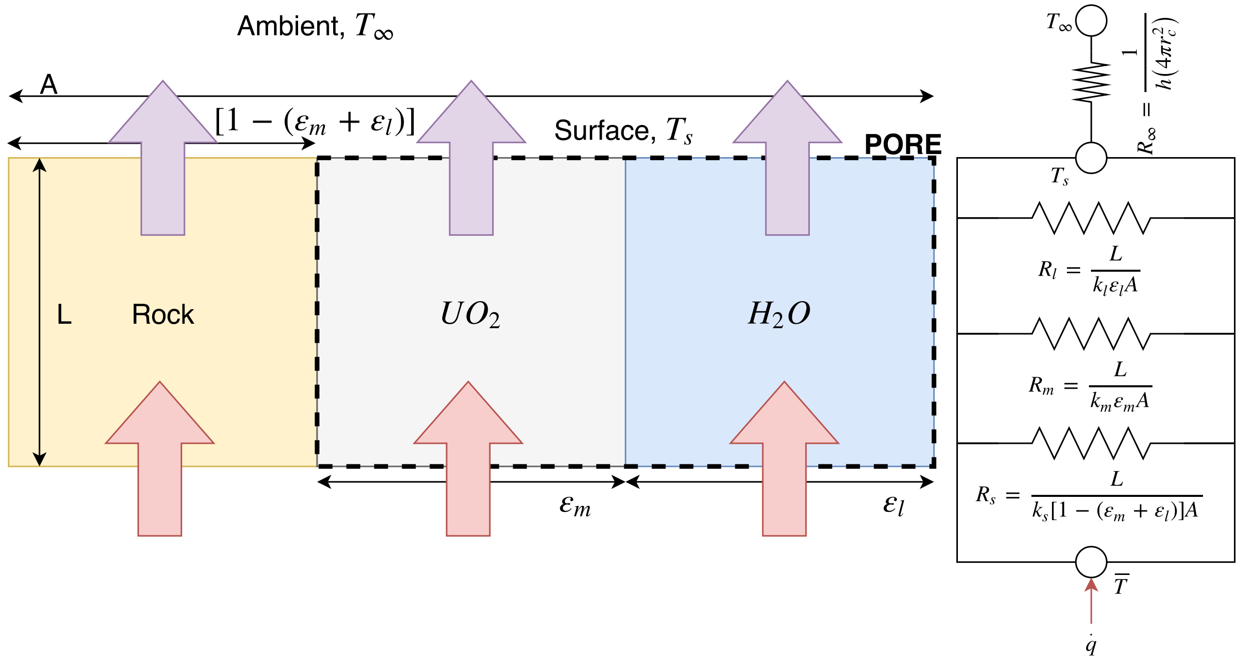

Figure E.2.1: Parallel representation of thermal resistances R in a porous medium with metal content ϵ_m and water content ϵ_l, where the source term in UO_2 is ignored.

representation of the average conductivity (k_e, not to be confused with k_{eff}) was derived by Maxwell for a solid matrix with spherical inclusions of fluid, and is shown in equation (E.2.12). [111] This expression is applicable when ϵ is a "small fraction," such that interference (in the electrical analog) is reduced by having small spherical radii relative to their separation distances. A threshold of 0.25 is suggested by Ref. [94], which accounts for the VVF of most critical masses.

$$k_e = k_s \frac{k_f + 2k_s - 2\epsilon\left(k_s - k_f\right)}{k_f + 2k_s + \epsilon\left(k_s - k_f\right)},\ \epsilon \lesssim 0.25 \tag{E.2.12}$$

To incorporate the effect of resistances caused by metal, water (l), and air (a), it is proposed that k_f be modified to include k_m, k_l, and k_a. If the thermal resistances of the pore components can be modeled in parallel, then the pore space conductivity can be described in equation (E.2.13), where S_l is the liquid saturation.

$$k_f = \frac{\epsilon_m k_m + \epsilon_f S_l k_l + \epsilon_f\left(1 - S_l\right) k_a}{\epsilon} \tag{E.2.13}$$

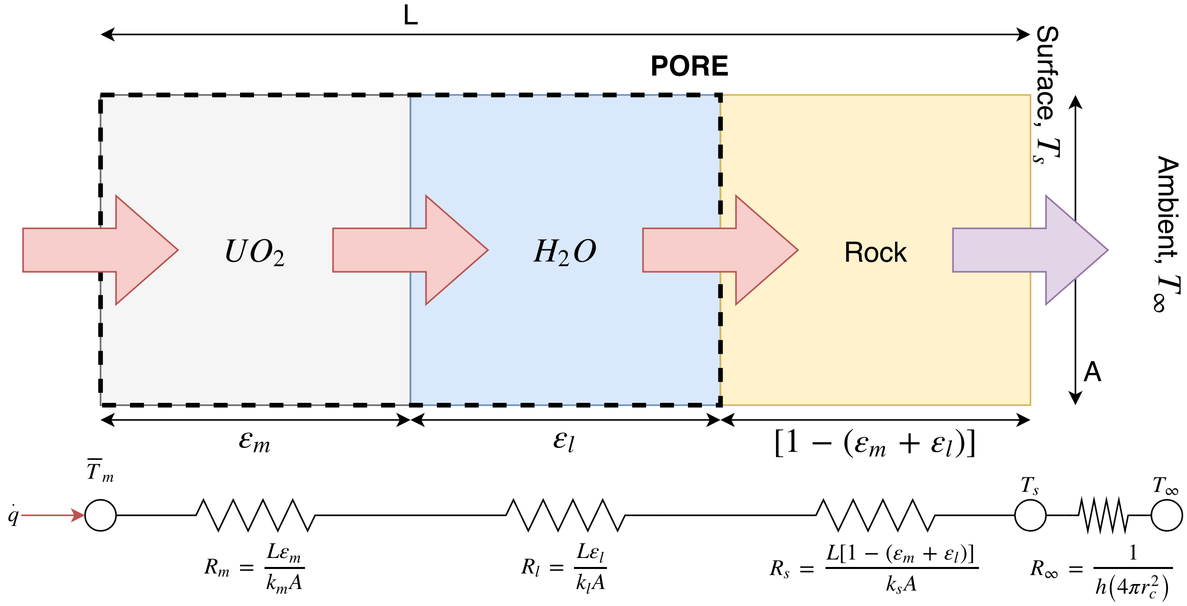

Figure E.2.2: Series representation of thermal resistances R in a porous medium with metal content ϵ_m and water content ϵ_l, where the source term in UO_2 is ignored.

Appendix F

Feedback models

Regression fit parameters for various feedback mechanisms are listed here.

F.1 Influx of U-235

Assume a critical configuration with a VVF capable of reaching $k_{eff} = 1.02$ for some HMVF and total uranium mass. A high-order polynomial fit (equation (F.1.1)) is used to model the change in reactivity observed when enriched metal is incrementally added to the void space until it is filled (i.e. when $HMVF = VVF$). The fit is applied to the reactivity in terms of the total amount in moles of U-235 added to the system, and the feedback coefficient is shown in equation (F.1.2). Results are shown in tables F.1.1 and F.1.2.

$$\rho\left(x\right) = a + bx + cx^2 + dx^3 + ex^4 + fx^5 + gx^6 \tag{F.1.1}$$

$$\frac{\partial \rho}{\partial n_{25}} = b + 2cx + 3dx^2 + 4ex^3 + 5fx^4 + 6gx^5 \tag{F.1.2}$$

F.2 Temperature

F.2.1 Piecewise function of exponential relationship and power law

A piecewise function is suggested to model the reactivity of a critical mass as the average temperature T changes within certain bounds of saturation S_l. The fit equations and associated derivatives are shown in F.2.1 and F.2.2, respectively. The first equation contains an exponential term, while the second follows a power law. Results are shown in tables F.2.1 and F.2.2. The median value of $1 + y$ is 0.76 for the homogeneous geometry and 0.78 for the fractured geometry.

$\tilde{e}$ [$wt\%$]	M_c [MTU]	VVF	HMVF	r_c [cm]	a	b	c	d	e	f	g
2	5*	0.33725	0.105	105.6	-2.00	1.91E-02	-7.31E-05	1.41E-07	-1.46E-10	7.56E-14	-1.56E-17
	10	0.33175	0.105	133.1	-1.90	9.27E-03	-1.78E-05	1.72E-08	-8.94E-12	2.34E-15	-2.46E-19
	100	0.281	0.10425	287.3	-1.82	9.91E-04	-2.17E-07	2.44E-11	-1.48E-15	4.60E-20	-5.76E-25
3	1	0.3225	0.075	69.1	-1.54	3.89E-02	-3.72E-04	1.77E-06	-4.51E-09	5.78E-12	-2.95E-15
	5	0.216	0.06	127.3	-1.23	5.92E-03	-1.11E-05	1.08E-08	-5.74E-12	1.56E-15	-1.71E-19
	10	0.1945	0.0595	160.8	-1.36	3.72E-03	-4.04E-06	2.26E-09	-6.87E-13	1.06E-16	-6.62E-21
4	0.5	0.2815	0.06	59.1	-1.12	3.49E-02	-4.17E-04	2.55E-06	-8.58E-09	1.47E-11	-1.00E-14
	1	0.222	0.06	74.4	-1.28	2.53E-02	-1.92E-04	7.37E-07	-1.54E-09	1.63E-12	-6.89E-16
	5	0.1505	0.045	140.1	-0.86	2.78E-03	-3.49E-06	2.27E-09	-7.82E-13	1.24E-16	-6.54E-21
5	0.5	0.2175	0.045	65.0	-0.97	2.25E-02	-1.98E-04	9.01E-07	-2.28E-09	2.98E-12	-1.56E-15
	1	0.1715	0.045	81.9	-1.03	1.50E-02	-8.32E-05	2.35E-07	-3.65E-10	2.92E-13	-9.39E-17
	5	0.1175	0.03	160.3	-0.56	9.84E-04	-5.13E-07	5.95E-11	4.03E-14	-1.53E-17	1.52E-21
6	0.1*	0.35975	0.045	38.0	-0.98	7.93E-02	-2.33E-03	3.25E-05	-2.35E-07	8.44E-10	-1.19E-12
	0.5	0.1805	0.03	74.4	-0.84	1.36E-02	-8.00E-05	2.39E-07	-3.97E-10	3.40E-13	-1.17E-16
	1	0.139	0.03	93.8	-0.65	6.00E-03	-2.05E-05	3.51E-08	-3.35E-11	1.65E-14	-3.22E-18
	5	0.0955	0.03	160.3	-0.20	-1.14E-04	7.48E-07	-6.73E-10	2.62E-13	-4.85E-17	3.47E-21

*Based on $k_{eff} = 1.00$

Table F.1.1: Polynomial fits of reactivity when enriched uranium is added to the pore space of critical configurations in the homogeneous geometry at $k_{eff} = 1.02$, corresponding to a functional form $\rho\left(x\right) = a + bx + cx^2 + dx^3 + ex^4 + fx^5 + gx^6$ where x is the change in moles of U-235.

$\tilde{e}$ [$wt\%$]	M_c [MTU]	VVF	HMVF	r_c [cm]	a	b	c	d	e	f	g
1.5	100	0.3075	0.16475	246.7	-3.15	3.23E-03	-1.39E-06	3.10E-10	-3.70E-14	2.24E-18	-5.39E-23
	500	0.29125	0.16425	422.3	-3.20	6.75E-04	-6.02E-08	2.78E-12	-6.89E-17	8.66E-22	-4.34E-27
	1000	0.28725	0.164	532.3	-3.24	3.46E-04	-1.57E-08	3.70E-13	-4.69E-18	3.02E-23	-7.74E-29
2	5	0.25075	0.13475	97.2	-2.64	3.77E-02	-2.34E-04	7.62E-07	-1.34E-09	1.20E-12	-4.26E-16
	10	0.21525	0.12	127.3	-2.76	1.87E-02	-5.54E-05	8.75E-08	-7.57E-11	3.36E-14	-6.01E-18
	100	0.16175	0.11625	277.1	-2.86	2.23E-03	-7.85E-07	1.51E-10	-1.61E-14	8.94E-19	-2.01E-23
3	0.5	0.32525	0.099	50.0	-1.52	9.75E-02	-2.46E-03	3.16E-05	-2.15E-07	7.39E-10	-1.01E-12
	1	0.2255	0.09	65.0	-1.76	6.04E-02	-8.78E-04	6.79E-06	-2.89E-08	6.29E-11	-5.51E-14
	5	0.10975	0.075	118.1	-1.86	1.28E-02	-3.77E-05	5.72E-08	-4.08E-11	7.61E-15	2.83E-18
	10	0.08575	0.07475	149.0	-1.28	7.33E-04	1.15E-05	-3.02E-08	3.23E-11	-1.62E-14	3.13E-18
4	0.5	0.1964	0.0749	54.9	-1.26	6.12E-02	-1.21E-03	1.26E-05	-7.12E-08	2.08E-10	-2.46E-13
	1	0.1265	0.06	74.4	-1.39	2.99E-02	-2.87E-04	1.58E-06	-5.08E-09	8.81E-12	-6.31E-15
	5	0.0564	0.0564	129.9	0.56	-1.85E-02	1.10E-04	-2.96E-07	4.17E-10	-3.00E-13	8.68E-17
	10	0.0509	0.0508	169.5	-0.66	-3.76E-04	1.30E-06	2.27E-09	-5.29E-12	3.34E-15	-6.99E-19
5	0.5	0.13125	0.05575	60.5	-1.00	3.34E-02	-4.50E-04	3.21E-06	-1.27E-08	2.66E-11	-2.33E-14
	1	0.07125	0.045	81.9	-0.13	-1.82E-02	3.67E-04	-2.87E-06	1.13E-08	-2.22E-11	1.75E-14
	5	0.035	0.035	152.3	0.47	-6.86E-03	1.78E-05	-1.14E-08	-1.56E-11	2.58E-14	-1.02E-17
	10	0.03175	0.03175	198.2	-0.95	9.76E-04	-1.32E-07	-2.13E-10	2.14E-14	6.95E-17	-2.07E-20
6	0.1	0.3225	0.06	34.5	-0.65	7.25E-02	-2.94E-03	5.82E-05	-6.12E-07	3.25E-09	-6.87E-12
	0.5	0.08125	0.045	65.0	-0.53	-3.32E-03	2.62E-04	-2.94E-06	1.43E-08	-3.26E-11	2.83E-14
	1	0.0425	0.04225	83.7	5.98	-2.77E-01	4.75E-03	-4.15E-05	1.98E-07	-4.96E-10	5.07E-13
	5	0.02825	0.02825	163.6	-0.41	1.76E-04	2.34E-07	4.98E-11	-9.65E-14	-8.78E-17	6.68E-20
	10	0.02725	0.027	209.2	-0.37	8.76E-05	5.13E-08	4.32E-12	-5.27E-15	-2.17E-18	8.30E-22

Table F.1.2: Polynomial fits of reactivity as enriched uranium is added to the pore space of critical configurations in the fractured geometry at $k_{eff} = 1.02$, corresponding to a functional form $\rho\left(x\right) = a + bx + cx^2 + dx^3 + ex^4 + fx^5 + gx^6$ where x is the change in moles of U-235.

$\tilde{e}$ $[wt\%]$	M_c $[MTU]$	a	b	c	d	x	y	z
2	5	0.0024	0.0196	-0.0148	-1.0603	-5.2900	-0.0286	4.2592
	10	0.0061	0.0198	-0.0143	-0.9515	-2.9189	-0.0439	1.8628
	100	-0.0002	0.0135	-0.0154	-1.0468	-0.1091	-0.2784	-1.2940
3	1	-0.0119	0.0096	-0.0185	-1.3427	-0.2150	-0.1868	-1.4624
	5	0.0145	0.0265	-0.0126	-0.6633	-2.9630	-0.0481	2.2420
	10	0.0167	0.0268	-0.0120	-0.5207	-0.0906	-0.3005	-1.0678
4	0.5	-0.0064	0.0147	-0.0164	-0.9966	-0.1653	-0.2089	-1.5326
	1	-0.0066	0.0118	-0.0167	-1.0738	-0.1753	-0.2269	-1.1556
	5	0.0299	0.0366	-0.0105	-0.3646	-0.1594	-0.2422	-0.7102
5	0.5	0.0074	0.0245	-0.0139	-0.8274	-0.0009	-0.8040	-1.7135
	1	0.0174	0.0268	-0.0126	-0.5809	-0.0907	-0.2751	-1.0435
	5	0.0344	0.0424	-0.0100	-0.4713	-0.1190	-0.2720	-0.5811
6	0.1	-0.0237	0.0044	-0.0208	-0.8246	-0.4426	-0.1108	-2.2340
	0.5	0.0047	0.0200	-0.0142	-0.8181	-0.1597	-0.2284	-1.0199
	1	0.0191	0.0279	-0.0120	-0.5472	-0.0518	-0.3395	-0.9519
	5	0.0568	0.0603	-0.0082	-0.2640	-0.0617	-0.3213	-0.5691

Table F.2.1: Piecewise fits of the form specified in equation (F.2.1) for the homogeneous configuration.

$$\rho(T) = \begin{cases} a - b \cdot e^{-cT+d} & 0 < S_l \leq 1 \\ z + \frac{x}{T^y} & S_l = 0 \end{cases} \tag{F.2.1}$$

$$\left.\frac{\partial \rho}{\partial T}\right|_T = \begin{cases} bc \cdot e^{-cT+d} & 0 < S_l \leq 1 \\ -\frac{xy}{T^{1+y}} & S_l = 0 \end{cases} \tag{F.2.2}$$

F.2.2 Gaussian fit

A Gaussian function is listed as an alternative to the regression model in section F.2.1. The reactivity is modeled according to equation (F.2.3), and the feedback coefficient is shown in equation (F.2.4). Results are shown in tables F.2.3 and F.2.4.

$$\rho(T) = a + \frac{d}{\sqrt{2\pi c^2}} e^{-\frac{(T-b)^2}{2c^2}} \tag{F.2.3}$$

$$\left.\frac{\partial \rho}{\partial T}\right|_T = -d \frac{T-b}{\sqrt{2\pi} c^3} e^{-\frac{(T-b)^2}{2c^2}} \tag{F.2.4}$$

$\tilde{e}$ [$wt\%$]	M_c [MTU]	a	b	c	d	x	y	z
1.5	100	0.0257	0.0105	-0.0163	-1.1107	-0.148	-0.218	-1.207
	500	0.0258	0.0077	-0.0164	-0.9235	-0.231	-0.184	-1.010
	1000	0.0233	0.0064	-0.0175	-1.0967	-0.224	-0.186	-1.008
2	5	0.0324	0.0202	-0.0136	-0.7358	-3.971	-0.028	3.021
	10	0.0334	0.0158	-0.0140	-0.7601	-2.057	-0.046	1.132
	100	0.0353	0.0223	-0.0134	-1.0293	-0.089	-0.262	-0.880
3	0.5	0.0047	0.0040	-0.0203	-0.9432	-0.181	-0.159	-1.885
	1	0.0115	0.0113	-0.0176	-1.2677	-0.003	-0.597	-1.799
	5	0.0412	0.0300	-0.0116	-0.6593	-0.668	-0.097	-0.105
	10	0.0447	0.0336	-0.0109	-0.6419	-0.077	-0.263	-0.742
4	0.5	0.0147	0.0154	-0.0161	-1.0410	-0.212	-0.156	-1.355
	1	0.0186	0.0115	-0.0157	-0.8460	-0.076	-0.251	-1.161
	5	0.0473	0.0272	-0.0109	-0.6909	-0.062	-0.255	-0.548
	10	0.0546	0.0201	-0.0117	-0.8228	-0.079	-0.226	-0.414
5	0.5	0.0223	0.0223	-0.0141	-0.8252	-0.164	-0.181	-1.191
	1	0.0242	0.0196	-0.0133	-0.6652	-0.067	-0.274	-0.940
	5	0.0549	0.0265	-0.0114	-0.9487	-0.084	-0.232	-0.414
	10	0.0478	0.0463	-0.0124	-2.0600	-0.053	-0.272	-0.379
6	0.1	-0.0009	0.0060	-0.0199	-0.8191	-0.312	-0.109	-2.404
	0.5	0.0259	0.0245	-0.0126	-0.5320	-0.132	-0.192	-0.975
	1	0.0452	0.0339	-0.0112	-0.7221	-0.086	-0.220	-0.658
	5	0.0561	0.0435	-0.0124	-2.0667	-0.049	-0.267	-0.341
	10	-7.7904	-0.7772	0.0001	2.3182	-0.078	-0.217	-0.219

Table F.2.2: Piecewise fits of the form specified in equation (F.2.1) for the fractured configuration (approach 1 in chapter 7).

F.2.3 Polynomial fit for dry configurations

A polynomial (equation (F.2.5)) was used to model the dry configurations of the fractured geometry according to approach 2. A maximum order of two was employed in regression, and feedback coefficients are linear, as shown in equation (F.2.6). Results are shown in table F.2.5.

$$\rho\left(T\right) = a + bT + cT^2 \tag{F.2.5}$$

$$\left.\frac{\partial\rho}{\partial T}\right|_T = b + 2cT \tag{F.2.6}$$

$\tilde{e}$ [$wt\%$]	M_c [MTU]	a	b	c	d
2	5	-2.248	20.45	272.7	1565.5
	10	-2.147	20.45	270.9	1484.9
	100	-2.097	20.45	276.3	1478.7
3	1	-2.306	20.45	265.9	1567.0
	5	-1.929	20.45	264.8	1300.1
	10	-1.825	20.45	-262.3	1216.4
4	0.5	-2.290	20.45	260.3	1520.5
	1	-2.043	20.45	265.8	1384.2
	5	-1.580	20.45	252.4	1010.9
5	0.5	-1.996	20.45	255.6	1299.7
	1	-1.676	20.45	248.5	1059.9
	5	-1.375	20.45	-253.5	884.1
6	0.1	-3.289	20.45	-264.6	2234.3
	0.5	-1.829	20.45	257.5	1199.0
	1	-1.513	20.45	249.2	957.5
	5	-1.141	20.45	-238.8	688.0

Table F.2.3: Gaussian fits of the form specified in equation (F.2.3) for the homogeneous configuration.

$\tilde{e}$ $[wt\%]$	M_c $[MTU]$	a	b	c	d
1.5	100	-1.927	20.45	271.0	1352.6
	500	-1.881	20.45	-269.9	1315.9
	1000	-1.872	20.45	272.2	1320.2
2	5	-1.851	20.45	261.5	1249.9
	10	-1.741	20.45	265.2	1196.3
	100	-1.458	20.45	260.1	984.5
3	0.5	-2.503	20.45	264.9	1714.4
	1	-2.070	20.45	260.6	1391.1
	5	-1.440	20.45	253.7	943.9
	10	-1.238	20.45	249.4	798.8
4	0.5	-2.030	20.45	254.5	1331.9
	1	-1.630	20.45	255.4	1074.3
	5	-0.926	20.45	247.6	601.5
	10	-0.803	20.45	253.5	546.2
5	0.5	-1.806	20.45	248.9	1155.2
	1	-1.410	20.45	247.5	897.6
	5	-0.843	20.45	255.2	574.8
	10	-0.738	20.45	261.1	517.7
6	0.1	-3.169	20.45	-260.0	2130.2
	0.5	-1.503	20.45	242.1	932.2
	1	-1.068	20.45	237.1	657.8
	5	-0.660	20.45	259.3	468.6
	10	-0.578	20.45	262.1	429.7

Table F.2.4: Gaussian fits of the form specified in equation (F.2.3) for the fractured configuration (approach 1 in chapter 7).

$\tilde{e}$ $[wt\%]$	M_c $[MTU]$	a	b	c
3	10	0.0021	-1.88E-05	-4.38E-09
4	5	0.0078	2.42E-05	-2.16E-08
	10	0.0036	3.72E-05	-2.49E-08
5	5	0.0083	7.68E-07	-1.08E-08
	10	0.0036	8.08E-06	-1.26E-08
6	1	0.0176	1.54E-06	-1.97E-08
	5	0.0211	2.50E-05	-2.13E-08
	10	0.0269	2.44E-05	-1.73E-08

Table F.2.5: Polynomial fits of the form specified in equation (F.2.5) for the fractured configuration (approach 2 in chapter 7).